Molecular modelling of species pertaining to the solvent extraction of tantalum penta-fluorides

MJ Ungerer

orcid.org 0000-0002-9073-1186

Thesis submitted in fulfilment of the requirements for the degree *Doctor of Philosophy in Chemistry* at the North-West University

Promoter:	Prof CGCE van Sittert
Co-promoter:	Prof HM Krieg
Assistant Promoter:	Mr DJ van der Westhuizen

Graduation May 2018

20068980

‘To develop a complete mind:
Study the science of art;

Study the art of science.

Develop your senses – especially learn how to see.

Realise that everything connects to everything else.’

~ Leonardo Da Vinci

‘Don’t only practice your art,

but force your way into its secrets,

for it and knowledge can raise men to the Divine.’

~ Ludwig van Beethoven

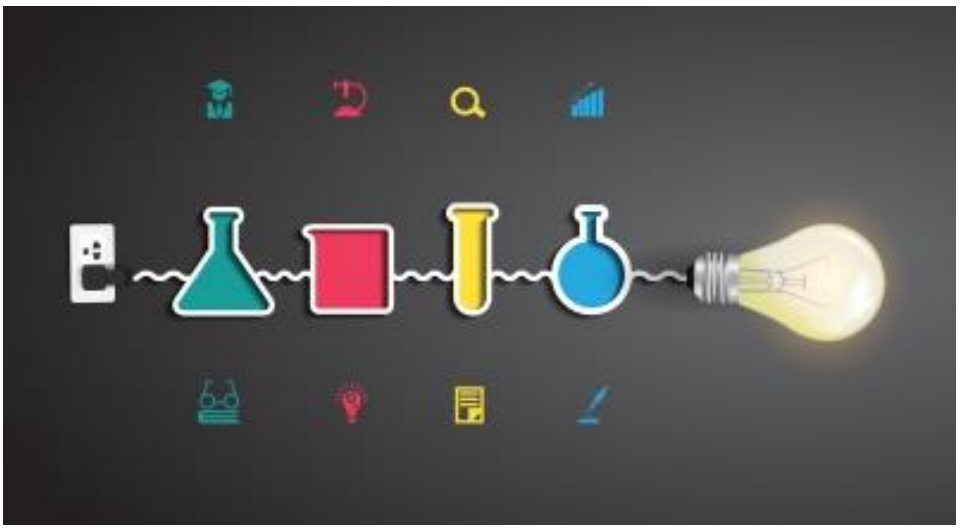

ACKNOWLEDGMENTS

Though only my name appears on the cover of this thesis, a great many people have contributed to its production. I would like to offer my special thanks and gratitude to:

- God Almighty

  He gave me the wisdom and strength to embark on this study and the perseverance to finish this project.

  "I will instruct thee and teach thee in the way which thou shalt go: I will guide thee with mine eye." *~ Psalm 32:8*

- Supervisors

  Prof. Cornie van Sittert, my research supervisor, for your professional guidance and support during this study. I appreciate all the help with regard to the modelling, the introduction into a vast new field of study and all your understanding and kindness.

  Prof. Henning Krieg, my co-supervisor, for your patient guidance, enthusiastic encouragement and useful critique during this study. I appreciate your vast knowledge and skill in many areas (e.g. vision, spiritual views, long talks about life and the journey) and your assistance in writing reports, articles and this thesis.

  Mr. Derik van der Westhuizen, for your constructive recommendations and valuable support in this project. I appreciate taking time out from your busy schedule to serve as my external reader and provider of fresh ideas.

  Dr. Johann Nel, coordinator of the New Metals Development Network (NMDN), for his valuable input and support.

- My family and friends

  My parents, Neels and Ronel Ungerer, for your unconditional love and faith in me and your support beyond measure. I appreciate all the phone calls, encouragement and weekends away to the Bushveld to gain and regain perspective.

All my friends at the NWU and in the Membrane Technology Group, for all your support and coffee sessions. Thank you for the camping weekends, it was a lot of fun.

Especially to Anzel Falch, you are my best friend. Thank you for all the coffee breaks, Skype sessions, philosophical debates, exchange of knowledge and venting of frustration during this study.

Patty (Patrizia) Cichon, my friend and sister all the way in Stuttgart, Germany. I miss our long conversations on anything and about everything. I enjoyed my visit to Germany tremendously. I hope to see you soon.

- Inanimate objects

  My Nikon camera – providing a different view to life, installing an appreciation for nature and capturing beauty beyond words.

  Coffee machine in the CRB kitchen – you were fully utilised to the maximum capacity, especially in the last months of writing this thesis.

- Financial institutions

  The South African Nuclear Energy Corporation Limited (Necsa) and the NMDN of the Advanced Metals Initiative (AMI) and the Department of Science and Technology (DST) for their financial support.

  The National Research Foundation (NRF – Grant number 89390) for their financial support.

  The Center for High Performance Computing (CHPC) in Cape Town and the North-West University High Performance Computing (NWU-HPC) center for their support and resources.

I thank you.

PREFACE

Introduction

This thesis is devoted to the field of molecular modelling in solvent extraction, i.e. molecular modelling is applied to solvent extraction in an attempt to identify and describe the species that form during solvent extraction of Ta and Nb. Since the species are a direct result of the mechanisms of solvent extraction, this study will also attempt to clarify the mechanism occurring during solvent extraction.

The thesis is submitted in chapter format, in accordance with the rules stated in the General Academic Rules (2015) for doctoral studies by the North-West University (NWU) [1]. The submitted articles written from the work done in this study were included as chapters in the thesis. The thesis will consequently not contain the conventional experimental and results and discussion chapters, but each of the experimental chapters (Chapters 3 to 6) will consist of an introduction, computational methods, results and discussion, as well as a conclusion section. The thesis, however, is still presented as a unit, as required by the General Academic Rules (2015), and therefore is supplemented with an inclusive problem statement, a literature overview and a general conclusion. Some repetition of ideas/text/figures may occur in some chapters.

Outcomes of the thesis

The framework, within which this doctoral degree is compiled, is prescribed in the faculty rules to attain the following specific outcomes [2]:

"*The student will write a thesis of high technical quality (with reference to language usage, illustrations, tables, graphic representations, etc.) that will demonstrate that the student:*

- *has skills in quantitative and qualitative research methodology and in scientific writing;*
- *is able to perform the following by integrating the above-mentioned skills and as a result of thorough investigation of existing knowledge as reflected by appropriate scientific literature:*
    - *identify a relevant research problem;*
    - *conduct the required research to solve the problem;*
    - *evaluate the results scientifically in the context of the problem statement;*

- *communicate the results scientifically.*

According to the requirements set out in the Yearbook 2015 for the Faculty of Natural Sciences, Potchefstroom Campus [3]:

"The student will demonstrate by means of a literature investigation that she has a thorough and in-depth knowledge of related scientific literature; has the ability to interpret and debate different viewpoints and theories on a scientific basis; has looked up a large enough quantity of recent and appropriate historic primary and secondary sources in the speciality area.

The student will provide proof by means of problem identification that she has a sound insight into the nature and aim of the research; has the ability to circumscribe the research topic properly at the level of a doctorate.

Apart from the literature investigation the student will demonstrate that the research method is appropriate to the speciality area in view of handling the problem identified and that the research method has been selected in a reflexive and responsible manner.

By scientific evaluation and communication of the results the student will demonstrate the following:

- *scientific processing of the thesis, with reference to the handling of appropriate quantitative or qualitative research methods and/or techniques, such as modelling, mathematical techniques of proof, experiments, observations, systematisation, founding of scientific statements, etc., as may be relevant to the problem investigated;*
- *the ability to formulate clearly; the ability to present a logical structure; a critical attitude and personal insight;*
- *the ability to formulate scientifically justified recommendations.*"

Rationale in submitting thesis in chapter format

Currently it is a prerequisite for submitting a PhD thesis for examination purposes at the NWU that one article is submitted to an ISI-accredited journal for review. The candidate prepared four articles, of which one was accepted for publication, and the other three are under review. The candidate's decision to submit in chapter format, where the four main chapters are based on the articles mentioned above, is motivated by the fact that the content of the chapters would already be peer reviewed, which will help ensure the scientific quality of the work presented.

List of articles

Ungerer, M.J., Van Sittert, C.G.C.E., Van der Westhuizen, D.J., Krieg, H.M. 2017. Molecular modelling of tantalum in an aqueous phase, *Journal of the Southern African Institute of Mining and Metallurgy* 117(6):541 – 544.

Ungerer, M.J., Van Sittert, C.G.C.E., Van der Westhuizen, D.J., Krieg, H.M. 2016. Molecular modelling of tantalum penta-halides during hydrolysis and oxidation reactions, *Computational and Theoretical Chemistry* 1090:112 – 119.

Ungerer, M.J., Van der Westhuizen, D.J., Krieg, H.M., Van Sittert, C.G.C.E. 2014. Molecular Modelling of the Hydrolysis of Tantalum and Niobium Pentafluoride, *Advanced Materials Research* Vol. 1019: 406 – 411, Trans Tech Publications, Switzerland.

De Beer, L., Ungerer, M.J., Van der Westhuizen, D.J., Krieg, H.M. 2014. The Time Dependant Solvent Extraction of Ta and Nb, *Advanced Materials Research* Vol. 1019: 433 – 438, Trans Tech Publications, Switzerland.

Ungerer, M.J., Van der Westhuizen, D.J., Lachmann, G., Krieg, H.M. 2014. Comparison of extractants for the separation of TaF_5 and NbF_5 in different acidic media, *Separation and Purification Technology* 144–145(1): 195 – 206.

List of conference outputs

Oral presentation at the Advanced Metals Initiative's (AMI) Precious Metals Development Network (PMDN) Precious Metals 2017 conference (17 – 19 October) at the Protea Hotel, Ranch Resort, Polokwane. Molecular modelling of various niobium fluoride hydrolysis and oxidation reactions.

Poster presentation at the Centre for High Performance Computing (CHPC) Annual Meeting held 5 – 9 December 2016 at ICC, East London. Output: M.J. Ungerer, D.J. van der Westhuizen, C.G.C.E. van Sittert, H.M. Krieg, 2016. Molecular modelling of tantalum pentahalides during hydrolysis and oxidation reactions.

Oral presentation at the Advanced Metals Initiative's (AMI) Ferrous and Base Metals Development Network (FMDN) Ferrous Metals 2016 conference (19 – 21 October) at the Southern Sun Elangeni & Maharani Hotel, Durban. Molecular modelling of tantalum pentahalides during hydrolysis and oxidation reactions.

Oral presentation at the 'Suid-Afrikaanse Akademie vir Wetenkap en Kuns' (SAAWK) Symposium held 27 – 28 October at North-West University, Potchefstroom Campus and obtained a certificate for second place. Output: M.J. Ungerer, D.J. van der Westhuizen, C.G.C.E. van Sittert, H.M. Krieg, 2016. 'Molekuulmodellering van tantaalpentahaliedes tydens hidrolise- en oksidasiereaksies'. ISBN: (Online) 2222-4173, (Print) 0254-3486.

Oral presentation at the 16th International Conference on Density Functional Theory and its Applications, 31 August – 4 September 2015, Debrecen, Hungary: Molecular Modelling of Tantalum Penta-Halides – A comparative DFT study, M.J. Ungerer, C.G.C.E van Sittert, D.J. van der Westhuizen, H.M. Krieg.

Oral presentation at the 5th National Research Conference on Environment and Development' 4 – 5 June 2015, Dilla University, Ethiopia. Conference Proceedings: Process for the treatment of acid mine drainage with membrane-based solvent extraction, M.J. Ungerer, G.C. du Preez, D.J. van der Westhuizen, H.M. Krieg, H. Fourie, pp. 262 – 266.

Oral presentation at the Advanced Metals Initiative's (AMI) Nuclear Materials Development Network (NMDN) Nuclear Materials 2015 conference (28 – 30 October) at the Nelson Mandela Metropolitan University, Port Elizabeth. Article output: M.J. Ungerer, C.G.C.E van Sittert, D.J. van der Westhuizen, H.M. Krieg, 2015. Molecular modelling of Tantalum in an Aqueous Phase. *Nuclear Materials 2015 Conference Proceedings*, Symposium Series S87, p. 27–32. ISBN: 978-1-920410-78-0.

Oral presentation at the Advanced Metals Initiative's (AMI) Light Metals Development Network (LMDN) Light Metals 2014 conference (15 – 17 October) at Pilanesberg National Park: Molecular Modelling of the Hydrolysis of Tantalum and Niobium Pentafluoride, M.J. Ungerer, D.J. van der Westhuizen, H.M. Krieg, C.G.C.E. van Sittert.

Oral presentation at the CHPC Annual Meeting held 1 – 5 December 2014 at Kruger National Park, Skukuza, Mpumalanga. Output: M.J. Ungerer, D.J. van der Westhuizen, C.G.C.E. van Sittert, H.M. Krieg, 2014. Investigation of solvent extraction – A DFT study.

Contributions to articles

Contributions of the various co-authors were as follows. All the modelling work, and most of the ideas and decisions were my own, with conceptual ideas and recommendations on the writing of articles by C.G.C.E. van Sittert (supervisor) and H.M. Krieg (co-supervisor), as well as recommendations on the solvent extraction, molecular modelling and writing of articles by

D.J. van der Westhuizen (auxiliary-supervisor). The co-authors give their consent to publish this work for thesis and examination purposes.

Bibliography

[1] Doctoral Degrees, General Academic Rules, North-West University, 2015, pp. 16.

[2] J.C. Geertsema, Quality Manual - Faculty of Natural Sciences, November 2014 ed., North-West University, Potchefstroom Campus, Potchefstroom, South Africa, 2014.

[3] Rules for the degree Philosophiae Doctor, Year book 2015, Faculty of Natural Sciences, Potchefstroom Campus, 2015, pp. 81-82.

ABSTRACT

Solvent extraction (SX) is used for the separation and purification of various metals, including tantalum (Ta) and niobium (Nb). Industrial processes for the separation of Ta and Nb traditionally use high concentrations of hydrofluoric acid (HF), sulphuric acid (H_2SO_4) and extractants including methyl isobutyl ketone (MIBK), making this process dangerous and detrimental to the environment. Ungerer et al. studied the separation of Ta and Nb, investigating safer chemicals and alternative techniques. During this study, separation was achieved in a H_2SO_4 medium using the extractants diisooctyl phosphinic acid (DioPA) and di-(2-ethylhexyl) phosphoric acid (D2EHPA). The main obstacle during this study remained the speciation of Ta and Nb, springing the question of why separation occurred with some extractants and not with the others. One method for determining the speciation of a reaction is by using computational techniques for molecular modelling.

Progress in computational chemistry over the last 20 years has made quantum mechanical calculations on large molecules, chemical systems as well as on macromolecule reactions possible. Calculations based on the density-functional theory (DFT) are now not only used on light elements and small molecules, but also on metal complexes, heavy metals and especially on metal separation in solvent extraction. The main current goal of computational methods for SX is the analysis of the extraction process on the molecular level, determining the molecular reactions as well as the system reactions occurring during SX from a thermodynamic point of view and thereby developing new methods for whole system analysis of the SX process of metals. The advances in computational chemistry consequently provide the possibility to determine with good approximation the outcome of proposed SX experiments before embarking on expensive, time consuming experiments and environmentally harmful waste generation.

To investigate the suitability of modelling for this application, a case study (Part 1) was selected where it was hypothesised that when TaF_5 is dissolved in water, it could react stepwise with water to finally form tantalum penta-hydroxide ($Ta(OH)_5$) and other oxyfluoride species including $TaOF_3$. Due to the fact that literature on TaF_5 reactions with water is limited, $TaCl_5$ and its reactions were used to develop the model (method). As part of the model development and verification, DFT was used to calculate the energy needed for these reactions, comparing different functionals and basis sets. The validated model was then applied to TaF_5 as a case study. From the results it was confirmed that the reaction of TaX_5 (X = Cl or F) with water to form $Ta(OH)_5$ and Ta_2O_5 is an endothermic reaction, while the formation of $Ta(H_2O)F_5$ and TaF_4OH was exothermic.

The next step (Part 2) in the study of the aqueous phase was to calculate the energy needed for various reactions of H_2SO_4 and H_2O in an aqueous phase. Again different functionals and basis set combinations were used and compared. According to the results, the deprotonation of H_2SO_4 was endothermic in a 1:1 acid-water ratio, exothermic forming HSO_4^- in a 1:5 acid-water ratio, while SO_4^{2-} formed exothermically by a double deprotonation in a 1:10 acid-water ratio. Furthermore, it was seen that hydration and dehydration of H_2SO_4 in a bulk H_2O solution was a continuous process. From the energy calculations it was determined that although the $H_2SO_4.H_2O$, $HSO_4^-.H_2O$ and $H_2SO_4.2H_2O$ species could form, they would most likely react with H_2O molecules to form HSO_4^-, H_3O^+ and H_2O.

The next step (Part 3) combined Part 1 (TaF_5 + H_2O) and Part 2 (H_2SO_4 + H_2O). The results obtained were used to attempt to predict the reaction mechanism occurring during SX. From previous modelling it was seen that by increasing the number of water molecules, the reaction energy decreased due to molecule stabilisation (hydrogen bonding) and subsequently a 1:1:10 metal:acid:water ratio was used. Results showed that in a 1:1:10 metal:acid:water ratio the deprotonation of H_2SO_4 was exothermic, leading to the formation of HSO_4^- and a lowering of the reaction energies from being endothermic to between -40 to -103 kcal/mol. Furthermore, from the various reactions and geometries between TaF_5, H_2SO_4 and H_2O investigated, it was observed that only three species will be available in the aqueous phase during solvent extraction, namely $TaF_5.H_2O$ in a water or diluted acid medium, $TaF_4.HSO_4$ in a concentrated H_2SO_4 medium and $TaF_3OH.HSO_4$ if the aqueous phase aged.

In an attempt to understand how extraction occurs, molecular dynamic simulations were used, whereby each species (identified in Part 3) was simulated in a 3D periodic box. The stoichiometry of each system was determined from previous experimental (SX) conditions and each species was investigated at 4 and 10 M H_2SO_4. Simulations started at a perfectly mixed point. The small-scale system results showed that $TaF_5.H_2O$ forms at low H_2SO_4 concentrations and can be extracted with D2EHPA in both 4 and 10 M acidic conditions. The ageing of the aqueous phase leads to the formation of TaF_4OH, which cannot be extracted with D2EHPA at either concentration. An H_2SO_4 medium leads to the formation of $TaF_4.HSO_4$, which could be extracted with D2EHPA from both 4 and 10 M H_2SO_4. The ageing of this solution results in the formation of $TaF_3OH.HSO_4$, which could not be extracted at either H_2SO_4 concentration. Furthermore, it was seen that, in the 4 M H_2SO_4 system, the aqueous phase tends to form a droplet within an organic bulk solution and when the H_2SO_4 concentration increased, both phases showed droplet properties with break-aways between the phases.

Key words: Solvent extraction, molecular modelling, tantalum, niobium, DFT, sulphuric acid.

OPSOMMING

Vloeistof-vloeistof-ekstraksie (SX) word gebruik vir die skeiding en suiwering van verskeie metale, insluitend tantaal (Ta) and niobium (Nb). Die industriële proses vir die skeiding van Ta en Nb gebruik tradisioneel hoë konsentrasies fluoorsuur (HF), swawelsuur (H_2SO_4) en ekstraheermiddels insluitend metiel-isobutiel-ketoon (MIBK), wat die proses onveilig en omgewingskadelik maak. Ungerer et al. bestudeer die skeiding van Ta en Nb, asook veiliger chemikalieë en alternatiewe tegnieke. Gedurende hierdie studie is skeiding verkry in ’n H_2SO_4-medium met die ekstraheermiddels di-iso-oktiel-fosfiensuur en di-(2-etielheksiel)-fosforsuur. Die hoofstruikelblok gedurende hierdie studie was die spesiëring van Ta en Nb, wat die vraag laat ontstaan hoekom skeiding met sommige ekstraheermiddels plaasvind en nie met ander nie. Een metode om die spesiëring van ’n reaksie te bepaal is die gebruik van berekeningstegnieke vir molekuulmodellering.

Vordering in rekenchemie oor die afgelope 20 jaar maak kwantum-meganiese berekeninge op groot molekule, chemiese stelsels asook op makromolekuulreaksies moontlik. Berekeninge gebaseer op die digtheidsfunksionaalteorie (DFT) word nou nie net op ligte elemente en klein molekule gebruik nie, maar ook op metaalkomplekse, swaarmetale en veral op metaalskeiding tydens vloeistof-vloeistof-ekstraksie. Die huidige hoofdoel van berekeningsmetodes vir vloeistof-vloeistof-ekstraksie is die analise van die ekstraksieproses op molekuulvlak, die bepaling van die molekuulreaksies sowel as die stelselreaksies wat vanuit ’n termodinamiese standpunt tydens vloeistof-vloeistof-ekstraksie plaasvind om sodoende nuwe metodes te ontwikkel vir die algehele stelselanalise van die vloeistof-vloeistof-ekstraksie proses van metale. Die vooruitgang in die rekenchemie bied gevolglik die moontlikheid om met goeie benadering die uitkoms van voorgestelde vloeistof-vloeistof-ekstraksie-eksperimente te bepaal voordat duur, tydrowende eksperimente en omgewingsskadelike afval gegenereer word.

Om die geskiktheid van modellering vir hierdie toepassing te ondersoek, is ’n gevallestudie (Deel 1) gekies waar dit veronderstel is dat wanneer TaF_5 in water opgelos word, dit stapsgewys met water kan reageer om uiteindelik tantaalpentahidroksied ($Ta(OH)_5$) en ander oksifluoriedspesies, insluitende $TaOF_3$, te vorm. As gevolg van die feit dat literatuur oor TaF_5-reaksies met water beperk is, is $TaCl_5$ en sy reaksies gebruik om die model (metode) te ontwikkel. As deel van die modelontwikkeling en -verifikasie is DFT met verskillende funksionele en basiese stelle gebruik om die energie wat nodig is vir hierdie reaksies te bereken. Die gevalideerde model is daarna op TaF_5 as ’n gevallestudie toegepas. Vanuit die resultate is bevestig dat die reaksie van TaX_5 (X = Cl of F) met water om $Ta(OH)_5$ en Ta_2O_5 te vorm ’n endotermiese reaksie is, terwyl die vorming van $Ta(H_2O)F_5$ en TaF_4OH eksotermies is.

Die volgende stap (Deel 2) in die studie van die waterfase was om die energie wat nodig is vir verskillende reaksies van H_2SO_4 en H_2O in 'n waterige fase te bereken. Weereens is verskillende funksionaal- en basisstelkombinasies aangewend en vergelyk. Volgens die resultate was die deprotonering van H_2SO_4 endotermies in 'n 1:1 suur-waterverhouding, eksotermies met die vorming van HSO_4^- in 'n 1:5 suur-waterverhouding, terwyl SO_4^{2-} eksotermies gevorm is deur 'n dubbele deprotonasie in 'n 1:10 suur-waterverhouding. Verder is daar gesien dat hidrasie en dehidrasie van H_2SO_4 in 'n oormaat H_2O-oplossing 'n deurlopende proses was. Uit die energieberekeninge is bepaal dat, hoewel die $H_2SO_4.H_2O$, $HSO_4^-.H_2O$ en $H_2SO_4.2H_2O$ spesies kan vorm, hulle waarskynlik met H_2O-molekules sou reageer om HSO_4^-, H_3O^+ en H_2O te vorm.

Die volgende stap (Deel 3) behels die kombinasie van Deel 1 (TaF_5 + H_2O) en Deel 2 (H_2SO_4 + H_2O). Die resultate wat verkry is, is gebruik om die reaksiemeganisme wat tydens SX plaasvind, te voorspel. Uit vorige modellering is gesien dat die reaksie-energie deur die toename in die aantal watermolekule verminder is as gevolg van molekuulstabilisasie (waterstofbindings) en dus is 'n 1:1:10 metaal-suur-waterverhouding gebruik. Resultate het getoon dat die deprotonering van H_2SO_4 in 'n 1:1:10-verhouding tussen metaal:suur:water eksotermies was, wat gelei het tot die vorming van HSO_4^- en 'n verlaging van die reaksie-energieë vanaf endotermies na tussen -40 tot -103 kcal/mol. Verder is daar vanuit die verskillende reaksies en geometrieë wat tussen TaF_5, H_2SO_4 en H_2O ondersoek is, waargeneem dat slegs drie spesies tydens vloeistof-vloeistof-ekstraksie in die waterfase beskikbaar sal wees, naamlik $TaF_5.H_2O$ in water of verdunde suurmedium, $TaF_4.HSO_4$ in 'n gekonsentreerde H_2SO_4 medium en $TaF_3OH.HSO_4$ indien die waterfase verouder word.

In 'n poging om te verstaan hoe ekstraksie plaasvind, is molekuuldinamika-simulasies gebruik, waardeur elke spesie (geïdentifiseer in Deel 3) in 'n 3D-periodiese boks gesimuleer is. Die stoïgiometrie van elke stelsel is bepaal uit vorige eksperimentele kondisies (vloeistof-vloeistof-ekstraksie) en elke spesie is by 4 en 10 M H_2SO_4 ondersoek. Simulasies het begin by 'n volmaakte gemengde punt. Die kleinskaal-stelsel resultate het getoon dat $TaF_5.H_2O$ by lae H_2SO_4 konsentrasies vorm en met D2EHPA in beide 4 en 10 M suur-toestande geëkstraheer kan word. Die veroudering van die waterfase lei tot die vorming van TaF_4OH, wat nie by enige van die konsentrasies met D2EHPA geëkstraheer kan word nie. 'n H_2SO_4-medium lei tot die vorming van $TaF_4.HSO_4$, wat met D2EHPA uit beide 4 en 10 M H_2SO_4 geëkstraheer kan word. Die veroudering van hierdie oplossing lei tot die vorming van $TaF_3OH.HSO_4$, wat nie by enige van die H_2SO_4 konsentrasies onttrek kan word nie. Verder is gesien dat die waterige fase in die 4 M H_2SO_4-stelsel geneig is om 'n druppel binne 'n organiese oormaat oplossing te vorm en wanneer die H_2SO_4-konsentrasie toegeneem het, het beide fases druppel-eienskappe getoon met wegbreek tussen die fases.

Sleutelwoorde: Vloeistof-vloeistof-ekstraksie, molekuulmodellering, tantaal, niobium, DFT, swawelsuur.

TABLE OF CONTENTS

List of figures

List of tables

CHAPTER 1
INTRODUCTION

1. Background and rationale

This chapter provides an introduction to the general theme of the thesis and includes a background combined with a concise literature overview, the problem statement, the aims and objectives of the study, and the methodology applied to achieve the specified aims and objectives.

Consumer electronics are used on a daily basis, especially for office productivity, communication and entertainment. The electronic industry is a major consumer of more than 40 elements for the electronic components as in Table 1.1 [1, 2].

Table 1.1 – Elements and their applications in the electronic industry [1, 2]

Elements	Applications
Aluminium	Protective oxide coatings
Antimony	Infrared detectors, diodes, batteries
Arsenic	Solid state transistors, laser material
Boron	Electrical insulator
Bromine	Fire retardation in plastic
Carbon	Plastics
Cobalt	Magnets, electroplating
Copper	Wires
Dysprosium	Reduce vibration, produce colours
Europium	Produce colours
Gadolinium	Magnets, produce colours, temperature sensors
Gold	Wires
Indium	Electricity conduction in touch screens, transistors, photoconductors
Lanthanum	Produce colours, alkali resistance in glass
Lead	Solder components, vibration reduction
Lithium	Batteries and dry cells
Neodymium	Magnets, reduce vibration, laser material
Nickel	Microphone, protective coating on other metals
Phosphorous	Semi-conductors
Potassium	Electroplating, produce colours
Praseodymium	Magnets, produce colours
Silicon	Strengthened glass screens, in semi-conductors, insulators and microchips
Silver	Wires, printed circuits, cement for glass, batteries, solder, electrical contacts
Tantalum	Capacitors, wire, electronic components
Terbium	Reduce vibration, produce colours
Tin	Electricity conduction in transparent touch screens, solder components
Yttrium	Produce colours

While Table 1.1 gives a summary of the applications of these elements in the electronic industry, these elements are also used in various other applications. In the case of tantalum (Ta) for example, about 60% of the total amount currently produced [3] is used for the production of

capacitors and electronic components. Due to the advantageous properties (high melting point (3017°C), strength and inertness), Ta is used in the nuclear industry as cladding material, in the aircraft industry as high power resistors, and to make high strength corrosion resistant alloys, cutting tools and military projectiles.

With the discovery of Ta at the beginning of the 18th century, scientists were unaware of the presence of its sister element niobium (Nb) [4]. A mineral sample was sent by John Winthrop F.R.S. from the United States to England for analysis. He called the mineral columbite after Columbia, the poetical name for the United States [5]. Therefore, elemental Ta and Nb were called columbium and only after 1866 when it was proven that two elements were present in the mineral, the names tantalum and niobium were used [3]. Similar to Ta, Nb also has a high melting point (2477 °C), is corrosion resistant and has superconductivity properties leading to high end applications including its use in super alloys for jet engines and heat resistant equipment, nuclear fuel cladding, optical lenses, medical implants and superconducting magnets [6, 7].

Metallic impurities such as iron (Fe), silicon (Si), titanium (Ti) and molybdenum (Mb) influence the super-conducting properties of Nb, while interstitial impurities such as Ta and vanadium (V) have a strong influence on the ductility and brittleness of Nb [8]. The hardness of Nb is used in industry as a sensitive indicator of purity. Two main melting methods used to produce metallic Nb are vacuum arc melting and electron-beam melting. The former method produces commercially-pure Nb with a hardness between 100 and 130 kg.mm^{-2}, while electron-beam melting provides a metal with a hardness of 45 kg.mm^{-2} [8]. Electron-beam melting introduces gaseous impurities leading to a lower metallic purity. On the other hand, if Ta is the main product with Nb as an impurity, the tensile strength of Ta decreases especially at high temperatures [9]. In concentrated hydrogen environments, Nb can absorb up to 222 ppm hydrogen and Ta up to 100 ppm leading to brittleness and metal failure. By using pure Ta and adding Tungsten (W) the effect of hydrogen absorption resistance and corrosion resistance increases [10].

Due to the similarities between the chemical and physical properties of Ta and Nb, separation has been problematic since their discovery. There are various methods available for the separation of these two metals [7] of which solvent extraction (SX) is used most frequently [7]. Traditional SX processes of Ta and Nb use the extractants methyl isobutyl ketone (MIBK) and tri-butyl phosphate (TBP) [7, 11]. MIBK gives separation factors up to 1600 for various metals [11] and purity up to 99% [7], is selective towards selenium (Se), tellurium (Te), antimony (Sb), zirconium (Zr), hafnium (Hf), Ta and Nb [12, 13], and is non-selective towards impurities such as calcium (Ca), manganese (Mn), copper (Cu), aluminium (Al), Ti and Fe [11, 12]. Furthermore, MIBK is available in a pure state in bulk quantities at reasonable cost [14] compared to other extractants. On the other hand, the disadvantages of MIBK include its low flash point (15°C) which

can result in explosions [15], health and environmental problems [16] and difficulties during phase separation caused by its high density [17].

The advantages of TBP are similar to those of MIBK, which include the cost on industrial scale, the selectivity towards the separation of rare earth metals, Zr, Hf, Ta and Nb [13] and it is non-volatile at room temperature [18]. However, TBP has a high viscosity, and when diluted with an inert diluent, water is dissolved to some extent into the organic phase [18]. An inert diluent that is commonly used in industry is kerosene [7] (a cost effective by-product from the petrochemical industry), with a viscosity below 2 mPa.s, boiling point between 420 K and 520 K, density ranging from 750 $kg.m^{-3}$ to 900 $kg.m^{-3}$ and a flash point temperature at least 25 K higher than the working temperature of the plant [19]. The main disadvantage, however, of using kerosene as diluent for TBP in the presence of concentrated nitric acid (HNO_3), is the possible formation of the explosive red oil [20, 21]. Various studies have been conducted to circumvent these disadvantages in commercial plants by, for example, using other extractants like D2EHPA (di-2-ethylhexyl phosphoric acid), DioPA (di-iso-octyl-phosphinic acid) [22] and ionic liquids [23].

In a recent study, Ungerer et al. [22] studied the SX-based separation of Ta and Nb using alternative and safer chemicals while investigating the suitability of membrane-based solvent extraction (MBSX). While partial separation of Ta and Nb was achieved, it was not possible to predict extraction behaviour prior to experimental testing due to the current absence of speciation data for Ta and Nb. A possible reason for the absence of speciation data may be due to their insolubility in most aqueous liquids [24, 25] and because they are UV inactive, making the detection and identification of the aqueous species difficult. An alternative method that could, however, be suitable for predicting the speciation and hence extraction of Ta and Nb is molecular modelling [26]. Applying molecular modelling to SX could, for example, entail a step-by-step analysis of the extraction process on a molecular level, thereby determining the molecular properties as well as the system reactions occurring during SX.

During the experimental screening to determine the optimum variables, including the type and concentration of acid, type and concentration of the extractant, diluent, E/M ratio and extraction time, significant amounts of chemicals are used which have both cost and waste implications. Again, molecular modelling might be a beneficial tool to determine the mechanism underlying the SX, while simultaneously reducing the experimental cost and time and minimising the environmental impact.

Additional advantages of using molecular modelling include accurate control over virtual experimental conditions, unlimited characterisation capabilities and high accuracy predictions [27]. Molecular modelling can be used to calculate molecular properties such as the structures of ground, excited and transition states, atomic charges and electrostatic potentials, bond energies

and reaction energies, dipole moments, polarisabilities and hyperpolarisabilities, vibrational frequencies (infrared and Raman spectra) and NMR chemical shifts. These could then be used to identify reaction pathways and mechanisms [28].

The disadvantages of using molecular modelling are that it is computer intensive, limited by computational resources and cannot predict effects not included in the simulation [27]. In addition, calculations can be performed on any system, even those that do not exist. Therefore, choosing a system to model requires some underlying verification based on either experimental or other modelling data [28].

2. Problem statement

SX, also known as liquid-liquid extraction, is a separation method based on the relative solubility of two or more compounds in two immiscible or partly immiscible liquids. These two immiscible liquids are usually water (forming the aqueous phase) and an organic solution (which forms the organic phase). Extraction is ideally achieved if one of the compounds is retained in the one liquid phase and the other compound(s) is extracted into the other liquid phase.

In a previous study, Ungerer et al. [22, 29] showed that the separation of Ta and Nb was possible with SX using sulphuric acid (H_2SO_4) in the aqueous phase, with phosphorous-based extractants (D2EHPA and DioPA) diluted with cyclohexane in the organic phase. The three most crucial parts in the understanding of the mechanistic extraction of Ta/Nb are the understanding of 1) the aqueous chemistry of the Ta and Nb species in acidic aqueous solutions; 2) the extractant (or active analogue) available for extraction in the organic solvent and 3) the interaction between the aqueous solute species and the extractant in the organic solvent on a molecular level.

The extraction mechanism with D2EHPA is well known for metallic ions with a 2+ [12, 30] and 4+ oxidation state [31-33], but Ta and Nb both are in the 5+ oxidation state. Numerous studies have been done on the SX of Ta and Nb [7, 11, 34], but no model exists to theoretically explain the three points stated above. Although some species of Ta and Nb in acidic media have been identified [3], the actual speciation both in the acidic media as well as during the extraction process is unknown. Hence experimental studies continue on a trial-and-error basis, showing the need for more theoretical insight.

An alternative method that could, however, be suitable for predicting the speciation and hence the extraction of Ta and Nb is molecular modelling [26], from which a theoretical model may be developed for future predictions of ligand choices (in both the aqueous and organic phases) and

possible differences between Ta and Nb to increase the separation efficiency of specific SX systems.

3. Aim and objectives

In view of the above mentioned, the aim of this study was the use of molecular modelling to investigate the SX process of Ta on a molecular level, comparing the theoretical obtained data with experimental data. To achieve this aim, the following objectives where identified:

i. Geometry optimisation of all the components (metal species, ions, acids and extractants) involved in the SX process.
ii. Compiling energy profiles to investigate various reaction equations to determine the most probable reaction pathway and the subsequent mechanisms of SX.
iii. Simulation of the organic and aqueous phases in periodic systems (creating unit cells).
iv. Combining the periodic organic and aqueous phases to simulate the SX process.
v. Comparing experimental SX results with the modelled SX results.

4. Outline of thesis

A visual representation of the thesis outline is given in Figure 1.1. **Chapter 1** includes an introduction to this study consisting of a short background on Ta and Nb, a problem statement, as well as a section stating the aim and objectives of this study followed by the outline of the thesis.

Chapter 2 gives a literature overview introducing the history of molecular modelling and the type of modelling to be used. The basic theory of SX is discussed with reference specifically to the Ta/Nb system and the modelling of the SX system.

Chapter 3 entails a model development and its verification, which was done by comparing experimental data of tantalum(V) chloride ($TaCl_5$) reactions with modelled data of $TaCl_5$ reactions — both in water. The model that closely represented the experimental $TaCl_5$ data was applied to a case study of tantalum(V) fluoride (TaF_5) reactions in water. From this the species with the highest probability to form were identified.

Chapter 4 covers the development and verification of a model of sulphuric acid reactions in a water phase.

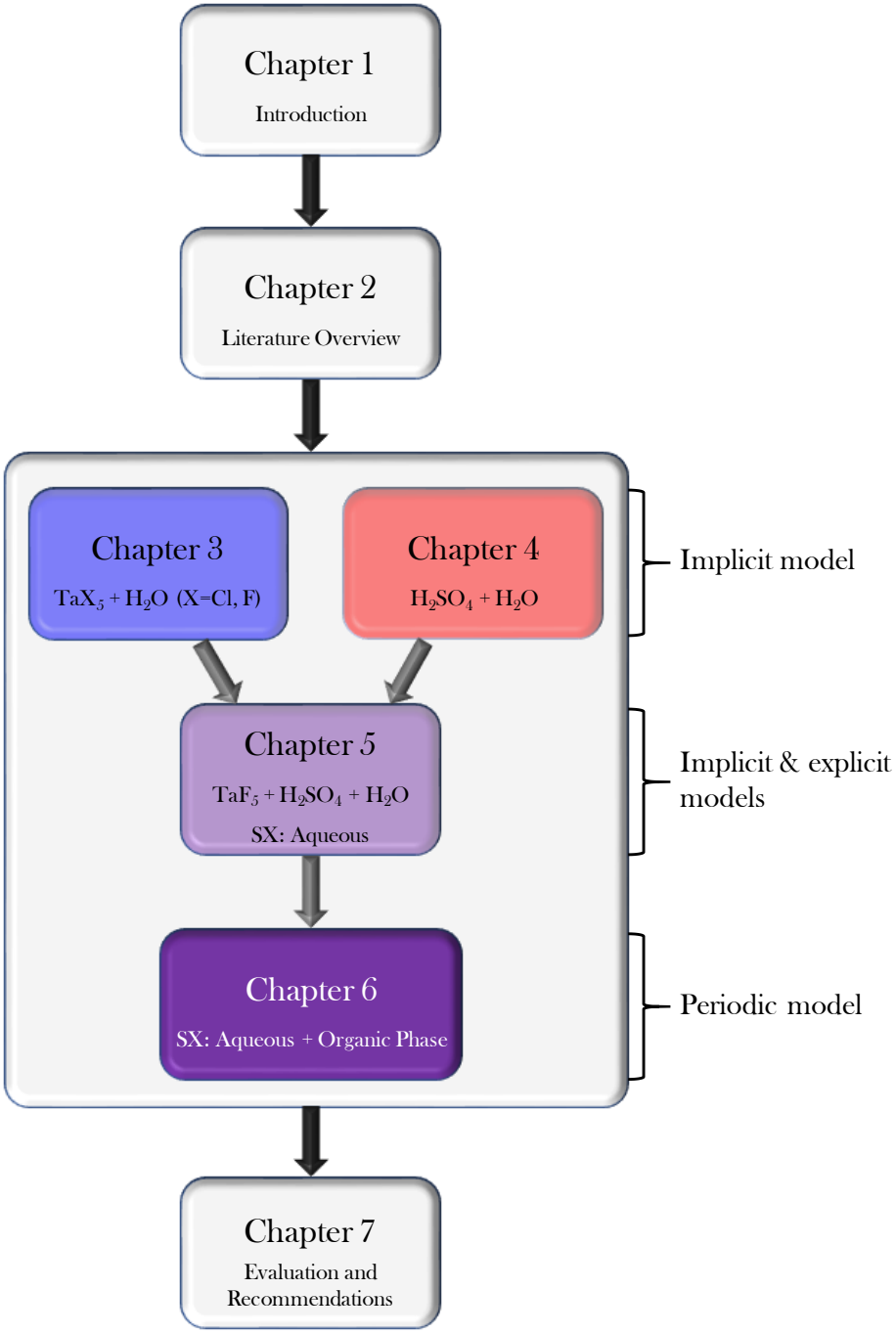

Figure 1.1 – Outline of thesis

The species identified in Chapter 3 were further optimised in **Chapter 5** by adding sulphuric acid (H_2SO_4) molecules to the modelled water phase to simulate the aqueous phase of the SX process. In addition, various functionals and basis sets were investigated to find a suitable model to describe the aqueous phase.

In **Chapter 6,** the periodic organic phase that is needed in the SX process was built and added to the periodic aqueous phase to simulate an SX process. In addition, the interface interactions that occur between these two phases were studied focussing on the mechanism of SX.

In **Chapter 7**, the evaluation and recommendation chapter, the modelling results obtained from Chapters 3 – 6 were reviewed, summarised and evaluated. Subsequently, recommendations are presented on future work focussing specifically on i) using the tetrameric form of TaF_5, ii) investigating macro systems of SX.

5. References

[1] C.R. Hammond, The elements, 96 ed., CRC Press, Taylor & Francis Group, Boca Raton, 2015 - 2016.

[2] S.E. Kesler, A.C. Simon, Mineral resources, economics and the environment, 2 ed., Cambridge University Press, Cambridge, United Kingdom, 2015.

[3] A. Agulyanski, The chemistry of Tantalum and Niobium fluoride compounds, Elsevier, San Diego, Oxford, London, 2004.

[4] C. Hatchett, An analysis of a mineral substance for North America, containing a metal hiterto unknown, Philosophical Transactions of the Royal Society of London, 92 (1802) 49 - 66.

[5] W.P. Griffith, P.J.T. Morris, Charles Hatchett FRS (1765–1847), Chemist and Discoverer of Niobium, Notes and Records of the Royal Society of London, 57 (2003) 299 - 316.

[6] G.J.-P. Deblonde, V. Wiegel, Q. Bellier, R. Houdard, F. Delvallée, S. Bélair, D. Beltrami, Selective recovery of niobium and tantalum from low-grade concentrates using a simple and fluoride-free process, Separation and Purification Technology, 162 (2016) 180 - 187.

[7] O.S. Ayanda, F.A. Adekola, A review of niobium-tantalum separation in hydrometallurgy, Journal of Minerals & Materials Characterization & Engineering, 10 (2011) 245 - 256.

[8] L.F. Myzenkova, Properties of niobium-zirconium superconducting alloys, in: E.M. Savitskii, V.V. Baron (Eds.) Physics and metallurgy of superconductors, Consultants Bureau, New York, USA, 1970, pp. 2 - 44.

[9] T.E. Tietz, J.W. Wilson, Behavior and properties of refractory metals, University of Tokyo Press, Tokyo, Japan, 1965.

[10] Handbook on rare earth metals and alloys (Properties, extraction, preparation and applications), Asia Pacific Business Press Inc., Delhi, India, 2009.

[11] Z. Zhu, C.Y. Cheng, Solvent extraction technology for the separation and purification of niobium and tantalum: A review, Hydrometallurgy, 107 (2011) 1 - 12.

[12] F.K. Crundwell, M. Moats, V. Ramachandran, T.G. Robinson, W.G. Davenport, Extractive metallurgy of nickel, cobalt and platinum group metals, Elsevier, Amsterdam, The Netherlands, 2011.

[13] D.S. Flett, New reagents or new ways with old reagents, Journal of Chemical Technology and Biotechnology, 74 (1999) 99 - 105.

[14] N.R. Council, Nuclear Wastes: Tehcnologies for separations and transmutations, National Academies Press1996.

[15] G.R. Astbury, J. Bugand-Bugandet, E. Grollet, K.M. Stell, Flash points of aqueous solutions of flammable solvents, IChemE: Hazards XVIII, Symposium Series no. 150 (2004) 18.

[16] R.A. Buzzi, Chemical hazards at water and wastewater treatment plants, Lewis Publishers, Boca Raton, 1992.

[17] B. Grinbaum, An integrated method for development and scaling up of extraction processes, Marcel Dekker, Inc., New York, 2002.

[18] V.S. Yemel'yanov, A.I. Yevstyukhin, The metallurgy of nuclear fuel: Properties and principles of the technology of uranium, thorium and plutonium, Pergamon Press, Oxford, London, 1969.

[19] K. Sundmacher, Z. Qi, Multifunctional Reactors, in: R. Pohorecki, J. Bridgwater, M. Molzahn, R. Gani, C. Gallegos (Eds.) Chemical engineering and chemical process technology - Chemical reaction engineering, Eolss Publishers Co. Ltd., United Kingdom, 2010, pp. 90 - 121.

[20] P.L. Gordon, C. O'Dell, J.G. Watkin, Synthesis and energetic content of red oil, Journal of Hazardous Materials, 39 (1994) 87 - 105.

[21] V.N. Usachev, G.S. Markov, Incidents caused by red oil phenomena at semi-scale and industrial radiochemical units, Radiochemistry, 45 (2003) 1 - 8.

[22] M.J. Ungerer, H.M. Krieg, G. Lachmann, D.J.v.d. Westhuizen, Comparison of extractants for the separation of TaF5 and NbF5 in different acidic media, Hydrometallurgy, 144-145 (2014) 195-206.

[23] M. Nete, W. Purcell, J.T. Nel, Separation and isolation of tantalum and niobium form tantalite using solvent extraction and ion exchange, Hydrometallurgy, 149 (2014) 31 - 40.

[24] A. Timofeev, A.A. Migdisov, A.E. Williams-Jones, An experimental study of the solubility and speciation of niobium in fluoride-bearing aqueous solutions at elevated temperature, Geochimica et Cosmochimica Acta, 158 (2015) 103 - 111.

[25] R.L. Linnen, I.M. Samson, A.E. Williams-Jones, A.R. Chakhmouradian, 13.21 Geochemistry of the rare-earth element, Nb, Ta, Hf and Zr deposits, Reference Module in Earth Systems and Environmental Sciences - Treatise on Geochemistry (Second Edition), 13: Geochemistry of Mineral Deposits (2014) 543 - 568.

[26] J. Narbutt, M. Czerwinski, Chapter 16 - Computational chemistry in modelling solvent extraction of metal ions, in: J. Rydberg, M. Cox, C. Musikas, G.R. Choppin (Eds.) Solvent extraction principles and practice, Wiley, New York, 1992.

[27] H. Dorsett, A. White, Overview of molecular modelling and ab initio molecular orbital methods suitable for use with energetic materials, in: D.o.D.D.S.T. Organisation (Ed.), DSTO Aeronautical and Marine Research Laboratory, Salisbury, Australia, 2000, pp. 46.

[28] C. Cramer, Essentials of computational chemistry - Theories and models, 2 ed., John Wiley & Sons Ltd, The Atrium, Southern Gate, Chichester, West Sussex, England, 2008.

[29] M.J. Ungerer, H.M. Krieg, G. Lachmann, D.J. Van der Westhuizen, Separation of tantalum and niobium by solvent extraction, Chemical Resource Beneficiation, North-West University, Potchefstroom Campus, South Africa, North-West University, Potchefstroom, South Africa, 2012, pp. 105.

[30] M. Gharabaghi, M. Irannejad, A.R. Azadmehr, Separation of nickel and zinc ions in a synthetic acidic solution by solvent extraction using D2EHPA and Cyanex 272, Physiochemical Problems of Mineral Processing, 49 (2013) 233 - 242.

[31] X. Li, C. Wei, Z. Deng, M. Li, C. Li, G. Fan, Selective solvent extraction of vanadium over iron from a stone coal/black shale acid leach solution by D2EHPA/TBP, Hydrometallurgy, 105 (2011) 359 - 363.

[32] M. Noori, F. Rashchi, A. Babakhani, E. Vahidi, Selective recovery and separation of nickel and vanadium in sulfate media using mixtures of D2EHPA and Cyanex 272, Separation and Purification Technology, 136 (2014) 265 - 273.

[33] A. Dartiguelongue, A. Changnes, E. Provost, W. Fürst, G. Cote, Modelling of uranium(VI) extraction by D2EHPA/TOPO from phosphoric acid within a wide range of concentrations, Hydrometallurgy, Under press (2015).

[34] S. Nashimura, J. Moriyama, I. Kushima, Extraction and separation of tantalum and niobium by liquid-liquid extraction in the HF-H_2SO_4-TBP system, Transactions of the Japan Institute of Metals, 5 (1964) 39 - 42.

CHAPTER 2
LITERATURE OVERVIEW

2.1 Introduction

The two sister elements tantalum (Ta) and niobium (Nb) are located in the same group (VB) in the periodic table. Due to their similar chemical and physical properties (Table 2.1), for example having the same ionic radius due to lanthanide contraction [1], Ta and Nb are usually found together in nature. This similarity of chemical and physical properties is also the reason for the difficulty in separating the two transition metals. However, there are subtle differences between the two elements and in theory these subtle differences could be exploited to achieve separation as has been demonstrated previously [2].

Table 2.1 – General information and properties of tantalum and niobium

Properties	**Tantalum**	**Niobium**
Discovery date [3]	1802	1801
Discovered by [3]	Anders G. Ekeberg	Charles Hatchet
Atomic Number [4]	73	41
Atomic mass [3]	180.95 $g.mol^{-1}$	92.91 $g.mol^{-1}$
Density [3]	16.4 $g.cm^{-3}$ (20 °C)	8.57 $g.cm^{-3}$ (20 °C)
Melting point [3]	3017 °C	2477 °C
Boiling point [3]	5458 °C	4744 °C
Van der Waals radius [5]	0.145 nm	0.145 nm
Ionic radius [1]	0.64 Å	0.64 Å
Electronic shell [4]	$[Xe]4f^{14}5d^{3}6s^{2}$	$[Kr]4d^{4}5s^{1}$
Energy of first ionisation [4]	7.5496 eV	6.7589 eV
Stable isotopes [6, 7]	^{180}Ta, ^{180m}Ta	^{93}Nb
Minerals [3]	Tantalite, microlite, wodginite	Colombite,
Crystal structure	Body centred cubic	Body centred cubic
Price (99.9% pure) [3]	USD 2 /g	USD 50 ¢/g

Ta and Nb are valuable transitional metals, with various high-end uses. Apart from its use in the nuclear industry as cladding material, Ta is used in capacitors and electronic components, high

power resistors, high strength corrosion resistant alloys, cutting tools, military projectiles and the aircraft industry. Nb, on the other hand, is used in super alloys for jet engines and heat resistant equipment, nuclear reactor fuel cladding, optical lenses, medical implants and superconducting magnets [8, 9]. The value of these metals increases with purity; therefore a highly efficient separation process is essential. Several methods have been used to separate Ta and Nb, wherein high concentrations of sulphuric acid (H_2SO_4) and hydrofluoric acid (HF) at high temperatures are often used [9, 10].

Traditionally two process routes are used for the separation of Ta and Nb, i.e. fluorination or chlorination [11]. The first process entails the fluorination of the raw mineral. In this process, concentrated HF or a mixture of concentrated HF and H_2SO_4 are used. The dissolved fluoride metals are firstly filtrated and then separated with fractional crystallisation, producing K_2TaF_7. Disadvantages of this process include the formation of soluble fluoride impurities, which could contaminate the end product. In addition, both the HF and the fluorinated by-products have an adverse effect on the environment. The second method entails the chlorination of the raw mineral, producing the pentachlorides $TaCl_5$ and $NbCl_5$, followed by a distillation process to separate and purify the metals. The latter process, however, produces a large amount of by-products, while being a lengthy and costly separation process.

A technology that has been used successfully for the separation and purification of various metals, including copper (Cu) [12], nickel (Ni) [13], iron (Fe) [14], platinum group metals (PGMs) [15-17], uranium (U) [18, 19], zirconium (Zr) [20], hafnium (Hf) [21], Ta [8, 9, 22, 23] and Nb [24], is solvent extraction (SX). SX can be used to exploit the subtle differences between Ta and Nb.

Ta and Nb can exist in several valence states such as +5, +4, +3, +2 and +1, but only Nb(V) and Ta(V) are stable in solution [2, 3], forming similar species in acidic media. The reduction of Ta(V) to its lower valence state cannot be achieved with strong reducing agents such as aluminium (Al), zinc (Zn) and cadmium (Cd) [2, 23]. Nb(V) is more reactive and can be reduced in acidic solutions to Nb(III), where complex anions $(NbCl_6)^{3-}$ or $(Nb(SO_4)_3)^{3-}$ are formed in concentrated solutions of hydrochloric acid (HCl) or sulphuric acid (H_2SO_4), respectively [2]. However, reduced Nb(III) is unstable and can be oxidized to Nb(V) by atmospheric oxygen. In neutral or acidic solutions, Nb and Ta hydrolyse to form hydrophilic colloids.

The soluble species of Nb(V) and Ta(V) form complex ions with anionic ligands in acidic solutions which can be represented as a distribution function of pH [23]. When the pH < -1, the cationic form $(Nb(OH)_4^+)$ is the dominant species (> 80%). As the pH increases, the amount in the cationic form decreases, while the amount of the neutral $Nb(OH)_5$ increases. At pH = -0.6, the cationic and neutral Nb complexes are at equilibrium, whereas only the neutral Nb compound is present at a pH > 1. Similar tendencies have been observed for Ta, albeit at higher pH values. When the

pH < 1, the relative content of the cationic $Ta(OH)_4^+$ dominates, while the neutral $Ta(OH)_5$ dominates at pH > 1, reaching 100% at pH > 3. At pH = 1 the two complexes are in equilibrium. In HF at low concentrations, $NbOF_5^{2-}$ and TaF_7^{2-} are formed, while at high concentrations NbF_6^- and TaF_6^- are formed [8, 23].

Apart from the above explained species distribution as a function of pH, the use and understanding of speciation data, specifically for SX processes, is limited due to the lack of detection methods [25]. In addition, it has been shown [26] that the speciation of mass transfer complexes do not always correspond to those represented in, for example, a pH distribution speciation graph. An alternative method for species identification could be molecular modelling, which in essence uses theoretical methods in combination with computational techniques to mimic the behaviour of molecules in various states and systems.

To date, molecular modelling has been used in a variety of fields of computational chemistry, such as the pharmaceutical industry for drug design, computational biology, biochemistry and material science to study various properties such as the structure, dynamics, surfaces and the thermodynamics of inorganic, organic, biological and polymeric systems. A broad range of systems have be considered in molecular modelling, ranging from isolated molecules through simple atomic [27, 28], ionic [29] and molecular liquids [30] to polymers [31, 32], biological macromolecules such as proteins [33] and DNA [34, 35], solids [36] and surfaces [37]. The types of predictions possible with molecular modelling include molecular geometry or structures of ground-, excited- and transition states, heats of formation, bond-, molecular- and reaction energies, thermochemical stabilities, energies and structures of transition states (activation energy), reaction pathways, kinetics and mechanisms, charge distributions in molecules, substituent effects, electron affinities, ionisation potentials, vibrational frequencies (infrared and Raman spectra), electronic transitions (ultraviolet (UV) / visible spectra) and magnetic shielding effects (nuclear magnetic resonance (NMR) spectra) [38, 39]. The drawback of molecular modelling is that the higher the required accuracy of your modelled system, the higher the functional and basis set levels used need to be, thus increasing computational time. With the advances in computational abilities, especially with regard to computer memory and speed, the molecular modelling abilities have improved.

In the following sections, a more detailed discussion on SX (Section 2.2) and molecular modelling (Section 2.3) is presented, followed by a discussion on combining both SX and modelling (Section 2.4).

2.2 Solvent Extraction (SX)

SX, also known as liquid-liquid extraction or partitioning, is a separation method based on the relative solubility of two or more compounds in two immiscible or partly immiscible liquids [40]. These two immiscible liquids are usually based on water (forming the aqueous phase) and an organic solvent (that forms the organic phase). Separation is ideally achieved if one of the compounds is retained in the one phase while another compound(s) is extracted into the other phase.

Traditional SX processes for Ta and Nb use the extractants methyl isobutyl ketone (MIBK) and tri-butyl phosphate (TBP) to selectively extract Ta over Nb as metal oxides (M_2O_5, M = Ta/Nb) from either a H_2SO_4 or HCl phase into the organic phase [23]. However, the drawback of using MIBK is its low flash point at 15°C, which can cause explosions in industry [41]. Health and environmental problems have been reported [42] and because of its high density difficulty in phase separation [43] was experienced. In addition TBP, when diluted in kerosene, can form an explosive red oil in the presence of concentrated nitric acid [44, 45].

In a recent study, Ungerer et al. [46] studied the solvent extraction (SX) based separation of Ta and Nb using alternative and safer chemicals, while investigating the suitability of membrane-based solvent extraction (MBSX). A small scale laboratory study was done using batch single stage extractions. In this process, shown in Figure 2.1, the aqueous phase consisted of $Ta(Nb)F_5$, dissolved in deionised water and H_2SO_4, while the organic phase consisted of an extractant (di-(2-ethylhexyl)-phosphoric acid (D2EHPA) or diiso-octyl phosphinic acid (DioPA)), diluent (cyclohexane) and modifier (1-octanol).

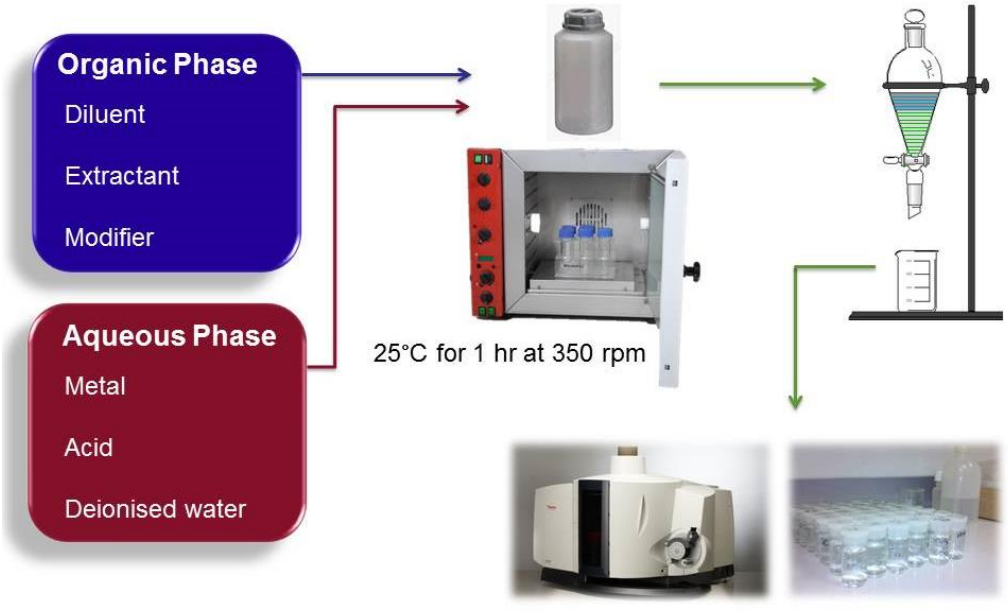

Figure 2.1 – Batch wise solvent extraction process [22]

While partial separation of Ta and Nb was achieved, it was not possible to predict extraction behaviour prior to experimental testing, due to the absence of speciation data for Ta and Nb, which may be due to i) their insolubility in most aqueous liquids [47, 48] and ii) their UV inactivity making the detection and identification of the aqueous species difficult. An alternative method that could be suitable for predicting the speciation and hence extraction of Ta and Nb is molecular modelling [49]. Applying molecular modelling to SX could, for example, entail a step-by-step analysis of the extraction process on a molecular level, thereby determining the molecular properties as well as the system reactions occurring during SX.

2.3 Molecular Modelling

The following section looks at the background of molecular modelling and the different functionals and basis sets that can be used, as well as at the advantages and disadvantages of using these methods.

2.3.1 Background

The SX process described above is conducted on a macroscopic level compared to molecular modelling which is conducted on an atomic level. This change in the process scale needs a change in the thinking and a different rationale. On a macroscopic level one can for example consider Newton's second law of motion for everyday objects (in use since 1687) [50]:

$$F = ma$$

where F is the force (N or $kg.m/s^2$), m is the mass (kg) and a is the acceleration (m/s^2). This law mathematically predicts various kinds of motion at any time after a known initial condition [51], but when it is applied to the smallest scale (atomic or subatomic level) this law no longer applies. Thus, quantum mechanics were established at the beginning of the twentieth century and was applied to develop the analogue to Newton's second law, i.e. Schrödinger's equation [52] for a system consisting of atoms, molecules and subatomic (free, bound or localized) particles. Experimental evidence suggested that atomic particles not only behaved like particles but also as waves. Taking the wave-like motion into account, the Schrödinger equation was derived in 1926 [52]:

$$\frac{\partial^2 \Psi}{\partial x^2} + \frac{8\pi^2 m}{\hbar^2}(E-V)\Psi = 0$$

where ∂^2 is the second derivative with respect to x, x is the position, m is the particle mass, ħ is the Planck constant (J.s) divided by 2π, Ψ is the Schrödinger wave function, E is the energy (equal to h*v,* with *v* the frequency) and V is the potential energy (equal to ½κx^2, with κ a positive constant and position x) influencing the particle. From this equation the general time-dependent Schrödinger equation is derived [53]:

$$i\hbar \frac{\partial}{\partial t}\Psi(\mathbf{r}, t)=\hat{H}\Psi(\mathbf{r}, t)$$

where i is an imaginary unit (√-1), Ψ(**r**, t) is the Schrödinger wave function defined over space and time, **r** is the particle's position in space and $\hat{H}$ is the Hamiltonian operator (which characterises the total energy of any given wave function). This time-dependent Schrödinger equation describes how the wave function changes as a result of forces acting on the particle over time. This equation can be simplified into the time-independent Schrödinger equation for standing waves or stationary states, which describes the atomic orbitals and molecular orbitals [53]:

$$E\Psi = \hat{H}\Psi$$

Solving these equations are time consuming, takes skill and could only be solved for hydrogen, containing only one electron. When a many-body problem is considered, these equations cannot be solved analytically. From the 1940s, development of faster and more efficient computer technologies made the solutions to elaborate wave equations of complex atomic systems a realisable objective [54]. This is where computational chemistry was born. Differing from theoretical chemistry, where chemistry is defined as a mathematical description, computational chemistry is defined by mathematics in the form of algorithms and computer programs. Both algorithms and computer programs have been sufficiently well developed by chemists, physicist and mathematicians to predict atomic and molecular properties and reactions pathways [55].

2.3.2 Modelling Methods

Due to the increased demand to simulate realistic systems consisting of large molecules and reaction pathways in different media, especially in biochemistry, various methods have been developed, each with different approaches and approximations. Current examples of such modelling methods include molecular mechanics, molecular dynamics, semi-empirical and empirical methods, modelling in the solid state, ab initio and density functional theory (DFT) [55, 56]. Ab initio methods have great accuracy for small molecules, but the computational cost increases up to a factor of N^4, where N is the relative measure of the system size [39]. DFT on

the other hand uses approximation methods and thus has greater accuracy for systems with larger molecules or larger systems with many smaller molecules [39].

Keeping the SX system that was discussed in Section 2.2 in mind, both ab initio and DFT modelling could be used for investigating how Ta and Nb are extracted from the water into the organic phase. Accordingly, a concise description of both ab initio and DFT will be discussed in this section.

Ab Initio

Two basic theories that have been developed to describe chemical bonding using quantum mechanics are the valence bond (VB) theory and the molecular orbital (MO) theory. According to the VB theory, a covalent bond is seen as the overlap of half-filled valence atomic orbitals, each containing one unpaired electron, to form weakly coupled orbitals. When a molecule is considered, the assumption is that the inner-shell orbitals and electrons remain unchanged during the formation of bonds [56]. In MO theory, it is assumed that each molecule has a set of molecular orbitals, where each orbital has a wave function [56]. In essence, electrons are treated as moving in the whole molecule, subject to the influence of the nuclei, and therefore not constrained to the individual bonds between atoms.

In 1950, the Hartree-Fock (HF) method for molecules was established as the rigorous and consistent approach where MOs were defined as Eigen functions of the self-consistent Hamiltonian field [57]. The fundamental assumption of the HF theory is that each electron sees all the other electrons as an average field and will be influenced by the remaining electrons present in the same system. In other words, the HF method gives an approximate solution for wave function and energy of a quantum many-body system in a stationary state. However, in the HF method the repulsion energy between two electrons is calculated between an electron and the average electron density for the other electron, suggesting that two electrons have the same probability of being in the same space or in a separate symmetry space. This neglect of electron correlation has chemical consequences when determining the accurate solutions of the wave functions and derived properties thereof [56]. In spite of its significant fundamental assumption, the HF theory has been adopted into the ab initio philosophy.

Ab initio is Latin for ‘from the beginning’, indicative of ‘from first principles of quantum mechanics’. Different from other computational methods, ab initio quantum chemistry is based solely on established laws of nature, i.e. quantum mechanics. Many types of ab initio calculations initiate with HF calculations, before correcting the electron-electron repulsion, also known as electronic correlation [55, 56] for the modelled system. The atom-centred functions used to describe the

atomic orbitals are in essence mathematical functions and are known as basis functions or collectively as a basis set. Larger basis sets have fewer restrictions on the wave function and thus give better approximations of the atomic orbitals, but at a higher computational cost [55]. Various basis sets have been developed to construct wave functions in an attempt to solve the Schrödinger equation. These different basis sets, approximations and functionals have given rise to different classes of ab initio modelling methods, having been carefully designed to give the best description at the lowest cost [56]. Some of the different ab initio modelling classes (such as Hartree-Fock, post-Hartree-Fock and multi-reference methods) with some of their dates of development are listed below [58, 59]:

Hartree-Fock methods

- Hartree-Fock (HF) (1928) [60]
- Restricted open-shell Hartree-Fock (ROHF) (1960) [61]
- Unrestricted Hartree-Fock (UHF) (1971) [62]

Post-Hartree-Fock methods

- Møller-Plesset perturbation theory (MPn) (1934) [63]
- Configuration interaction(CI) (1977) [64]
- Coupled cluster (CC) (1958) [65, 66]
- Quadratic configuration interaction (QCI) (1987) [67]
- Quantum chemistry composite methods

Multi-reference methods

- Multi-configurational self-consistent field (MCSCF) (1985) [68, 69]
- Multi-reference configuration interaction (MRCI) (1973) [69, 70]
- n-electron valence state perturbation theory (NEVPT) (2001) [71]
- Complete active space perturbation theory (CASPTn) (1982) [72]
- State universal multi-reference coupled-cluster theory (SUMR-CC) (1981) [73]

The advantages of ab initio methods include absolute control over ‘experimental’ conditions, unlimited characterisation capabilities and high accuracy predictions [39]. The disadvantages of using ab initio are that they are computer intensive, hence limited by computational resources and cannot predict effects not included in the simulation [39]. To speed up the computation time, semi-empirical methods, based on quantum mechanics, were developed which replaced explicit calculations with experimentally based approximations [39].

DFT (Density Functional Theory)

DFT focusses on functionals (functions of functions) that return the energy of the system, in other words instead of using a wave function, the total energy of a system is expressed in terms of the one-electron density. DFT has its conceptual roots in the Thomas-Fermi (TF) model, which was established in 1927 [74-76]. The TF model is a statistical model to determine the distribution of electrons in an atom, with the approximation that the electrons are distributed uniformly in each small volume, but the electron density can still vary from one small volume to the next. Due to limited accuracy in the resulting kinetic energy, correction terms were needed to improve this model by adding approximations, for example the exchange energy by Dirac (1928) [77], the kinetic energy by von Weizsäcker (1935) [78] and others [79]. The TF model and its approximations were widely used for solid-state physics, but had little impact on chemistry, due to the deviations in the exchange energy and the complete disregard of electron correlation causing large errors in molecular calculations. However, in 1964 Hohenberg and Kohn provided two theorems [80] that established DFT as a legitimate quantum chemical methodology [56]. These theorems proved that i) the ground-state electronic density determines the Hamiltonian, which in turn determines the ground-state electronic wave function and ii) the electronic energy assumes its minimum for the correct ground-state density [56, 79].

Even with all these equations and theorems there was no satisfactory level of accuracy. For this reason, Kohn and Sham proposed a method (KS method) of combining wave functions and the electron density approach [55]. Within the KS method [81], the many-particle problem of interacting electrons in a static external potential is reduced to a system of non-interacting electrons moving in an effective potential. Now the exact ground state energy and electron density could be calculated if the electronic exchange correlation functional was known. However, in reality, this exact functional is unknown, but extensive research has been done and new variations are published regularly. The density approximations/variations to date can be depicted as a ladder (Jacob's ladder shown in Figure 2.2), where each step on the ladder represents increasing chemical accuracy.

The first step on the ladder is the local spin density approximation (LDA) of the KS method. The LDA takes the difference between classical and quantum electron-electron repulsion into account, as well as the kinetic energy difference between the real system and the non-interacting system. On average, the LDA gives reasonable geometries and vibrational frequencies, but overestimates correlation and bond energies and underestimates the exchange energy, due to the lack of spatial variation [79].

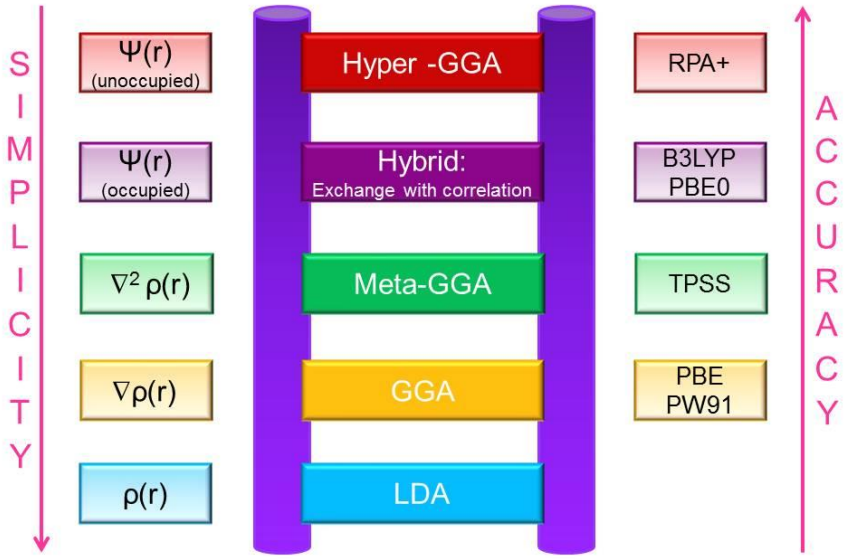

Figure 2.2 – Jacob's ladder of density functional approximations (reproduced from [82])

The next step on the ladder is the generalised gradient approximation (GGA). The GGA gives a better description of spatial variation by including the gradient of density [79, 82]. The GGA improves the binding energies and geometries.

The third step in the Jacob's ladder is meta-GGA, which includes the Laplacian of the density ($\nabla^2\rho(r)$ second derivative of density) [79, 82]. While Meta-GGA gives better results, it does have poor numerical stability. An examples of meta-GGA is TPSS (Tao, Perdew, Staroverov and Scuseria correlation) [83].

The fourth step is the hybrid functionals where GGAs or meta-GGAs with exact exchanges are combined with HF theory (wave function approximation) [82]. Examples of hybrid functionals are B3LYP (Becke exchange plus Lee-Yang-Parr correlation [84, 85]) and PBE0 (mixing of PBE exchange energy with HF exchange energy at a 3 to 1 ratio, with the full PBE correlation energy [86]).

The fifth and currently the last step on the ladder is hyper-GGA. Hyper-GGA has the correct formal properties of the hybrid functionals in the previous step, but the correlation part is more compatible with exact exchange. An example of hyper-GGA is RPA+ (random phase approximation [87, 88]). As you move down the ladder, the calculations are simpler to run, but accuracy in terms of exchange and correlation energies decrease, moving up on the ladder the accuracy increases exponentially with an increase in mathematical difficulty. Development of better approximations to determine the true exchange-correlation functional is certain to remain an attractive and promising subject for years to come.

As seen from the above discussion on ab initio and DFT methods, many molecular properties can be computed [56]. The drawback of modelling these properties listed is that calculations can be very expensive in terms of computational power and time required; also, calculations can be performed on any chemical system, including those that do not exist. Therefore, choosing a system to model has to have some underlying part in experimental or existing literature work. As such, DFT usage tends to favour a more sophisticated user. On the other hand, modelling has the advantage of becoming less expensive, whereas experiments are becoming more costly, calculations are relatively easy to perform, whereas experiments are often difficult, calculations are safe, whereas many experiments have an intrinsic danger associated with them [56].

From the discussion above, it is evident that molecular modelling can be used for investigating a variety of properties in various fields of application. One such field is hydrometallurgy, where SX plays a vital role in the extraction, separation and recovery of a range of metals. Instead of carrying out a myriad of experiments to optimise an SX process, molecular modelling could be used to investigate this process on a molecular level, which in turn could lead to expertly designed SX processes.

2.4 Modelling of the SX system

The SX process for the purification or separation of metals (Figure 2.1) can be divided into three parts: 1) the aqueous phase containing water-soluble metal salts or ore, 2) the organic phase containing the extractant and diluent, and 3) the interface where these two phases make contact. Various papers have been published on the use of molecular modelling of these three parts to improve the SX process on various levels and will be discussed in the following paragraphs.

2.4.1 Aqueous Phase Modelling

DFT modelling of cobalt (Co) and nickel (Ni) complexes with dithiophosphinic acid was carried out by Otero-Calvi et al. [89] using Gaussian 03 with the B3LYP functional [90-92]. For the calculations of H, O, phosphorous (P) and sulphur (S) atoms the 6-31G* basis set was used. The non-relativistic ECP of Hay and Wadt [93] and the valence basis set LanL2DZ were used for the Ni and Co atoms. In a first step, various geometries of Co and Ni complexes were identified and their probability to exist discussed. This was followed by a thermochemical interpretation where reactions with these identified complexes were simulated. The HOMO (highest occupied molecular orbital) and LUMO (lowest unoccupied molecular orbital) energy gaps of these complexes were reported where the energy difference between HOMO and LUMO was used as

a measure of the stability of the complexes as well as the likelihood of these extraction reactions of Co and Ni to occur. Although the results from crystal field theory and equilibrium processes showed that the tetrahedral complexes form preferentially, the small difference in energy showed that the octahedral Co complexes might also form. Results also showed that dithiophosphinic acid separated Ni and Co due to the difference in bonding between the metals and acid.

Similar to this paper on Co and Ni, Siodmiak et al. [94, 95] modelled tantalum(V) chloride ($TaCl_5$) using the Gaussian 98 program with Hartree-Fock (HF), Møller-Plesset perturbation theory (MP2) [63] and B3LYP [91] functionals for comparison. A quasi-relativistic ECP with a valence basis set (441/2111/21), which was derived from Hay and Wadt [93], was used for Ta, the (4/5)/[2s3p] valence basis set [96] for chlorine (Cl) and the 6-31G** basis set [97] for the O and H atoms. Step-wise reactions of $TaCl_5$ with H_2O forming tantalum(V) oxide (Ta_2O_5) in the gas phase were investigated. It was shown that the first two hydrolysis reactions forming $TaCl_4OH$ and $TaCl_3(OH)_2$ are exothermic, while a stable hydrated $TaCl_5.H_2O$ molecule is formed. The formation of tantalum(V) oxychloride ($TaOCl_3$) and Ta_2O_5 is endothermic. These two papers were a first attempt to understand the speciation chemistry of Ta in water. As part of the aqueous phase, acid and water are also present with the metal species and therefore play an important role in the understanding of how these metal species interact within the acidic medium.

In a study by Loukonen et al. [98], the stability and dynamics of small sulphuric acid-ammonia/dimethylamine clusters were investigated by varying the number of H_2SO_4 molecules in clusters of ammonia and dimethylamine. The CP2K program package was used for the simulations with the Quickstep module [99] by selecting the PBE functional [86] and the GTH (Goedecker-Teter-Hutter) pseudo-potentials [100] for the core electrons. Since the temperature of the calculations was 300 K, the molecules moved constantly, resulting in a range of cluster configurations that are relevant to this study. With this constant movement of the molecules, the danger lies in the dissociated protons of the H_2SO_4 molecules transferring back to the acid or the initial H_2SO_4 molecules leaving the cluster completely. The PBE functional used to describe the polar hydrogen bonds compared with literature and the clusters stayed intact as expected.

When metals are dissolved in acidic media, other ions may also be present in the solution. Kurtén et al. [101] investigated the effect of different ions (H_3O^+, OH^-, Li^+, Na^+, F^- and Cl^-) in the presence of H_2O and H_2SO_4. Gaussian 03 software was used for the simple ions at the MP2(full)/6-311++G(3df,3pd) level [63, 102] with default convergence criteria. For the more complex ions the Spartan, SIESTA [103] and Turbomole [104] software programs were used with BLYP/DZP geometries and RI-MP2 or RI-CC2 for vibrational frequencies and energy corrections. The results showed that the anionic species bind much more strongly to H_2SO_4 than the cations. The binding energies of the H_2SO_4-anion lay between 45 and 55 kcal/mol and 18 – 22 kcal/mol for the H_2SO_4-cation binding energy. This indicates that not only does the acid have an influence when the

metals are extracted, but also that the presence of other ions in solutions influence the acid, which in turn effects the extraction into the organic phase.

2.4.2 Organic Phase Modelling

Various papers have been written, especially on extractant design for specific SX processes. In

Table 2.2, a list is given of papers on the molecular modelling of extractants and their complexes, highlighting the software used and the objectives of the respective studies.

Table 2.2 – Some research trends of molecular modelling of the organic phase

Author (Year) [Ref.]	Modelling Method Metal/ extractant/ solvent	Objective / Results
McCann et al. (2016) [105]	• HostDesigner 3.0 Software [106], MM3 force field, MP2/cc-pVTZ level of theory • Lanthanides/ bis-phosphine oxide ligands	In this DFT study, the influence of structural effects on selectivity was investigated. The structural effects included the length, alkyl chains, degree of alkylation and different ligand substitutes on a P=O back bone. The angle of M-O-P should be larger for sufficient chelating with larger metal ions. The solvent effect was not considered.
Arora et al. (2015) [107]	• Gaussian 09 software, B3LYP functional [85, 91] and LANL2DZ-ECP basis set • Sb(III), Sb(V), Zr(IV), Co(II)/ thiourea/ polystyrene	DFT calculations in the gas phase differed from experimental data. With the inclusion of solvation, the experimental and modelled adsorption data correlated.
Dartiguelongue et al. (2015) [108]	• Mathematical software Scilab© 5.4.0 [109] • U(VI)/ D2EHPA and n-octyl phosphine oxide/ kerosene	A Gibbs free energy based algorithm was used to calculate the aqueous phase speciation. The modelled data correlated with experimental data whereby one U(VI) was extracted by two monomeric extractant molecules in the presence of five H_2O molecules.
Pahan et al. (2015) [110]	• Turbomole 6.3, with BP86 functional and split valence plus polarisation basis set (similar to 6-31G* basis set) • UO_2^{2+} and Pu^{4+} / tetra methyl di-glycol amide/ dodecane	Molecular modelling was performed in both the gas phase and with COSMO to simulate solute interactions. The experimental and modelled selectivity did not correlate, possibly due to omission of hydrated nitrate ions that would be present during an experiment. The free energy of extraction was high in dodecane, which has a low dielectric constant.

Ali (2014) [111]	• Turbomole software with BP86 functional [90, 112], the TZVP basis set [113, 114] and COSMO [115] were used for both an implicit and explicit solvation effect • Sr^{2+} / crown ether ligands	The results indicated that metal extractions with crown ether increased when an organic solvent with a moderate dielectric constant was used. Results with regard to the partition coefficients, solubility and solvent extraction effects correlated with experimental data. However, the metal ion selectivity, in both models, did not correlate with experimental selectivity, possibly due to not having enough solute molecules in the solvation sphere while the effect of the nitrate ion on this system was not considered.
Ali (2008) [116]	• B3LYP [91] functional with a 6-311++G(d,p) split valence basis function • Li and Na/ different crown ethers/ solvent effect not considered	In this DFT study, geometry optimisation was based on semi-empirical PM3 (parametrised model number 3 [117, 118]) with ions in the gas phase. Binding enthalpy for Li^+ with crown ether was found to be higher than expected, but the results with Na^+ correlated with experimental data.
Sieffert and Wipff (2006) [119]	• Molecular dynamic (MD) simulation with AMBER 7.0 • Na^+, K^+, Rb^+, Cs^+ and the $PF_6^-$and Tf_2N^- anions in the gas phase/ different calix crown ligands/ different ionic liquids	Cs^+ was best extracted with the calix crown ligands into the ionic liquid. The modelled complexation results were shown to be predictive. The modelled extraction results correlated with experimental data.
Krishna et al. (2004) [120]	• DFT hybrid B3LYP[85, 91] with Lanl2sz and TZP basis sets • Zr and Hf/ MIBK and TBP / acetone and tri methyl phosphate	The Hf complexes had a larger stability in the two solvents (acetone and tri-methyl phosphate) and therefore Hf was preferably extracted into the organic phase. The data from the gas phase calculations was sufficient to explain the experimentally observed separation of Zr and Hf.
Lumetta et al. (2002) [121]	• Ab initio MP2/aug-cc-pVDZ functional/basis set settings • M^{3+} lanthanides and actinides/ alkylated malonamides/ solvent effect not considered	Different ligands were investigated both theoretically (modelling) and experimentally. The new ligands (alkylated malonamides) showed an increase in Eu^{3+} extraction affinity. The increased acid concentration leads to an increased extraction percentage. The modelled data correlated with the experimental data.

From these papers on the molecular modelling of extractants and their complexes, it is evident that different models or methods within molecular modelling yield results that are always an approximate to experimental values. Some points to consider when modelling that will influence the obtained results include:

- State of the system to be modelled – gas phase or simulated liquid phase. The gas phase gives adequate approximations, whereas a liquid environment better imitates the experimental setup but usually at the cost of computation time.
- Temperature of the system – by modelling at 0 K, a more ideal system is selected with less vibrational modes, which works well for single molecules or small systems. However, at 298.15 or 300 K, the molecules have higher kinetic energy, resulting in an increasing number of possible geometries with a closer mimicking of experimental results, while again increasing computational cost.
- Functional and basis sets chosen – for single molecules or small systems basic settings will give good experimental approximation. However, when these single molecules are collectively added to form a large system, the choice of functional/basis sets is important. This choice depends on the interaction or result the researcher wants to investigate, for instance if the systems contain ionic species, a functional/basis set designed with dispersion corrections could be used.

In Sections 2.4.1 and 2.4.2, it was shown that both the aqueous and organic phases can be described with molecular modelling. However, for SX the emphasis is on the metal(s) being extracted from the aqueous to the organic phase. Therefore, the interface between these phases is of vital importance for understanding how the SX process occurs.

2.4.3 Interface Modelling

Table 2.3 lists some research papers on the molecular modelling of the interface as well as the SX process as a whole, again showing the modelling software used and some of the objectives or results.

Table 2.3 – Research trends of the molecular modelling of the interface and the SX process

Author (Year) [Ref.]	Modelling Method Metal/ extractant/ solvent	Objectives / Results
Holte et al. (2014) [122]	• Molecular dynamic (MD) simulations with AMBER 12 software with POL3 polarisable water model [123] • Na^+ and water/ lauric acid/ chloroform and hexane	The lauric acid molecule stayed near the interface, with its orientation changing with the depth of the organic layer. In the layer nearest to the water, the carbonyl oxygen pointed toward the aqueous phase and the hydrophobic tail towards the organic phase. In the water layer the carbonyl oxygen pointed toward the organic phase. This phenomenon was supported by experimental frequency studies.

Kujawski and Bogacki (2012) [124]	• AMBER 10 software, atoms and bond types were estimated with Antechamber software and atom charges with the B3LYP/DGDZVP functional/basis set settings. • $ZnCl_2$ / TBP / Chloroform	In this MD study, it was seen that TBP molecules adsorbed at the interface after 350 ps, with the polar parts pointed toward the aqueous phase and the alkyl chains pointed toward the organic phase. When simulating 30 TBP molecules in this system, the TBP pulled 2 – 3 water molecules into the organic phase. The observed TBP dimers (or water fingers) were confirmed with experimental research.
Cao et al. (2010) [125]	• TURBOMOLE [104] with all electron calculations using the Wood-Boring scalar-relativistic HF approach • Am(III), Cm(III) and Eu(III)/ Cyanex 301 / kerosene	Am(III) had 6- and 7-fold coordination and Eu(III) had a 7-fold coordination between the metal and ligand in the presence of water. The Gibbs free energy in the gas phase was Am(III)>Cm(III)>Eu(III), while it was reverted for the aqueous solution and extraction. It was suggested that the hydration Gibbs free energy calculations are a more accurate measure of extraction.
Chaumont and Wipff (2007) [126]	• AMBER 7.0 software • S^- or Cl^- and S^+ or Na^+ in water / 1-butyl-3-methyl-imidazolium cation (BMI^+) or 1-octyl-3-methylimidazolium cation (OMI^+) /PF_6	With the MD runs it was seen that the less the charge on solutes, the more hydrophobic their character and therefore the more soluble they are in the ionic liquid. This phenomenon likely explains why the extraction mechanism changed, i.e. neutral complexes extracted with [OMI][PF_6] and the charged complexes extracted with [BMI][PF_6].
Coupez et al. (2004) [127]	• AMBER 5.1, with the TIP3P and OPLS models • M^{3+} lanthanides and actinides, HNO_3 and water/ calixarene ligands/ chlorinated cobalt dicarbollide ions $[Co(C_2B_9H_8Cl_3)_2]^-$ (CCD^-)	During the MD simulations, the CCD^- showed high surface activity resulting in the high attraction of the Eu^{3+} cations promoting the extraction by the ligands. Where usually the interface repels ions, the CCD^- ions created a negative potential. Only the 1:1 stoichiometry was investigated, therefore the possibility of the formation of aggregates, oligomers and supramolecular assemblies are possible but were not investigated.
Coupez et al. (2003) [128]	• AMBER 5.1, AMBER force field [129], HF calculations with 6-31G* basis set [130] • M^{3+} lanthanides and actinides/ TBP and Cyanex 301/ chloroform	Chloroform was chosen due to shorter relaxation times compared to long chain linear alkanes. As the [TBP] increased, more H_2O molecules where absorbed into the interface, leading to the decrease in surface tension, facilitating extraction into the organic phase.
Baaden et al. (2002) [131]	• AMBER 5.0 software, AMBER force field [129]	Modelling data from the MD simulations differed from experimental data due to modelling at a neutral pH, whereas nuclear waste solutions

	• $UO_2(NO_3)_2$ / TBP/ supercritical CO_2	have a low pH. A micro emulsion of the water and organic phase formed at the interface.
Baaden et al. (2001) [132]	• AMBER 5.0 software, AMBER force field [129] (ab initio method) using the 6-31G* basis set. • HNO_3 / TBP/ chloroform	Acid and extractant concentrations were varied in this MD study to determine the chemical and physical interactions at the interface. At low [TBP], the biphasic solution separated in less than 1 ns, at high [TBP] water formed a vertical slab or micro droplets at the interface.

It can be seen that a wide range of software packages, models, functional/basis sets are available for molecular modelling, which all give an insight into what is happening at the interface during SX. This data is all based on models and therefore cannot give exact answers. From this table (Table 2.3) it is evident that various variables have to be considered when molecular modelling is used for interface modelling:

- The starting system is important. Simple molecules or small systems are easy enough to simulate and then progress to larger systems. However, if a simulation is started with a large system with many unknown factors (geometry of ligands, ion-ion exchange, ligand interactions, secondary reactions, etc.) the various approximations and assumptions cause some of these interactions to be missed [133], which influences the outcome of the modelling and how well the modelling data fits experimental data.
- It is also important to note whether the species of the starting material are all ionic, half-ionic, half-neutral or neutral species as this dictates which functional/basis set to use.
- The size of the system, in other words should only the interface be studied or is there a need to ‘track’ the molecules from the bulk aqueous phase through the interface into the bulk organic phase. Again, the disadvantage of the bigger system is the cost in computational time.

From these papers on the molecular modelling of extractants and their complexes it is evident that, by using different models or methods within molecular modelling, the results are always an approximate to experimental values. However, molecular modelling is still a useful tool in understanding and visualising how molecules behave in certain environments, while also helping in the understanding of certain phenomena, thereby possibly improving the SX systems in terms of chemicals used, extraction time, extraction efficiency and waste created.

2.5 Conclusion

Since the two sister metals Ta and Nb are found together in nature and have similar properties, there have been more than 200 years of investigations on the separation of these two metals. In spite thereof, the separation to date remains tedious and expensive with numerous challenges. These metals have significant applications in the modern world, of which the most important are for structural purposes and nuclear power plant use.

The results presented in this overview show the viability of using molecular modelling to understand how metal species behave, react and change during homogeneous processing like solvent extraction. In most cases presented, the modelling data were validated with experimental results. For molecular modelling to be truly effective in yielding large scale results, the small scale interactions need to be investigated before leading up to the complete solvent extraction system. It is likely that more emphasis will be focussed on this technology in future.

2.6 References

[1] R.D. Shannon, Revised effective ionic radii and systematic studies of interatomic distances in halides and chalcogenides, Acta Crystallography, A32 (1976) 751 - 767.

[2] A. Agulyanski, The chemistry of Tantalum and Niobium fluoride compounds, Elsevier, San Diego, Oxford, London, 2004.

[3] C.R. Hammond, The elements, 96 ed., CRC Press, Taylor & Francis Group, Boca Raton, 2015 - 2016.

[4] W.C. Martin, Electron configuration and ionization energy of neutral atoms in the ground state, 96 ed., CRC Press, Taylor & Francis Group, Boca Raton, 2015 - 2016.

[5] J.C. Slater, Atomic radii in crystals, Journal of Chemical Physics, 41 (1964) 3199 - 3205.

[6] G. Baccolo, Tantalizing tantalum, Nat Chem, 7 (2015) 854-854.

[7] A. Nystrom, M. Thoennessen, Discovery of yttrium, zirconium, niobium, technetium, and ruthenium isotopes, Atomic Data and Nuclear Data Tables, 98 (2012) 95 - 119.

[8] G.J.-P. Deblonde, V. Wiegel, Q. Bellier, R. Houdard, F. Delvallée, S. Bélair, D. Beltrami, Selective recovery of niobium and tantalum from low-grade concentrates using a simple and fluoride-free process, Separation and Purification Technology, 162 (2016) 180 - 187.

[9] O.S. Ayanda, F.A. Adekola, A review of niobium-tantalum separation in hydrometallurgy, Journal of Minerals & Materials Characterization & Engineering, 10 (2011) 245 - 256.

[10] S. Nashimura, J. Moriyama, I. Kushima, Extraction and separation of tantalum and niobium by liquid-liquid extraction in the HF-H_2SO_4-TBP system, Transactions of the Japan Institute of Metals, 5 (1964) 39 - 42.

[11] D.R. Sadoway, S.N. Flengas, A new process for the separation of tantalum and niobium, Metallurgical Transactions B, 11B (1980) 57 - 62.

[12] J. Lu, D. Dreisinger, Two-stage countercurrent solvent extraction of copper from cuprous chloride solution: Cu(II) loading coupled with Cu(I) oxidation by oxygen and iron scrubbing, Hydrometallurgy, 150 (2014) 41 - 46.

[13] A. Fernandes, J.C. Afonso, A.J.B. Dutra, Separation of nickel(II), cobalt(II) and lanthanides from spent Ni-MH batteries by hydrochloric acid leaching, solvent extraction and precipitation, Hydrometallurgy, 133 (2013) 37 - 43.

[14] W. Qifeng, R. Xiulian, G. Jingjing, C. Yongxing, Recovery and separation of sulfuric acid and iron from dilute acidic sulfate effluent and waste sulfuric acid by solvent extraction and stripping, Journal of Hazardous Materials, 304 (2016) 1 - 9.

[15] J.R. Kumar, H.I. Lee, J.Y. Lee, J.S. Kim, J.S. Sohn, Comparison of liquid-liquid extraction studies on platinum(IV) from acidic solutions using bis(2,4,4-trimethylpentyl) monothiophosphinic acid, Separation and Purification Technology, 63 (2008) 184 - 190.

[16] C.-Y. Yin, A.N. Nikoloski, M.W. Wang, Microfluidic solvent extraction of platinum and palladium from a chloride leach solution using Alamine 336, Minerals Engineering, 45 (2013) 18 - 21.

[17] M.K. Jha, D. Gupta, J.-C. Lee, V. Kumar, J. Jeong, Solvent extraction of platinum using amine based extractants in different solutions: A review, Hydrometallurgy, 142 (2014) 60 - 69.

[18] D. Beltrami, A. Chagnes, M. Haddad, H. Laureano, H. Mokhtari, B. Courtaud, S. Jugé, G. Cote, Solvent extraction studies of uranium(VI) from phosphoric acid: Role of synergistic reagents in mixture with bis(2-ethylhexyl) phosphoric acid, Hydrometallurgy, 144-145 (2014) 207 - 214.

[19] Z. Zhu, Y. Pranolo, C.Y. Cheng, Uranium recovery from strong acidic solutions by solvent extraction with Cyanex 923 and a modifier, Minerals Engineering, 89 (2016) 77 - 83.

[20] R.K. Biswas, M.A. Hayat, Solvent extraction of zirconium(IV) from chloride media by D2EHPA in kerosene, Hydrometallurgy, 63 (2002) 149 - 158.

[21] L.Y. Wang, M.S. Lee, Development of a separation process for the selective extraction of hafnium(IV) over zirconium(IV) from sulfuric acid solutions by using D2EHPA, Hydrometallurgy, 160 (2016) 12 - 17.

[22] M.J. Ungerer, H.M. Krieg, G. Lachmann, D.J. Van der Westhuizen, Separation of tantalum and niobium by solvent extraction, Chemical Resource Beneficiation, North-West University, Potchefstroom Campus, South Africa, North-West University, Potchefstroom, South Africa, 2012, pp. 105.

[23] Z. Zhu, C.Y. Cheng, Solvent extraction technology for the separation and purification of niobium and tantalum: A review, Hydrometallurgy, 107 (2011) 1 - 12.

[24] O.M. El Hussaini, Extraction of niobium from sulfate leach liquor of Egyptian ore sample by triazoloquinazolinone, Transactions of Nonferrous Metals Society of China, 19 (2009) 474 - 478.

[25] R.K. Winge, W.A. Fassel, Atomic emission methods, Academic Press, Inc., Harcourt Brace Jovanovich Publishers, Orlando, Florida, 1984.

[26] G.M. Ritcey, Solvent extraction in hydrometallurgy: Present and future., Tsinghua Science and Technology, 11 (2006) 137 - 152.

[27] F. Noritake, K. Kawamura, Structural transformations in sodium silicate liquids under pressure: A molecular dynamics study, Journal of Non-Crystalline Solids, 447 (2016) 141- 149.

[28] A.R. Zolghadr, M.H. Ghatee, F. Moosavi, The effect of various quantum mechanically derived partial atomic charges on the bulk properties of chloride-based ionic liquids, Chemical Physics, 475 (2016) 23 - 31.

[29] V. Venkatraman, B.K. Alsberg, Quantitative structure-property relationship modelling of thermal decomposition temperatures of ionic liquids, Journal of Molecular Liquids, 223 (2016) 60 - 67.

[30] O. Gereben, L. Pusztai, Understanding the structure of molecular liquids via combinations of molecular dynamics simulations and Reverse Monte Carlo modeling: Handling information deficiency, Journal of Non-Crystalline Solids, 407 (2015) 213 - 219.

[31] D. Ballal, R. Srivastava, Modeling the interfacial properties of Poly(Ethylene oxide-Co-Propylene oxide) polymers at water-toluene interface, Fluid Phase Equilibria, 427 (2016) 209 - 218.

[32] V.S. Bystrov, Molecular modeling and molecular dynamics simulation of the polarization switching phenomena in the ferroelectric polymers PVDF at the nanoscale, Physica B: Condensed Matter, 432 (2014) 21 - 25.

[33] A. Tarakanova, M. Buehler, Molecular modeling of protein materials: case study of elastin, Modelling and Simulation in Materials Science and Engineering, 21 (2013) 063001.

[34] A. Rescifina, C. Zagni, M.G. Varrica, V. Pistarà, A. Corsaro, Recent advances in small organic molecules as DNA intercalating agents: Synthesis, activity, and modeling, European Journal of Medicinal Chemistry, 74 (2014) 95 - 115.

[35] A. Kundu, A. Dutta, P. Biswas, A. Das, A. Ghosh, Functional insights from molecular modeling, docking, and dynamics study of a cypoviral RNA dependent RNA polymerase, Journal of Molecular Graphics and Modelling, 61 (2015) 160 - 174.

[36] V. Turlo, O. Politano, F. Baras, Dissolution process at solid/liquid interface in nanometric metallic multilayers: Molecular dynamics simulations versus diffusion modeling, Acta Materialia, 99 (2015) 363 - 372.

[37] N.A. Lvova, O.Y. Ananina, A.I. Ryazanova, Fluorine and carbon fluoride interaction with a diamond surface: Quantum-chemical modeling, Computational Materials Science, 124 (2016) 30 - 36.

[38] A. Chatterjee, Structure property correlations for nanoporous materials, CRC Press, Taylor & Francis Group, Boca Raton, London, New York, 2010.

[39] H. Dorsett, A. White, Overview of molecular modelling and ab initio molecular orbital methods suitable for use with energetic materials, in: D.o.D.D.S.T. Organisation (Ed.), DSTO Aeronautical and Marine Research Laboratory, Salisbury, Australia, 2000, pp. 46.

[40] N.M. Rice, H.M.N.H. Irving, M.A. Leonard, Nomenclature for liquid-liquid distribution (solvent extraction), International Union of Pure and Applied Chemistry, 65 (1993) 2373 - 2396.

[41] G.R. Astbury, J. Bugand-Bugandet, E. Grollet, K.M. Stell, Flash points of aqueous solutions of flammable solvents, IChemE: Hazards XVIII, Symposium Series no. 150 (2004) 18.

[42] R.A. Buzzi, Chemical hazards at water and wastewater treatment plants, Lewis Publishers, Boca Raton, 1992.

[43] B. Grinbaum, An integrated method for development and scaling up of extraction processes, Marcel Dekker, Inc., New York, 2002.

[44] P.L. Gordon, C. O'Dell, J.G. Watkin, Synthesis and energetic content of red oil, Journal of Hazardous Materials, 39 (1994) 87 - 105.

[45] V.N. Usachev, G.S. Markov, Incidents caused by red oil phenomena at semi-scale and industrial radiochemical units, Radiochemistry, 45 (2003) 1 - 8.

[46] M.J. Ungerer, H.M. Krieg, G. Lachmann, D.J.v.d. Westhuizen, Comparison of extractants for the separation of TaF_5 and NbF_5 in different acidic media, Hydrometallurgy, 144-145 (2014) 195 - 206.

[47] A. Timofeev, A.A. Migdisov, A.E. Williams-Jones, An experimental study of the solubility and speciation of niobium in fluoride-bearing aqueous solutions at elevated temperature, Geochimica et Cosmochimica Acta, 158 (2015) 103 - 111.

[48] R.L. Linnen, I.M. Samson, A.E. Williams-Jones, A.R. Chakhmouradian, 13.21 Geochemistry of the rare-earth element, Nb, Ta, Hf and Zr deposits, Reference Module in Earth Systems and Environmental Sciences - Treatise on Geochemistry (Second Edition), 13: Geochemistry of Mineral Deposits (2014) 543 - 568.

[49] J. Narbutt, M. Czerwinski, Chapter 16 - Computational chemistry in modelling solvent extraction of metal ions, in: J. Rydberg, M. Cox, C. Musikas, G.R. Choppin (Eds.) Solvent extraction principles and practice, Wiley, New York, 1992.

[50] I. Newton, Newton's Principia - The mathematical principles of natural philosophy, in: A. Motte (Ed.) Newton's system of the world, Daniel Adee, 45 Liberty Street, New York, 1846, pp. 594. Reprinted in English in Ref [51].

[51] A.R. Plastino, J.C. Muzzio, On the use and abuse of Newton's second law for variable mass problems, Celestial Mechanics and Dynamical Astronomy (Netherlands: Kluwer Academic Publishers), 53 (1992) 227 - 232.

[52] E. Schrödinger, An undulatory theory of the mechanics of atoms and molecules, Physical Review, 28 (1926) 1049 - 1070.

[53] R. Shankar, Principles of quantum mechanics, Kluwer Academic/Plenum Publishers1994.

[54] E. Clementi, Computational chemistry: attempting to simulate large molecular systems, in: C.E. Dykstra, G. Frenking, K.S. Kim, G.E. Scuseria (Eds.) Theory and applications of computational chemistry: The first forty years, Elsevier, Amsterdam, Netherlands, 2005, pp. 89 - 114.

[55] K.I. Ramachandran, G. Deepa, K. Namboori, Computational chemistry and molecular modeling, Springer-Verlag, Berlin, Heidelberg, 2008.

[56] C. Cramer, Essentials of computational chemistry - Theories and models, 2 ed., John Wiley & Sons Ltd, The Atrium, Southern Gate, Chichester, West Sussex, England, 2008.

[57] G.G. Hall, The molecular orbital theory of chemical valency. VI. Properties of equivalent orbitals, Proceedings of the Royal Society of London A, 202 (1950) 336 - 344.

[58] H. Nakano, T. Nakajima, T. Tsundeda, K. Hirao, Recent advances in ab initio, density functional theory and relativistic electronic structure theory, in: C.E. Dykstra, G. Frenking, J.S. Kim, G.E. Scuseria (Eds.) Theory and applications of computational chemistry - The first forty years, Elsevier, Amsterdam, The Netherlands, 2005, pp. 507 - 557.

[59] P.E.S. Wormer, A. Van der Avoird, Forty years of ab initio calculations on intermolecular forces, in: C.E. Dykstra, G. Frenking, K.S. Kim, G.E. Scuseria (Eds.) Theory and applications of

computational chemistry: The first forty years, Elsevier, Amsterdam, The Netherlands, 2005, pp. 1047 - 1072.

[60] D.R. Hartree, The wave mechanics of an atom with a non-Coulomb central field. Part I. Theory and methods, Mathematical Proceedings of the Cambridge Philosophical Society, 24 (1928) 89 - 110.

[61] C.C.J. Roothaan, Self-consistent field theory for open shells of electronic systems, Reviews of Modern Physics, 32 (1960) 179 - 185.

[62] H. Fukutome, Theory of the unrestricted Hartree-Fock equation and its solutions. I., Progress if Theoretical Physics, 45 (1971) 1382 - 1406.

[63] C. Møller, M.S. Plesset, Note on an approximation treatment for many-electron systems, Physical Review, 46 (1934) 618 - 622.

[64] E.M. Siegbahn, The direct configuration interaction method with a contracted configuration expansion, Chemical Physics, 25 (1977) 197 - 205.

[65] F. Coester, Bound states of a many-particle system, Nuclear Physics, 7 (1958) 421 - 424.

[66] F. Coester, H.G. Kummel, Coupled cluster method, ibid., 17 (1960) 477.

[67] J.A. Pople, M. Head-Gordon, Quadratic configuration interaction. A general technique for determining electron correlation energies, The Journal of Chemical Physics, 87 (1987) 5968 - 35975.

[68] M. Brack, C. Guet, H. H.-B., Selfconsistent semiclassical description of average nuclear properties — a link between microscopic and macroscopic models, Physics Reports, 123 (1985) 275 - 364.

[69] P.G. Szalay, T. Müller, G. Gidofalvi, H. Lischka, R. Shepard, Multiconfiguration self-consistent field and multireference configuration interaction methods and applications, Chemical Reviews, 112 (2012) 108 - 181.

[70] B. Liu, Ab initio potential energy surface for linear H_3, The Journal of Chemical Physics, 58 (1973) 1925 - 1937.

[71] C. Angeli, R. Cimiraglia, S. Evangelisti, T. Leininger, J.-P. Marlrieu, Introduction of n-electron valence states for multireference perturbation theory, The Journal of Chemical Physics, 114 (2001) 10252.

[72] B. Roos, P. Linse, P.E.M. Siegbahn, M.R.A. Blomberg, A simple method for the evaluation of the second-order-perturbation energy from external double-excitations with a CASSCF reference wavefunction, Chemical Physics, 66 (1982) 197 - 207.

[73] B. Jeziorski, H. Monkhorst, Coupled-cluster method for multideterminantal reference states, Physical Review A, 24 (1981) 1668.

[74] L.H. Thomas, The calculation of atomic fields, Mathematical Proceedings of the Cambridge Philosophical Society, 23 (1927) 542 - 548.

[75] E. Fermi, Un Metodo Statistico per la Determinazione di alcune Prioprietà dell'Atomo, Atti della Accademia Nazionale dei Lincei, 6 (1927) 602 - 607.

[76] N.H. March, Self-consistent fields in atoms: Hartree and Thomas-Fermi atoms, Pergamon, Oxford, 1975.

[77] P.E.M. Dirac, Note on exchange phenomena in the Thomas atom, Mathematical Proceedings of the Cambridge Philosophical Society, 26 (1930) 376 - 385.

[78] C.F.v. Weizsäcker, Zur Theorie der Kernmassen, Zeitschrift für Physik, 96 (1935) 431 - 458.

[79] G.E. Scuseria, V.N. Staroverov, Progress in the development of exchange-correlation functionals, in: C.E. Dykstra, G. Frenking, K.S. Kim, G.E. Scuseria (Eds.) Theory and applications of computational chemistry: The first forty years, Elsevier, Amsterdam, The Netherlands, 2005, pp. 669 - 724.

[80] P. Hohenberg, W. Kohn, Inhomogeneous electron gas, Physical Review, 136 (1964) B864 - B871.

[81] W. Kohn, L.J. Sham, Self-consistent equations including exchange and correlation effects, Physical Review, 140 (1965) A1133 - A1138.

[82] J.P. Perdew, K. Schmidt, Jacob's ladder of density functional approximations for the exchange-correlation energy, American Institute of Physics Conference Antwerp, Belgium, 2001, pp. 12.

[83] V.N. Staroverov, G.E. Scuseria, Comparative assessment of a new nonempirical density functional: Molecules and hydrogen-bonded complexes, Journal of Chemical Physics, 119 (2003) 12129 - 12137.

[84] A.D. Becke, Experimental investigation of highly exergonic outer sphere electron transfer reactions, Journal of Physical Chemistry, 88 (1984) 2547-2551.

[85] C. Lee, W. Yang, R.G. Parr, Development of the Colle-Solvetti correlation-energy formula into a functional of the electron density, Physical Review B, 37 (1988) 785-789.

[86] J.P. Perdew, K. Burke, M. Ernzerhof, Generalized gradient approximation made simple, Physical Review Letters, 77 (1996) 3865 - 3868.

[87] F. Furche, Molecular tests of the random phase approximation to the exchange-correlation energy functional, Physical Review B, 64 (2001) 195120.

[88] M. Fuchs, Y.-M. Niquet, X. Gonze, K. Burke, Describing static correlation in bond dissociation by Kohn–Sham density functional theory, The Journal of Chemical Physics, 122 (2005) 094116.

[89] A. Otero-Calvi, L.A. Montero, W.-D. Stohrer, DFT modelling of cobalt and nickel complexes with dithiophosphinic acid, Journal of Molecular Structure: THEOCHEM, 859 (2008) 93 - 97.

[90] A.D. Becke, Density-functional exchange-energy approximation with correct asymptotic behavior, Physical Review A, 38 (1988) 3098 - 3100.

[91] A.D. Becke, Densityfunctional thermochemistry. III. The role of exact exchange, Journal of Chemical Physics, 98 (1993) 5648 - 5652.

[92] A.D. Becke, A new mixing of Hartree–Fock and local density-functional theories, Journal of Chemical Physics, 98 (1993) 1372 - 1377.

[93] P.J. Hay, W.R. Wadt, Ab initio effective core potentials for molecular calculations. Potentials for K to Au including the outermost core orbitals, Journal of Chemical Physics, 82 (1985) 299 - 310.

[94] M. Siodmiak, G. Frenking, A. Korkin, Initial reactions in chemical vapor deposition of Ta_2O_5 from $TaCl_5$ and H_2O. An ab initio study., Journal of Chemical Physics A, 104 (2000) 1186 - 1195.

[95] M. Siodmiak, G. Frenking, A. Korkin, On the mechanism of chemical vapor deposition of Ta_2O_5 from $TaCl_5$ and H_2O. An ab initio study of gas phase reactions, Materials Science in Semiconductor Processing, 3 (2000) 65 - 70.

[96] A. Bergner, M. Dolg, W. Küchle, H. Stoll, H. Preuss, Ab initio energy-adjusted pseudopotentials for elements of groups 13-17, Molecular Physics: An International Journal at the Interface Between Chemistry and Physics, 80 (1993) 1431 - 1441.

[97] S. Huzinaga, J. Andzelm, M. Klobukowski, E. Radzio-Andzelm, Y. Sakai, H. Tatewaki, Physical Sciences Data 16, in: S. Huzinaga (Ed.) Gaussian basis sets for molecular calculations, Elsevier, Amsterdam, 1984.

[98] V. Loukonen, I.-F.W. Kuo, M.J. McGarth, H. Vehkamäki, On the stability and dynamics of (sulfuric acid)(ammonia) and (sulfuric acid)(dimethylamine) clusters: A first-principles molecular dynamics investigation, Chemical Physics, 428 (2014) 164 - 174.

[99] J. VandeVondele, M. Krack, F. Mohamed, M. Parrinello, T. Chassaing, J. Hutter, Quickstep: Fast and accurate density functional calculations using a mixed Gaussian and plane waves approach, Computer Physics Communications, 167 (2005) 103 - 128.

[100] S. Goedecker, M. Teter, J. Hutter, Separable dual-space Gaussian pseudopotentials, Physical Review B, 54 (1996) 1703 - 1710.

[101] T. Kurtén, I.K. Ortega, H. Vehkamäki, The sign preference in sulfuric acid nucleation, Journal of Molecular Structure: THEOCHEM, 901 (2009) 169 - 173.

[102] M.J. Frisch, J.A. Pople, J.S. Binkley, Self-consistent molecular orbital methods 25. Supplementary functions for Gaussian basis sets, The Journal of Chemical Physics, 80 (1984) 3265 - 3269.

[103] J.M. Soler, E. Artacho, J.D. Gale, A. García, J. Junquera, P. Ordejón, D. Sánchez-Portal, The SIESTA method for ab initio order-N materials simulation, Journal of Physics: Condensed Matter, 14 (2002) 2745 - 2779.

[104] R. Ahlrichs, M. Bär, M. Häser, H. Horn, C. Kölmel, Electronic structure calculations on workstation computers: The program system turbomole, Chemical Physics Letters, 162 (1989) 165 - 169.

[105] B.W. McCann, N. De Silva, T.L. Windus, M.S. Gordon, B.A. Moyer, V.S. Bryantsev, B.P. Hay, Computer-aided molecular design of bis-phosphine oxide lanthanide extractants, Inorganic Chemistry, (2016).

[106] B.P. Hay, T.K. Firman, HostDesigner: A program for the de Novo structure-based design of molecular receptors with binding sites that complement metal ion guests, Inorganic Chemistry, 41 (2002) 5502 - 5512.

[107] J.S. Arora, U. Joshi, V.G. Gaikar, S.M. Ali, Experimental and DFT studies for selective separation of Sb(iii) and Sb(v) from mixtures with Zr(iv)/Co(ii) using thiourea grafted polystyrene adsorbent, RSC Advances, 5 (2015) 71393 - 71401.

[108] A. Dartiguelongue, A. Changnes, E. Provost, W. Fürst, G. Cote, Modelling of uranium(VI) extraction by D2EHPA/TOPO from phosphoric acid within a wide range of concentrations, Hydrometallurgy, Under press (2015).

[109] S.A.S. SciLab Enterprises, SciLab, Copyright ©, Orsay Cedex, France, 1989-2005.

[110] S. Pahan, A. Boda, S.M. Ali, Density functional theoretical analysis of structure, bonding, interaction and thermodynamic selectivity of hexavalent uranium (UO_2^{2+}) and tetravalent

plutonium (Pu^{4+}) ion complexes of tetramethyl diglycolamide (TMDGA), Theoretical Chemistry Accounts, 134 (2015) 1 - 16.

[111] S.M. Ali, Design and screening of suitable ligand/diluents systems for removal of Sr2+ ion from nuclear waste: Density functional theoretical modelling, Computational and Theoretical Chemistry, 1034 (2014) 38 - 52.

[112] J.P. Perdew, Density-functional approximation for the correlation energy of the inhomogeneous electron gas, Physical Review B, 33 (1986) 8822 - 8824.

[113] F. Weigend, M. Häser, H. Patzelt, R. Ahlrichs, RI-MP2: optimized auxiliary basis sets and demonstration of efficiency, Chemical Physics Letters, 294 (1998) 143 - 152.

[114] M. Kaupp, P.v.R. Schleyer, H. Stoll, H. Preuss, Pseudopotential approaches to Ca, Sr, and Ba hydrides. Why are some alkaline earth MX2 compounds bent?, Journal of Chemical Physics, 94 (1991) 1360 - 1366.

[115] A. Klamt, G. Schüürmann, COSMO: a new approach to dielectric screening in solvents with explicit expressions for the screening energy and its gradient, Journal of the Chemical Society, Perkin Transactions 2, (1993) 799 - 805.

[116] S.M. Ali, D.K. Maity, S. De, M.R.K. Shenoi, Ligands for selective metal ion extraction: A molecular modeling approach, Desalination, 232 (2008) 181 - 190.

[117] J.J.P. Steward, Optimization of parameters for semiempirical methods. I. Method, Journal of Computational Chemistry, 10 (1989) 209 - 220

[118] J.J.P. Steward, Optimization of parameters for semiempirical methods. II. Applications, Journal of Computational Chemistry, 10 (1989) 221 - 264.

[119] N. Sieffert, G. Wipff, Alkali cation extraction by calix[4]crown-6 to room-temperature ionic liquids. The effect of solvent anion and humidity investigated by molecular dynamics simulations, The Journal of Physical Chemistry A, 110 (2006) 1106 - 1117.

[120] G.G. Krishna, R.S. Reddy, P. Raghunath, K. Bhanuprakash, M.L. Kantam, B.M. Choudary, A computational study of ligand interactions with hafnium and zirconium metal complexes in the liquid−liquid extraction process, The Journal of Physical Chemistry B, 108 (2004) 6112 - 6120.

[121] G.J. Lumetta, B.M. Rapko, P.A. Garza, B.P. Hay, R.D. Gilbertson, T.J.R. Weakley, J.E. Hutchison, Deliberate design of ligand architecture yields dramatic enhancement of metal ion affinity, Journal of the American Chemical Society, 124 (2002) 5644 - 5645.

[122] L.K. Holte, B.A. Kuran, G.L. Richmond, K.E. Johnson, Computational modeling of lauric acid at the organic-water interface, Journal of Physical Chemistry C, 118 (2014) 10024 - 10032.

[123] J.W. Caldwell, P.A. Kollman, Structure and properties of neat liquids using nonadditive molecular dynamics: Water, methanol, and N-methylacetamide, The Journal of Physical Chemistry, 99 (1995) 6208 - 6219.

[124] P. Kujawski, M.B. Bogacki, Molecular dynamics study of the behaviour of TBP-zinc-chloride complex at the chloroform/water interfacial system, Separation Science and Technology, 47 (2012) 1285 - 1295.

[125] X. Cao, D. Heidelberg, J. Ciupka, M. Dolg, First-principles study of the separation of AmIII/CmIII from EuIII with Cyanex301, Inorganic Chemistry, 49 (2010) 10307 - 10315.

[126] A. Chaumont, G. Wipff, Solvation of 'big' spherical solutes in room temperature ionic liquid and at their aqueous interface: A molecular dynamics simulation study, Journal of Molecular Liquids, 131-132 (2007) 36 - 47.

[127] B. Coupez, G. Wipff, The synergistic effect of cobalt-dicarbollide anions on the extraction of M^{3+} lanthanide cations by Calix[4]arenes: A molecular dynamics study at the water–'oil' interface, Comptes Rendus Chimie, 7 (2004) 1153 - 1164.

[128] B. Coupez, C. Boehme, G. Wipff, Importance of interfacial phenomena and synergistic effects in lanthanide cation Extraction by dithiophosphinic ligands: A molecular dynamics study, The Journal of Physical Chemistry B, 107 (2003) 9484 - 9490.

[129] W.D. Cornell, P. Cieplak, C.I. Bayly, I.R. Gould, K.M. Merz, D.M. Ferguson, D.C. Spellmeyer, T. Fox, J.W. Caldwell, P.A. Kollman, A second generation force field for the simulation of proteins, nucleic acids, and organic molecules, Journal of the American Chemical Society, 117 (1995) 5179 - 5197.

[130] C. Boehme, G. Wipff, The energetic and structural effects of steric crowding in phosphate and dithiophosphinate complexes of lanthanide cations M^{3+}: A computational study, Chemistry A European Journal, 7 (2001) 1398 – 1407.

[131] M. Baaden, R. Schurhammer, G. Wipff, Molecular dynamics study of the uranyl extraction by tri-n-butylphosphate (TBP): Demixing of water/"oil"/TBP solutions with a comparison of supercritical CO2 and chloroform, The Journal of Physical Chemistry B, 106 (2002) 434 - 441.

[132] M. Baaden, M. Burgard, G. Wipff, TBP at the water-oil interface: The effect of TBP concentration and water acidity investigated by molecular dynamics simulations, The Journal of Physical Chemistry B, 105 (2001) 11131 - 11141.

[133] C.J. Fennel, K.A. Dill, Physical modeling of aqueous solvation, Journal of Statistical Physics, 145 (2011) 209 - 226.

CHAPTER 3

Chapter 3 consists of the article titled 'Molecular modelling of tantalum penta-halides during hydrolysis and oxidation reactions', which is added into this thesis in the exact format in which it was published in the *Journal of Computational and Theoretical Chemistry (2016) 1090: 112 – 119.* The journal can be found at http://www.sciencedirect.com/science/journal/2210271X/1090/supp/C. (Date of submission: 5 February 2016)

3.1 Introduction

While several techniques have been proposed for separation and purification of various metals [1], solvent extraction (SX) is widely used for amongst others copper (Cu), nickel (Ni), iron (Fe), platinum group metals (PGMs), zirconium (Zr), hafnium (Hf), tantalum (Ta) and niobium (Nb). Ta and Nb are valuable metals with various high-end uses, where Ta is used in the nuclear industry as cladding material, as capacitors, as high power resistors and to make high strength corrosion resistant alloys, while Nb is used in super alloys for jet engines and heat resistant equipment. Ta and Nb, which co-occur in mineral deposits, have near identical properties making their separation challenging.

In a recent study Ungerer et al. [2] studied the SX based separation of Ta and Nb, using alternative and safer chemicals while investigating the suitability of membrane-based solvent extraction (MBSX). While partial separation of Ta and Nb was achieved, it was not possible to predict extraction behaviour prior to experimental testing, due to the current absence of speciation data for Ta and Nb. Speciation data for Ta and Nb is not available, possibly due to their insolubility in most aqueous liquids [3, 4] and because they are UV inactive making the detection and identification of the aqueous species difficult. An alternative method that could however be suitable for predicting the speciation and hence extraction of Ta and Nb is molecular modelling [5]. Applying molecular modelling to SX could for example entail a step-by-step analysis of the extraction process on a molecular level, thereby determining the molecular properties as well as the system reactions occurring during SX.

According to the previously published data [2], the SX process of Ta and Nb can be divided into three parts: 1) the aqueous phase containing water soluble tantalum(V) penta-fluoride (TaF_5) , 2) the organic phase containing the extractant and diluent and 3) the interface where these two phases make contact. For the modelling of the first step (TaF_5 in an aqueous environment), the molecular structure of TaF_5 is required. Since single crystals of TaF_5 do not form readily, they exist as oligomeric penta-fluorides with three possible structure types [6], neither the experimentally determined molecular structure of TaF_5 is well known, nor have these properties been modelled. However, for $TaCl_5$ both the molecular structure [7] as well as its interaction in an aqueous environment have been modelled [8, 9]. If it is assumed that TaF_5 has a similar symmetrical structure and behaviour in water than $TaCl_5$, (an assumption that will be evaluated in this paper), then $TaCl_5$ could be used to validate the novel modelling approach before applying the modelling to a compound of which the structure and behaviour is unknown.

According to Agulyansky [7] $TaCl_5$ has a trigonal bipyramidal structure, assuming above mentioned similarity, TaF_5 would have a similar trigonal bipyramidal structure. The differences between TaF_5 and $TaCl_5$ will be discussed further in Section 3.3.

Using the above information, it is the aim of this paper to develop a molecular modelling approach to validate the structure of TaF_5 while determining the possible hydrolysis and subsequent oxidation reactions thereof in an aqueous environment. However, as stated above limited experimental or modelling data is available for the reactions of TaF_5 to verify the suitability of the newly developed model. Hence, the paper was subdivided into two sections. Firstly, the model will be verified in terms of the structure of $TaCl_5$ as well as its possible hydrolysis and oxidation reactions. Once the correlation of the modelled and literature data has been demonstrated for $TaCl_5$, a case study is presented where the verified model will be used to confirm the structure of TaF_5 as well as to calculate its possible hydrolysis and oxidation reactions. In a final step a brief section is presented discussing the possible transition states found during the most likely hydrolysis reaction of TaF_5 to $TaF_4(OH)$.

3.2 Computational Methods

3.2.1 Model Verification ($TaCl_5$)

For the molecular modelling of $TaCl_5$ and its reactions with H_2O in an aqueous environment, the DMol^3 module of the Biovia Materials Studio 6.1 software from Dassault Systems (previously Accelrys) [10] was used in conjunction with the DFT semi-empirical dispersion interaction correction module (DFT-SEDC). For comparison five different combinations of functional and basis sets were used to determine the structure of the $TaCl_5$ molecule (geometry optimisation [11, 12]), as well as its hydrolysis and oxidation reactions.

1) Generalized-gradient approximation (GGA) with Perdew-Wang correlation functional (PW91) [11] and DND (double-numeric polarization plus d-functions) basis set with basis file 4.4 and OBS dispersion correction. (DND is comparable with the Gaussian 6-31G* basis set.)
2) GGA PW91 functional with basis set DNP (double-numeric polarization functions), with basis file 4.4 and OBS dispersion correction. (DNP is comparable with the Gaussian 6-31G** basis set.)
3) GGA PW91 functional with basis set DNP+ (double numerical plus polarization, with addition of diffuse functions) with basis file 4.4 and OBS dispersion correction. (DNP+ is more accurate than a Gaussian basis set (Gaussian 6-31G**) of the same size.)
4) GGA with Perdew-Burke-Ernzerhof (PBE) [13] correlation, with basis set DNP+ and basis file 4.4.
5) Becke exchange plus Lee-Yang-Parr correlation (B3LYP) [14, 15] hybrid exchange-correlations energy functional, with basis set DNP and basis file 4.4.

For the calculations done with PBE(DNP+) and B3LYP(DNP), no dispersion correction was added. Only Tkatchenko-Scheffler (TS) [16] and Grimme [17] dispersion corrections were available in these settings and in both TS and Grimme the element coverage for Ta was unavailable. Under the electronic properties, smearing of 0.005 Hartree (Ha) was chosen for all the calculations [18]. Furthermore, the conductor-like screening model (COSMO) [19] was used to simulate the molecules within a solvent. In this case the solvent was water, with a dielectric constant of 78.54.

After the geometry optimisation process, single point energy calculations were done to calculate various electronic properties with the same settings that were used for the geometry optimisations. The calculations were done at 0 K and an energy correction term was added to give Gibbs free energy values at 298.15 K. The zero-point vibrational energy (ZPVE) was included in all calculations. Frequency calculations were used to confirm optimised structures (minimum energy) and transition states (one imaginary frequency).

3.2.2 Case Study (TaF_5)

For the molecular modelling of TaF_5 and its hydrolysis and oxidation reactions, the DMol^3 module of the Biovia Materials Studio 6.1 software from Dassault Systems (previously Accelrys) [10] was used with the GGA PBE functional [13]. The basis set used was DNP+ with basis file 4.4, which includes diffuse functions. Under the electronic properties, smearing of 0.005 Hartree (Ha) was chosen [18]. The single point energy calculations were done as described in Section 2.1. A potential energy surface (PES) scan was done by a stepwise shortening of the distance between the Ta atom of TaF_5 and the O atom of one of the surrounding H_2O to determine the energy and geometry change during the formation of $Ta(H_2O)F_5$.

3.3 Results and Discussion

3.3.1 Model Verification ($TaCl_5$)

3.3.1.1 Geometry optimisation of $TaCl_5$

The $TaCl_5$ molecule was geometrically optimised with the five functional and basis set settings (Section 3.2.1). The bond lengths and bond angles between the Ta and the five Cl atoms were measured and compared to experimental literature as shown in Table 3.1.

Table 3.1 – Calculated and experimental literature values of bond lengths and bond angles of $TaCl_5$

Bond/Angle	Literature [6]	PW91 (DND)	PW91 (DNP)	PW91 (DNP+)	PBE (DNP+)	B3LYP (DNP)
Ta-Cl1 [Å]	2.284	2.327	2.327	2.327	2.321	2.331
Ta-Cl3 [Å]	2.426	2.381	2.381	2.379	2.379	2.385
Ta-Cl4 [Å]	2.426	2.381	2.381	2.379	2.380	2.385
Ta-Cl5 [Å]	2.284	2.317	2.317	2.317	2.321	2.314
Ta-Cl6 [Å]	2.284	2.317	2.317	2.317	2.322	2.321
Cl1-Ta-Cl6 [°]	120.00	120.61	120.61	120.80	119.96	122.40
Cl1-Ta-Cl5 [°]	120.00	120.61	120.61	120.80	120.13	121.16
Cl1-Ta-Cl3 [°]	90.00	89.28	89.28	89.54	89.99	88.94
Cl1-Ta-Cl4 [°]	90.00	89.28	89.28	89.54	90.00	89.94

From Table 3.1 it can be seen that according to the modelled values the two Ax Cl atoms (Cl3 and Cl4) have longer bond lengths than the three Eq Cl atoms (Cl1, Cl5 and Cl6), which correlates with various literature sources [6, 20, 21]. This implies that the three Eq Cl atoms push the two Ax Cl atoms out of the plane, making the Ax bond lengths longer and hence the bond strength weaker. From the experimental literature values [6] the difference in bond lengths between the Ax and Eq Cl atoms is 0.142 Å, where with the modelling it was found to be 0.065 ± 0.006 Å. This difference is due to literature values are for crystals where the modelled values are simulated for a liquid. Previous theoretical values calculated with ab initio B3LYP method [8] showed Ax and Eq bond length to be 2.337 Å and 2.287 Å respectively. The modelled bond lengths are closer to the experimentally observed values [6] than the values presented by Siodmiak et al. [8]. In terms of the bond angle the values with PW91(DND), PW91(DNP) and PW91(DNP+) were similar with a 0.22 ± 0.04° deviation from each other and differed by 0.66 ± 0.006° from literature [6]. The bond angles calculated with PBE(DNP+) differed by 0.007 ± 0.006° from literature [6]. The modelled data from B3LYP(DNP) showed a 1.42 ± 1° average deviation from literature [6]. Calculations with PW91(DND), PW91(DNP), PW91(DNP+) and PBE(DNP+) yielded realistic values in a relatively short calculation time, whereas B3LYP(DNP) calculations were time consuming with a generally greater deviation in bond lengths and angles.

To further confirm the stability of the molecule structure, the model was used to determine the vibrational frequencies of the $TaCl_5$ which were compared to experimental literature values. Since $TaCl_5$ is a nonlinear molecule with 3N-6 degrees of freedom and N = 6 atoms, $TaCl_5$ has 12 degrees of freedom and therefore 12 types of molecular vibrations (stretching and bending modes). Of these 12 only 8 vibrations are experimentally observed because the symmetry class E is double degenerated, which means that both the degenerated modes are observed as a single infrared absorption band [8]. Table S1 shows the experimental literature and modelled vibrational

frequencies for the 8 molecular vibrations of $TaCl_5$ calculated with the five functional and basis set settings stated in Section 3.2.1.

Comparing all five functional and basis sets with each other, the frequencies are within 6 cm^{-1} from each other. The frequencies obtained with PW91(DND), PW91(DNP) and PW91(DNP+) were similar with a deviation less than 4 cm^{-1} from each other. The modelled values are lower than the experimental literature values, because the experimental frequencies of $TaCl_5$ are in the gas phase and the modelling within an ideal system cannot simulate all the stretching and bending vibrations. Also the frequencies shown here are calculated harmonic vibrational frequencies (ω) without a scaling factor [22, 23] to account for the error between harmonic vibrational frequency and fundamental vibrational frequency (v). The modelled frequencies had a standard deviation of less than 10% with literature, except for ω_6 and ω_8. The e'' vibrational mode is formally symmetry forbidden, but coupling may let the ω_6 and ω_8 vibration mode mix with other vibrations, leading to this error in symmetry assignment [24]. The obtained results of vibrational frequencies are shifted higher because of electron correlation and anharmonicity effects in the theoretical treatment used within the modelling, which in turn could cause the bond length over estimation seen previously.

3.3.1.2 Hydrolysis and oxidation reactions of $TaCl_5$

In Figure 3.1, the most important hydrolysis (shown as Reaction 1 – 5) and oxidation (Reaction 6 – 12) reactions that might occur are presented. While various other reactions and geometries may occur during this reaction, the probability of only those reactions shown in Figure 3.1 was determined. For the purpose of this discussion, first the hydrolysis reactions (Reaction 1 – 5) and then the oxidation reactions (Reaction 6 – 12) will be discussed.

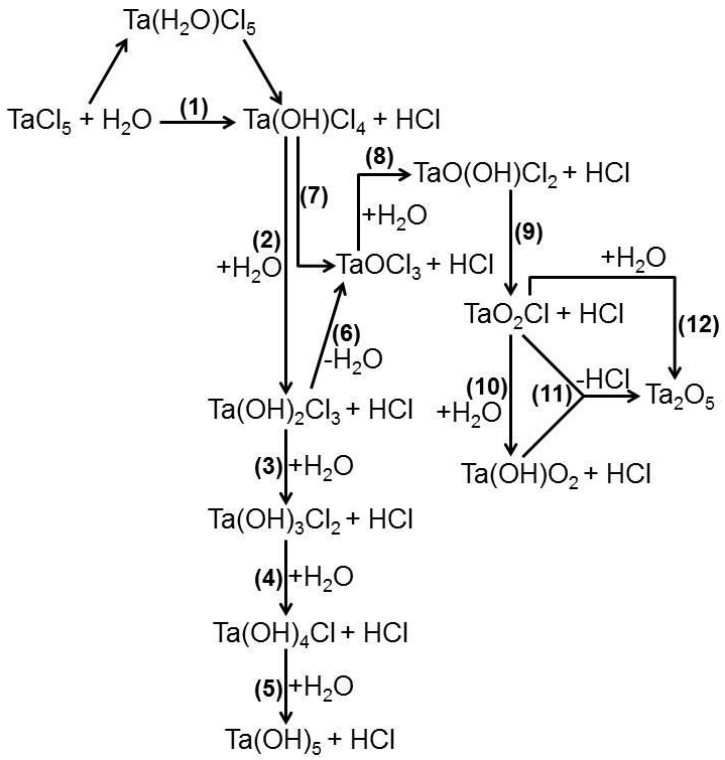

Figure 3.1 – Possible hydrolysis and oxidation reaction scheme of $TaCl_5$ with H_2O

$TaCl_5$ has five Cl atoms that can be individually replaced by OH groups (Reaction 1 – 5), when reacting with five consecutive H_2O molecules, finally resulting in the formation of tantalum penta-hydroxide ($Ta(OH)_5$). During these reactions with H_2O, the OH group can either substitute a Cl in the axial (Ax) or in the equatorial (Eq) positions. When considering these orientations of the substitution (Reaction 1 – 5 (Figure 3.1)) a significant number of conformers can be produced as is shown in Figure 3.2.

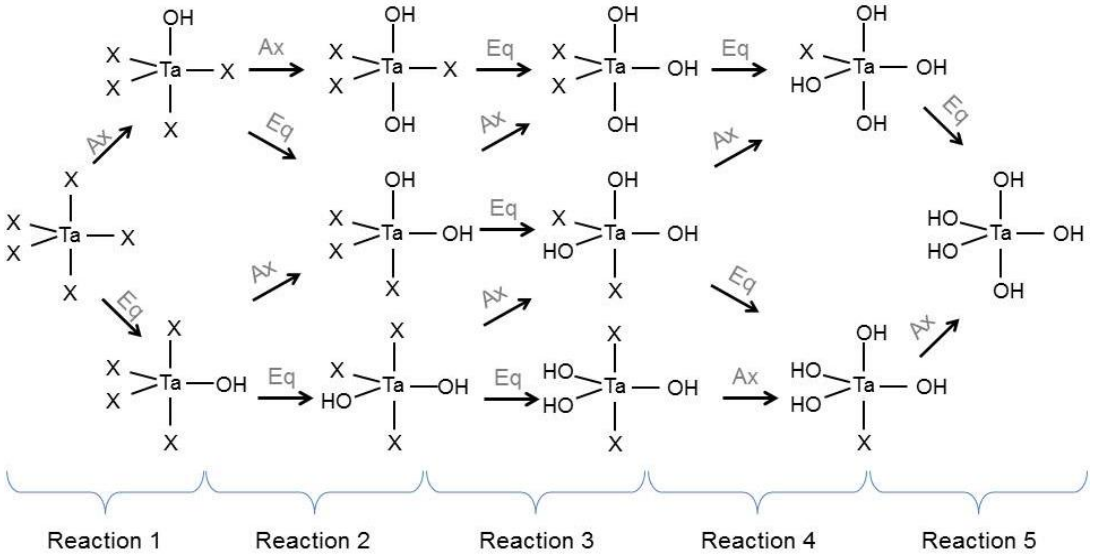

Figure 3.2 – Proposed TaX_5 (X = Cl or F) hydrolysis reaction scheme considering the orientation of substitution

All 12 geometries presented in Figure 3.2 were geometrically optimised and single point energy calculations were done. Again the five functionals and basis set settings were compared as had been done in Section 3.3.1.1 for the bond lengths, angles and vibrational frequencies. The relative energies of the conformers are presented (Table 3.2) relative to the conformer where a single OH group was Eq coordinated.

Table 3.2 – Relative energies (kcal/mol) of tantalum hydroxyl chloride conformers

Molecule*	PW91 (DND)	PW91 (DNP)	PW91 (DNP+)	PBE (DNP+)	B3LYP (DNP)
$TaCl_4OH$					
E	0.0	0.0	0.0	0.0	0.0
A	1.32	1.03	0.27	1.52	1.38
$TaCl_3(OH)_2$					
EE	0.0	0.0	0.0	0.0	0.0
AE	1.35	1.08	1.51	1.34	1.99
AA	2.92	3.00	3.95	2.44	2.91
$TaCl_2(OH)_3$					
EEE	0.0	0.0	0.0	0.0	0.0
AEE	1.70	2.00	2.24	1.43	0.56
AAE	0.41	0.48	-0.73	0.74	0.84
$TaCl(OH)_4$					
AAEE	0.0	0.0	0.0	0.0	0.0
AEEE	0.05	0.10	-0.84	0.16	0.51

* E and A refer to the equatorial or axial position of the OH group respectively

$TaCl_4OH$ has two conformers, one where the OH group is in the Eq position (OH-E) and one where it is in the Ax position (OH-A). The OH-E conformer has a lower energy than the OH-A conformer for all the functionals and basis sets and is therefore most likely to form. Siodmiak et al. [8, 9] also found the OH-A conformer to have a higher energy than OH-E, by an average of 1.03 kcal/mol, which correlates best with the results obtained from the PW91(DNP) calculation. The lowest correlation was observed for PW91(DNP+). $TaCl_3(OH)_2$ has three conformers, i) both OH groups are in the Eq position (EE), ii) one OH group is Ax and the other Eq (AE) and iii) both OH groups are Ax (AA). The EE conformer was lower in energy, followed by the AE conformer and then the AA conformer according to all the functionals and basis sets. This was confirmed by Siodmiak et al. [8, 9] who found the AE conformer to have a higher energy than EE, by an average of 0.85 kcal/mol with the AA conformer having the highest energy with an average of 1 kcal/mol. While the tendency is the same the differences observed in this study were slightly higher, which could be attributed to the fact that different models being compared. The literature values stated here were done with Gaussian 98, Ta had a quasi-relativistic core potential and the oxygen and hydrogen atoms were calculated with a 6-31G** basis set.

$TaCl_2(OH)_3$ has three conformers, where the OH can be oriented either EEE, AEE or AAE. The EEE conformer had the lowest energy, followed by AEE and then AAE. Similar tendencies were again observed by Siodmiak et al. [8, 9]. With $TaCl(OH)_4$ two conformers were investigated, i.e. AAEE and AEEE. According to Table 3.2, the AAEE conformer has a lower energy than the AEEE conformer. From these results it seems when an OH group bonds and evicts an HCl, both the first and the second OH will preferentially replace an Eq Cl. However, with the introduction of the third OH group, a rearrangement takes place to preferentially yield either AAE or AEE in almost equal form, with an energy difference less than 1.52 kcal/mol . In the fourth replacement again an Eq attachment was observed yielding AAEE preferentially before $Ta(OH)_5$ is formed in the final step.

When considering the subsequent oxidation reactions (Figure 3.1, Reaction 6 - 12), various oxyfluoride species are formed. Due to their importance much of this discussion will however focus on $TaOCl_3$ and TaO_2Cl. $TaOCl_3$ and TaO_2Cl, the structure of which is shown in the supplementary section (Figure S1 and Figure S2 respectively), were also geometrically optimised with the five functional and basis set settings described in Section 3.2.1. The obtained bond lengths, angles and vibrational frequencies are given for $TaOCl_3$ and TaO_2Cl in Table S2 and Table S3 respectively. Since there are no experimentally determined bond lengths and angles for the molecular structure of these two molecules, the modelled values were compared to modelled values obtained by Siodmiak et al. [8] who used an ab initio method with B3LYP at 0 K.

For $TaOCl_3$ the modelled values (Table S2) with regards to bond lengths differed 0.038 ± 0.007 Å from literature and less than 0.013 Å from each other. Comparing the bond angles the modelled

data differed by less than 1° from literature and less than 0.4° from each other. $TaOCl_3$ is a nonlinear molecule with 9 degrees of freedom, where only 6 vibrations are experimentally observed. Table S2 shows the literature and modelled vibrational frequencies for the 6 molecular vibrations of $TaOCl_3$ ($\omega_1 - \omega_6$), where ω_1 is assigned to the Ta-O bond stretch, ω_2 to the Ta-Cl symmetric bond stretch, ω_3 to the Cl–Ta-Cl symmetric bending, ω_4 to the Ta-Cl asymmetric bond stretch, ω_5 to the O-Ta-Cl bending and ω_6 to the Cl-Ta-Cl asymmetric bending. All the modelled values correlate with literature values (error = 10%), except for ω_6 (error = 15%) which probably mixes with other vibrations as was observed for $TaCl_5$ (see Table S1). The core treatment parameter with these calculations was 'All Electron' and this theoretical treatment of electron correlation and anharmonicity might account for the difference in frequency between the literature and modelled values.

While Ta in the +5 valence state is expected to have an sd^4 hybridisation structure, TaO_2Cl has most likely an sd^2 hybridisation structure because of the double bonds with oxygen. Accordingly, one could expect that $TaOCl_2$ had a planar structure, however the modelling results revealed a nonplanar structure as shown in Figure S2. In an ideal sd^2 structure, the ligand-metal-ligand angle would be 90°, but because of ligand-ligand repulsion and metal-ligand overlap these angles deviate from 90° [25], resulting in a trigonal pyramidal structure which has been confirmed by Siodmiak et al. [9]. According to the results obtained (Table S3) the bond length error with all five functional and basis sets were 0.01 Å compared to each other and less than 0.03 Å compared to literature. With regards to the modelled bond angles, the O-Ta-O angle with PBE(DNP+) and PW91(DND, DNP, DNP+) was slightly smaller than the literature value, while being bigger when modelled with B3LYP(DNP). Comparing the values obtained from the modelling to the literature modelled results there were a less than 2% deviation in bond angle. When the planar structure was modelled, the bonds became longer (Ta-O = 1.768 Å, Ta-Cl = 2.404 Å) and the energy was higher, indicating a more unstable structure.

TaO_2Cl is a nonlinear molecule with 6 degrees of freedom, while only 4 vibrations are experimentally observed. Table S3 shows the literature and modelled vibrational frequencies for the 4 molecular vibrations of TaO_2Cl. The vibration of ω_1 is assigned to the Ta-O bond symmetric stretch, ω_2 to the Ta-Cl bond stretch, ω_3 to the Cl-Ta-O_2 symmetric bending and ω_4 to the Ta-O bond asymmetric stretch. Again the literature values were obtained from the modelled values of Siodmiak et al. [8]. The modelled frequencies differed by 6% from literature values, except for ω_3 that had an error of 17%, which mixes with other vibrations of O-Ta-O bending.

While in the previous paragraphs the energies of individual reagents and products were presented, Table 3.3 shows the modelled energies of formation ($\Delta H_f^{298.15\,K}$ / kcal/mol) for Reaction 1 – 12 with all five functional and basis set settings, to determine a possible reaction mechanism

for the formation of oxyhalide species. Accordingly, Reaction 1 and 2 were moderately endothermic with the PW91 functional and three basis sets, while being exothermic with PBE(DNP+) and B3LYP(DNP). Theoretical literature [8, 9] also showed Reaction 1 and 2 to be exothermic. Reactions 3-12 were moderately endothermic (except for Reaction 9 which was strongly endothermic) irrespective of the functional used, which is possibly why the experimental observation of the oxychloride has been particularly difficult [26].

Table 3.3 – Energy of formation ($\Delta H_f^{298.15\ K}$ / kcal/mol) of tantalum chloride and oxychloride reactions with water.

	Literature [8, 9]	PW91 (DND)	PW91 (DNP)	PW91 (DNP+)	PBE (DNP+)	B3LYP (DNP)
1) $TaCl_5 + H_2O \rightarrow TaCl_4OH + HCl$	-8.6	2.13	1.82	2.25	-0.94	-2.67
2) $TaCl_4OH + H_2O \rightarrow TaCl_3(OH)_2 + HCl$	-7.4	1.06	1.11	2.41	-0.13	-3.89
3) $TaCl_3(OH)_2 + H_2O \rightarrow TaCl_2(OH)_3 + HCl$		4.15	4.06	4.67	3.53	0.80
4) $TaCl_2(OH)_3 + H_2O \rightarrow TaCl(OH)_4 + HCl$		6.50	6.18	7.13	5.18	2.29
5) $TaCl(OH)_4 + H_2O \rightarrow Ta(OH)_5 + HCl$		11.01	10.92	10.43	10.61	9.39
6) $TaCl_3(OH)_2 \rightarrow TaOCl_3 + H_2O$	16.6	5.61	6.13	8.51	8.18	1.14
7) $TaCl_4(OH) \rightarrow TaOCl_3 + HCl$	9.2	6.68	7.24	10.92	8.05	-2.76
8) $TaOCl_3 + H_2O \rightarrow TaO(OH)Cl_2 + HCl$	78.7	4.99	4.83	5.12	3.77	1.54
9) $TaO(OH)Cl_2 \rightarrow TaO_2Cl + HCl$		52.54	52.67	53.62	52.41	46.61
10) $TaO_2Cl + H_2O \rightarrow Ta(OH)O_2 + HCl$		10.46	10.31	10.36	8.52	6.93
11) $TaO_2Cl + Ta(OH)O_2 \rightarrow Ta_2O_5 + HCl$		6.01	6.13	6.62	7.22	3.55
12) $2\ TaO_2Cl + H_2O \rightarrow Ta_2O_5 + 2\ HCl$		16.47	16.44	16.98	15.74	10.49

With regard to Reaction 1 and 2, the modelling results with PW91(DND), PW91(DNP), PW91(DNP+) showed the reactions to be endothermic and had an average of 2 kcal/mol deviation from each other and differed by 9.6 ± 1.2 kcal/mol from theoretical literature. B3LYP(DNP) and PBE(DNP) correlated to literature and also showed Reaction 1 and 2 to be exothermic, with an average deviation of 5.5 ± 1.2 kcal/mol, but B3LYP(DNP) was computationally the most expensive to use and had the highest bond angle deviation of 1.42 ± 1°. Theoretical literature [8] did not show the formation of $TaO(OH)Cl_2$ in Reaction 8, but showed Reaction 8 and 9 together where $TaOCl_3$ reacted with water to form TaO_2Cl directly with the reaction energy at 78.7 kcal/mol. This

high energy value could indicate a multistep reaction taking place and by indicating a two-step reaction (as shown by Reaction 8 and 9) the energy values decreased. The lowest energy values for both Reaction 8 and 9 were achieved with B3LYP(DNP) (1.54 and 46.61 kcal/mol respectively) followed by PBE(DNP+) (3.77 and 52.41 kcal/mol respectively), which implies that the two-step reaction proposed in this study is more likely.

Based on all these results it was decided that calculations on TaF_5 and its related species will be done with PBE(DNP+) combination which gave the best computational time to accuracy compromise.

3.3.2 Case Study (TaF_5)

The Case Study follows the same outline as was used in the Model Verification presented in Section 3.3.1 where first the geometry variables (bond lengths, bond angles and vibrational frequencies) were modelled and compared to literature values, before calculating the hydrolysis and oxidation reactions of TaF_5 and comparing these to the results presented on the reactions discussed for $TaCl_5$. Finally a more detailed reaction mechanism is presented for the most likely hydration mechanism of TaF_5 forming $Ta(H_2O)F_5$.

3.3.2.1 Geometry optimisation of TaF_5

The TaF_5 molecule was geometrically optimised (as in Section 3.2.2) and the bond lengths and bond angles between the Ta and the five F atoms were determined (Table 3.4) and compared to experimental literature values.

Table 3.4 – Modelled and experimental literature values of bond lengths and angles of TaF_5

	Experimental literature		
Bond/Angle	Edwards [27]	Ischenko [6]	PBE(DNP+)
Ta-F1 [Å]	1.75 ± 0.02	1.846 ± 0.005	1.89 ± 0.02
Ta-F3 [Å]	2.06 ± 0.02	2.062 ± 0.002	1.93 ± 0.02
Ta-F4 [Å]	2.07 ± 0.02	2.062 ± 0.002	1.93 ± 0.02
Ta-F5 [Å]	1.78 ± 0.05	1.846 ± 0.005	1.89 ± 0.02
Ta-F6 [Å]	1.78 ± 0.05	1.846 ± 0.005	1.89 ± 0.02
F1-Ta-F6 [°]	103.6 ± 2	96.4 ± 1.5	120 ± 0.5
F1-Ta-F5 [°]	123.6 ± 2	173.1 ± 2.1	120 ± 0.5
F1-Ta-F3 [°]	94.8 ± 2	96.4 ± 1.5	90 ± 0.5
F1-Ta-F4 [°]	95.8 ± 2	83.5 ± 0.6	90 ± 0.5

From Table 3.4 it can be seen that the two Ax F atoms (F3 and F4) have longer bond lengths than the three Eq F atoms (F1, F5 and F6), which has been confirmed in experimental literature [20, 21], as was observed with $TaCl_5$. The bond angle between the Ax F atom and Eq F atom of TaF_5 (Table 3.4) was 90° ± 0.01, while the bond angle between the Eq F atoms was 120° ± 0.1, as was expected and seen in the modelling of $TaCl_5$. Modelled and experimental literature values differ because the modelled values in this study were obtained from a single TaF_5 molecule where the experimental literature values were derived from four metal atoms as a unit cell (Ta_4F_{20}) [27] and a trimeric unit cell (Ta_3F_{15}) [6]. Because of the rigidity of the crystal structure, distortion of bonds and angles can occur [28], which explains the deviation from unity (90° and 120°) observed when working with tetra- and trimeric unit cells. When comparing the results of TaF_5 with $TaCl_5$, the bond length of Ta-F was shorter than the bond length of Ta-Cl, as the atom radius of F is smaller than that of Cl. Similar to $TaCl_5$, TaF_5 is a nonlinear molecule with 12 vibrational modes of which 8 were observed as shown in Table 3.5.

Table 3.5 – Modelled vibrational frequencies* (cm^{-1}) with PBE(DNP+) for TaF_5

Frequency	Wavenumber (cm^{-1})
$\omega_1(a'_1)$	674
$\omega_2(a'_1)$	640
$\omega_3(a_2'')$	642
$\omega_4(a_2'')$	239
$\omega_5(e')$	642
$\omega_6(e')$	191
$\omega_7(e')$	89
$\omega_8(e'')$	240

* Modelled vibrational frequencies indicate the harmonic vibrational frequency without a scaling factor.

Because the availability of vibrational data for TaF_5 is limited, 0.1g TaF_5 salt (Sigma-Aldrich product, 99.5% purity) was used to determine the infrared (IR) spectrum on a Bruker bench top diamond tip infrared spectrometer, where two main peaks were observed at 634 and 682 cm^{-1}. The IR spectrum of TaF_5 was also obtained from vibrational calculations and again two main peaks were observed at ~ 640 and 674 cm^{-1}, which correlates with the experimental values (modelling data error = 5%). A shift in the modelled data was observed which could be due to the correction term used in COSMO which was added to account for H_2O molecules surrounding TaF_5.

3.3.2.2 Hydrolysis and oxidation reactions of TaF_5

Both the energies of formation of the hydrolysis and oxidation reactions are presented in Table 3.6, including the orientation of the hydrolysis substitutes, as has been done for $TaCl_5$ (Section 3.1.2) using the same reactions and conformers shown in Figure 3.1 and Figure 3.2 respectively.

Table 3.6 – Energy of formation of TaF_5 reactions with water (PBE(DNP+))

		$\Delta H_f^{298.13\ K}$ / (kcal/mol)
1) $TaF_5 + H_2O \rightarrow TaF_4OH + HF$	E	-2.35
	A	-4.80
2) $TaF_4OH + H_2O \rightarrow TaF_3(OH)_2 + HF$	EE	5.87
	AA	5.32
	AE	5.20
3) $TaF_3(OH)_2 + H_2O \rightarrow TaF_2(OH)_3 + HF$	EEE	6.29
	AEE	7.67
	AAE	6.20
4) $TaF_2(OH)_3 + H_2O \rightarrow TaF(OH)_4 + HF$	AAEE	10.93
	AEEE	10.32
5) $TaF(OH)_4 + H_2O \rightarrow Ta(OH)_5 + HF$		10.90
6) $Ta(OH)_2F_3 \rightarrow TaOF_3 + H_2O$		12.35
7) $TaF_4(OH) \rightarrow TaOF_3 + HF$		15.78
8) $TaOF_3 + H_2O \rightarrow TaO(OH)F_2 + HF$		5.93
9) $TaO(OH)F_2 \rightarrow TaO_2F + HF$		54.92
10) $TaO_2F + H_2O \rightarrow Ta(OH)O_2 + HF$		7.66
11) $TaO_2F + Ta(OH)O_2 \rightarrow Ta_2O_5 + HF$		6.35
12) $2\ TaO_2F + H_2O \rightarrow Ta_2O_5 + 2\ HF$		14.01

When considering the hydrolysis reaction (Reaction 1 – 5 in Table 3.6), the energy of TaF_4OH with the OH group in the Ax and Eq position was -2.35 and -4.80 kcal/mol respectively for Reaction 1, implying that although the reaction was instigated from an Eq position, the molecules shifted to form a lower energy product where the OH group is in the Ax position. These values and transitions are similar to those observed for the $TaCl_5$ reactions. From the differences observed between the Ax and Eq position of the H_2O molecule, the energy of the TaF_4OH molecule was calculated where the OH group was situated in the Ax and Eq positions (Supplementary Data - Figure S4).

For Reaction 2, the energy of $TaF_3(OH)_2$ was higher at 5.20 and 5.32 kcal/mol with the OH groups in the axial-equatorial (AE) and axial-axial (AA) positions respectively, followed by the equatorial-equatorial positions (EE) at 5.87 kcal/mol. Since the Eq OH groups are 120° from each other in the EE position, the two Ax F groups have longer bond lengths, because they are pushed out of

the plane which therefore could result in these bonds more readily participating in the substitution reaction.

In Reaction 3, three OH groups were substituted onto the Ta atom for which three different molecules for $TaF_2(OH)_3$ were identified, i.e. AAE, with the relative energy 6.20 kcal/mol, AEE, which yielded a relative energy of 7.67 kcal/mol and EEE with a relative energy of 6.29 kcal/mol. From these results it can be seen that the energy between the AAE and EEE conformer are similar with the AEE conformer at a higher energy. These results are similar to the conformers formed during the hydrolysis of $TaCl_5$, where EEE was at the lowest energy followed by AAE and then AEE.

For Reaction 4, two geometries were identified for $TaF(OH)_4$, i.e. AAEE (OH group added Eq to AAE), with a relative energy of 10.93 kcal/mol, while a similar relative energy (10.32 kcal/mol) was attained for AEEE (OH group added Eq to AEE). In the last reaction (Reaction 5), all five F atoms are replaced by five OH groups to form $Ta(OH)_5$ which has a relative energy of 10.90 kcal/mol. It is clear from Table 3.6 that the energy increased with increasing OH groups. From these results it is clear that although the OH group approached from an Eq position the molecule rearranges to form the OH-A conformer, where a second OH group approaches again form the Eq position to form the AE conformer. Rearrangement takes place again to form AA conformer and when the third substitution takes place, the AAE conformer is formed, followed by AAEE.

As shown for $TaCl_5$ (Table 3.3), it is again apparent that the oxidation of TaF_5 (Reaction 6 – 12 in Table 3.6) is unlikely to occur spontaneously. Unlike for $TaCl_5$ where the first two hydrolysis reactions were likely (exothermic), only the first hydrolysis reaction (Reaction 1) was exothermic when using TaF_5 (Table 3.6) with a significant difference between the E and A conformers.

In an attempt to explain this difference in energies between the two conformers, the transition energies for the first hydrolysis reaction were determined and are presented in Figure 3.3. It is clear from this analysis that between the reagent (TaF_5 – Point A) and the product (TaF_4OH – Point E), three transition states (Points B, C and D) are possible. Point A in Figure 3.3 shows the reagents TaF_5 and H_2O of which the energies were set to 0 kcal/mol. All subsequent energies were calculated relative to these two molecules. After optimisation of the structure, the H_2O molecule was modelled from both an Ax and Eq position respectively. However, at the lowest energy for the first transition (Point B), the H_2O was in the Eq position in both cases, with energies of approximately -20 kcal/mol, indicating an exothermic reaction with no distinct orientation preference.

In the next step it seems that the H_2O bonded to the TaF_5 (Point C). For this state the only observable difference was that when the H_2O molecule approached from the Ax position (Figure 3.3 point C), the H atoms of the H_2O molecule turned towards the Eq position while when the H_2O

molecule approached from the Eq position, the H atoms had turned towards the Ax position. The reaction energy at this point was only slightly higher than Point B at -18 kcal/mol, confirming that the formation of $Ta(H_2O)F_5$ was also exothermic. It is interesting to note that the two Ax F atoms in Point C were distorted from a 90° angle to accommodate the H_2O molecule and possibly due to the formation of hydrogen bonds. To determine the degree of distortion, the bond lengths and bond angles were calculated and shown in Supplementary Data (Figure S3).

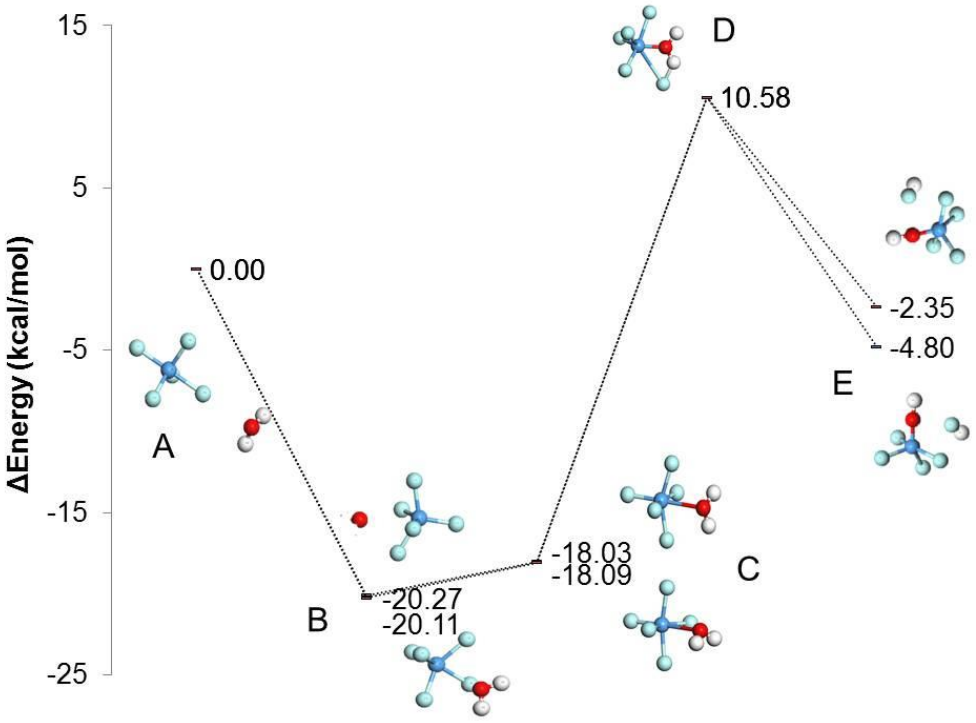

Figure 3.3 – Hydrolysis reaction of TaF_5 with regards to transition state energies

In the third step, Point D in Figure 3.3, a four membered cyclic ring was formed between the TaF_5 and bonded H_2O, by the association of an F atom and an adjacent H atom, which ultimately results in the release of HF and the formation of TaF_4OH, with the remaining OH group either in the Ax or Eq position. At this point the geometry changed from trigonal bi-pyramidal to square pyramidal. As the HF molecule moved further away from TaF_4OH, the geometry changed back to trigonal bi-pyramidal. It is interesting to note that Point D correlates perfectly with the mechanism proposed by Siodmiak et al. [9] for $TaCl_5$, when calculating the hydrolysis of $TaCl_5$ in water showing that the water molecule first bonded to the metal atom before evicting HCl. It can thus be concluded that when TaF_5 is dissolved in water, the water molecule firstly bonds to the Ta to form $Ta(H_2O)F_5$, followed by the formation of a cyclic transition state where one H atom of the water molecule bonds with one F atom, before evicting the HF group from TaF_4OH. This can also be expressed as shown in Figure 3.4.

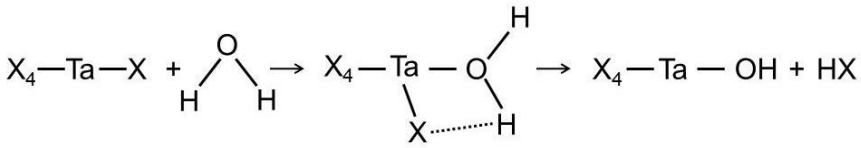

Figure 3.4 – Proposed mechanism for the reaction of TaX_5 (X = Cl or F) with one H_2O molecule (reproduced from Siodmiak et al. [9])

According to Figure 3.3 10.58 kcal/mol was needed for the formation of the four membered cyclic ring, while the energy of the final TaF_4OH was -4.80 and -2.35 kcal/mol in the Ax and Eq position respectively, indicating that the Ax position yielded a lower energy state and therefore was more favourable to form. This correlates with the calculation made in Table 3.4, where the length of the Ax F atom was shown to be longer, therefore more unstable and thus favouring a reaction in this position.

3.4 Conclusion

Due to a lack of speciation data, molecular modelling was used to confirm the molecular structure of both $TaCl_5$ and TaF_5 while calculating the energies of the hydrolysis and oxidation reactions. To confirm the suitability of the model, the model was developed and then verified for $TaCl_5$ for which data is available before applying the verified model to TaF_5.

For the calculated bond lengths and bond angles of $TaCl_5$ PW91(DND), PW91(DNP), PW91(DNP+) and PBE(DNP+) gave values that were closest to theoretical literature with an average deviation of 0.065 ± 0.006 Å for PW91 and 0.66 ± 0.006° for PBE(DNP+). While PBE(DNP+) had the smallest bond angle deviation of 0.007 ± 0.006, B3LYP(DNP) had the highest bond angle deviation of 1.42 ± 1° as well as a high computational cost. With regards to the frequency calculations the overall deviation between the functional and basis sets was 6 cm^{-1} and less than 10% with literature. When using this approach on a range of molecules it was shown that the larger basis set combination PBE(DNP+) was the most suitable.

When comparing the results from $TaCl_5$ (method verification) and TaF_5 (case study), similar data and trends were observed, verifying the suitability of the model for studying TaF_5 reactions with H_2O. For the hydrolysis reactions only TaX_4OH or $TaCl_3(OH)_2$ will form with lower energies when substituents were in the Eq position. From the proposed oxidation reactions, it is evident that the oxyfluoride species $TaOX_3$ and TaO_2X will not form via these reactions as all oxidation reactions were endothermic both for $TaCl_5$ and TaF_5. According to the transition state energy calculations

of TaF_5 with H_2O one H_2O molecule bonded to TaF_5 to form a stable $Ta(H_2O)F_5$ before the eviction of HF forming TaF_4OH, with a transition state energy of 10.58 kcal/mol.

Future work will entail the investigation of molecular modelling to determine the influence of acid on the metal-H_2O interaction thereby identifying the possible speciation in an aqueous phase as found during SX.

3.5 References

[1] O.S. Ayanda, F.A. Adekola, A review of niobium-tantalum separation in hydrometallurgy, Journal of Minerals & Materials Characterization & Engineering, 10 (2011) 245 - 256.

[2] M.J. Ungerer, H.M. Krieg, G. Lachmann, D.J.v.d. Westhuizen, Comparison of extractants for the separation of TaF_5 and NbF_5 in different acidic media, Hydrometallurgy, (2014) 195-206.

[3] A. Timofeev, A.A. Migdisov, A.E. Williams-Jones, An experimental study of the solubility and speciation of niobium in fluoride-bearing aqueous solutions at elevated temperature, Geochimica et Cosmochimica Acta, 158 (2015) 103 - 111.

[4] R.L. Linnen, I.M. Samson, A.E. Williams-Jones, A.R. Chakhmouradian, 13.21 Geochemistry of the rare-earth element, Nb, Ta, Hf and Zr deposits, Reference Module in Earth Systems and Environmental Sciences - Treatise on Geochemistry (Second Edition), 13: Geochemistry of Mineral Deposits (2014) 543 - 568.

[5] J. Narbutt, M. Czerwinski, Chapter 16: Computational chemistry in modelling solvent extraction of metal ions, in: J. Rydberg, C. Musikas, G.R. Choppin (Eds.) Solvent extraction principles and practice, 1992.

[6] A.A. Ischenko, V.P. Spiridonov, T.G. Strand, Joint Norwegian - Soviet electron diffraction studies of molecular structures in the gas phase. II. Inorganic compounds, Acta Chemica Scandinavica A, 42 (1964) 651-673.

[7] A. Agulyansky, The chemistry of tantalum and niobium fluoride compounds, Elsevier, Amsterdam2004.

[8] M. Siodmiak, G. Frenking, A. Korkin, Initial reactions in chemical vapor deposition of Ta_2O_5 from $TaCl_5$ and H_2O. An ab initio study., Journal of Chemical Physics A, 104 (2000) 1186 - 1195.

[9] M. Siodmiak, G. Frenking, A. Korbin, On the mechanism of chemical vapor deposition of Ta_2O_5 from $TaCl_5$ and H_2O. An ab initio study of gas phase reactions, Materials Science in Semiconductor Processing, 3 (2000) 65 - 71.

[10] Material Studio Modelling Environment, Accelrys Software Inc., San Diego, 2012.

[11] J.P. Perdew, Y. Wang, Accurate and simple analytic representation of the electron-gas correlation energy, Physical Review B, 45 (1992) 13244-13249.

[12] B. Delley, Ground-state enthalpies: evaluation of electronic structure approaches with emphasis on the density functional method, The Journal of Physical Chemistry A, 110 (2006) 13632 - 13639.

[13] J.P. Perdew, K. Burke, M. Ernzerhof, Generalized gradient approximation made simple, Physical Review Letters, 77 (1996) 3865-3868.

[14] A.D. Becke, Experimental investigation of highly exergonic outer sphere electron transfer reactions, Journal of Physical Chemistry, 88 (1984) 2547-2551.

[15] C. Lee, W. Yang, R.G. Parr, Development of the Colle-Solvetti correlation-energy formula into a functional of the electron density, Physical Review B, 37 (1988) 785-789.

[16] A. Tkatchenko, M. Scheffler, Accurate Molecular Van Der Waals Interactions from Ground-State Electron Density and Free-Atom Reference Data, Physical Review Letters, 102 (2009) 073005.

[17] S. Grimme, Semiempirical GGA-Type Density Functional Constructed with a Long-Range Dispersion Correction", J. Comput. Chem., 27, 1787 (2006). , Journal of Computational Chemistry, 27 (2006) 1787 - 1799.

[18] B. Delley, Modern Density Functional Theory: A tool for chemistry, in: J.M. Seminario, P. Politzer (Eds.) Theoretical and Computational Chemistry, 1995.

[19] B. Delley, The conductor-like screening model for polymers and surfaces, Molecular Simulation, 32 (2006) 117 - 123.

[20] F. Marchetti, G. Pampaloni, S. Zacchini, ^{19}F NMR spectroscopy as useful tool for determining the structure of coordination compounds of MF_5 (M = Nb, Ta), Journal of Fluorine Chemistry, 131 (2010) 21 - 28.

[21] M. Hargittai, Molecular structure of metal halides, Chemical Reviews, 100 (2000) 2233-2301.

[22] A.P. Scott, L. Radom, Harmonic vibrational frequencies: An evaluation of Hartree-Fock, Møller-Plesset, quadratic configuration, density functional theory and semiemperical scale factors, Journal of Physical Chemistry, 100 (1996) 16502 - 11700.

[23] J.P. Merrick, D. Moran, L. Radom, An evaluation of vibrational frequency scale factors, Journal of Physical Chemistry A, 111 (2007) 11683 - 11700.

[24] S.K. Kang, H. Tang, T.A. Albright, Structures for d^0 ML_6 and ML_5 complexes, Journal of American Chemical Society, 115 (1993) 1971 - 1981.

[25] C.R. Landis, T. Cleveland, T.K. Firman, Making sense of the shapes of simple metal hydrides, Journal of American Chemical Society, 117 (1995) 1859 - 1860.

[26] J. Aarik, K. Kukli, A. Aidla, L. Pung, Mechanisms of suboxide growth and etching in atomic layer deposition of tantalum oxide from $TaCl_5$ and H_2O, Applied Surface Science, 103 (1996) 331-341.

[27] A.J. Edwards, The structures of niobium and tantalum pentafluorides, Journal of Chemical Society, (1964) 3714-3718.

[28] D.G. Gorenstein, D. Kar, Effect of bond angle distortion on torsional potentials. Ab Initio and CNDO/2 calculations on dimethoxymethane and dimethyl phosphate, Journal of the American Chemical Society, 99 (1977) 672-677.

3.6 Supplementary Data

Table S1 – Experimental literature and modelled vibrational frequencies* (cm^{-1}) for $TaCl_5$

Frequency	Literature [8]	PW91 (DND)	PW91 (DNP)	PW91 (DNP+)	PBE (DNP+)	B3LYP (DNP)
$\omega_1(a'_1)$	406	369	368	369	367	372
$\omega_2(a'_1)$	324	306	306	310	305	304
$\omega_3(a_2'')$	371	342	342	346	340	340
$\omega_4(a_2'')$	155	147	147	150	146	151
$\omega_5(e')$	402	376	376	374	374	379
$\omega_6(e')$	181	123	123	124	120	124
$\omega_7(e')$	54	54	54	55	51	53
$\omega_8(e'')$	127	167	167	166	166	172

* Modelled vibrational frequencies indicate the harmonic vibrational frequency without a scaling factor.

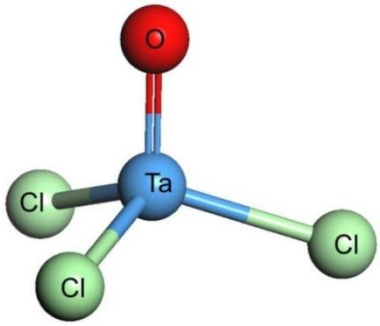

Figure S1 – Molecular structure of $TaOCl_3$

Table S2 – Calculated and literature values of bond lengths, angles and vibrational frequencies (cm^{-1}) of $TaOCl_3$

	Literature [8]	PW91 (DND)	PW91 (DNP)	PW91 (DNP+)	PBE (DNP+)	B3LYP (DNP)
Bond/Angle						
Ta-O [Å]	1.710	1.753	1.753	1.753	1.754	1.741
Ta-Cl [Å]	2.289	2.327	2.327	2.328	2.329	2.334
O-Ta-Cl [°]	107.70	106.92	107.00	106.81	106.80	108.61
Cl-Ta-Cl [°]	111.18	111.90	111.83	111.98	112.01	110.31
Frequency*						
$\omega_1(a)$	1017	971	971	956	971	998
$\omega_2(a)$	398	366	366	366	364	385
$\omega_3(a)$	123	108	108	106	107	115
$\omega_4(e)$	410	383	383	382	382	385
$\omega_5(e)$	227	202	202	204	201	206
$\omega_6(e)$	108	92	92	91	92	94

* Modelled vibrational frequencies indicate the harmonic vibrational frequency without a scaling factor.

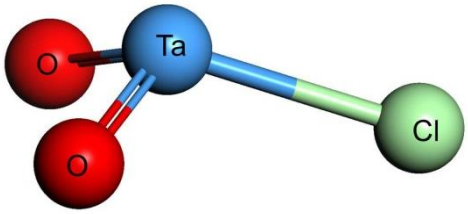

Figure S2 – Molecular structure of TaO_2Cl

Table S3 – Calculated and literature values of bond lengths, angles and vibrational frequencies (cm^{-1}) of TaO_2Cl

	Literature [8]	PW91 (DND)	PW91 (DNP)	PW91 (DNP+)	PBE (DNP+)	B3LYP (DNP)
Bond/Angle						
Ta-O [Å]	1.733	1.774	1.774	1.775	1.756	1.764
Ta-Cl [Å]	2.324	2.376	2.376	2.374	2.376	2.392
O-Ta-Cl [°]	110.51	106.14	106.14	106.41	106.50	108.48
O-Ta-O [°]	106.48	103.49	103.49	103.58	103.59	105.30
Frequency*						
ω1(a')	999	948	948	947	946	985
ω2(a')	392	365	366	366	364	368
ω3(a')	156	139	138	127	134	112
ω4(a'')	946	907	907	899	906	940

* Modelled vibrational frequencies indicate the harmonic vibrational frequency without a scaling factor.

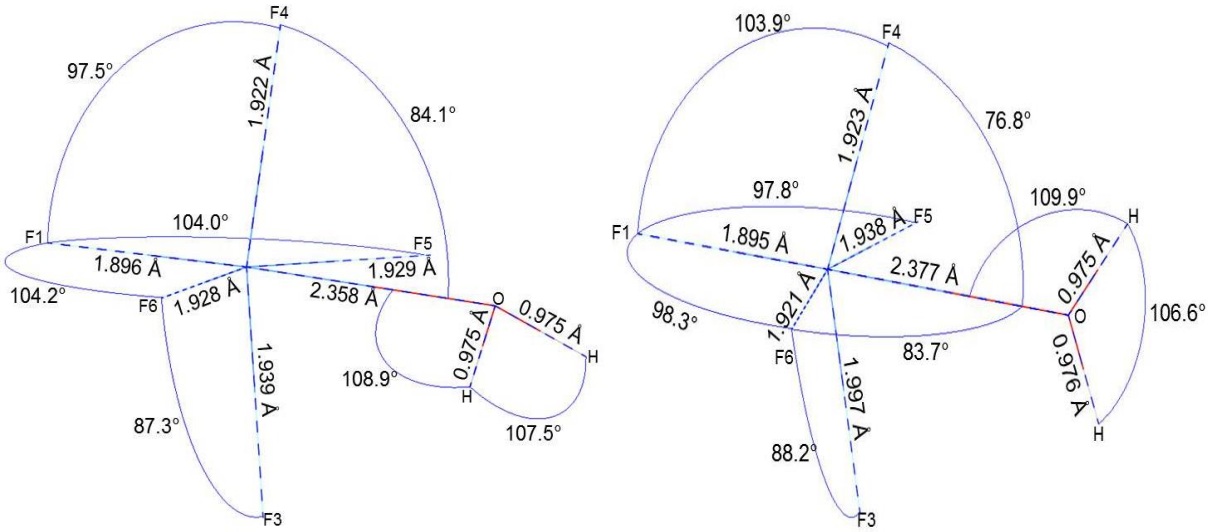

Figure S3 – Bonds lengths and angles of $Ta(H_2O)F_5$ from an Ax (left) and Eq (right) position

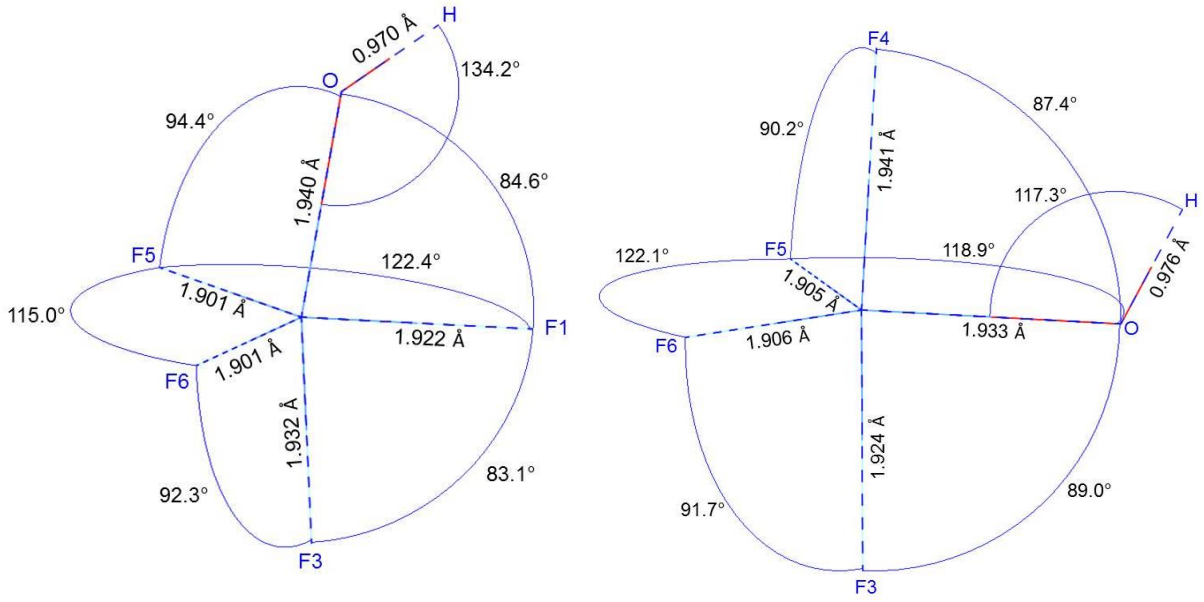

Figure S3 – Bond lengths and angles of TaF_4OH with the OH in Ax (left) and Eq (right) position

CHAPTER 4

Chapter 4 consists of the article titled 'Molecular modelling of H_2SO_4 reactions in an aqueous environment: A DFT study', which is added into this thesis in the exact format in which it was submitted for review in the *Journal of Computational and Theoretical Chemistry (2017)*.

4.1 Introduction

Tantalum (Ta) and niobium (Nb) are two metals found in the same group (VB) of the periodic table, with similar chemical and physical properties, making their separation difficult. Ta with its numerous advantages is used in a variety of applications including capacitors in electronic circuits, rectifiers, pins for bones fixtures, surgical and dental instruments and in chemical heat exchangers [1]. For many of its applications, pure Ta is needed; however, there is a proportional increase in production cost with increasing purity. One way of ensuring an economically viable process for the production of high purity Ta is to find a cost-effective way to separate Ta and Nb. One separation method is solvent extraction (SX). Ungerer et al. [2] studied the separation of Ta and Nb (in the form of $Ta(Nb)F_5$), where partial separation was achieved in a sulphuric acid (H_2SO_4) medium with the extractants diiso-octyl phosphinic acid (DioPA) and di-(2-ethylhexyl) phosphoric acid (D2EHPA). While a degree of separation between the aforementioned metals was plausible, it was not possible to fully explain the distribution data obtained due to the lack of experimental data on the speciation of Ta and Nb compounds [3].

An alternative method that could be used to determine the speciation could be computational methods [4], including programs that simulate thermodynamic properties such as FactSage™, mathematical simulations such as Matlab®, or molecular modelling of processes and reactions such as BIOVIA Materials Studio. When applying molecular modelling to SX, a step-by-step analysis of the extraction process on a molecular level can be achieved. From this, the molecular reactions as well as the system reactions occurring during SX from a thermodynamic point could be determined, which might lead to the development of a new method for the system analysis of the SX process of Ta and Nb.

However, before the SX process of Ta and Nb can be analysed, the reaction mechanism of H_2SO_4 and H_2O occurring in the aqueous phase during SX should be understood. Despite the industrial importance of H_2SO_4 [5, 6], according to the authors of this work, the speciation of metal sulphate aqueous mixtures has not been presented in literature. From previous modelling [7, 8], it was shown that H_2SO_4 dissociates to form HSO_4^- and H_3O^+, or in concentrated solutions SO_4^{2-} and $2H_3O^+$. Nadykto et al. [9] investigated $HSO_4^-.(H_2O)_n$ and $H_3O^+.H_2SO_4.(H_2O)_n$ (n=1-5) in the gas phase and found that the ionic hydrates were more stable than the neutral species, especially when the amount of H_2O molecules increased. It is assumed that when the dissociated ions of H_2SO_4 are in water, they are surrounded by concentric shells of H_2O molecules, where each successive shell is more weakly bonded until a bulk water structure is reached [10]. Using both diffraction and modelling data, Cannon et al. [11] showed that the first hydration shell of the ion, depending on the temperature, has 6 to 14

surrounding H_2O molecules. Kakizaki et al. [12] investigated the formation of $H_2SO_4.(H_2O)_n$ (n = 1-9) and found that when the cluster size increased, the acid dissociation probability also increased.

However, in molecular modelling an increase in the number of atoms in a system means that more resources and computational time will be needed to complete calculations. The computational cost is proportional to N^2, where N is the number of atoms [13]. Therefore, to simulate H_2SO_4 in an infinite dilution will be too expensive. An alternative to this is to use a model, the conductor-like screening model (COSMO), which simulates infinite dilution of solvents of varying polarity [14, 15] and includes the short range interactions of the solute particles.

Therefore, in this study we investigated the suitability of molecular modelling in determining the behaviour of H_2SO_4 in an aqueous environment. In a first step, the dissociation of H_2SO_4 (reactions 1 and 2), forming the bisulphate (HSO_4^-) and sulphate ions (SO_4^{2-}), with and without COSMO and the effect it has on the geometry, vibrational frequency and reaction energy was investigated. The second step investigated the likelihood of various H_2SO_4 water interactions (reaction 3 – 5) and the formation of monohydrated sulphuric acid ($H_2SO_4.H_2O$) and bisulphate ion ($HSO_4^-.H_2O$) as well as the di-hydrated sulphuric acid ($H_2SO_4.2H_2O$):

$$H_2SO_4 + H_2O \rightarrow HSO_4^- + H_3O^+ \quad (1)$$
$$HSO_4^- + H_2O \rightarrow SO_4^{2-} + H_3O^+ \quad (2)$$
$$H_2SO_4 + H_2O \rightarrow H_2SO_4.H_2O \quad (3)$$
$$HSO_4^- + H_2O \rightarrow HSO_4^-.H_2O \quad (4)$$
$$H_2SO_4 + 2\ H_2O \rightarrow H_2SO_4.2H_2O \quad (5)$$

Various geometries may exist during this interaction and will be discussed in the Results and Discussion section. The third step in this investigation was to determine the effect the amount of water molecules had on the system by increasing the acid-water ratio from 1:1 to 1:5 and 1:10.

4.2 Computational Methods

For the molecular modelling of H_2SO_4 with water, the DMol^3 module of the Biovia Materials Studio 2016 software from Dassault Systèmes Biovia Corp. [16] was used. The density-functional theory (DFT) semi-empirical dispersion interaction correction module (DFT-SEDC) was applied. For all the calculations on the different molecules of reactions 1 – 5, a geometry optimisation [17, 18] was initially done using the following combination of functional and basis sets:

1) Generalised-gradient approximation (GGA) with Perdew-Wang correlation functional (PW91) with the DNP+ (double numerical plus polarisation, with addition of diffuse functions) basis set, basis file 4.4 and the Ortmann, Bechstedt and Schmidt (OBS) dispersion correction [19].
2) GGA with Perdew-Burke-Ernzerhof (PBE) [20] correlation functional with basis set DNP+, basis file 4.4 and Tkatchenko-Scheffler (TS) dispersion correction [21].
3) Becke exchange plus Lee-Yang-Parr correlation (B3LYP) [22, 23] hybrid exchange-correlations energy functional, with basis set DNP+, basis file 4.4 and TS dispersion correction [21].

The core treatment parameter was set to 'All Electron' and therefore the electrons were calculated as if they were valence electrons. Furthermore, under the electronic properties, a smearing of 0.005 Hartree (Ha) was chosen for all the calculations [24] which contributed to the 4 kcal/mol margin of error obtained as an average for all the experiments. For the comparison with the use of COSMO [14, 15], the same geometries and settings as above were used but by only adding water as the solvent (dielectric constant = 78.54) to simulate these reaction in a bulk H_2O solution.

After the geometry optimisation process, single point energy calculations were done to calculate various electronic properties using the same settings that were used for the geometry optimisations. The calculations were done at 0 K and the energy correction term was added to give Gibbs free energy and energy of formation (H^f) values at 298.15 K. The zero-point vibrational energy (ZPVE) was included in all calculations. Frequency calculations were used to confirm optimised structures (minimum energy and no imaginary frequency) and transition states (maximum energy and one imaginary frequency).

4.3 Results and Discussion

This section is divided into three parts. Section 4.3.1 will focus on the comparison of the geometry optimisation results and reaction energies of the species present in reactions 1 and 2. Section 4.3.2 focuses on the geometry optimisation and reaction energies of reactions 3 – 5, where the H_2SO_4:H_2O ratio is 1:1, followed by Section 4.3.3, where the influence of water on these reaction will be investigated by changing the H_2SO_4:H_2O ratio to 1:5 and 1:10.

4.3.1 Comparison with and without COSMO

All the participating species in reactions 1 and 2 (H_2SO_4, HSO_4^-, SO_4^{2-}, H_2O and H_3O^+) were geometrically optimised as described in Section 4.2. The geometry data and harmonic vibrational frequencies for H_2SO_4 (cis- and trans-conformer), HSO_4^- and SO_4^{2-} are given in the Supplementary Data Tables S1 – S6.

The first species to be modelled was H_2SO_4 of which its cis- and trans-conformers are shown in Figure 4.1, with C_s and C_2 symmetry, respectively. The bond lengths and angles of both the cis- and trans-conformers of H_2SO_4, calculated by using the different functional/basis set combinations with and without COSMO, were compared. By comparing each functional/basis set where either COSMO was added or left out, it can be seen that the bond lengths deviated by less than 0.019 Å for both the cis- and trans-conformers. However, the bond angles deviated by up to 3°. Comparing the different functional/basis set combinations with COSMO with each other, a deviation of less than 0.02 Å and 1.6° for all the bond lengths and angles were obtained. The modelled bond lengths and angles were in the same order of magnitude compared to the previously modelled data [25]. The margin of error for the cis-conformer was ±0.02 Å and ±2.3° for the bond length and angle, respectively, and ±0.02 Å and ±2.7°, respectively, for the trans-conformer. Comparing our modelled data to experimental data, it was seen that overall the modelled data deviated by less than 0.03 Å and 1.35° with COSMO and 0.05 Å and 1.55° without COSMO.

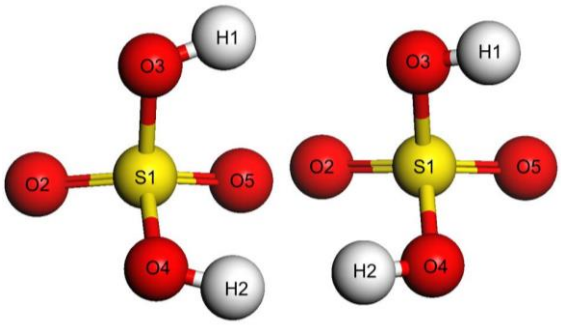

Figure 4.1 – Molecular structure of the cis- and trans-conformers (left and right) of H_2SO_4

H_2SO_4 is a nonlinear molecule and will have 3N-6 degrees of freedom, with N = 7 atoms in the molecule, thus H_2SO_4 has 15 degrees of freedom and therefore 15 types of molecular vibrations (stretching and bending modes). The vibrational frequencies (Table S2) were shifted higher because of electron correlation and anharmonicity effects in the theoretical treatment used within the modelling. Also, the frequencies shown are calculated harmonic vibrational frequencies (ω (cm^{-1})) without a scaling factor [26, 27] to account for the error between

harmonic vibrational frequency and fundamental vibrational frequency (v (cm^{-1})). However, comparing the results it was seen that overall the data when COSMO was added correlated more with experimental data.

For both the cis- and trans-conformers of H_2SO_4, the thermodynamic properties are given in Table 4.1 in terms of electronic energy, Gibbs free energy, enthalpy and entropy calculated from the different functional/basis set combinations used. From these results it can be seen that the energy values for the different modelling methods investigated were similar. However, by adding COSMO, the electronic energy decreased over all the functional/basis sets used, indicating a more stable system. Steyl [28] reported an E_0 value of −702.078 Ha for H_2SO_4 with DFT modelling (Material Studio v.4.2) using the Vosko-Wilk-Nusair functional (VWN(DNP)) and basis set superposition errors (BSSE). Similarly, it can be seen that (Table 4.1) the energies for the cis- and trans-conformers were equivalent. For example, the differences in the energies (ΔE^o) between the cis- and trans-conformers were 0.398, 0.383, 0.154 kcal/mol with COSMO and 1.111, 1.025, 1.004 kcal/mol without COSMO for PW91(DNP+), PBE(DNP+) and B3LYP(DNP+), respectively. The trans-conformer was at a lower energy than the cis-conformer for all the functional/basis set combinations used. When the cis- and trans-conformers of H_2SO_4 were modelled with both ab initio modelling software (Gaussian 03 with the B3LYP and Møller-Plesset (MP2) functionals) and MOLPRO software (with the CCSD(T) functional), Demaison et al. [25] found that the trans-conformer had a lower energy with a difference of 5.5 kJ/mol (1.3 kcal/mol). This expected difference is due to differences in the type of modelling (DFT versus ab initio).

Table 4.1 – The calculated electronic energy (E_0), Gibbs free energy (G), enthalpy (H) and entropy (S) of H_2SO_4 (cis- and trans-conformers)

Bond/Angle	PW91 (DNP+)		PBE (DNP+)		B3LYP (DNP+)	
	With COSMO	Without COSMO	With COSMO	Without COSMO	With COSMO	Without COSMO
H_2SO_4, cis						
E_0, Ha	−700.39	−700.37	−700.01	−699.99	−730.81	−730.79
G, kcal/mol	6.003	5.253	5.743	4.976	6.360	5.881
H, kcal/mol	27.627	27.553	27.335	27.452	28.035	28.243
S, kcal/mol.K	0.072	0.075	0.073	0.075	0.073	0.075
H_2SO_4, trans						
E_0, Ha	−700.39	−700.37	−700.01	−699.99	−730.81	−730.79
G, kcal/mol	6.114	5.947	5.973	5.906	6.814	6.655
H, kcal/mol	27.596	27.628	27.562	27.582	28.162	28.256
S, kcal/mol.K	0.072	0.073	0.072	0.073	0.072	0.073
Relative Energy, ΔE_0 (trans-cis) (kcal/mol)	0.398	1.111	0.383	1.025	0.154	1.004

The next species investigated were HSO_4^- and SO_4^{2-} (shown in Figure 4.2). The modelling values of HSO_4^- (Table S3 and Table S4) from the different functionals with COSMO were similar, with a 0.01 Å bond length and a 0.4° bond angle deviation, except for the H1-O3-S1 bond angle determined with B3LYP(DNP+), which differed by 1.55°. Comparing the COSMO and without COSMO data, it can be seen that the data had a 0.05 Å bond length and a 1.67° bond angle deviation, and especially the H1-O3-S1 bond angle differed by up to 4.13°. The modelled values correlated with previously modelled data [9], with a less than 0.04 Å bond length and 3.5° bond angle deviation, except for the H1-O3-S1 bond angle determined with B3LYP(DNP+), which differed by 5.07°. On average the modelled values differed by less than 3% from previously modelled data [9]. Comparing the modelled vibrational data to experimental infrared data, it can be seen that the values were in the same order of magnitude. However, the experimental data was given without the influence of H_2O and this could explain the deviation.

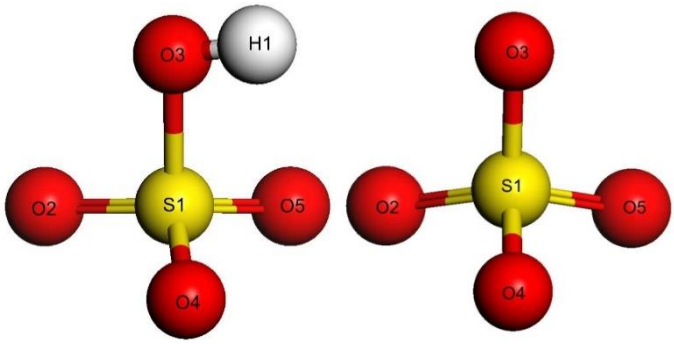

Figure 4.2– Molecular structure of HSO_4^- (left) and SO_4^{2-} (right)

The modelled data of SO_4^{2-} (Table S5 and Table S6), using the different functional/basis set combinations, showed deviations of less than 0.02 Å and 0.3° for the bond lengths and angles, respectively, irrespective of whether COSMO was added or not. The bond lengths and angles differed by less than 0.08 Å and 0.3°, respectively, from previously modelled data [10].

In Table 4.1 it was shown that the relative energies of the cis- and trans-H_2SO_4 conformers differed by less than 0.4 kcal/mol with COSMO and 1.2 kcal/mol without COSMO and based on those results it would hence not be possible to determine which would form preferentially. In an attempt to determine this, the energy of formation (H^f (kcal/mol)) for the H_2SO_4 conformers and their transition states (Figure 4.3) was determined. Accordingly, the ΔH^f for the cis-conformer was less than 0.2 kcal/mol, with the transition state less than 1 kcal/mol, indicating that a nearly free rotation around one of the S-OH bonds in H_2SO_4 took place, forming both conformers when COSMO was added. As expected, the data without COSMO

showed higher energy of formation for both the transition states and conformers, as this simulates this transition in the gas phase which requires more energy than in a liquid phase. Therefore, both the cis- and trans-conformers may participate in the reactions with H_2O. Demaison et al. [25] showed that the trans-conformer had a lower energy with a difference of 5.5 kJ/mol (1.3 kcal/mol) in the gas phase. Although the lowest energy of the cis-H_2SO_4 conformer was calculated with B3LYP(DNP+), this functional also had the highest energy for the transition state. Both PW91 and PBE fall in the non-local or gradient-corrected functional class and will show similar data with regard to predicted energies and structures because PBE was developed to mimic PW91 [29]. However, B3LYP fall in the hybrid functional class where the exchange-correlation energy functional was changed by incorporation of a portion of exact exchange from the Hartree-Fock theory. Therefore, B3LYP can accurately calculate electronic energy and formation energy of small molecules and early transition metals. However, transition states had a mean error of up to 2.14 kcal/mol [29, 30].

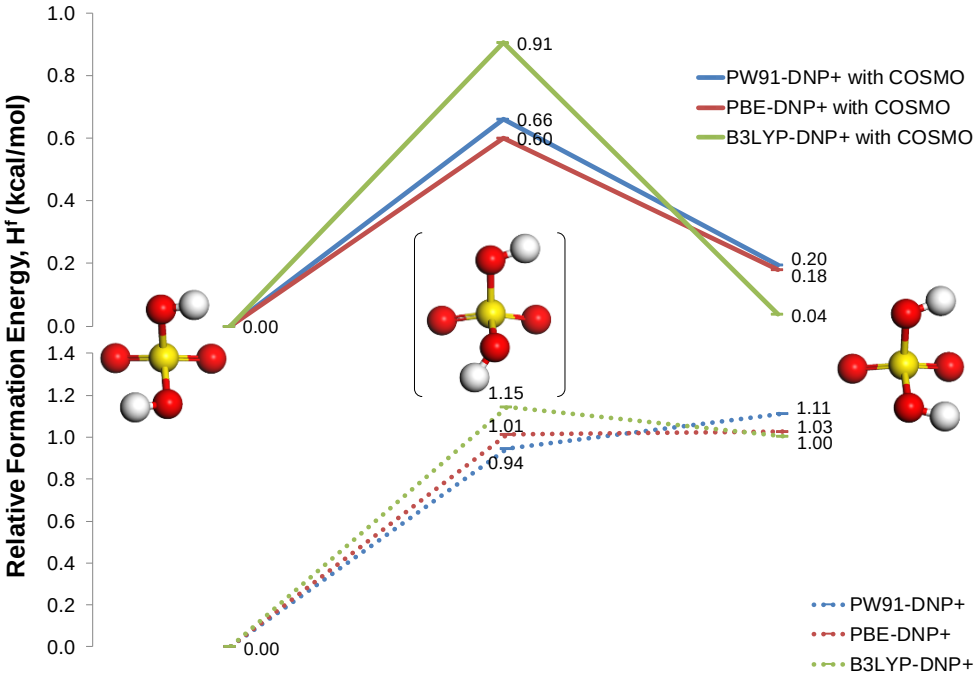

Figure 4.3 – Relative formation energy (H^f (kcal/mol)) between the cis- and trans-H_2SO_4 conformers, top graph with COSMO and bottom graph without COSMO

The relative energy of formation for reaction 1 ($H_2SO_4 + H_2O \rightarrow HSO_4^- + H_3O^+$) and reaction 2 ($HSO_4^- + H_2O \rightarrow SO_4^{2-} + H_3O^+$) was determined both for the cis- and trans-conformers of H_2SO_4 and are shown in Figure 4.4. Accordingly, with COSMO, 7.20, 10.64 and 11.21 kcal/mol (calculated with PW91(DNP+), PBE(DNP+) and B3LYP(DNP+), respectively) are needed to from HSO_4^- form the cis-H_2SO_4 conformer. The energy values, calculated with the different

functionals, deviated by less than 4 kcal/mol from each other, which was in the margin of error range. For reaction 2, 31.30, 34.58 and 35.31 kcal/mol were needed to form SO_4^{2-} from the cis-H_2SO_4 conformer with the aforementioned functionals. Without COSMO, the energy was significantly higher, indicating that this reaction does not occur in the gas phase. However, even with the addition of COSMO to simulate infinite dilution, this reaction will not take place.

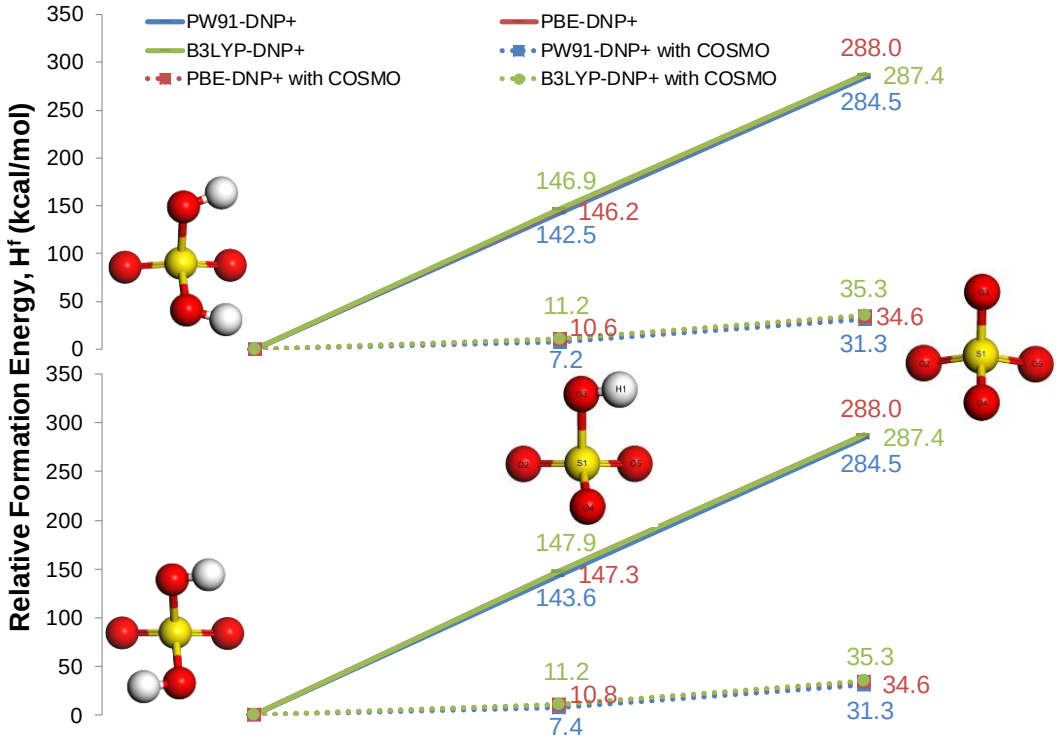

Figure 4.4 – Relative energy of formation (H^f (kcal/mol)) of HSO_4^- and SO_4^{2-} from both the cis-and trans-conformers of H_2SO_4

The second graph in Figure 4.4 shows the results with respect to the trans-H_2SO_4 conformer. The results were within 0.20 kcal/mol of the cis-conformer results. While the results for both the cis- and trans-H_2SO_4 conformers show that these reactions occur endothermically, it is known that H_2SO_4 reacts exothermically with water. Even though these calculations were done using COSMO to account for the interactions with water (hydrogen bonds), it does not fully account for the long range water interactions. In Section 4.3.3, the effect of explicitly adding H_2O molecules is investigated.

Comparing the data from Figure 4.3 and Figure 4.4, it can be seen that, when neutral species (cis- and trans-H_2SO_4) were modelled, the calculated energy of formation with and without COSMO was within 1 kcal/mol from each other. However, when ionic species were considered (HSO_4- and SO_4^{2-}), the calculated energy with and without COSMO deviated by as much as

~250 kcal/mol. Therefore, to obtain more reliable formation energies for ionic reactions, it is recommended to use the COSMO model to account for the solvation effect.

4.3.2 Reactions of H_2SO_4 and H_2O in a 1:1 H_2SO_4/H_2O environment

Considering the monohydrated $H_2SO_4.H_2O$ (likely from reaction 3), various geometries both from experimental [31] and theoretical [32-34] data have been proposed and considered for this study. Due to the difference in data between with and without COSMO presented in section 3.1, it was decided to report the geometry data with COSMO only.

The three most stable configurations obtained are shown in Figure 4.5. Figure 4.5A shows the configuration where the H_2O molecule is bound to the OH group of the H_2SO_4 molecule, while Figure 4.5B1 and B2 show the configuration where the H_2O molecule is bound to the S=O group of the H_2SO_4 molecule in two different conformers.

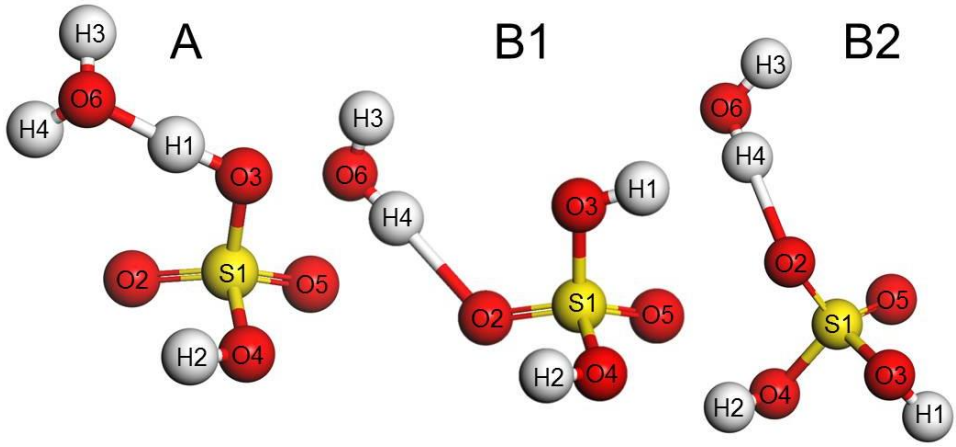

Figure 4.5 – Optimised geometries of the three sulphuric acid monohydrate ($H_2SO_4.H_2O$) configurations A, B1 and B2

The geometry data, obtained with the use of COSMO, for all three configurations is shown in Table 4.2 and compared to similar geometries for $H_2SO_4.H_2O$ that have been proposed by Arstila et al. [32] using a DFT-based Car-Parrinello ab initio molecular dynamics method [35] also using, amongst other functionals, B3LYP. Firstly, the $H_2SO_4.H_2O$ configuration A will be discussed. It is clear when comparing the bond lengths and angles, obtained with the different functionals, that the data differed by less than 0.06 Å and 0.8°, respectively, except for the H1-O6 bond (bond distance between H_2SO_4 and H_2O) where the difference was 0.2 Å and 4.3° for the angle between H_2SO_4 and H_2O (H4-O6-H1), respectively. The modelled data correlated

with the modelled data from literature, except the angle of the two H atoms on the H_2O (H3-O6-H4). Literature [32] showed this angle to be 107.9°, possibly due to the interaction between the H atom of H_2O and =O of H_2SO_4, which increased the bond angle. The modelling data showed the H3-O6-H4 angle to be 104.63 ± 0.24°, which correlates with literature data [36] where it was shown that this H-O-H angle on H_2O was 104.5° when water was alone. The main difference between our modelled system and the experimental system is that we found the lowest energy conformer when the H_2O bonded to a cis-H_2SO_4 molecule, where for the experimental system the H_2O is bound to a trans-H_2SO_4 molecule. Even with this deviation in geometry, our modelled data correlates to the experimentally obtained data.

Table 4.2 – Calculated (with COSMO) and literature values of bond lengths and angles of $H_2SO_4.H_2O$ in configuration A

Bond/Angle	Literature (modelled) [32]	Literature (experimental) [31]	PW91 (DNP+)	PBE (DNP+)	B3LYP (DNP+)
S1-O2 [Å]	1.48	1.464	1.457	1.456	1.438
S1-O3 [Å]	1.60	1.567	1.555	1.566	1.555
S1-O4 [Å]	1.64	1.578	1.618	1.617	1.587
S1-O5 [Å]	1.45	1.410	1.447	1.448	1.431
O4-H2 [Å]	0.99	0.95	0.979	0.981	0.974
O3-H1 [Å]	1.04	1.009	1.096	1.066	1.036
H1-O6 [Å]	1.64	1.645	1.370	1.448	1.511
O6-H3 [Å]	0.99	0.98	0.975	0.976	0.969
O6-H4 [Å]	0.99	0.98	0.976	0.976	0.971
S1-O4-H2 [°]	108.5	108.5	108.78	108.98	110.50
O2-S1-O4 [°]	107.5	-	108.58	108.93	108.85
O4-S1-O5 [°]	105.5	104.71	103.60	103.61	104.59
O5-S1-O3 [°]	108.1	-	108.90	108.46	108.48
O2-S1-O3 [°]	109.0	106.7	110.11	110.02	109.23
S1-O3-H1 [°]	109.0	108.6	111.29	111.06	111.07
H4-O6-H1 [°]	–	-	105.51	108.08	109.83
H3-O6-H4 [°]	107.9	107.0	104.87	104.39	104.87
O3-S1-O4 [°]	102.9	101.8	104.12	103.91	103.90
O2-S1-O5 [°]	122.2	123.3	120.20	120.51	120.50

Comparing the modelled data (Table 4.3) of configuration B1 and B2 of $H_2SO_4.H_2O$ with regard to bond length and angle, the modelling data was within 0.057 Å and 0.24°, except the two H angles in H_2SO_4 (S1-O4-H2 and S1-O3-H1), calculated with B3LYP(DNP+), which differed by 1.66 Å and 1.56 Å, respectively. Similarly, the angle between H_2O and H_2SO_4 for B1 calculated with B3LYP(DNP+) differed by 16.79 ± 0.06° when comparing the different functionals,

possibly due to a greater calculated repulsion of O3. When comparing the bond lengths shown in literature and the modelled data, it differed by less than 0.046 Å, except for the bond length between H_2O and H_2SO_4, which differed by 0.11 Å. The bond angle of H_2O and H_2SO_4 differed by 7.52° from the modelling data. The bond lengths between B1 and B2 differed with 0.002 Å. No experimental data has been published on these configurations of $H_2SO_4.H_2O$, leading to the conclusion that, although they were found to be stable during the modelling they are short lived species in solution.

Table 4.3 – Calculated (with COSMO) and literature values of bond lengths and angles of $H_2SO_4.H_2O$ in configurations B1 & B2 (in brackets)

Bond/Angle	Literature [32]	PW91 (DNP+)	PBE (DNP+)	B3LYP (DNP+)
S1-O2 [Å]	1.46	1.449 (1.450)	1.449 (1.451)	1.437 (1.438)
S1-O3 [Å]	1.63	1.600 (1.598)	1.602 (1.601)	1.586 (1.586)
S1-O4 [Å]	1.63	1.599 (1.599)	1.601 (1.602)	1.584 (1.582)
S1-O5 [Å]	1.46	1.442 (1.443)	1.444 (1.444)	1.430 (1.431)
O4-H2 [Å]	1.00	0.981 (0.981)	0.982 (0.982)	0.974 (0.974)
O3-H1 [Å]	0.99	0.981 (0.982)	0.982 (0.983)	0.974 (0.974)
O2-H4 [Å]	2.10	1.991 (1.944)	2.048 (2.000)	2.017 (1.953)
H4-O6 [Å]	0.99	0.977 (0.978)	0.976 (0.978)	0.968 (0.968)
O6-H3 [Å]	0.99	0.972 (0.972)	0.972 (0.972)	0.965 (0.964)
S1-O4-H2 [°]	109.2	109.64 (109.45)	109.35 (109.47)	111.01 (110.58)
O2-S1-O4 [°]	108.7	110.35 (110.31)	110.28 (110.27)	110.29 (110.1)
O4-S1-O5 [°]	105.8	104.71 (104.82)	104.70 (104.68)	104.97 (105.37)
O5-S1-O3 [°]	109.6	111.05 (111.11)	110.87 (111.02)	111.11 (110.84)
O2-S1-O3 [°]	105.2	104.17 (103.83)	104.29 (103.96)	104.36 (103.80)
S1-O3-H1 [°]	109.0	109.49 (109.36)	109.44 (109.27)	111.00 (111.01)
O3-S1-O4 [°]	102.2	103.90 (103.95)	103.99 (104.03)	103.83 (103.97)
O2-S1-O5 [°]	123.4	121.44 (121.61)	121.51 (121.67)	121.08 (121.53)
S1-O2-H4 [°]	128.6	121.21 (119.68)	121.08 (119.05)	104.36 (120.82)
H4-O6-H3 [°]	104.8	104.01 (104.04)	104.18 (103.52)	104.57 (104.25)

From first principles it is known that polyprotic acids like H_2SO_4 have the ability to produce multiple hydronium ions in aqueous solutions. The first acid dissociation constant pK_{a1} for H_2SO_4 is −2.00 and the second dissociation constant pK_{a2} is 1.99 [37], indicating that the loss of the first H atom should occur readily. To determine whether this phenomenon takes place in hydrated H_2SO_4, the deprotonated monohydrate sulphuric acid (possibly due to reaction 4) was studied. Various geometries have been reported and considered [32, 33, 38]. Figure 4.6 shows the optimised geometry of two possible $HSO_4^-.H_2O$ configurations found to be the most stable. Figure 4.6C is where the H_2O molecule is bound to the H atom of the HSO_4^- molecule, while Figure 4.6D is where the H_2O molecule is bound to the S=O group of the HSO_4^- molecule.

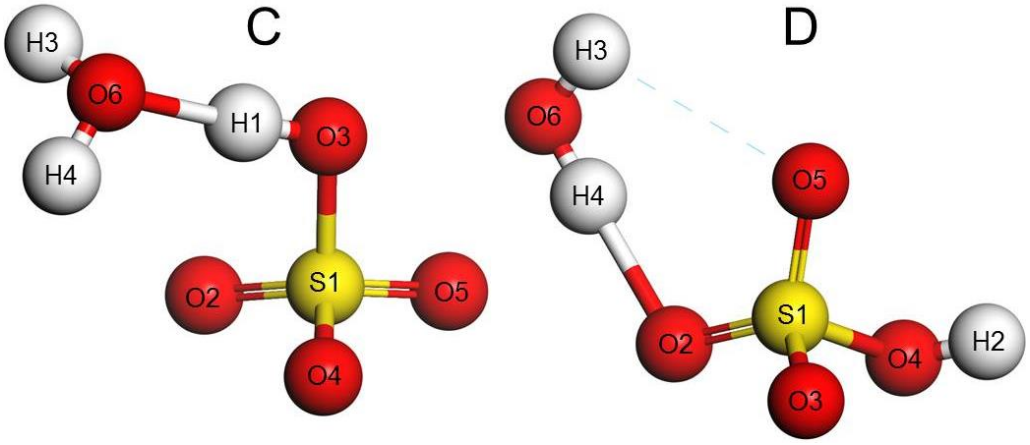

Figure 4.6 – Optimised geometries of the two deprotonated monohydrate ($HSO_4^-.H_2O$) configurations C and D

Table 4.4 shows the modelled data for the bond lengths and angles of both configurations C and D of $HSO_4^-.H_2O$. For configuration C, the bond lengths and angles were within 0.027 Å and 0.5°, respectively, from each other, except for the bond length between H_2O and HSO_4^-, which differed by up to 0.133 Å. This bond length deviation (H1-O6) led to the H4-O2 deviation of up to 0.1 Å, while the H_2O to $H_2SO_4^-$ angle (H4-O6-H1) deviated up to 6.8°. For configuration D, the bond lengths and angles were within 0.020 Å and 1.49°, respectively, from each other. Similar to configuration D, Arstila et al. [32] proposed a $HSO_4^-.H_2O$ configuration where the H_2O molecule is bound to the =O atom of HSO_4^-. The main difference between configuration C and D was that the H_2O molecule was rotated clockwise and to the back forming a hydrogen bond between the O of H_2O and the H on HSO_4^- (between O6 and H2). Arstila et al. [32] found a bond length between H_2O and HSO_4^- of 1.68 Å, which correlated with configuration C (1.657 ± 0.067 Å), but not with configuration D (1.822 ± 0.017 Å).

Table 4.4 – Modelled data (with COSMO) for the bond lengths and angles of $HSO_4^-.H_2O$ (C and D)

Bond/Angle	Configuration C			Configuration D		
	PW91 (DNP+)	PBE (DNP+)	B3LYP (DNP+)	PW91 (DNP+)	PBE (DNP+)	B3LYP (DNP+)
S1-O2 [Å]	1.482	1.482	1.472	1.481	1.482	1.467
S1-O3 [Å]	1.632	1.624	1.616	1.474	1.474	1.462
S1-O4 [Å]	1.482	1.482	1.465	1.659	1.660	1.640
S1-O5 [Å]	1.476	1.477	1.463	1.474	1.475	1.463
O3-H1 [Å]	1.019	1.008	0.992	-	-	-
O4-H2 [Å]	-	-	-	0.977	0.978	0.970
H1-O6 [Å]	1.590	1.686	1.723	-	-	-
O6-H3 [Å]	0.973	0.974	0.967	0.971	0.972	0.964
O6-H4 [Å]	0.973	0.974	0.968	0.988	0.988	0.976
H3-O5 [Å]	-	-	-	2.924	2.929	2.943
H4-O2 [Å]	3.446	3.560	3.557	1.805	1.813	1.839
O2-S1-O4 [°]	112.74	112.97	112.02	100.66	100.57	101.01
O4-S1-O5 [°]	113.87	113.90	113.85	106.24	106.22	105.91
O5-S1-O3 [°]	102.59	102.32	102.66	114.19	114.19	113.63
O2-S1-O3 [°]	106.35	106.12	106.17	113.93	113.86	114.23
S1-O2-H4 [°]	-	-	-	110.98	110.77	112.23
S1-O3-H1 [°]	108.27	107.58	108.95	-	-	-
S1-O4-H2 [°]	-	-	-	107.17	107.21	108.66
H4-O6-H1 [°]	102.76	108.50	109.55			
H4-O6-H3 [°]	-	-	-	103.35	102.98	103.64
H3-O6-H4 [°]	104.38	103.73	103.33	-	-	-
O3-S1-O4 [°]	106.30	106.22	106.84	106.16	106.29	106.41
O2-S1-O5 [°]	113.56	114.07	114.26	114.04	114.10	114.11

For the last step of this section, the di-hydrated sulphuric acid molecule $H_2SO_4.2H_2O$ was modelled. Figure 4.7 shows the two configurations of $H_2SO_4.2H_2O$ (E1 and E2) that were considered. Following the logic from the formation of configurations A, B1 and B2 of the $H_2SO_4.H_2O$ molecule, it was assumed that a second H_2O molecule could attach to either an OH group (as with the formation of configuration A), or it could attach to the =O of the H_2SO_4 molecule (as with the formation of configurations B1 and B2). Both these approaches were investigated and the results (Table 4.5) show that stable configurations were obtained with the first approach where the H_2O molecule attached to the OH group of H_2SO_4 to form the two configurations E1 and E2 shown in Figure 4.7. This was also compared to the modelled data of $H_2SO_4.2H_2O$ by Arstila et al. [32].

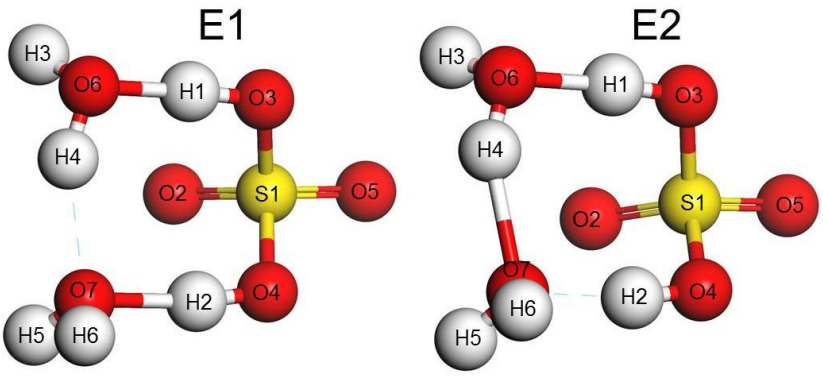

Figure 4.7 – Optimised geometry of two di-hydrate sulphuric acid ($H_2SO_4.2H_2O$) configurations E1 and E2

Comparing the result from the three functionals with each other, it can be seen that the bond lengths and angles deviated by less than 0.20 ± 0.01 Å and 1°, respectively. However, the bond angles with respect to the attached H_2O molecules (H6-O7-H2) deviated up to 2.59°. Comparing the literature values to the modelled values, the bond lengths deviated by less than 0.26 Å and 0.15 Å with respect to configurations E1 and E2, respectively. The difference in bond angles from literature and the modelled data deviated by less than 1.46°. The two geometries shown by Arstila et al. [32] show the attachment of the two H_2O molecules to the OH groups of a trans-H_2SO_4 conformer and not to the cis-conformer as was obtained in this study. Similar to the geometry of $H_2SO_4.H_2O$, we have found the cis-configuration of $H_2SO_4.2H_2O$ to be more stable than the trans-configuration, even though the trans-H_2SO_4 molecule has a lower energy.

Table 4.5 – Calculated (with COSMO) and literature values of bond lengths and angles of $H_2SO_4.2H_2O$ (E1 and E2 (in brackets))

Bond/Angle	Literature [32]	PW91 (DNP+)	PBE (DNP+)	B3LYP (DNP+)
S1-O3 [Å]	1.61	1.566	1.577	1.563
	(1.59)	(1.564)	(1.578)	(1.567)
O3-H1 [Å]	1.04	1.098	1.061	1.034
	(1.06)	(1.103)	(1.064)	(1.032)
H1-O6 [Å]	1.64	1.379	1.478	1.520
	(1.52)	(1.369)	(1.468)	(1.529)
O6-H3 [Å]	0.99	0.973	0.974	0.966
	(0.99)	(0.973)	(0.974)	(0.967)
S1-O4 [Å]	1.61	1.593	1.595	1.579
	(1.65)	(1.595)	(1.598)	(1.578)
O4-H2 [Å]	1.04	1.032	1.022	1.004
	(0.99)	(1.029)	(1.021)	(1.005)
H2-O7 [Å]	1.64	1.533	1.616	1.645
	(-)	(1.540)	(1.623)	(1.645)
O7-H5 [Å]	0.99	0.972	0.975	0.967
	(0.99)	(0.972)	(0.975)	(0.967)
H4-O7 [Å]	-	1.657	1.854	1.837
	(1.77)	(1.640)	(1.847)	(1.847)
O3-S1-O4 [°]	103.8	104.58	104.73	104.59
	(102.9)	(104.74)	(104.71)	(104.49)
S1-O3-H1 [°]	108.8	110.26	110.26	110.67
	(111.6)	(110.80)	(110.22)	(110.25)
H1-O6-H4[°]	-	100.85	103.42	103.26
		(100.27)	(103.02)	(103.20)
H4-O6-O3 [°]	-	99.66	102.25	101.02
		(105.94)	(105.13)	(105.58)
S1-O4-H2 [°]	108.8	108.68	109.17	109.67
	(107.6)	(109.30)	(109.05)	(110.00)
H2-O7-H6 [°]	-	111.03	111.59	112.56
		(110.33)	(111.31)	(113.52)
H6-O7-O4 [°]	-	112.28	112.67	114.39
		(112.26)	(114.10)	(112.28)

Figure 4.8 shows the results for reaction 3 ($H_2SO_4 + H_2O \rightarrow H_2SO_4.H_2O$), where one H_2O molecule is explicitly added to both the cis- and trans-H_2SO_4 molecules to determine the pathway to form configuration A of $H_2SO_4.H_2O$ shown previously in Figure 4.3. The first graph in Figure 4.8 shows the results with respect to the cis-H_2SO_4 conformer. In a first step, a H_2O molecule was positioned between the two OH groups of H_2SO_4 to exothermically form a stable intermediate species with −14.01, −9.56 and −7.31 kcal/mol calculated with PW91(DNP+), PBE(DNP+) and B3LYP(DNP+), respectively. In the second step an intermediate state formed

where the H_2O group was shifted to form a hydrogen bond with one of the OH groups of the H_2SO_4 with −8.27, −11.22 and −15.75 kcal/mol, respectively. In the third step, configuration A was formed at −14.94, −10.67 and −18.94 kcal/mol, respectively. These results indicate an exothermic reaction. This reaction was also modelled without COSMO and the formation energy with regard to the transition states and the formation of $H_2SO_4.H_2O$ followed the same trend, albeit at a slightly higher energy (~ 3 kcal/mol), showing that this reaction was also exothermic in the gas phase.

The second graph in Figure 4.8 shows the results with respect to the trans-H_2SO_4 conformer. In the first step the H_2O molecule coordinated with one of the OH groups of H_2SO_4 and formed an intermediary state at −16.27, −10.74 and −8.92 kcal/mol, calculated with PW91(DNP+), PBE(DNP+) and B3LYP(DNP+), respectively. These results differed by less than 2.26 kcal/mol from the cis-conformer data. The second step shows that the other OH group of H_2SO_4 rotated to form a second intermediary species at −8.23, −11.04 and −15.55 kcal/mol. These results were within 0.2 kcal/mol from the cis-conformer data. Step 3 shows the formation of configuration A requiring −14.75, −10.50 and −18.90 kcal/mol, respectively. These results deviated by less than 0.19 kcal/mol from the cis-conformer data. Hence both reactions from the cis- and trans-conformers are exothermic. Similar to the top graph, when this reaction was repeated without COSMO, the trends were similar and overall deviated by less than 3 kcal/mol.

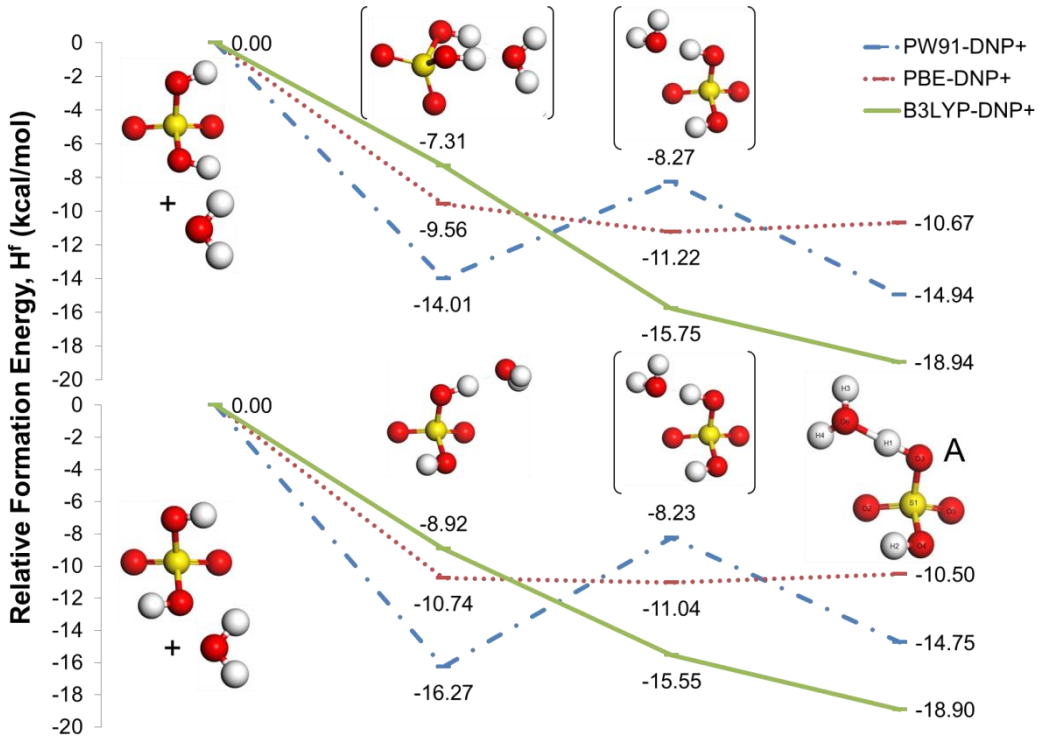

Figure 4.8 – Relative energy of formation (H^f (kcal/mol)) of $H_2SO_4.H_2O$ (configuration A) from both the cis- and trans-conformer of H_2SO_4

Figure 4.9 shows the relative energy of formation for reaction 3 ($H_2SO_4 + H_2O \rightarrow H_2SO_4.H_2O$) with respect to configurations B1 and B2 of $H_2SO_4.H_2O$, as was shown in Figure 4.3. Again the first graph in Figure 4.9 shows the results with respect to the cis-H_2SO_4 and the second the trans-H_2SO_4 conformer. The first step (top graph) shows the formation of an intermediary by the rotation of the OH group on H_2SO_4 and the coordination of the H_2O molecule with −3.57, −2.73 and −1.87 kcal/mol, calculated with PW91(DNP+), PBE(DNP+) and B3LYP(DNP+), respectively. The second step shows the formation of configuration B1 with −3.19, −2.47 and −0.77 kcal/mol, respectively. The third step is again the formation of an intermediate. Rotation around the =O is not possible, therefore the H_2O molecule detached and coordinated from behind the H_2SO_4 molecule to form B2 (as shown in Figure 4.9) at −4.24, −3.87 and −2.08 kcal/mol. Both the intermediaries are similar in geometry and therefore have energies within 1.14 kcal/mol from each other. The fourth step is the formation of configuration B2 at −3.03, −2.42 and −0.80 kcal/mol, respectively. The energy of formation of configuration B1 and B2 are similar and within 0.16 kcal/mol from each other. These results indicate that both the formation of configuration B1 and B2 with respect to the cis-H_2SO_4 was exothermic.

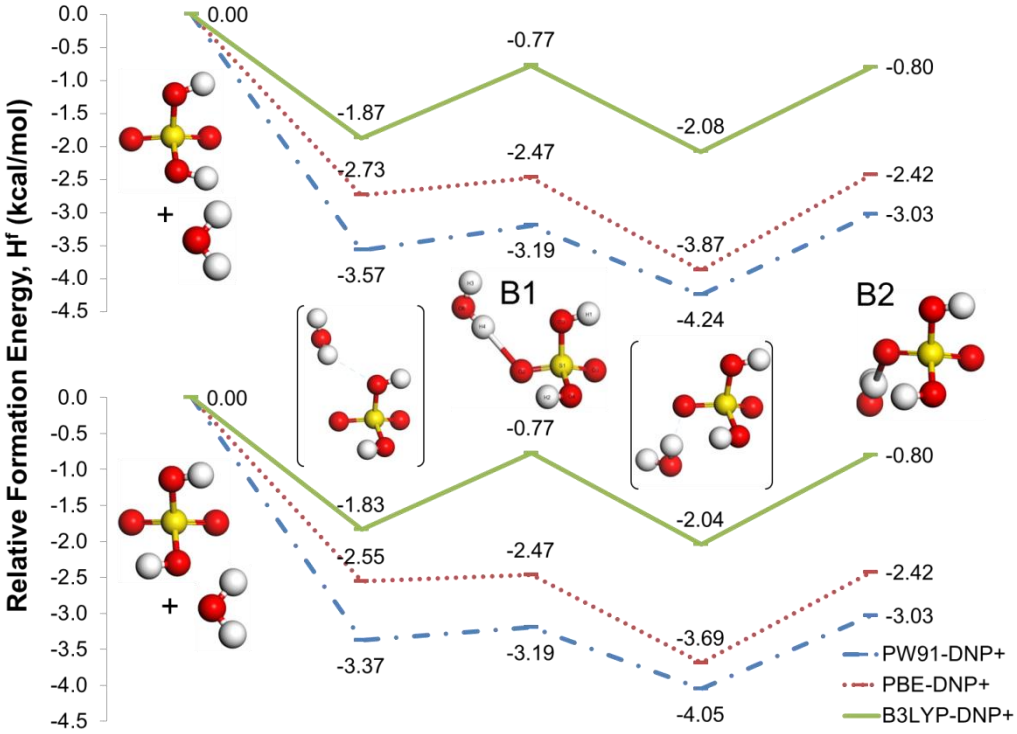

Figure 4.9 – Relative energy of formation (H^f (kcal/mol)) of $H_2SO_4.H_2O$ (configurations B1 and B2)

The second graph in Figure 4.9 shows the formation of configurations B1 and B2 with respect to the trans-H_2SO_4 conformer. The energy values were within 0.2 kcal/mol when comparing

the formation of B1 and B2 via the cis- and trans-conformers. Similar to the cis-conformer, the data with respect to the trans-conformer showed that the formation of configuration B1 and B2 was exothermic in both cases and that both the cis- and trans-H_2SO_4 conformations may form configuration B1 and B2. Comparing the data obtained without using COSMO, it was seen that again this reaction was exothermic, however, the data deviated by as much as 15 kcal/mol even though the same geometries of the molecules were used.

Comparing the formation of $H_2SO_4.H_2O$ through the formation of configuration A or B1 and B2, it can be seen that the overall energy of formation of A is lower than for B1 or B2. This can be attributed to the type of bond that is formed between H_2O and H_2SO_4. In configuration A there is initially a hydrogen bond between the O atom of H_2O and H1 of H_2SO_4, which changes to a covalent bond, causing H1 to have two bonds. In configuration B, H_2O is bound to the =O of H_2SO_4, causing O2 to have three bonds, which in turn could increase the reaction energy even though the intermediary species in both pathways (A and B1&B2) were similar. Yacovitch et al. [38] also considered two similar geometries and predicted that configuration A, in a 1:1 ratio, was more stable (0.382 kcal/mol) than configuration B.

Table 4.6 shows the deprotonation reactions to form $HSO_4^-.H_2O$ (configuration C and D in Figure 4.6). The reaction energies (reaction 4) calculated with all three functionals showed that this reaction was exothermic for both C and D. To confirm that the formation of $HSO_4^-.H_2O$ is dependent on the formation of HSO_4^- and not the direct reaction from H_2SO_4, reaction energies were calculated for when H_2SO_4 is surrounded by 2 H_2O molecules to form $HSO_4^-.H_2O$ (configuration C or D) and an additional H_3O^+ (second reaction in Table 4.6). The positive values calculated with all three functionals indicate that this was an endothermic reaction. However, the reaction values were lower than 10 kcal/mol, indicating that this reaction was possible, but may occur in two or more steps. This correlates with the previous reaction (reaction 4), i.e. that a multistep reaction occurs during the formation of $HSO_4^-.H_2O$. However, when these two reactions were repeated without COSMO the data deviated significantly. When the direct hydration of HSO_4^- was considered to lead to the formation of $HSO_4^-.H_2O$ (configuration C or D), the energy of formation was ~12.6 – 18.9 kcal/mol for all three functionals. This can again be due to the ionic state of the species modelled. In the second reaction though ($H_2SO_4 + 2H_2O \rightarrow HSO_4^-.H_2O + H_3O^+$), where a second H_2O molecule was added, the energy of formation increased to ~123 – 132 kcal/mol.

Table 4.6 – Reaction energies (kcal/mol) for the formation of $HSO_4^-.H_2O$ (configuration C and D)

	Config.	PW91 (DNP+)	PBE (DNP+)	B3LYP (DNP+)
$HSO_4^- + H_2O \rightarrow HSO_4^-.H_2O$	C	−9.48	−6.65	−4.40
	D	−5.27	−4.46	−2.40
$H_2SO_4 + 2H_2O \rightarrow HSO_4^-.H_2O + H_3O^+$	C	2.28	3.99	6.80
	D	1.94	6.19	8.80

Although it was shown (Table 4.6) that $HSO_4^-.H_2O$ forms from the reaction between HSO_4^- and H_2O (reaction 4), it leaves the question whether $HSO_4^-.H_2O$ could form from the deprotonation of $H_2SO_4.H_2O$. Due to the similarities in configuration of the species it is presumed that configuration A (Figure 4.5) could deprotonate to form configuration C (Figure 4.6) and similarly that configurations B1 & B2 could form configuration D.

Figure 4.10 shows two possible mechanisms for the decomposition of $H_2SO_4.H_2O$ from configuration A to either form $HSO_4^-.H_2O$ (configuration C) or $HSO_4^- + H_3O^+$. The top graph (Figure 4.10) shows how the bond length of H2 (H bound to H_2SO_4) increases to form configuration C with an additional H^+ atom. Again the positive reaction energies calculated with all three functionals indicate endothermic reactions or possible multistep reactions. If configuration A does not lead to the formation of configuration C, could configuration A lead to the formation of HSO_4^- and H_3O^+? The bottom graph (Figure 4.10) shows a mechanism where the bond length between O3 (O bound to H_2O) and H1 (H bound to H_2SO_4) is increased to form HSO_4^- and H_3O^+. The results from PW91(DNP+) and PBE(DNP+) show this to be an exothermic reaction with a transition state at 3.60 and 5.87 kcal/mol, respectively. The results with B3LYP(DNP+) follow the same trend as with PW91(DNP+) and PBE(DNP+), but it shows this reaction to be endothermic. Bourassa et al. [39] and Bryantsev et al. [40] both showed an increase in the calculated energy of ions when using B3LYP; however, they found that the energy decreased when explicit H_2O molecules were added. Therefore, in Section 4.3.3, the effect of explicitly adding H_2O molecules is discussed.

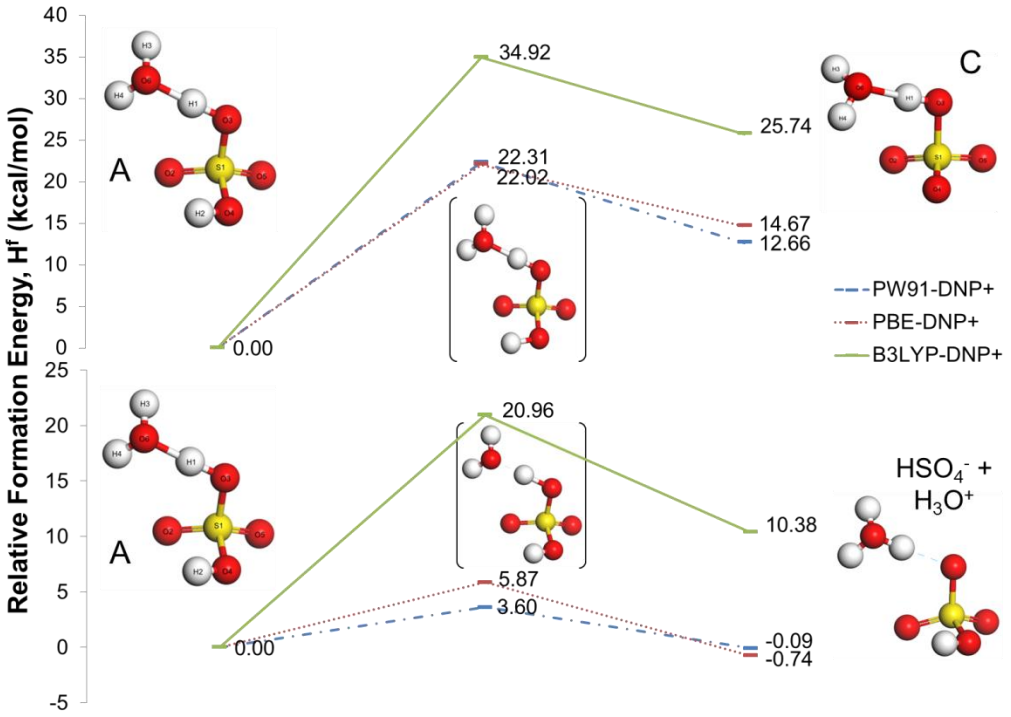

Figure 4.10 – Possible mechanism for the decomposition of $H_2SO_4.H_2O$ (A) to either form $HSO_4^-.H_2O$ (C) (top) or HSO_4^- + H_3O^+ (bottom)

Similar results were obtained when it was proposed that configurations B1 & B2 deprotonate ($H_2SO_4.H_2O \rightarrow HSO_4^-.H_2O + H^+$) to form configuration D (data not shown). In configuration B1 the H1-O3 bond length was increased until deprotonation occurred. The transition states were at 21.15, 21.61 and 24.07 kcal/mol when calculated with PW91(DNP+), PBE(DNP+) and B3LYP(DNP+), respectively. The formation of configuration D was at 5.13, 8.65 and 9.57 kcal/mol, respectively. In configuration B2 the H1-O3 bond length was increased again, which yielded a transition state at 21.46, 21.68, 23.74 kcal/mol and configuration D at 4.96, 8.61 and 9.60 kcal/mol with PW91(DNP+), PBE(DNP+) and B3LYP(DNP+), respectively. These results confirm that both the mechanism for the formation of configuration C and D are likely to take place via reaction 4.

It was shown in Figure 4.5 that, during the hydration of H_2SO_4 (configuration A, B1 and B2), another H_2O molecule could bind to form two possible di-hydrated $H_2SO_4.2H_2O$ species via reaction 5. Accordingly, two possible reactions for the formation of $H_2SO_4.2H_2O$ (configuration E1 and E2) are shown in Table 4.7. The first reaction assumes that di-hydration occurs simultaneously and the reaction energies for both E1 and E2 with all three functionals showed this reaction to be exothermic and therefore possible. The low energy values (between −17.30 and −32.76 kcal/mol) confirm that the H_2SO_4 molecule is stabilised in a water medium before

the formation of ionic species. The second reaction assumes that configuration A ($H_2SO_4.H_2O$) already formed before another H_2O molecule attached to form the di-hydrated E1 and E2. The reaction energies calculated with PW91(DNP+) and PBE(DNP+) again indicated exothermic reactions for the formation of both E1 and E2. The reaction energies calculated with B3LYP(DNP+) were 1.64 and 1.55 kcal/mol for configurations E1 and E2, respectively, with an error margin of 3 kcal/mol and therefore considered to still occur. These two reactions (Table 4.7) were also modelled without COSMO; surprisingly, the data for the energy of the first reaction was between -24 and -37 kcal/mol and for the second reaction between -12.4 and -19.4 kcal/mol. This indicates that by explicitly adding at least one H_2O molecule to the system, the H_2SO_4 molecule was stabilised, resulting in lower reaction energies.

Table 4.7 – Reaction energies (kcal/mol) for the formation of $H_2SO_4.2H_2O$ (E1 and E2)

Reactions	Config.	PW91 (DNP+)	PBE (DNP+)	B3LYP (DNP+)
$H_2SO_4 + 2H_2O \rightarrow H_2SO_4.2H_2O$	E1	−31.89	−21.74	−17.30
	E2	−32.76	−22.16	−17.39
$H_2SO_4.H_2O + H_2O \rightarrow H_2SO_4.2H_2O$	A→E1	−16.94	−11.07	1.64
	A→E2	−17.82	−11.48	1.55

When considering all 5 reactions presented in Section 4.1, it is clear that reaction 1 and 2 (formation of HSO_4^- and SO_4^{2-}, respectively) would most probably not occur when a 1:1 acid-to-water ratio or the gas phase (without COSMO) was used. Reaction 3 (the formation of hydrated H_2SO_4) would, however, occur exothermically with the formation of three possible configurations of $H_2SO_4.H_2O$ (A, B1 and B2). Reaction 4 could occur by configuration A dissociating to form HSO_4^- and H_3O^+, after which the HSO_4^- ion could hydrate to form either C or D. Reaction 5, which entails the formation of two possible di-hydrated H_2SO_4 species, i.e. E1 and E2, could occur exothermically via two possible mechanisms: one where di-hydration occurred simultaneously or two where configuration A is initially formed before E1 or E2 is formed. In all these cases it was seen that adding one H_2O molecule increased the stabilisation of the other molecules or ions present during the reaction. To investigate this effect further, the following section will focus on the influence of additional H_2O molecules (1:5 and 1:10 acid-water ratios) on the likelihood of the above-mentioned five reactions with the addition of COSMO.

4.3.3 Reactions of H_2SO_4 and H_2O in a 1:5 and a 1:10 H_2SO_4/H_2O environment

All the species participating and formed in reactions 1 – 5 were again geometrically optimised in the presence of additional H_2O molecules (acid-water ratio: 1:5 and 1:10) and COSMO before calculating the energies as described in Section 4.2. The reactions and calculated energies using the three base sets for the 1:5 and 1:10 H_2SO_4:H_2O are presented in Table 4.8. The same configuration letters are used as in Section 4.3.1. However, if the geometry of a species changed it will be indicated by for example A'.

It is clear that all the reactions were exothermic. As expected the reaction energies with the 1:5 ratio were generally less negative than for the 1:10 ratio. Arrouvel et al. [41], using the Gaussian 98 software with the B3LYP functional and 6-31+G** basis set, showed that by increasing the number of hydrogen bonds (by increasing the number of H_2O:H_2SO_4 molecules), the ionic species became more stable, resulting in more negative reaction energies. Jiang et al. [42] investigated the behaviour of H^+ in H_2O systems ranging from 4 to 8 H_2O molecules (Gaussian 94 with the B3LYP functional and 6-31+G* basis set) and showed that the total energy of each system decreased (from −67 kcal/mol to −115 kcal/mol) when the number of H_2O molecules increased from 4 to 8. Ding and Laasonen [43] confirmed this when investigating the influence of the number of H_2O molecules on the deprotonation of H_2SO_4 (by using DMol^3 4.2 in Cerius^2 with BLYP(DNP) and PW91(DNP)) showing that, by increasing the number of H_2O molecules from 5 to 9, the energy decreased from −55 kcal/mol to −96 kcal/mol and −68 kcal/mol to −122 kcal/mol with BLYP(DNP) and PW91(DNP), respectively. This confirms the trend observed in literature, i.e. the reactions become more likely when increasing the number of H_2O molecules in a system.

For reaction 1 (cis- or trans-H_2SO_4 → HSO_4^-), it was found when using a 1:1 ratio that 7.2 to 11.24 kcal/mol was needed to form HSO_4^-. When increasing the water content to a 1:5 ratio, the reaction energy required decreased to between −32.44 and −65.46 kcal/mol, respectively when the cis- and trans conformer data was compared within each functional. The same trend as for the 1:1 ratio was observed in the 1:5 reaction, where PW91(DNP+) showed the lowest reaction energy, followed by PBE(DBP+) and B3LYP(DNP+). Similar to the 1:5 ratio, the 1:10 ratio showed that the reaction energy required decreased to between −57.46 and −89.45 kcal/mol when the cis- and trans conformer data was compared within each functional. However, with the 1:10 ratio, PBE(DNP+) had the lowest energy followed by PW91(DNP+) and B3LYP(DNP+).

Table 4.8 – Relative energy of formation (H^f (kcal/mol)) of the H_2SO_4 reactions (Reactions 1 to 5) in a 1:5 and 1:10 ratio with H_2O

	Reactions	PW91 (DNP+)	PBE (DNP+)	B3LYP (DNP+)
	1:5 acid-water ratio			
(1)	$H_2SO_4^*$ + 5 H_2O → HSO_4^- + H_3O^+ + 4 H_2O			
	*cis-conformer	−65.46	−44.59	−32.48
	*trans-conformer	−65.26	−44.41	−32.44
(2)	HSO_4^- + 5 H_2O → SO_4^{2-} + H_3O^+ + 4 H_2O	−65.36	−43.61	−32.50
(3)	H_2SO_4 + 5 H_2O → $H_2SO_4.H_2O^*$ + 4 H_2O			
	*Configuration A	−50.62	−35.64	−25.15
	*Configuration B1’	−41.27	−28.82	−18.84
	*Configuration B2’	−73.88	−48.75	−35.82
(4)	HSO_4^- + 5 H_2O → $HSO_4^-.H_2O^*$ + 4 H_2O			
	*Configuration C’	−45.42	−31.44	−21.35
	*Configuration D’	−46.11	−30.11	−20.05
(5)	H_2SO_4 + 5 H_2O → $H_2SO_4.2H_2O^*$ + 3 H_2O			
	*Configuration E1	−68.82	−42.79	−30.84
	*Configuration E2	−67.44	−43.15	−28.36
	1:10 acid-water ratio			
(1)	$H_2SO_4^*$ + 10 H_2O → HSO_4^- + H_3O^+ + 9 H_2O			
	*cis-conformer	−68.34	−84.72	−57.50
	*trans-conformer	−68.24	−84.54	−57.46
(2)	HSO_4^- + 10 H_2O → SO_4^{2-} + H_3O^+ + 9 H_2O	−69.59	−89.45	−36.45
(3)	H_2SO_4 + 10 H_2O → $H_2SO_4.H_2O^*$ + 9 H_2O			
	*Configuration A	−77.39	−89.21	−62.30
	*Configuration B1’	−68.43	−89.05	−64.09
	*Configuration B2’	−65.93	−85.42	−49.94
(4)	HSO_4^- + 10 H_2O → $HSO_4^-.H_2O^*$ + 9 H_2O			
	*Configuration C’	−58.97	−70.12	−48.85
	*Configuration D’	−63.55	−77.14	−51.52
(5)	H_2SO_4 + 10 H_2O → $H_2SO_4.2H_2O^*$ + 8 H_2O			
	*Configuration E1’	−65.95	−74.79	−53.06
	*Configuration E2’	−65.89	−82.40	−49.20

For reaction 2 it was shown that after HSO_4^- had formed in a 1:1 ratio (Figure 4.4), an additional 24 kcal/mol was needed to form SO_4^{2-}. In a 1:5 and 1:10 ratio, this reaction also became exothermic. Again (see reaction 1), the same energy trend was observed in that the 1:5 ratio PW91(DNP+) had the most negative energy, followed by PBE(DBP+) and B3LYP(DNP+), whereas it was PBE(DNP+), followed by PW91(DNP+) and B3LYP(DNP+) when using an 1:10 ratio.

Reaction 3 shows the formation of $H_2SO_4.H_2O$ in three configurations (A, B1 and B2). While it was shown that, in a 1:1 ratio (Figure 4.8 and Figure 4.9), A had the lowest energy, followed by B1 and then B2, this trend was not always observed in the 1:5 and 1:10 ratios. When B1 was surrounded by an additional four H_2O molecules, the distance of the already bonded H_2O molecule (O2-H4 distance) changed and was therefore called B1'. The O2-H4 distance of B1' decreased to 1.970 and 1.955 Å with PBE(DNP+) and PW91(DNP+), respectively, which also contributed to the increase in reaction energy. However, with B3LYP(DNP+) this distance increased to 2.043 Å, resulting in the higher than expected reaction energy. Similar to the B1' configuration, in B2' the O2-H4 distance decreased with all three functionals to 1.705, 1.817 and 1.909 Å, using PW91(DNP+), PBE(DBP+) and B3LYP(DNP+), respectively. This dehydration of $H_2SO_4.H_2O$ caused the reaction energy to decrease. However, the decreasing reaction energy observed could also be possible due to a neighbouring H_2O molecule stabilising the bonded H_2O molecule with a hydrogen bond. In the 1:10 ratio the O2-H4 distance of B1' increased to 3.770, 3.995, 4.166 Å with PW91(DNP+), PBE(DBP+) and B3LYP(DNP+), respectively, and deprotonated to form HSO_4^- and H_3O^+ with 9 surrounding H_2O molecules. B2' showed similar results whereby HSO_4^- and H_3O^+ formed with 9 surrounding H_2O molecules.

Reaction 4 presents the formation of $HSO_4^-.H_2O$. Similar to B1' and B2', the distance of the bonded H_2O molecule changed and the two $HSO_4^-.H_2O$ conformers were therefore named configuration C' and D'. The H1-O6 distance in configuration C' in the 1:5 ratio shortened to 1.440, 1.541 and 1.609 Å with PW91(DNP+), PBE(DBP+) and B3LYP(DNP+), respectively, while the H4-O2 distance of configuration D' decreased to 1.740 and 1.776 Å, and increased to 1.860 Å with PW91(DNP+), PBE(DBP+) and B3LYP(DNP+), respectively. In the 1:10 ratio the H1-O6 distance for C' was 1.488, 1.468 and 1.543 Å with PW91(DNP+), PBE(DBP+) and B3LYP(DNP+), respectively, and these distances were dependant on the position of the surrounding H_2O molecules and the resulting hydrogen bonds that formed. The H2-O2 distance in the 1:10 ratio increased to 1.845, 1.878 and 1.983 Å with PW91(DNP+), PBE(DBP+) and B3LYP(DNP+), respectively, resulting in the formation of HSO_4^- and H_3O^+ with 9 surrounding H_2O molecules similar to B1' and B2'.

Finally, reaction 5 presents the formation of $H_2SO_4.2H_2O$. The addition of 3 H_2O molecules to form the 1:5 ratio stabilised both configurations E1 and E2 to give reaction energies similar to reaction 1. In the 1:10 ratio, the additional H_2O molecules caused simultaneous dehydration and protonation of the molecule in both E1 and E2 to form HSO_4^- and H_3O^+ with 9 surrounding H_2O molecules (similar to the reaction of B1' and B2').

From the above results it can be seen that, although different configurations between H_2SO_4 and H_2O exist, the addition of 5 and 10 H_2O molecules resulted in a hydration sphere around H_2SO_4, which lead to the lowering in reaction energies. While it was shown in the 1:1 ratio that various species of $H_2SO_4.H_2O$ (A, B1 & B2), $HSO_4^-.H_2O$ (C and D) and $H_2SO_4.2H_2O$ (E1 & E2) could form, the additional H_2O molecules lead to the stabilisation of the system and a geometry change in some of the species. In the 1:5 ratio, the most likely species to exist are HSO_4^- + H_3O^+, $H_2SO_4.H_2O$ (A) and $H_2SO_4.2H_2O$ (E1 & E2). However, in the 1:10 ratio, more geometry changes occurred and therefore the most likely species to exist are HSO_4^- + H_3O^+ and $H_2SO_4.H_2O$ (A). Therefore, it seems that in the presence of excess, H_2O will bind to H_2SO_4 to form $H_2SO_4.H_2O$ (A), which will then lead to the formation of HSO_4^- + H_3O^+ and hence interact with metals in a water phase.

4.4 Conclusion

In this study the aqueous phase used during the SX of Ta and Nb was investigated to calculate the energy needed for various reactions of H_2SO_4 and H_2O in an aqueous phase, thereby determining which H_2SO_4 species is most likely to exist in an aqueous environment. For this purpose, 5 different reactions were studied in a 1:1, 1:5 and 1:10 acid-water ratio. In the first part the energies of the two reactions were considered in the gas phase (without COSMO) and in a 1:1 acid:water ratio. It was shown that free rotation (<1 kcal/mol needed) for both the cis- and trans-H_2SO_4 conformers exist. Subsequently, it was shown that the dissociation energy for H_2SO_4 was endothermic in both the gas and aqueous simulations, while the formation of $H_2SO_4.H_2O$, $HSO_4^-.H_2O$ and $H_2SO_4.2H_2O$ was exothermic. Furthermore, it was shown that $H_2SO_4.H_2O$ does not form $HSO_4^-.H_2O$ directly, but rather lead to the possible formation of HSO_4^- and H_3O^+.

With the addition of H_2O molecules to form 1:5 and 1:10 acid-water ratios, multiple hydrogen bonds formed, which stabilised the different acid species, resulting in the lowering of the reaction energies. Although it was shown that different conformers of $H_2SO_4.H_2O$ (A, B1 and B2), $HSO_4^-.H_2O$ (C and D) and $H_2SO_4.2H_2O$ (E1 and E2) could form, the most stable acid species in the 1:10 acid-water ratio were HSO_4^- and H_3O^+ with 9 surrounding H_2O molecules. Therefore, it can be assumed that the HSO_4^- would be the most likely species to interact with the Ta and Nb in a water phase. In a follow-up paper, the influence of adding Ta ions to the optimised acidic aqueous phase will be investigated.

4.5 References

[1] R.E. Krebs, The History and Use of Our Earth's Chemical Elements: A Reference Guide, 2 ed., Greenwood Press, Westport, USA, 2006.

[2] M.J. Ungerer, H.M. Krieg, G. Lachmann, D.J.v.d. Westhuizen, Comparison of extractants for the separation of TaF_5 and NbF_5 in different acidic media, Hydrometallurgy, 144-145 (2014) 195 - 206.

[3] A. Timofeev, A.A. Migdisov, A.E. Williams-Jones, An experimental study of the solubility and speciation of niobium in fluoride-bearing aqueous solutions at elevated temperature, Geochimica et Cosmochimica Acta, 158 (2015) 103 - 111.

[4] J. Narbutt, M. Czerwinski, Chapter 16 - Computational chemistry in modelling solvent extraction of metal ions, in: J. Rydberg, M. Cox, C. Musikas, G.R. Choppin (Eds.) Solvent extraction principles and practice, Wiley, New York, 1992.

[5] J.A. Allen, G. Rowe, J.T. Hinkley, S.W. Donne, Electrochemical aspects of the hybrid sulfur cycle for large scale hydrogen production, International Journal of Hydrogen Energy, 39 (2014) 11376 - 11389.

[6] H. Jin, M.B. Ansari, S.E. Park, Sulfonic acid functionalized mesoporous ZSM-5: Synthesis, characterization and catalytic activity in acidic catalysis, Catalysis Today, 245 (2015) 116 - 121.

[7] A.D. Hammerich, V. Buch, F. Mohamed, Ab initio simulations of sulfuric acid solutions, Chemical Physics Letters, 460 (2008) 423 - 431.

[8] C.G. Ding, T. Taskila, K. Laasonen, A. Laaksonen, Reliable potential for small sulfuric acid-water clusters, Chemical Physics, 287 (2003) 7 - 19.

[9] A.B. Nadykto, F. Yu, J. Herb, Theoretical analysis of the gas-phase hydration of common atmospheric pre-nucleation $(HSO_4^-)(H_2O)_n$ and $(H_3O^+)(H_2SO_4)(H_2O)_n$ cluster ions, Chemical Physics, 360 (2009) 67 - 73.

[10] C.C. Pye, W.W. Rudolph, An ab initio and Raman investigation of sulfate ion hydration, Journal of Physical Chemistry A, 105 (2001) 905 - 912.

[11] W.R. Cannon, B.M. Pettitt, J.A. McCammon, Sulfate anion in water: Model structural, thermodynamics and dynamic properties, Journal of Physical Chemistry, 98 (1994) 6225 - 6230.

[12] A. Kakizaki, H. Motegi, T. Yoshikawa, T. Takayanagi, M. Shiga, M. Tachikawa, Path-integral molecular dynamics simulations of small hydrated sulfuric acid clusters H_2SO_4 $(H_2O)n$ (n = 1–6) on semiempirical PM6 potential surfaces, Journal of Molecular Structure: THEOCHEM, 901 (2009) 1 - 8.

[13] D.Y. Zubarev, B.M. Austin, W.A.J. Lester, Practical aspects of quantum Monte Carlo for the electronic structure of molecules, in: J. Leszczynski, M.K. Shukla (Eds.) Practical aspects of computational chemistry I, Springer, Dordrecht, Holland, 2012, pp. 255 - 292.

[14] A. Klamt, G. Schüürmann, COSMO: a new approach to dielectric screening in solvents with explicit expressions for the screening energy and its gradient, Journal of the Chemical Society, Perkin Transactions 2, (1993) 799 - 805.

[15] B. Delley, The conductor-like screening model for polymers and surfaces, Molecular Simulation, 32 (2006) 117 - 123.

[16] Material Studio Modelling Environment, Accelrys Software Inc., San Diego, 2012.

[17] J.P. Perdew, Y. Wang, Accurate and simple analytic representation of the electron-gas correlation energy, Physical Review B, 45 (1992) 13244 - 13249.

[18] B. Delley, Ground-state enthalpies: evaluation of electronic structure approaches with emphasis on the density functional method, The Journal of Physical Chemistry A, 110 (2006) 13632 - 13639.

[19] F. Ortmann, F. Bechstedt, W.G. Schmidt, Semiempirical van der Waals correction to the density functional description of solids and molecular structures, Physical Review B, 73 (2006) 205101.

[20] J.P. Perdew, K. Burke, M. Ernzerhof, Generalized gradient approximation made simple, Physical Review Letters, 77 (1996) 3865 - 3868.

[21] A. Tkatchenko, M. Scheffler, Accurate Molecular Van Der Waals Interactions from Ground-State Electron Density and Free-Atom Reference Data, Physical Review Letters, 102 (2009) 073005.

[22] A.D. Becke, Experimental investigation of highly exergonic outer sphere electron transfer reactions, Journal of Physical Chemistry, 88 (1984) 2547-2551.

[23] C. Lee, W. Yang, R.G. Parr, Development of the Colle-Solvetti correlation-energy formula into a functional of the electron density, Physical Review B, 37 (1988) 785-789.

[24] B. Delley, Modern Density Functional Theory: A tool for chemistry, in: J.M. Seminario, P. Politzer (Eds.) Theoretical and Computational Chemistry, 1995.

[25] J. Demaison, M. Herman, J. Liévin, H.D. Rudolph, Equilibrium structure of sulfuric acid, Journal of Physical Chemistry A, 111 (2007) 2602 - 2609.

[26] A.P. Scott, L. Radom, Harmonic vibrational frequencies: An evaluation of Hartree-Fock, Møller-Plesset, quadratic configuration, density functional theory and semiemperical scale factors, Journal of Physical Chemistry, 100 (1996) 16502 - 16513.

[27] J.P. Merrick, D. Moran, L. Radom, An evaluation of vibrational frequency scale factors, Journal of Physical Chemistry A, 111 (2007) 11683 - 11700.

[28] J.D.T. Steyl, Kinetic modelling of chemical processes in acid solution at t<200C. (i) thermodynamics and speciation in H_2SO_4-Metal (ii) SO_4-H_2O system, Hydrometallurgy Conference, The Southern African Institute of Mining and Metallurgy, 2009, pp. 401 - 444.

[29] B.T. Teng, X.D. Wen, M. Fan, F.M. Wu, Y. Zhang, Choosing a proper exchange–correlation functional for the computational catalysis on surface, Physical Chemistry Chemical Physics, 16 (2014) 18563 - 18569.

[30] R. Peverati, D.G. Truhlar, M11-L: A Local Density Functional that provides improved accuracy for electronic structure calculations in chemistry and physics, Journal of Chemical Physics Letters, 3 (2012) 117 - 124.

[31] D.L. Fiacco, S.W. Hunt, K.R. Leopold, Microwave investigation of sulfuric acid monohydrate, Journal of American Chemical Society, 124 (2002) 4504 - 4511.

[32] H. Arstila, K. Laasonen, A. Laaksonen, Ab initio study of gas-phase sulphuric acid hydrates containing 1 to 3 water molecules, Journal of Chemical Physics, 108 (1998) 1031 - 1039.

[33] T. Kurtén, M. Noppel, H. Vehkamäki, M. Salonen, M. Kulmala, Quantum chemical studies of hydrate formation of H_2SO_4 and HSO_4^-, Boreal Environment Research, 12 (2007) 431 - 453.

[34] A.A. Natsheh, A.B. Nadykto, K.V. Mikkelsen, F. Yu, J. Ruuskanen, Sulfuric acid and sulfuric acid hydrates in the gas phase: A DFT investigation, Journal of Physical Chemistry A, 108 (2004) 8914 - 8929.

[35] R. Car, M. Parrinello, Unified approach for molecular dynamics and density-functional theory, Physical Review Letters, 55 (1985) 2471 - 2474.

[36] R.N. Barnett, U. Landman, Structure and energetics of ionized water clusters: $(H_2O)_n^+$, n = 2–5, Journal of Physical Chemistry A, 101 (1997) 164 - 169.

[37] P. Atkins, J.d. Paula, Atkins' Physical Chemistry, 8 ed., W.H. Freeman and Company, New York, 2006.

[38] T.I. Yacovitch, T. Wende, L. Jiang, N. Heine, G. Meijer, D.M. Neumark, K.R. Asmis, Infrared spectroscopy of hydrated bisulfate anion clusters: HSO_4-$(H_2O)_{1-16}$, The journal of Physical Chemistry Letters, 2 (2011) 2135 - 2140.

[39] P. Bourassa, J. Bouchard, S. Robert, Quantum chemical calculations of pristine and modified crystalline cellulose surfaces: benchmarking interactions and adsorption of water and electrolyte, Cellulose, 21 (2014) 71 - 86.

[40] V.S. Bryantsev, M.S. Diallo, A.C.T. van Duin, W.A. Goddard III, Evaluation of B3LYP, X3LYP, and M06-class density functionals for predicting the binding energies of neutral, protonated, and deprotonated water clusters, Journal of Chemical Theory and Computation, 5 (2009) 1016 - 1026.

[41] C. Arrouvel, V. Viossat, C. Minot, Theoretical study of hydrated sulfuric acid: Clusters and periodic modelling, Journal of Molecular Structure: THEOCHEM, 718 (2005) 71 - 76.

[42] J.C. Jiang, Y.S. Wang, H.C. Chang, S.H. Lin, Y.T. Lee, G. Niedner-Schatterburg, H.C. Chang, Infrared spectra of $H^+(H_2O)_{5-8}$ clusters: Evidence for symmetric proton hydration, Journal of American Chemical Society, 122 (2000) 1398 - 1410.

[43] C.G. Ding, K. Laasonen, Partially and fully deprotonated sulfuric acid in $H_2SO_4(H_2O)_n$ (n = 6 - 9) clusters, Chemical Physics Letters, 390 (2004) 307 - 313.

[44] R.L. Kuczkowski, R.D. Suenram, F.J. Lovas, Microwave spectrum, structure, and dipole moment of sulfuric acid, Journal of American Chemical Society, 103 (1981) 2561 - 2566.

[45] G.E. Walrafen, D.M. Dodd, Infra-red absorption spectra of concentrated aqueous solutions of sulphuric acid, Transactions of the Faraday Society, 57 (1960) 1286 - 1296.

[46] K. Kunimatsu, M.G. Samant, H. Seki, In-situ FT-IR spectroscopic study of bisulfate and sulfate adsorption on platinum electrodes, Journal of Electroanalytical Chemistry, 258 (1989) 163 - 177.

4.6 Supplementary Information

Table S1 – Calculated and literature values of bond lengths and angles of H_2SO_4 (cis- and trans-conformers)

Bond/Angle	Literature (modelled) [25]	Literature (exprimental) [44]	PW91 (DNP+)		PBE (DNP+)		B3LYP (DNP+)	
			COSMO	Without COSMO	COSMO	Without COSMO	COSMO	Without COSMO
H_2SO_4, cis								
O3-H1 [Å]	0.964	0.97 ± 0.01	0.983	0.977	0.981	0.978	0.973	0.969
S1-O3 [Å]	1.576	1.574 ± 0.01	1.606	1.622	1.606	1.624	1.587	1.605
S1-O2 [Å]	1.411	1.422 ± 0.01	1.447	1.440	1.446	1.442	1.433	1.429
S1-O3-H1 [°]	108.51	108.5 ± 1.5	109.10	106.95	109.06	106.98	110.67	108.45
O3-S1-O5 [°]	-	108.6 ± 0.5	109.47	108.15	109.51	108.16	109.69	108.15
O3-S1-O2 [°]	105.74	106.4 ± 0.5	105.21	105.96	105.03	105.79	105.31	106.41
O3-S1-O4 [°]	102.21	101.3 ± 1.0	103.29	101.80	103.60	102.09	103.63	102.05
O2-S1-O5 [°]	124.02	123.3 ± 1.0	122.51	124.56	122.51	124.63	121.70	124.04
H_2SO_4, trans								
O3-H1 [Å]	0.964	0.97 ± 0.01	0.981	0.978	0.982	0.979	0.974	0.970
S1-O3 [Å]	1.576	1.574 ± 0.01	1.603	1.622	1.605	1.624	1.587	1.606
S1-O2 [Å]	1.411	1.422 ± 0.01	1.444	1.439	1.445	1.440	1.434	1.427
S1-O3-H1 [°]	108.51	108.5 ± 1.5	109.14	107.17	109.05	107.10	110.52	108.56
O3-S1-O5 [°]	-	108.6 ± 0.5	110.56	109.07	110.48	108.94	110.35	108.88
O3-S1-O2 [°]	105.74	106.4 ± 0.5	104.49	104.92	104.47	104.95	104.83	105.36
O3-S1-O4 [°]	102.21	101.3 ± 1.0	103.40	102.07	103.54	102.261	103.91	102.37
O2-S1-O5 [°]	124.02	123.3 ± 1.0	121.95	124.65	122.02	124.69	121.34	124.01

Table S2 – Literature and modelled vibrational frequencies for trans-H_2SO_4 (cis-conformer is in brackets)

Mode	Literature (modelled) [25]	Literature (experimental) [44]	PW91 (DNP+)		PBE (DNP+)		B3LYP (DNP+)	
			COSMO	Without COSMO	COSMO	Without COSMO	COSMO	Without COSMO
1 (OH sym stretch)	3610.0	3610	3624.8 (3653.7)	3670.1 (3678.4)	3610.7 (3621.2)	3661.2 (3669.7)	3725.5 (3722.2)	3765.2 (3780.6)
2 (OH asym stretch)	3605.2	-	3613.9 (3615.5)	3662.6 (3670.9)	3599.9 (3611.3)	3653.2 (3663.0)	3703.7 (3712.1)	3761.1 (3774.0)
3 ($S=O_2$ asym stretch)	1462.1	1450	1350.6 (1377.9)	1412.8 (1416.2)	1348.2 (1352.7)	1411.5 (1414.2)	1369.9 (1379.4)	1446.5 (1447.8)
4 ($S=O_2$ sym stretch)	1211.5	1223	1192.0 (1268.4)	1159.6 (1170.8)	1186.7 (1158.8)	1156.4 (1163.2)	1215.1 (1211.9)	1195.1 (1209.9)
5 (SOH asym bend)	1161.2	1159	1161.8 (1154.0)	1150.2 (1136.7)	1172.0 (1131.6)	1148.4 (1124.1)	1186.0 (1183.2)	1181.3 (1171.9)
6 (SOH sym bend)	1142.5	1138	1125.5 (1143.6)	1134.7 (1125.6)	1124.0 (1129.4)	1134.4 (1111.6)	1146.4 (1158.0)	1165.1 (1166.8)
7 ($S(OH)_2$ asym bend)	850.1	883	803.9 (810.5)	805.6 (809.3)	798.7 (797.7)	802.5 (805.2)	838.3 (832.3)	844.6 (842.3)
8 ($S(OH)_2$ sym stretch)	796.4	834	765.0 (765.9)	750.7 (750.5)	760.2 (759.7)	747.8 (746.7)	799.9 (799.3)	790.7 (792.8)
9 (O-S=O rock)	536.9	568	518.9 (574.2)	516.1 (517.1)	517.6 (520.7)	515.2 (517.2)	546.0 (534.9)	542.6 (535.7)
10 ($S=O_2$ bend)	535.6	550	500.9 (512.0)	505.2 (504.9))	499.9 (506.4)	503.2 (502.2)	519.4 (524.5)	529.9 (528.4)
11 ($S=O_2$ wagging)	483.8	-	473.5 (506.5)	465.6 (468.0)	476.8 (489.2)	463.4 (463.0)	494.1 (505.5)	482.8 (498.5)
12 (O-S=O bend)	404.5	-	468.5 (427.3)	423.2 (401.6)	465.0 (436.9)	422.9 (398.2)	449.3 (418.9)	429.5 (419.8)
13 (O-S=O twist)	353.6	-	385.4 (375.3)	356.4 (343.2)	414.2 (383.0)	351.7 (342.7)	397.3 (384.2)	367.1 (361.4)

14 (OH asym torsion)	290.9	-	372.6 (345.0)	343.0 (334.3)	374.3 (345.8)	344.3 (328.5)	393.5 (335.5)	338.1 (340.3)
15 (OH sym torsion)	232.7	-	289.6 (229.6)	249.9 (90.9)	288.2 (221.5)	258.3 (70.3)	309.1 (200.7)	239.1 (63.7)

* Modelled vibrational frequencies indicate the harmonic vibrational frequency without a scaling factor.

Table S3 – Calculated and literature values of bond lengths and angles of HSO_4^-

Bond/Angle	Literature (modelled) [9]	PW91(DNP+)		PBE(DNP+)		B3LYP (DNP+)	
		COSMO	Without COSMO	COSMO	Without COSMO	COSMO	Without COSMO
O3-H1 [Å]	0.97	0.977	0.973	0.978	0.974	0.970	0.965
O3-S1 [Å]	1.68	1.666	1.714	1.668	1.716	1.647	1.691
S1-O2 [Å]	1.46	1.471	1.467	1.473	1.469	1.461	1.456
S1-O4 [Å]	1.46	1.476	1.476	1.478	1.478	1.464	1.464
S1-O5 [Å]	1.46	1.476	1.476	1.477	1.478	1.465	1.464
H1-O3-S1 [°]	103.4	106.93	102.85	106.92	102.79	108.47	104.71
O3-S1-O5 [°]	103.7	105.65	104.10	105.70	104.07	105.80	104.20
O3-S1-O2 [°]	101.3	101.01	101.06	101.01	101.06	101.14	101.10
O2-S1-O4 [°]	115.8	114.56	115.58	114.52	115.53	114.40	115.48
O4-S1-O5 [°]	113.9	113.56	113.96	113.56	113.96	113.57	113.98
O2-S1-O5 [°]	115.2	114.63	115.62	114.60	115.63	114.41	115.45
O3-S1-O4 [°]	103.7	105.70	104.03	105.74	104.11	105.89	104.25

Table S4 – Literature and modelled vibrational frequencies for HSO_4^-

Mode	Literature (modelled) [9]	Literature (experimental) [45]	PW91(DNP+)		PBE(DNP+)		B3LYP(DNP+)	
			COSMO	Without COSMO	COSMO	Without COSMO	COSMO	Without COSMO
1	3702		3686.5	3712.5	3656.2	3702.5	3756.3	3812.7
2	1254	1341	1232.9	1250.0	1206.5	1248.9	1234.1	1284.5
3	1203	1237	1190.9	1191.4	1154.9	1189.1	1187.1	1224.7
4	1095	1053-1036	1122.8	1110.9	1119.3	1109.6	1147.1	1163.5
5	1004	895	1007.6	989.6	989.6	988.4	1023.5	1024.0
6	662	595	693.1	654.6	674.2	652.1	710.9	687.2
7	524		531.8	533.0	529.8	531.5	554.9	556.5
8	523		528.5	521.3	526.0	519.9	550.4	549.2
9	511	417	515.2	506.8	513.8	504.7	542.3	535.0
10	393		385.9	389.2	388.3	387.6	404.8	408.3
11	367		379.1	365.9	378.8	387.6	396.3	386.0
12	69		66.8	-	187.6	365.4	188.0	103.5

Table S5 – Calculated and literature* values of bond lengths and angles of SO_4^{2-}

Bond/Angle	Literature [10]	PW91(DNP+)		PBE(DNP+)		B3LYP(DNP+)	
		COSMO	Without COSMO	COSMO	Without COSMO	COSMO	Without COSMO
S1-O3 [Å]	1.581	1.511	1.522	1.512	1.523	1.499	1.510
S1-O2 [Å]	1.581	1.511	1.523	1.512	1.523	1.500	1.510
O3-S1-O5 [°]	109.4	109.41	109.47	109.47	109.47	109.45	109.46
O3-S1-O4 [°]	109.4	109.48	109.49	109.49	109.47	109.71	109.61
O2-S1-O5 [°]	109.4	109.45	109.44	109.45	109.46	109.30	109.39

Table S6 – Literature and modelled vibrational frequencies (cm^{-1}) for SO_4^{2-}

Mode	Literature (modelled) [10]	Literature (experimental) [46]	PW91 (DNP+)		PBE (DNP+)		B3LYP (DNP+)	
			COSMO	Without COSMO	COSMO	Without COSMO	COSMO	Without COSMO
1	1106.0 ± 2.0	1105	1056.7	1005.7	1010.8	1004.1	1030.2	1033.9
2			1053.3	1005.1	1007.1	1002.9	1028.2	1033.2
3			1050.3	1004.8	1004.9	1002.4	1024.8	1029.5
4	981.4 ± 0.2	983	908.2	863.9	894.0	862.8	927.3	896.7
5			567.9	562.1	559.0	560.2	581.0	589.8
6			562.5	560.1	556.2	558.3	571.4	586.5
7	617.0 ± 2.0		560.5	559.2	552.7	56.5	565.1	583.1
8			413.9	402.1	408.4	400.5	416.5	420.9
9	451.0 ± 2 .0		412.1	399.0	406.0	397.2	415.0	416.5

CHAPTER 5

Chapter 5 consists of the article titled ‘Molecular modelling of tantalum fluoride in a sulphuric acid medium – A DFT study’, which is added into this thesis in the exact format in which it was submitted for review in the *Journal of Computational and Theoretical Chemistry (2017)*.

5.1 Introduction

Tantalum (Ta) and niobium (Nb) are two metals found in the same group (VB) of the periodic table of elements, with similar chemical and physical properties, which is the reason why they are difficult to separate. They are usually found together in various minerals of which the most important are columbite ((Fe, Mn, Mg)(Nb, Ta)$_2O_6$) and tantalite ((Fe, Mn)(Nb, Ta)$_2O_6$) [1]. One possible way to separate these metals is by means of solvent extraction (SX) unit operations [2-8] in hydrometallurgy. Ungerer et al. [9] studied the separation of Ta and Nb (in the form of MF_5) using SX and observed partial separation from a sulphuric acid (H_2SO_4) environment with the extractants diiso-octyl phosphinic acid (DioPA) and di-(2-ethylhexyl) phosphoric acid (D2EHPA).

However, it was not possible in that study to fully explain the separation data obtained in view of the lack of available data on the speciation of Ta and Nb compounds, which in turn is due to the difficulties in determining the speciation data experimentally. An alternative method for predicting the speciation could be molecular modelling, which entails the step-by-step analysis of the extraction process on a molecular level. Molecular modelling could in turn prove information on the possible reactions occurring during SX from a thermodynamic point, which might lead to the development of a new method for the system analysis of the SX process of Ta and Nb. To determine the speciation of for example Ta or Nb in an acidic aqueous environment, the molecular structure of the metal salt in the presence of an acid (in this case H_2SO_4) has to be determined.

In previous modelling [10, 11] it was shown that H_2SO_4 dissociates in H_2O to form either HSO_4^- or SO_4^{2-} (in concentrated solutions) and H_3O^+. The water dissociated ions of H_2SO_4, namely HSO_4^- and SO_4^{2-}, are surrounded by concentric shells of H_2O molecules, where each successive shell is more weakly bonded until a bulk water structure is reached [12]. It was shown by Cannon et al. [13] from diffraction and early modelling data that the first hydration shell of the sulphate ion, depending on the temperature, contains 6 to 14 H_2O molecules [14]. In Chapter 4, it was shown that when H_2SO_4 reacts with water, various species could form including $H_2SO_4.H_2O$, $HSO_4^-.H_2O$ and $H_2SO_4.2H_2O$. However, when increasing the amount of surrounding H_2O molecules, the species reacted further to mainly form HSO_4^-, H_3O^+ and H_2O.

Similarly, the hydration of divalent transition metal cations, including Mg^{2+} [14], Fe^{2+} [15], Zn^{2+} [16] and Cu^{2+} [17] were investigated and found to be strongly hydrated with six H_2O molecules in a dilute aqueous environment. During the hydration of for example V_2O_5, it was found that the V^{4+}-V^{5+} ion pair was mainly present with a hydration sphere consisting of 4 to 6 H_2O molecules [18]. Hydrated Ta^{5+} and Nb^{5+} were found to have a poly-nuclear metal cluster having a $M_6X_{14}.8H_2O$ (where M = Ta/Nb, X = Br/Cl) structure [19] in the presence of alkali halide salts at temperatures exceeding 650°C in the absence of other hydrated species. Ischenko et al. [20] showed that Ta^{5+} and Nb^{5+} exist as oligomeric penta-fluorides in the solid state, while a mono-nuclear metal cluster of Ta(Nb)F_5

formed only in the gas phase. In light of the complexity of these structures, it was assumed that $Ta(Nb)F_5$ will have a trigonal bipyramidal symmetry structure as was also shown by Agulyansky [21].

In this study, molecular modelling was used to determine the behaviour of Ta in an aqueous H_2SO_4 environment. Various interactions between TaF_5 and H_2O, TaF_5 and H_2SO_4, and H_2SO_4 and H_2O were investigated. Since it was shown in a previous paper [22] that only $TaF_5.H_2O$ and TaF_4OH formed when contacting TaF_5 and H_2O, the reactions of these three species (TaF_5, $TaF_5.H_2O$ and TaF_4OH) with H_2SO_4 and water were investigated, yielding 22 possible reactions (Figure 5.1).

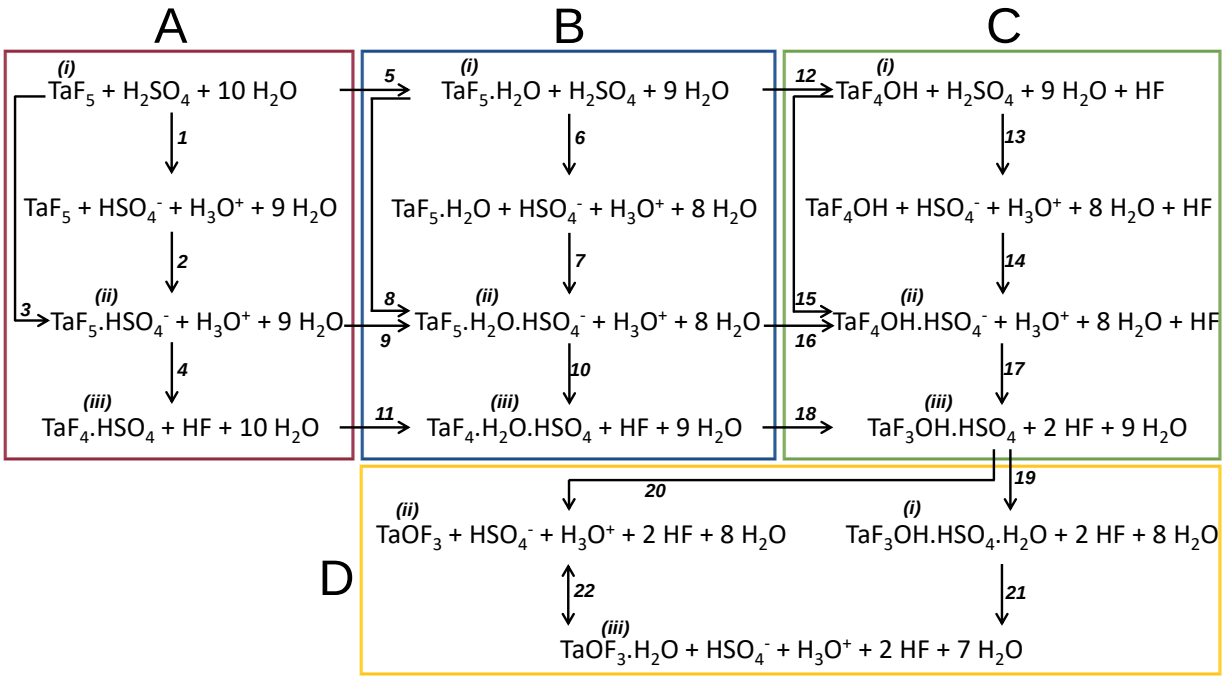

Figure 5.1 – Scheme showing reactions between H_2SO_4, H_2O and TaF_5 (A), $TaF_5.H_2O$ (B) or TaF_4OH (C) and the reactions when $TaF_3OH.HSO_4$ reacts further (D)

For the purpose of this discussion, the reactions of the three Ta species (TaF_5, $TaF_5.H_2O$, TaF_4OH) were presented in Block A (TaF_5), B ($TaF_5.H_2O$) and C (TaF_4OH), respectively, while block D shows secondary reactions of the product of block C ($TaF_3OH.HSO_4$) forming either $TaF_3OH.HSO_4$ (D_i), or two oxyfluoride spesies, i.e. $TaOF_3$ (D_{ii}) and $TaOF_3.H_2O$ (D_{iii}). While the reactions across the four blocks were labelled 1 – 22, the Ta species that could possible form in the various blocks were labelled i – iii. Accordingly, block A shows three different species (A_i – A_{iii}) and four reactions (1 – 4). Similarly block B and C each have three species, (B_i – B_{iii} and C_i – C_{iii}, respectively) and four reactions (reactions 6 – 8, 10 and 13 – 15, 17, respectively). However, reactions could also occur across block A and B (reactions 5, 9 and 11) and block B and C (reactions 12, 16 and 18). The remaining reactions (19 – 22) are found in Block D. When more than one configuration was possible for a specific species, these molecules were labelled a or b, yielding molecules such as A_{ii}a and A_{ii}b. While Section 5.3.1. will focus on the properties of the Ta species only, Section 5.3.2 will present a discussion on the

energy of the various systems. In these systems, the energy will, however, also be dependant on the Ta associated H_2SO_4, which can either be H_2SO_4 or HSO_4^- (see reactions 1, 6 and 13). When using a deprotonated HSO_4^-, the abbreviation (dep) will be used, for example in reaction 1 where both A_i to $A_{i(dep)}$ can form.

For this study, a 1:1:10 metal:acid:water ratio was used in accordance with the previous study by Ungerer et al. [22], where it was shown that a 1:10 acid:water ratio gave the lowest energies. The paper was divided into two sections, the first (Section 5.3.1) on the block specific geometry optimisations of the various species (A_i – D_{iii}) and the second (Section 5.3.2) on the specific energies of formations of all reactions (1 – 22) presented in Figure 5.1.

5.2 Computational Methods

For the molecular modelling of TaF_5 and H_2SO_4 with water, the density functional theory (DFT) type DMol^3 module of the Biovia Materials Studio 2016 software from Dassault Systèmes Biovia Corp. [23] was used. Firstly, a geometry optimisation [24, 25] was done for all the different molecules. In the case study presented by Ungerer et al. [22], the Perdew-Burke-Ernzerhof (PBE) [26] correlation gave the best results in terms of modelled reaction energy versus computational time for the Ta reactions. Accordingly, the generalised-gradient approximation (GGA) with the PBE [26] correlation, with the DNP+ (double numerical plus polarisation, with addition of diffuse functions) basis set, basis file 4.4 and Tkatchenko-Scheffler (TS) dispersion correction [27] was used. The core treatment parameter was set to ‘All Electron’, thus treating the electrons as if they were valence electrons. Furthermore, smearing of 0.005 Hartree (Ha) was chosen for all the calculations under the electronic properties [28], while the solvation model COSMO (conductor-like screening model) [29, 30] was chosen with water as the solvent having a dielectric constant of 78.54.

After the geometry optimisation, single point energy calculations were done with the same settings as for the geometry optimisation. The calculations were done at 0 K and the energy correction term was added to give the energy of formation (H_f) values at 298.15 K. The zero-point vibrational energy (ZPVE) was included in all calculations. Frequency calculations were used to confirm optimised structures (minimum energy without any imaginary frequency) and transition states (one imaginary frequency and maximum energy).

5.3 Results and Discussion

As mentioned previously, this section is divided into two parts, where the geometry optimisations of all the species involved in the reactions shown in Figure 5.1 are presented in Section 5.3.1

(Sections 5.3.1.1 – 5.3.1.4 for Block A – D), while the energies of formation of these reactions are discussed in Section 5.3.2.

5.3.1 Geometry optimisation of species in the TaF_5:H_2SO_4:H_2O system

For the purpose of this discussion, the different species and geometries that may occur from the reactions presented in Figure 5.1 will be discussed according to the various blocks (A - D), focussing only on the Ta^{5+} species since H_2SO_4, HSO_4^-, H_2O and H_3O^+ have been discussed in Chapter 4. The geometry of all the species are relative to the Ta^{5+} metal centre, unless otherwise stated.

5.3.1.1 Block A species

The first species in block A is TaF_5 (A_i), which has a trigonal bipyramidal structure [22]. From TaF_5, $TaF_5.HSO_4^-$ is formed by the association of the HSO_4^- and TaF_5 (reactions 2 and 3 in Figure 5.1), resulting in a change of the geometry to octahedral, with two possible configurations ($A_{ii}a$ and $A_{ii}b$) as shown in Figure 5.2. The two configurations were similar, differing only in the rotation around the Ta-O4 bond, forming a hydrogen bond between F3 and H1 in configuration $A_{ii}b$.

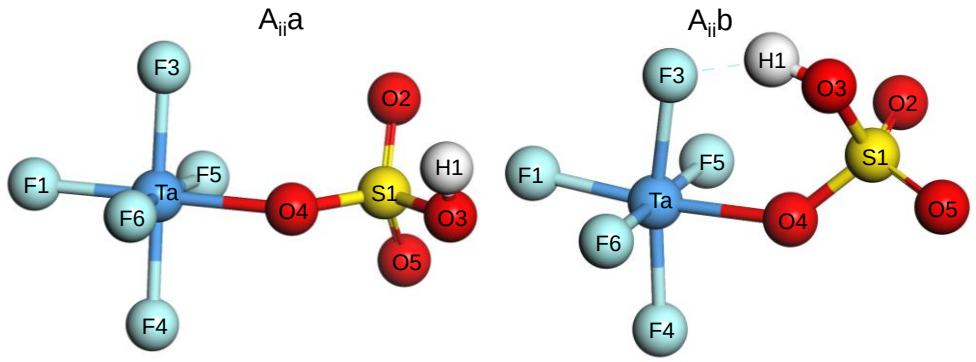

Figure 5.2 –$TaF_5.HSO_4^-$ species ($A_{ii}a$ and $A_{ii}b$)

Table 5.1 shows the bond lengths and angles of species $A_{ii}a$ and $A_{ii}b$. The bond lengths of $A_{ii}a$ and $A_{ii}b$ differed by less than 0.05 Å for all the bonds. From previous modelling [22] it was seen that the bond length between Ta^{5+} and an equatorially bound F^- anion is 1.89 Å, which correlates with both $A_{ii}a$ and $A_{ii}b$, which had an average equatorially Ta-F bond length of 1.93 Å. This slight elongation is due to the geometry change from trigonal bipyramidal to octahedral. The bond lengths between Ta^{5+} and the axially bound F^- anions for $A_{ii}a$ and $A_{ii}b$ were 1.954 and 1.994 Å respectively, while it was 1.93 Å for TaF_5 [22], confirming an increase in the axially bound F^- anion bond lengths. For the HSO_4^- part of $A_{ii}a$ and $A_{ii}b$, the bond lengths differed by less than 0.014 Å. Compared to previous modelling (Chapter 4), where the O4-S1 bond length was 1.478 Å, it was 1.546 and 1.554 Å for $A_{ii}a$ and $A_{ii}b$, respectively. This elongation can be ascribed to O4 being bound to Ta^{5+}, which might lead to some repulsion of HSO_4^- due to the high electronegativity and inductive effect of the bound O^{2-} atoms. The

main difference between $A_{ii}a$ and $A_{ii}b$ is the F3-H1 distances, which were 4.733 Å and 1.768 Å, respectively. The hydrogen bond (F3-H1) in $A_{ii}b$ not only did not contribute to molecule stabilisation as expected, but caused bond strain in Ta-O4-S1, which could lead to higher reaction energies.

Table 5.1 – Calculated bond lengths and angles of $TaF_5.HSO_4^-$ ($A_{ii}a$ and $A_{ii}b$)

Bond length (Å)			**Bond angle (°)**		
Bond	**$A_{ii}a$**	**$A_{ii}b$**	**Angle**	**$A_{ii}a$**	**$A_{ii}b$**
Ta-F1	1.934	1.929	F1-Ta-F5	92.57	89.78
Ta-F3	1.954	1.994	F1-Ta-F3	90.04	90.87
Ta-O4	2.101	2.093	F3-Ta-O4	89.72	83.47
O4-S1	1.546	1.554	Ta-O4-S1	136.89	137.14
S1-O3	1.615	1.606	O4-S1-O3	101.42	103.32
O3-H1	0.981	0.995	S1-O3-H1	108.68	107.80
S1-O2	1.455	1.455	O2-S1-O5	119.32	118.63
S1-O5	1.451	1.451	O3-S1-O2	109.03	109.63
F3-H1	4.733	1.768	O4-S1-O5	110.93	109.39

The bond angles of $A_{ii}a$ and $A_{ii}b$ were within 2° from each other, except for F1-Ta-F5 and F3-Ta-O4 in $A_{ii}b$ where they decreased by 2.79° and 6.25°, respectively, due to the distortion from the hydrogen bond (F3-H1). Although the geometry is octahedral, the bond angles of the equatorially bound atoms (F1, F5, F6 and O4) were not 90° due to these atoms having different atomic radii.

A neutral species can be obtained by removing an F^- from $TaF_5.HSO_4^-$, forming $TaF_4.HSO_4$ (A_{iii}) (reaction 4, Figure 5.1). By systematically removing the various F^- anions from $A_{ii}a$ and $A_{ii}b$, two possible configurations ($A_{iii}a$ and $A_{iii}b$) were obtained (Figure 5.3, of which the respective bond lengths and angles are presented in Table 5.2). On closer inspection, it was observed that configurations $A_{iii}a$ and $A_{iii}b$ are rotamers, obtained when rotating around the Ta-O4 bond (Figure 5.2). Similar to A_i, $A_{iii}a$ had a trigonal bipyramidal structure. Due to the low electron density on the Ta^{5+} and the high electron density on the O2, a bidentate bond between Ta^{5+} and HSO_4^- was formed resulting in the formation of $A_{iii}b$. It would be expected that the $A_{iii}b$ isomer would be lower in energy, but due to the distortion of the octahedral configuration, the energy was similar to the energy of $A_{iii}a$. For this reason, both configurations could be present during the formation reactions. The bond lengths (Table 2) deviated by less than 0.05 Å, except the Ta-O4 and S1-O2 bonds in configuration $A_{iii}a$, which were longer by 0.13 Å and 0.07 Å, respectively, due to the formation of the bidentate. In configuration $A_{ii}b$, F3 and F4 were in the axial position in terms of Ta^{5+}, while in the $A_{iii}a$ configuration F3 and F4 were equatorial, while F5 and O4 were axial. In both $A_{iii}a$ and $A_{iii}b$, the equatorially bound F^- anions had shorter bond lengths than the axially bound F^- anions, as was also seen with $A_{ii}a$ and $A_{ii}b$ from previous modelled data of TaF_5 [22]. The bond lengths of the HSO_4^- part of $A_{iii}a$ and $A_{iii}b$

were similar to $A_{ii}a$ and $A_{ii}b$, differing by less than 0.017 Å, except for O4-S1 and S1-O2. Again O4-S1 had an elongated bond length due to the bond to Ta^{5+}. The S1-O2 bond length in $A_{iii}b$ was elongated (0.066 Å longer than $A_{iii}a$) due to O2 being bound to Ta^{5+} forming the bidentate with HSO_4^-

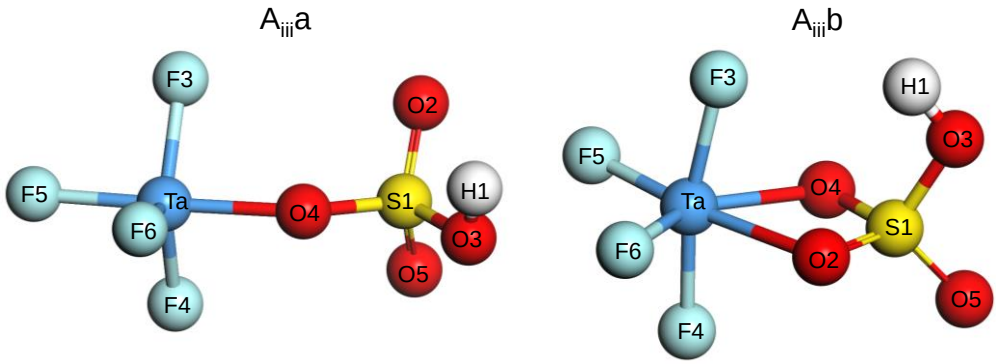

Figure 5.3 – $TaF_4.HSO_4$ species ($A_{iii}a$ and $A_{iii}b$)

The bond angles of configuration $A_{iii}a$ and $A_{iii}b$ deviated more from each other than the bond lengths due to the bidentate distortion. The F4-Ta-F6 angle of $A_{iii}a$ was 119.86°, which correlates with the equatorial bound F^- anion bond angle of 120° within a trigonal bipyramidal structure. The angle between the axial and equatorial bound F^- anion in $A_{iii}a$ deviated slightly from 90° (88.80°) due to the distortion caused by the bound HSO_4^-. This distortion can also be seen in the bond angle between Ta^{5+} and HSO_4^- at F6-Ta-O4 and F3-Ta-O4 being 91.57° and 88.49°. The distorted octahedral configuration of $A_{iii}b$ was also confirmed through the bond angles of the equatorially bound ions (F5, F6, O2 and O4) deviating slightly from 90°.

Table 5.2 – Calculated bond lengths and angles of $TaF_4.HSO_4$ ($A_{iii}a$ and $A_{iii}b$)

Bond length (Å)			Bond angle (°)		
Bond	**$A_{iii}a$**	**$A_{iii}b$**	**Angle**	**$A_{iii}a$**	**$A_{iii}b$**
Ta-F3	1.896	1.942	F4-Ta-F6	119.86	95.57
Ta-F4	1.895	1.927	F5-Ta-F3	88.80	91.06
Ta-F5	1.923	1.899	F6-Ta-O4	91.57	145.25
Ta-F6	1.888	1.891	F3-Ta-O4	88.49	83.54
Ta-O4	2.014	2.143	Ta-O4-S1	146.56	99.21
Ta-O2	-	2.265	O4-S1-O3	101.11	106.92
O4-S1	1.582	1.544	S1-O3-H1	109.63	111.00
S1-O3	1.597	1.580	O3-S1-O2	110.52	106.04
O3-H1	0.982	0.985	O2-S1-O5	121.05	118.14
S1-O2	1.448	1.514			
S1-O5	1.445	1.433			
F3-H1	4.960	2.593			

5.3.1.2 Block B species

When TaF_5 reacts with H_2O (reaction 5, Figure 5.1), $TaF_5.H_2O$ (B_i) can form where the H atoms of the H_2O are either in the axial or the equatorial position [22]. The $TaF_5.H_2O$ (B_i) can then react with HSO_4^- (reactions 7 and 8 in Figure 5.1) to form $TaF_5.H_2O.HSO_4^-$ in two corresponding configurations $B_{ii}a$ and $B_{ii}b$ shown in Figure 5.4. $B_i a$ leads to the formation of configuration $B_{ii}a$ and similarly, $B_i b$ leads to the formation of configuration $B_{ii}b$. The bond lengths and angles of $TaF_5.H_2O.HSO_4^-$ are presented in Table 5.3.

With the addition of the HSO_4^- group (as was the case for A_{ii} in Figure 5.2) or H_2O [22] to TaF_5, the geometry changed from a trigonal bipyramidal to an octahedral geometry. However, when both H_2O and HSO_4^- are bound to the Ta^{5+} center, the geometry changed yet again to a pentagonal bipyramidal geometry. In configuration $B_{ii}a$, F5 and F6 are in the axial orientation, while F1, F4, O1, F3 and O4 form the pentagonal equatorial plane. In addition, the H_2O was not covalently bound to Ta^{5+}, but rather stabilised in its position by hydrogen bonds to both F3 and F5. In contrast, for configuration $B_{ii}b$, F3 and F4 were in the axial positions and F1, O4, F6, O1 and F5 in the equatorial position, which again yields a pentagonal bipyramidal geometry. It seems that $B_{ii}a$ could be a transition product between $A_{ii}a$ and $B_{ii}b$.

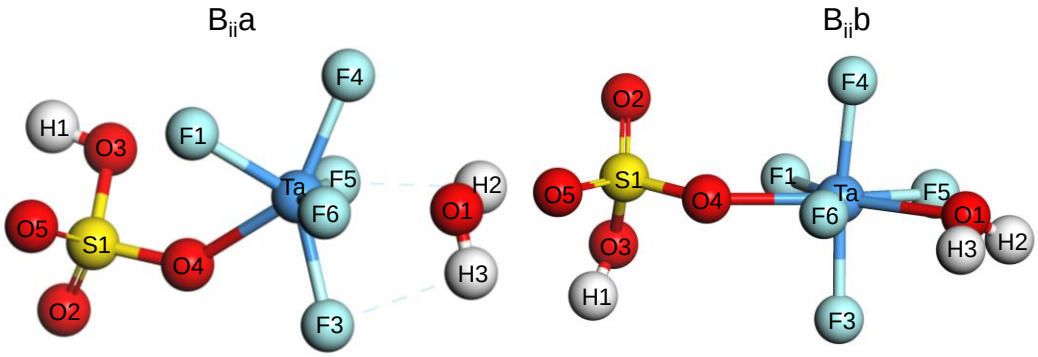

Figure 5.4 – $TaF_5.H_2O.HSO_4^-$ species ($B_{ii}a$ and $B_{ii}b$)

Similar to the TaF_5 species [22], the equatorially bound atoms in both $B_{ii}a$ and $B_{ii}b$ have shorter bond lengths than the axially bound atoms (see Table 5.3). In both configurations ($B_{ii}a$ and $B_{ii}b$), the average Ta-F bond length was 1.970 ± 0.025 Å. While the average Ta-O (bound to O4 from HSO_4^-) bond lengths were 2.079 ± 0.07 Å in configurations $A_{iii}a$ and $A_{iii}b$, they were 2.204 ± 0.01 Å for $B_{ii}a$ and $B_{ii}b$. This elongation will prevent orbital overlap of the seven atoms bound to Ta^{5+}. The Ta-O distance in $B_{ii}a$ and bond length in $B_{ii}b$ (bound to O1 from H_2O) was on average 2.362 ± 0.023 Å. The average bond lengths in the HSO_4^- bound group deviated by less than 0.06 Å in both $B_{ii}a$ and $B_{ii}b$ configurations.

Table 5.3 – Calculated bond lengths and angles of $TaF_5.H_2O.HSO_4^-$ ($B_{ii}a$ and $B_{ii}b$)

Bond length (Å)			Bond angle (°)		
Bond	**$B_{ii}a$**	**$B_{ii}b$**	**Angle**	**$B_{ii}a$**	**$B_{ii}b$**
Ta-F1	1.945	1.957	F4-Ta-F6	88.65	87.44
Ta-F3	1.975	1.959	F5-Ta-F3	92.04	88.99
Ta-F4	1.967	1.955	F5-Ta-F1	118.46	77.97
Ta-F5]	1.964	1.979	F6-Ta-O4	123.77	70.20
Ta-F6	1.961	1.990	F3-Ta-O4	73.30	90.79
Ta-O4	2.205	2.203	Ta-O4-S1	137.87	138.98
O4-S1	1.521	1.528	O4-S1-O3	99.94	105.51
S1-O3	1.634	1.626	S1-O3-H1	107.64	107.88
O3-H1	0.980	0.978	O3-S1-O2	108.09	104.11
S1-O2	1.463	1.455	O2-S1-O5	116.19	117.78
S1-O5	1.460	1.462	F6-Ta-O1	79.37	68.00
Ta-O1	2.385	2.339	H3-O1-H2	104.62	107.53

The bond angles of the equatorially bound atoms in a perfect pentagonal bipyramidal structure are 72°. However, the $B_{ii}a$ configuration had a distorted pentagonal bipyramidal structure resulting in strained bond angles (see Figure 5.4). Configuration $B_{ii}b$ had less distortion, where the slight deviations in bond angles could be ascribed to the difference in the radius of the equatorial atoms bound to the Ta^{5+} center. The structure distortion in configuration $B_{ii}a$ could lead to higher reaction energies, whereas $B_{ii}b$ could be the more stable species.

To form the neutral $TaF_4.H_2O.HSO_4$ (B_{iii}) species, an F^- can be removed from $TaF_5.H_2O.HSO_4^-$ (B_{ii}) (reaction 10, Figure 5.1). By removing different F^- anions, three possible configurations of $TaF_4.H_2O.HSO_4$ were obtained (Figure 5.5). When removing an F^- anion from $B_{ii}a$, both $B_{iii}a$ and $B_{iii}b$ could form, while $B_{iii}b$ and $B_{iii}c$ can both form from $B_{ii}b$. $B_{iii}a$ and $B_{iii}c$ are similar in that the H_2O and HSO_4^- groups are oriented on either side of the Ta^{5+} centre, leading to a trans configuration. They differ due to the rotations around the Ta-O4 and Ta-O1 bonds. In configuration $B_{iii}b$, the H_2O and HSO_4^- groups are at a right angle from each other, leading to a cis configuration. All three configurations have a distorted octahedral geometry. The bond lengths and angles of $TaF_4.H_2O.HSO_4$ ($B_{iii}a$, $B_{iii}b$ and $B_{iii}c$) are shown in Table 5.4.

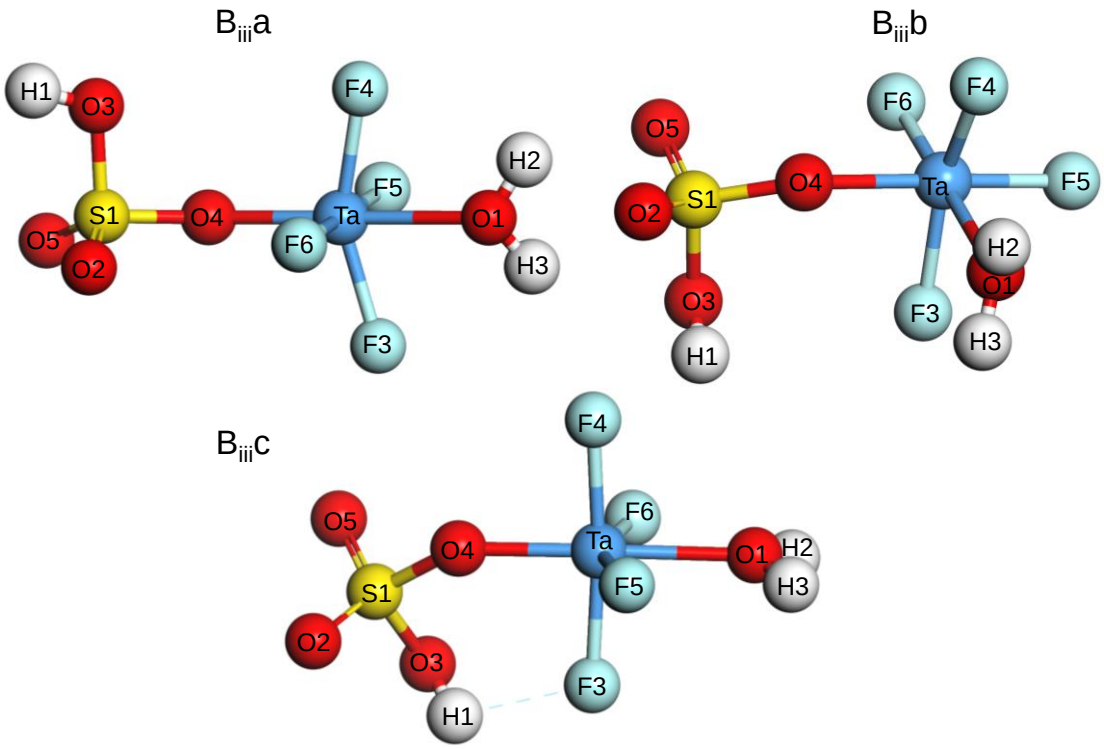

Figure 5.5 – $TaF_4.H_2O.HSO_4$ species ($B_{iii}a$, $B_{iii}b$ and $B_{iii}c$)

The bond lengths of the corresponding atoms on all three configurations differed by less than 0.03 Å. By rotating the O4-Ta bond in $B_{iii}a$, configuration $B_{iii}c$ was formed, where the hydrogen bond between H1 (of HSO_4^-) and F3 leads to the elongation of the Ta-F3 bond length by 0.027 Å. In $B_{iii}a$, the bound O^{2-} ions were in the axial position and the F^- anions in an equatorial plane, which should therefore yield similar Ta-F bond lengths. However, due to the distortion of F4 and F3 toward H2 and H3, respectively, the average Ta-F bond length was 0.01 Å shorter than for F5 and F6. $B_{iii}c$ had a similar geometry than $B_{iii}a$, with O1 and O4 axially bound and F3 – F6 equatorially bound. F5 and F6 were distorted toward H3 and H2, respectively, with F3 having a hydrogen bond with H1 resulting in similar bond lengths for F3 – F5. In the case of $B_{iii}b$, the F^- anions had similar Ta-F bond lengths except for F3 showing elongation due to a hydrogen bond between F3 and H3.

In all three configurations, the bond angles differed from each other and from a perfect octahedral structure due to the distortion of the F^- anions caused by the abundance of O atoms. In $B_{iii}a$ and $B_{iii}b$, the angle deviation of the bound F^- anions (F3 and F4) were towards the bound H_2O, possibly due to hydrogen bonding. Similarly the bound F^- anions in $B_{iii}c$ (F5, F6 and F3) were distorted towards the bound H^+ cations (H3, H2 and H1 respectively).

Table 5.4 – Calculated bond lengths and angles of $TaF_4.H_2O.HSO_4$ ($B_{iii}a$, $B_{iii}b$ and $B_{iii}c$)

Bond length (Å)				Bond angle (°)			
Length	**$B_{iii}a$**	**$B_{iii}b$**	**$B_{iii}c$**	**Angle**	**$B_{iii}a$**	**$B_{iii}b$**	**$B_{iii}c$**
Ta-F3	1.929	1.929	1.956	F4-Ta-F6	89.62	103.18	92.79
Ta-F4	1.930	1.924	1.935	F5-Ta-F3	89.76	89.70	88.93
Ta-F5	1.943	1.926	1.929	F5-Ta-F6	179.74	90.04	153.72
Ta-F6	1.940	1.911	1.928	F6-Ta-O4	90.20	88.65	99.67
Ta-O4	1.992	2.046	1.997	F3-Ta-O4	102.94	88.72	87.04
O4-S1	1.582	1.565	1.590	Ta-O4-S1	145.92	146.06	141.46
S1-O3	1.606	1.607	1.601	O4-S1-O3	96.10	103.14	103.04
O3-H1	0.983	0.982	0.983	S1-O3-H1	108.60	109.14	109.46
S1-O2	1.448	1.450	1.446	O3-S1-O2	110.31	109.86	110.91
Ta-O1	2.235	2.250	2.210	O2-S1-O5	119.45	120.56	121.25
O1-H2	0.976	0.975	0.975	F6-Ta-O1	89.28	179.99	76.07
F3-H1	-	-	2.241	H3-O1-H2	107.56	107.61	108.25

5.3.1.3 Block C species

$TaF_5.H_2O$ (B_i) can react further to form TaF_4OH (C_i) (reaction 12, Figure 5.1) before reacting with HSO_4^- to form $TaF_4OH.HSO_4^-$ (C_{ii}) (via reactions 14 and 15 in Figure 5.1). The OH^- group of TaF_4OH can be either in the axial (trigonal bipyramidal geometry (C_ib)) or equatorial position (trigonal bipyramidal geometry (C_ic)) with a transition product which had a square pyramidal structure (C_ia) [22]. Subsequently, the formation of $TaF_4OH.HSO_4^-$ also yielded three configurations ($C_{ii}a$, $C_{ii}b$ and $C_{ii}c$) as shown in Figure 5.6.

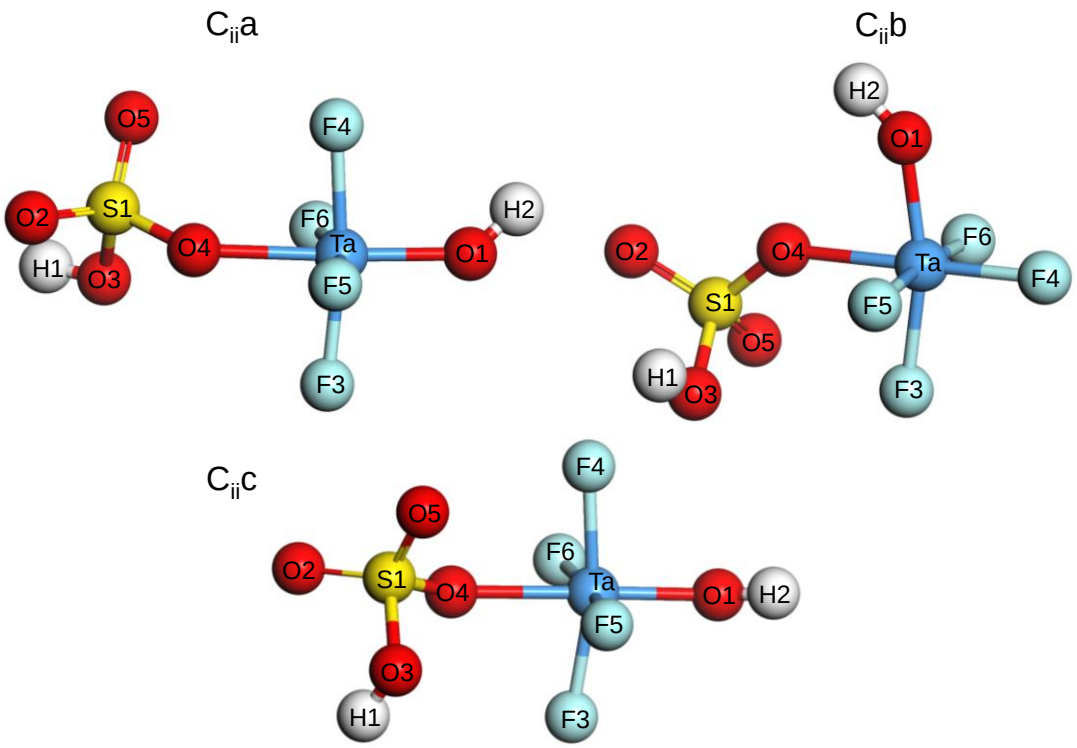

Figure 5.6 – $TaF_4OH.HSO_4^-$ species ($C_{ii}a$, $C_{ii}b$ and $C_{ii}c$)

When reacting with HSO_4^-, TaF_4OH (C_ia, C_ib and C_ic) formed configuration $C_{ii}a$, $C_{ii}b$ and $C_{ii}c$, respectively. All three of these had distorted octahedral configurations. The HSO_4^- and OH^- groups were bound to opposite sides (axially) of the Ta^{5+} centre, leading to the trans configuration in $C_{ii}a$ and $C_{ii}c$. Due to the rotation of Ta-O1 and S1-O3, these two bound groups were at a near right angle from each other (OH was axial, HSO_4^- equatorial) leading to a cis configuration in $C_{ii}b$. The bond lengths and angles of $TaF_4OH.HSO_4^-$ ($C_{ii}a$, $C_{ii}b$ and $C_{ii}c$) are shown in Table 5.5.

The Ta-F bond length of all three configurations were 1.964 ± 0.004 Å, except for Ta-F4 of configuration $C_{ii}b$, which decreased to 1.891 Å, correlating with the expected Ta-F bond length of 1.894 Å [22]. The Ta-O4 bond length was 2.18 ± 0.013 Å and the Ta-O1 bond length was 1.923 ± 0.009 Å. This elongation in Ta-O4 is probably due to the electronegativity of the other O atoms in HSO_4^-. The bond angles of all three geometries correlated with each other (2.5 ± 0.56°), except for O4-S1-O3 of $C_{ii}a$, which decreased by 5.37 ± 0.28° from $C_{ii}b$ and $C_{ii}c$, due to the O4-S1-O3 bond angle which is dependent on the bond angle between Ta^{5+} and HSO_4^-. The different atoms (F3 – F6, O1 and O4) bound to Ta^{5+}, due to their attraction or repulsion depending on the differing positions of these atoms, caused the structure deviation from a perfect octahedron.

Table 5.5 – Calculated bond lengths and angles of $TaF_4OH.HSO_4^-$ ($C_{ii}a$, $C_{ii}b$ and $C_{ii}c$)

Bond length (Å)				Bond angle (°)			
Length	**$C_{ii}a$**	**$C_{ii}b$**	**$C_{ii}c$**	**Angle**	**$C_{ii}a$**	**$C_{ii}b$**	**$C_{ii}c$**
Ta-F3	1.961	1.965	1.963	F4-Ta-F6	90.37	90.50	88.52
Ta-F4	1.962	1.891	1.965	F5-Ta-F3	88.39	86.81	91.37
Ta-F5	1.963	1.969	1.968	F5-Ta-F6	166.52	172.77	171.34
Ta-F6	1.959	1.969	1.962	F6-Ta-O4	86.69	89.86	86.10
Ta-O4	2.193	2.167	2.178	F3-Ta-O4	86.97	83.66	83.88
O4-S1	1.518	1.532	1.528	Ta-O4-S1	138.52	138.25	138.85
S1-O3	1.633	1.625	1.628	O4-S1-O3	99.17	104.81	104.26
O3-H1	0.980	0.980	0.980	S1-O3-H1	107.57	108.50	107.97
S1-O2	1.462	1.461	1.461	O3-S1-O2	107.80	108.17	108.09
Ta-O1	1.914	1.931	1.914	O2-S1-O5	116.58	118.15	118.29
O1-H2	0.973	0.972	0.973	F6-Ta-O1	95.39	93.64	96.22
				Ta-O1-H2	136.92	139.91	139.98

To form the neutral species $TaF_3OH.HSO_4$ (C_{iii}), a F^- anion was removed from $TaF_4OH.HSO_4^-$ (C_{ii}) (via reaction 17 Figure 5.1). It was found that by removing different positional F^- anions from $C_{ii}b$, configuration $C_{iii}a$ and $C_{iii}b$ were obtained, while $C_{iii}c$ was obtained when removing a F^- ion from either $C_{ii}a$ or $C_{ii}b$ (Figure 5.7). Similar to C_i, the geometry of configuration $C_{iii}a$ was square pyramidal, while configurations $C_{iii}b$ and $C_{iii}c$ had a trigonal bipyramidal geometry. The main difference between the configurations is that for $C_{iii}b$ the OH^- group is in the axial and HSO_4^- in the equatorial position, while in $C_{iii}c$ both the OH and HSO_4^- groups are in axial positions where $C_{iii}a$ is a transition product between $C_{iii}b$ and $C_{iii}c$. The bond lengths and angles of $TaF_4.H_2O.HSO_4$ ($C_{iii}a$, $C_{iii}b$ and $C_{iii}c$) are shown in Table 5.6.

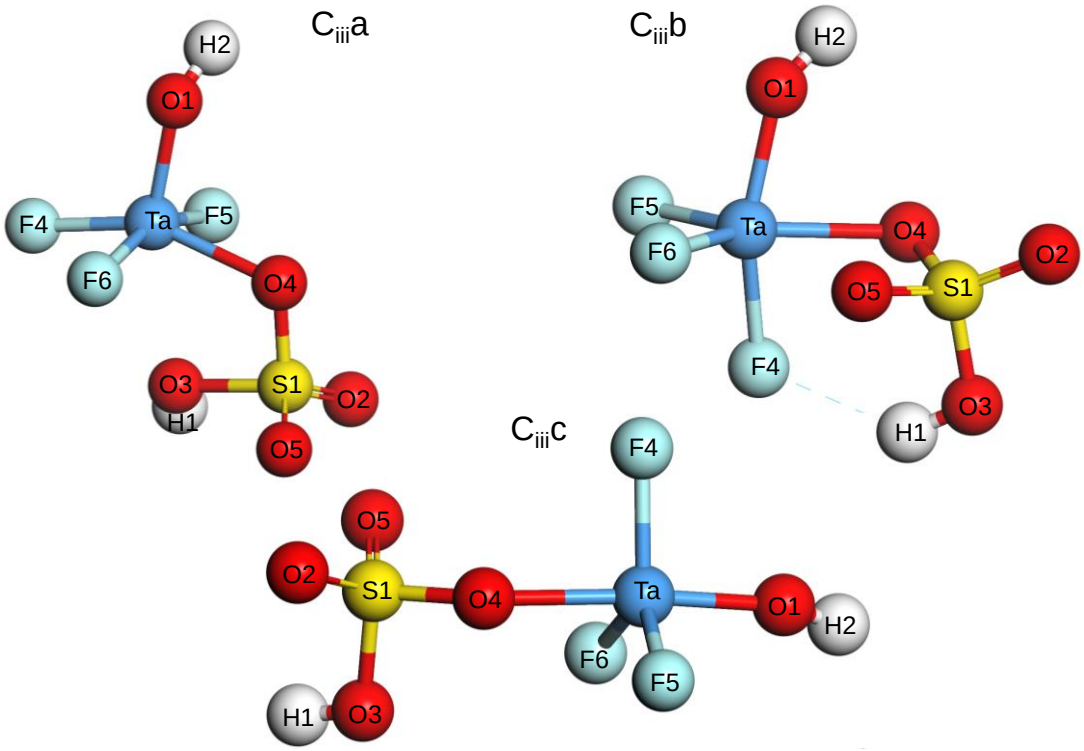

Figure 5.7 – $TaF_3OH.HSO_4$ species (C_{iii}a, C_{iii}b and C_{iii}c)

In C_{iii}a, both F5 and F6 neighbour O1 and O4, which lead to bond elongation in F5 and F6 compared to F4. In C_{iii}b, F4 was axially bound and F5 and F6 equatorially bound. Due to the hydrogen bond between F4 and H1, the Ta-F4 bond length increased when compared to the bond with F5 and F6. In C_{iii}c, O1 and O4 were axially bound while the three F^- anions were equatorially bound resulting in similar Ta-F bond lengths for F4 – F6.

The bond angles of all three configurations differed due to the differences in geometry and the bond positions of H_2O and HSO_4^-. In C_{iii}a (square pyramidal geometry), the F-Ta-F bond angles deviated slightly from the ideal 90° due to the Ta-O bonds in neighbouring positions. In C_{iii}b, the F5-Ta-F6 angle differed by 2.31° from the ideal trigonal bipyramidal structure (120°) due to the Ta-O4 bond. Similarly, the F5-Ta-F4 bond angle would be 90° in an ideal trigonal bipyramidal structure, where in C_{iii}b it deviated to 85.93° due to the hydrogen bond between F4 and H1 (on HSO_4^-). In C_{iii}c, the bond angle between the equatorially bound atoms (F4 – F6) deviated with less than 2.9° from the ideal 120°. This deviation could be ascribed to the electronegative groups (OH^- and HSO_4^-) in the axial positions.

Table 5.6 – Calculated bond lengths and angles of $TaF_4OH.HSO_4^-$ ($C_{iii}a$, $C_{iii}b$ and $C_{iii}c$)

Bond length (Å)				Bond angle (°)			
Length	**$C_{iii}a$**	**$C_{iii}b$**	**$C_{iii}c$**	**Angle**	**$C_{iii}a$**	**$C_{iii}b$**	**$C_{iii}c$**
Ta-F4	1.921	1.967	1.901	F4-Ta-F6	89.29	101.90	119.17
Ta-F5	1.938	1.916	1.900	F5-Ta-F4	88.34	85.93	117.09
Ta-F6	1.933	1.900	1.908	F5-Ta-F6	158.06	99.48	122.31
Ta-O4	2.120	2.207	2.090	F6-Ta-O4	86.38	142.09	83.20
O4-S1	1.548	1.529	1.544	F4-Ta-O4	153.52	78.05	88.59
S1-O3	1.700	1.590	1.602	Ta-O4-S1	109.87	98.00	142.67
O3-H1	0.982	0.989	0.984	O4-S1-O3	94.07	106.94	98.43
S1-O2	1.445	1.436	1.456	S1-O3-H1	109.08	108.35	107.52
Ta-O1	1.878	1.900	1.884	O3-S1-O2	107.14	106.07	109.33
O1-H2	0.978	0.975	0.975	O2-S1-O5	120.18	117.49	118.19
				F6-Ta-O1	101.22	100.49	90.75
				Ta-O1-H2	134.79	140.24	153.53

5.3.1.4 Block D species

In the presence of H_2O, configuration C_{iii} reacted in two ways, forming either $TaF_3OH.HSO_4.H_2O$ (configuration D_i – reaction 19, Figure 5.1) as is shown in Figure 5.8, or $TaOF_3$ (D_{ii}) (reaction 20, Figure 5.1, described previously [22]). From Figure 5.8 it can be seen that $TaF_3OH.HSO_4.H_2O$ had a distorted octahedral geometry, with the HSO_4^- and OH^- groups in the axial position and H_2O at a right angle from these groups in the equatorial position with F4 – F6.

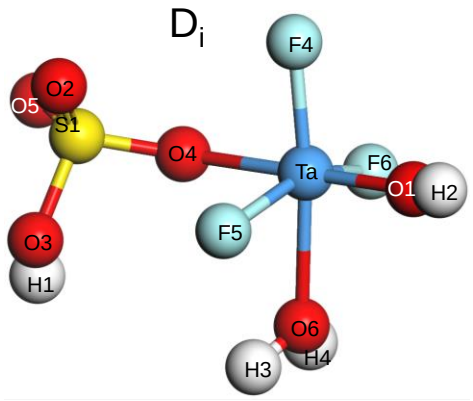

Figure 5.8 – $TaF_3OH.HSO_4.H_2O$ species (D_i)

The bond lengths and angles of $TaF_3OH.HSO_4.H_2O$ (D_i) are shown in Table 5.7. The Ta-F5 and Ta-F6 bond lengths were elongated due to the proximity of the three atoms O1, O4 and O6. The Ta-O6 bond length was also elongated due to steric hindrance of the surrounding atoms. While the bond

angle between F5-Ta-F4 and F4-Ta-T6 in a tradtitional octahedral geometry is 90°, it was 102.54° and 103.00°, respectively, in D_i, due to hydrogen bonding between F5 to H3 and F6 to H4.

Table 5.7 – Calculated bond lengths and angles of $TaF_3OH.HSO_4.H_2O$ (D_i) and $TaOF_3.H_2O$ ($D_{iii}a$ and $D_{iii}b$)

Bond length (Å)				Bond angle (°)			
Length	**D_i**	**$D_{iii}a$**	**$D_{iii}b$**	**Angle**	**D_i**	**$D_{iii}a$**	**$D_{iii}b$**
Ta-F4	1.918	1.938	1.928	F4-Ta-F6	103.00	95.37	115.78
Ta-F5	1.940	1.952	1.929	F5-Ta-F4	102.54	96.25	116.05
Ta-F6	1.932	1.951	1.929	F5-Ta-O6	76.09	76.73	78.14
Ta-O4	2.116	-	-	F6-Ta-O4	85.10	-	-
O4-S1	1.545	-	-	F4-Ta-O4	86.00	-	-
S1-O3	1.618	-	-	Ta-O4-S1	139.09	-	-
O3-H1	0.981	-	-	O4-S1-O3	103.14	-	-
S1-O2	1.451	-	-	S1-O3-H1	108.84	-	-
Ta-O1	1.893	1.757	1.766	O3-S1-O2	104.04	-	-
O1-H2	0.973	-	-	O2-S1-O5	119.15	-	-
Ta-O6	2.272	2.295	2.463	F6-Ta-O1	96.49	107.14	100.44
O6-H3	0.975	0.977	0.974	Ta-O1-H2	147.03	-	-
				O1-Ta-O6	93.37	97.29	176.98
				Ta-O6-H3	119.71	114.60	118.63
				H3-O6-H4	107.06	106.51	104.87

Both $TaF_3OH.HSO_4.H_2O$ (D_i) and $TaOF_3$ (D_{ii}) can react (via reactions 21 and 22, respectively, in Figure 5.1) to form $TaOF_3.H_2O$ (configuration D_{iii}), also shown in Figure 5.9 (see Table 5.7 for its bond lengths and angles). While $D_{iii}a$ had a square pyramidal geometry, $D_{iii}b$ had a distorted trigonal bipyramidal geometry. The Ta-F bond length in configuration $D_{iii}a$ was elongated by 0.024 Å due to the square pyramidal geometry forcing the F^- anions outward. In $D_{iii}b$, the average Ta-F bond length was 1.929 Å, which deviated by 0.033 Å from the modelled TaF_5 molecule [22]. This deviation was due to the electronegative O1 and O6 in the axial positions forcing the F^- anions outward. Even though the geometries of $D_{iii}a$ and $D_{iii}b$ differed, the Ta-O1 bond lengths were similar at 1.761 ± 0.005 Å. The Ta-O6 bond length and the bond angles in $D_{iii}a$ and $D_{iii}b$ differed due to the differences in geometries.

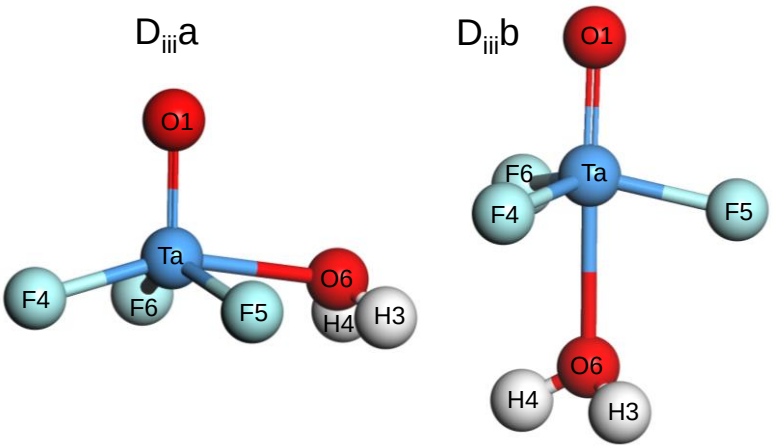

Figure 5.9 – $TaOF_3.H_2O$ species ($D_{iii}a$ and $D_{iii}b$)

The ideal bond angle of a square pyramidal geometry is 90°, where in $D_{iii}a$ hydrogen bonding between F6-H4 and F5-H3 caused the F-Ta-F bond angles to increase (95.8 ± 0.5°) and the F-Ta-O angles to decrease (76.73°). Similarly, in $D_{iii}b$, the equatorially bound F^- anions deviated from 120° to 115.9 ± 0.2° and the angle between axial and equatorial ions deviated from 90° to 78.14°, again due to the hydrogen bonding between F^- and H of the bound H_2O.

5.3.2 Reactions of the TaF_5:H_2SO_4:H_2O system

The energy of formation of all the reactions between TaF_5, H_2SO_4 and H_2O (Figure 5.1) in a 1:1:10 ratio were calculated at 298.15 K, as described in Section 5.2, to determine which of these reactions will likely occur. The relative energies of all 22 reactions are presented in Figure 5.10 in terms of the energy of the starting material (TaF_5 (A) + H_2SO_4 + 10 H_2O) where H_2SO_4 was in the cis-configuration. Instead of showing this for all possible configurations, only the most probable configurations, according to the results of Section 5.3.1, are shown. These results will again be discussed in terms of the blocks described in Figure 5.1. In addition, remember that for the purpose of this discussion the (dep) in for example $A_ia_{(dep)}$ refers to the deprotonation of the H_2SO_4 forming HSO_4^-.

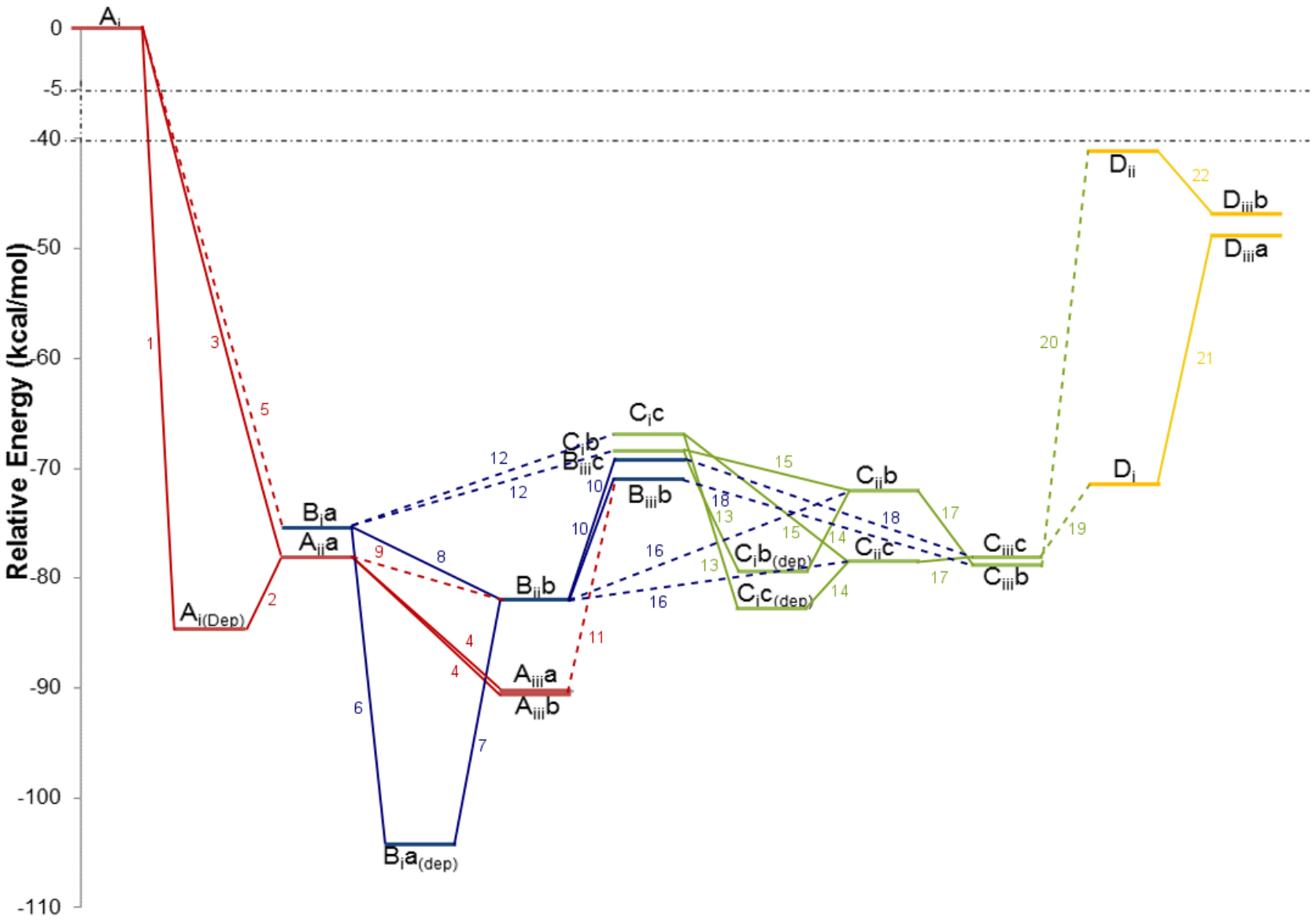

Figure 5.10 – Relative energy of the various products formed when combining TaF_5:H_2SO_4:10H_2O (line colours indicate a reaction from a specific block, solid lines are reactions within a block and dotted lines the reactions between blocks)

Initially, the energy of each molecule (TaF_5 + H_2SO_4 + 10 H_2O) were implicitly added and set to a relative energy of 0 kcal/mol, while all the other energy values are for the explicit systems (block A – D). It is apparent that all the reaction products had lower energies (ranging from -40 to -110 kcal/mol) than the initial system. For the sake of readability, the y-axis (Relative Energy) in Figure 5.10 was modified by removing the sections between -5 and -40 kcal/mol (see grey dotted lines). From Chapter 4 it was shown that the trans-H_2SO_4 conformer has a lower energy than the cis-conformer. However, the energy difference between the conformers was only 0.18 kcal/mol, indicating that both species may participate in the reactions. In this study, it has to be kept in mind that all the reaction energies were calculated relative to TaF_5 (A_i) + cis-H_2SO_4 + 10H_2O.

In Figure 5.1 the reactions of A_i to form $A_{i(dep)}$, A_{ii}a and B_ia are shown. B_ib had a similar reaction energy than B_ia, and was hence omitted from Figure 5.10 to increase readability. All three reactions were exothermic, showing a dramatic decrease in energy. As mentioned in Section 5.3.1, A_{ii}b with its strained crystal structure had an increased reaction energy and is therefore unlikely to form (omitted in Figure 5.10). If A_i(dep) formed during the first step of the mechanism (-84.72 kcal/mol), 6.58 kcal/mol energy will be needed to convert A_i(dep) to A_{ii}a. The energy from the first step (reaction 1 in Figure 5.1) may be adequate for reaction 2 (Figure 5.1) to occur to form A_{ii}a. This means A_{ii}a could form directly via reaction 3 (Figure 5.1) or via a combination of reactions 1 and 2 (Figure 5.1). A_{ii}a will then further react exothermally to form A_{iii} ($TaF_4.HSO_4$), which is one of the stable products that is expected to form from Block A.

There are three reactions (5, 9 and 11) when moving from Block A to B, while there are four reactions (6, 7, 8 and 10) in Block B itself (Figure 5.1). According to reaction 5, A_i formed both B_ia and B_ib exothermically (Figure 5.10). During reaction 6, B_ia + H_2SO_4 deprotonate to form B_ia(dep) ($TaF_5.H_2O$ + HSO_4^-). While this product seems very stable, requiring 22.2 kcal/mol to convert to B_{ii} via reaction 7, B_{ii} can also be formed via reactions 8 and 9 via B_ia or A_{ii}a respectively. As both these reactions are exothermic, B_{ii}b ($TaF_5.H_2O.HSO_4^-$) will probably form. In Section 5.3.1.2, it was seen that B_{iii}a and B_{iii}c had similar geometries. However, in B_{iii}c the hydrogen bond increased its stability, thereby lowering the reaction energy compared to B_{iii}a. It is thus more likely that B_{iii}b and B_{iii}c would be formed from B_{ii}b (reaction 10) requiring 11.4 and 12.7 kcal/mol to remove the HF, or from A_{iii} (reaction 11) requiring 21.2 kcal/mol by adding H_2O. As these values are relatively low, B_{iii}b and B_{iii}c could form during slight heating or ageing of the solution, most probably via reaction 10.

When moving from Block B to C there are again three reactions (12, 16 and 18) and four reactions (13, 14, 15 and 17) in Block C itself. For C_ib and C_ic to form via reaction 12, 7.1 and 8.5 kcal/mol are required. In view of the residual energy contained in the system from the

preceding exothermic reactions 1, 3, 4, 5 and 8, it is possible that C_ib and C_ic could form especially during ageing.

When comparing the probability of formation of A_{iii}, B_{ii} and C_i, it is clear that A_{iii} and B_{ii} are more likely to form than C_i as the reactions forming A_{iii} and B_{ii} are exothermic. Once formed, C_i + H_2SO_4 exothermally deprotonates via reaction 13 to form C_ib(dep) or C_ic(dep). At the same time, C_{ii}b and C_{ii}c can form exothermically via reaction 15. The amount of energy needed by C_ib(dep) and C_ic(dep) to form C_{ii}b and C_{ii}c is 7.4 and 4.4 kcal/mol, respectively. Hence it is clear that if C_i is formed, then the formation of C_ic(dep) and C_{ii}c will likely follow. Finally, there are two possible reactions when forming C_{iii}, namely from C_{ii} via reaction 17 or from B_{iii} via reaction 18. Reaction 18 is exothermic, while reaction 17 requires a small amount of energy to occur. This implies that C_{iii} will likely form if B_{iii} or if C_{ii} are present.

When moving from Block C to D there are only two reactions (19 and 20) and two reactions (21 and 22) in Block D itself. From C_{iii}c, via reaction 19, the formation of D_i was endothermic. However, since the chances of C_{iii}c forming is small, the formation of D_i is also unlikely. In addition, the chance of D_{ii} forming is also low considering the 37.7 kcal/mol needed to form D_{ii} from C_{iii}b via reaction 20. Accordingly, the probability of D_{iii} (reaction 22) forming is very small.

Summarising the results for all the reactions, it seems that three events are most likely to occur. The first one would be the exothermic formation of A_{iii}a or A_{iii}b ($TaF_4.HSO_4$) (~ -90 kcal/mol) via the formation of A_{ii}a ($TaF_5.HSO_4^-$) (-78 kcal/mol). The second event is the hydration of TaF_5 (A_i) to form $TaF_5.H_2O$ (B_ia) via reaction 5, yielding ~-75 kcal/mol, which could then lead to the formation of either B_ia(dep) (~-103 kcal/mol) or B_{ii}b (~-81.8 kcal/mol). Through ageing or heating it has been shown [22] that TaF_4OH (C_i) could form, which will then lead to the formation of $C_ib_{(dep)}$ or $C_ic_{(dep)}$ (at -79.4 and -82.8 kcal/mol, respectively), C_{ii}c (at -78.4 kcal/mol) and C_{iii} (b or c at -78.7 and -78.1 kcal/mol, respectively). Accordingly, the most abundant species available for extraction from a bulk solution will probably be $TaF_5.H_2O$ (B_i) and $TaF_4.HSO_4$ (A_{iii}), and after ageing TaF_4OH (C_i) and to a lesser degree $TaF_3OH.HSO_4$ (C_{iii}).

5.4 Conclusion

Due to a lack in speciation data, especially of Ta and Nb, molecular modelling was used in this paper to determine the behaviour of TaF_5 in a H_2SO_4 medium. From the various reactions investigated in a 1:1:10 metal:acid:water ratio, multiple hydrogen bonds formed, which stabilised the different acid species, resulting in the lowering of the reaction energies. Although it was shown that different reactions (1 - 22) and geometries (A_i – D_{iii}) are possible between

TaF_5, H_2SO_4 and H_2O, according to their energies, only four species are most probably available during extraction, namely $TaF_5.H_2O$ (B_i) and $TaF_4.HSO_4$ (A_{iii}) and if ageing occurred TaF_4OH (C_i) and to a lesser degree $TaF_3OH.HSO_4$ (C_{iii}). From this it is assumed that when TaF_5 is dissolved in H_2O, the most likely species to form will be $TaF_5.H_2O$, while $TaF_4.HSO_4$ is the most likely species available when H_2SO_4 is added. If the aqueous phase is left to age, TaF_4OH and $TaF_3OH.HSO_4$ are most likely the species present. The formation of all the other species, including $TaOF_3$, were endothermic.

5.5 References

[1] A. Agulyanski, The chemistry of Tantalum and Niobium fluoride compounds, Elsevier, San Diego, Oxford, London, 2004.

[2] E. Bidari, M. Irannejad, M. Gharabaghi, Solvent extraction recovery and separation of cadmium and copper from sulphate solution, Journal of Environmental Chemical Engineering, 1 (2013) 1269 - 1274.

[3] M. Noori, F. Rashchi, A. Babakhani, E. Vahidi, Selective recovery and separation of nickel and vanadium in sulfate media using mixtures of D2EHPA and Cyanex 272, Separation and Purification Technology, 136 (2014) 265 - 273.

[4] X. Li, C. Wei, Z. Deng, M. Li, C. Li, G. Fan, Selective solvent extraction of vanadium over iron from a stone coal/black shale acid leach solution by D2EHPA/TBP, Hydrometallurgy, 105 (2011) 359 - 363.

[5] J.R. Kumar, H.I. Lee, J.Y. Lee, J.S. Kim, J.S. Sohn, Comparison of liquid-liquid extraction studies on platinum(IV) from acidic solutions using bis(2,4,4-trimethylpentyl) monothiophosphinic acid, Separation and Purification Technology, 63 (2008) 184 - 190.

[6] R.K. Biswas, M.A. Hayat, Solvent extraction of zirconium(IV) from chloride media by D2EHPA in kerosene, Hydrometallurgy, 63 (2002) 149 - 158.

[7] M.S. Lee, R. Banda, S.H. Min, Separation of Hf(IV)–Zr(IV) in H_2SO_4 solutions using solvent extraction with D2EHPA or Cyanex 272 at different reagent and metal ion concentrations, Hydrometallurgy, 152 (2015) 84 - 90.

[8] Z. Zhu, C.Y. Cheng, Solvent extraction technology for the separation and purification of niobium and tantalum: A review, Hydrometallurgy, 107 (2011) 1 - 12.

[9] M.J. Ungerer, H.M. Krieg, G. Lachmann, D.J.v.d. Westhuizen, Comparison of extractants for the separation of TaF_5 and NbF_5 in different acidic media, Hydrometallurgy, 144-145 (2014) 195 - 206.

[10] A.D. Hammerich, V. Buch, F. Mohamed, Ab initio simulations of sulfuric acid solutions, Chemical Physics Letters, 460 (2008) 423 - 431.

[11] C.G. Ding, T. Taskila, K. Laasonen, A. Laaksonen, Reliable potential for small sulfuric acid-water clusters, Chemical Physics, 287 (2003) 7 - 19.

[12] C.C. Pye, W.W. Rudolph, An ab initio and Raman investigation of sulfate ion hydration, Journal of Physical Chemistry A, 105 (2001) 905 - 912.

[13] W.R. Cannon, B.M. Pettitt, J.A. McCammon, Sulfate anion in water: Model structural, thermodynamics and dynamic properties, Journal of Physical Chemistry, 98 (1994) 6225 - 6230.

[14] J.D.T. Steyl, Kinetic modelling of chemical processes in acid solution at t<200C. (i) thermodynamics and speciation in H_2SO_4-Metal (ii) SO_4-H_2O system, Hydrometallurgy Conference, The Southern African Institute of Mining and Metallurgy, 2009, pp. 401 - 444.

[15] P.V. Kumar, B.L. Tembe, Solvation structure and dynamics of the Fe^{2+}-Fe^{3+} ion pair in water, The Journal of Chemical Physics, 97 (1992) 4356 - 4367.

[16] E. Cauët, S. Bogatko, J.H. Weare, J.L. Fulton, G.K. Schenter, E.J. Bylaska, Structure and dynamics of the hydration shells of the Zn2+ ion from ab initio molecular dynamics and combined ab initio and classical molecular dynamics simulations, The Journal of Chemical Physics, 132 (2010) 194502.

[17] J. Chaboy, A. Muñoz-Pàez, P.J. Merkling, E.S. Marcos, The hydration of Cu^{2+}: Can the Jahn-Teller effect be detected in liquid solution?, Journal of Chemical Physics, 124 (2006) 64509.

[18] A.E. Saatci, F.P. Gökdemir, U.D. Menda, P. Kavak, O. Özdemir, K. Kutlu, Ionic conduction in different hydrated V_2O_5 film, 2nd International Advances in Applied Physics and Materials Science Congress, American Institute of Physics, 2012, pp. 289 - 295.

[19] F.W. Koknat, J.A. Parsons, A. Vongvusharintra, Metal cluster halide complexes. I. Efficient synthesis of hydrated hexanuclear niobium and tantalum cluster halides $M_6X_{14}.8H_2O$, Inorganic Chemistry, 13 (1974) 1699 - 1702.

[20] A.A. Ischenko, V.P. Spiridonov, T.G. Strand, Joint Norwegian - Soviet electron diffraction studies of molecular structures in the gas phase. II. Inorganic compounds, Acta Chemica Scandinavica A, 42 (1964) 651 - 673.

[21] A. Agulyansky, The chemistry of tantalum and niobium fluoride compounds, Elsevier, Amsterdam2004.

[22] M.J. Ungerer, C.G.C.E. van Sittert, D.J. van der Westhuizen, H.M. Krieg, Molecular modelling of tantalum penta-halides during hydrolysis and oxidation reactions, Computational and Theoretical Chemistry, 1090 (2016) 112 - 119.

[23] Material Studio Modelling Environment, Accelrys Software Inc., San Diego, 2012.

[24] J.P. Perdew, Y. Wang, Accurate and simple analytic representation of the electron-gas correlation energy, Physical Review B, 45 (1992) 13244 - 13249.

[25] B. Delley, Ground-state enthalpies: evaluation of electronic structure approaches with emphasis on the density functional method, The Journal of Physical Chemistry A, 110 (2006) 13632 - 13639.

[26] J.P. Perdew, K. Burke, M. Ernzerhof, Generalized gradient approximation made simple, Physical Review Letters, 77 (1996) 3865 - 3868.

[27] A. Tkatchenko, M. Scheffler, Accurate Molecular Van Der Waals Interactions from Ground-State Electron Density and Free-Atom Reference Data, Physical Review Letters, 102 (2009) 073005.

[28] B. Delley, Modern Density Functional Theory: A tool for chemistry, in: J.M. Seminario, P. Politzer (Eds.) Theoretical and Computational Chemistry, 1995.

[29] A. Klamt, G. Schüürmann, COSMO: a new approach to dielectric screening in solvents with explicit expressions for the screening energy and its gradient, Journal of the Chemical Society, Perkin Transactions 2, (1993) 799 - 805.

[30] B. Delley, The conductor-like screening model for polymers and surfaces, Molecular Simulation, 32 (2006) 117 - 123.

5.6 Supplementary

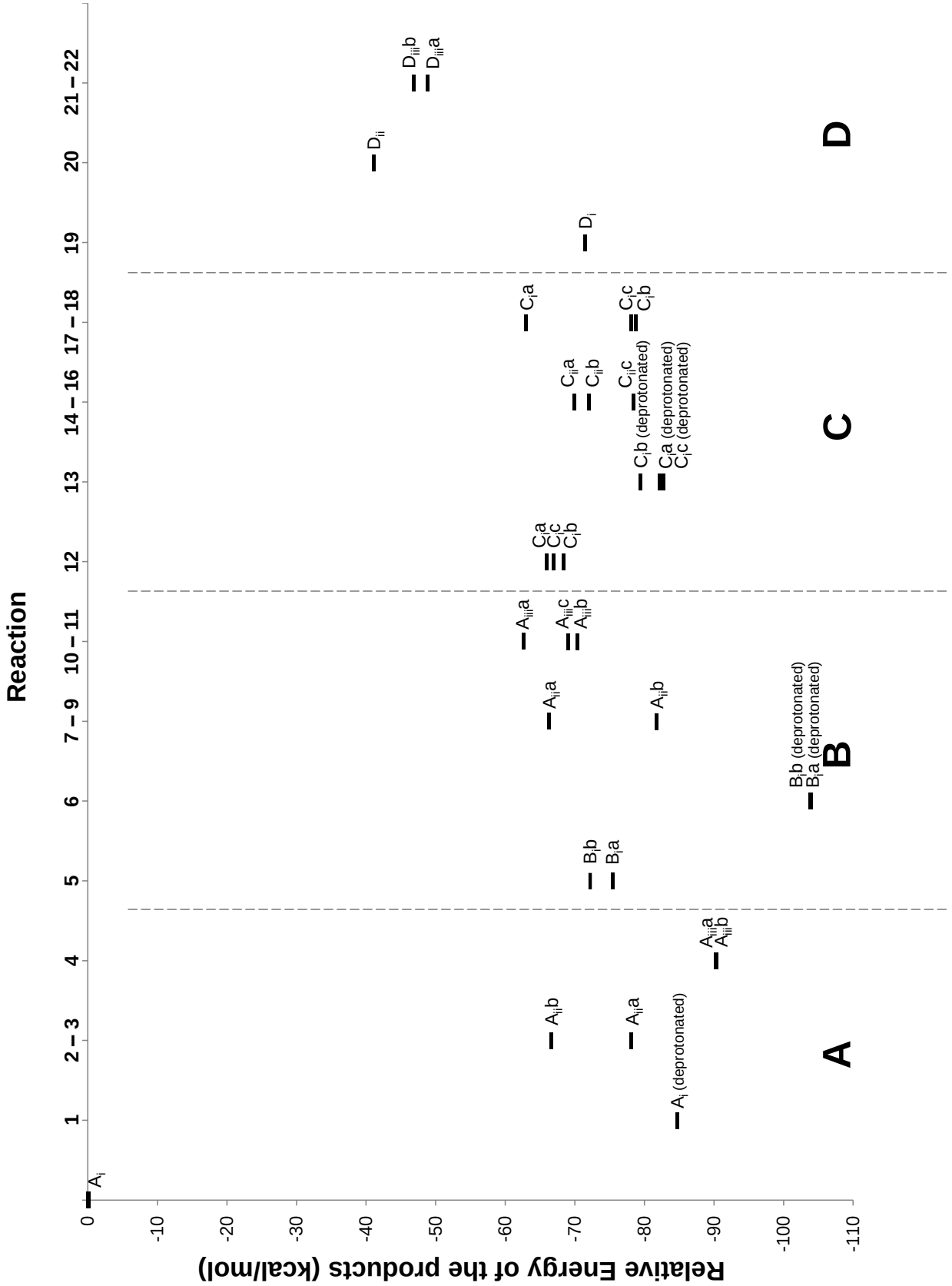

Figure S1 – Relative energy of the products from a TaF_5:H_2SO_4:10H_2O system

CHAPTER 6

Chapter 6 consists of the article titled ‘DFT modelling of tantalum penta-fluoride extraction with phosphor-based extractants’, which is added into this thesis in the exact format in which it was submitted for review in the *Journal of Computational and Theoretical Chemistry (2017)*.

6.1 Introduction

While the recovery of metals has advanced over the years, the diminishing high-grade supplies, the increasing demand for purified metals and the added pressure to recycle is driving the increased development of new and greener technologies. One such existing and developing technology is solvent extraction (SX), which is widely used in hydrometallurgy [1-7] for both the separation and extraction of high-purity metals. During a typical SX process, metal ions are selectively transferred from an aqueous solution to an organic solvent, often containing an extractant. In this system, the liquid-liquid interface is of particular interest due to the ion transfer of extractant molecules occurring across this interface. Extractants, which can be divided into acidic, basic and neutral extractants, not only determine the extraction process but also influence the specific characteristics of the organic phase as well as the interface reactions, kinetics and behaviour.

Since both tantalum (Ta) and niobium (Nb) are in the same group (VB) of the periodic table, they have similar chemical and physical properties, resulting in laborious and expensive separation processes [8, 9]. In a recent SX study, Ungerer et al. [10] investigated the separation of Ta and Nb (as MF_5), where partial separation was achieved when extracting from a sulphuric acid (H_2SO_4) medium. For the SX study of $Ta(Nb)F_5$ [10], the extractants di-iso-octyl phosphinic acid (DioPA) and di-(2-ethylhexyl) phosphoric acid (D2EHPA), which are both acidic extractants [11], were used.

The main obstacle found during the experimental SX study on $Ta(Nb)F_5$ was the lack of data on the speciation of Ta and Nb compounds, without which it was not possible to fully explain the separation data obtained. In a more recent study, molecular modelling was used to determine the molecular reactions as well as the system reactions that might occur during SX using a thermodynamic approach. Various reactions of TaF_5 and H_2O were investigated and it was shown that only $TaF_5.H_2O$ and TaF_4OH formed exothermically. In addition, it was shown that various interactions between TaF_5 and H_2O (Chapter 3), TaF_5 and H_2SO_4 (Chapter 5), and H_2SO_4 and H_2O (Chapter 4) may occur, of which the most likely species to be present in a H_2SO_4 environment are HSO_4^-, H_3O^+, H_2O, $TaF_4.HSO_4$ and, to a lesser extent, $TaF_3OH.HSO_4$.

Following the previous studies, where the species were identified [12] (Chapters 3 – 5), the next step entails determining the behaviour of these species in a biphasic system. The specific aim is to use molecular modelling to determine the extraction behaviour of Ta^{5+} from a H_2SO_4 medium when contacted with D2EHPA. Based on the previous data (Chapter 5), the following five species were included: TaF_5, $TaF_5.H_2O$, TaF_4OH, $TaF_4.HSO_4$ and $TaF_3OH.HSO_4$. For the purpose of this study they will be referred to using Roman numerals I-X differentiating between species extracted from a 4 M and a 10 M H_2SO_4 solution as is shown in Table 6.1.

Table 6.1 – Letters used for the Ta^{5+} species in the 1x1x1 4 M and 10 M H_2SO_4 systems

Ta^{5+} species	1x1x1 3D System	
	4 M H_2SO_4	10 M H_2SO_4
TaF_5	I	II
$TaF_5.H_2O$	III	IV
TaF_4OH	V	VI
$TaF_4.HSO_4$	VII	VIII
$TaF_3OH.HSO_4$	IX	X

The stoichiometry of the three-dimensional (3D) periodic system was determined from previous experimental conditions [10] and is given in Table 6.2. During experimental SX runs [10] it was found that, for every metal species, 2 to 3 extractant molecules were required for extraction. However, to simulate a system in these correct ratios, the 3D system would contain more than 11 000 molecules, which was not attainable with the current hardware available to us. Therefore, the water:acid and diluent:modifier ratios were kept constant at 8.5:1 (4 M H_2SO_4), 1.1:1 (10 M H_2SO_4) and 16:1, respectively, while 3 extractant (D2EHPA) species were added per Ta^{5+} species (Table 6.1). Lastly, two mixed 4x4x2 systems (see Table 6.2), one for 4 M H_2SO_4 and one for 10 M H_2SO_4, containing all the Ta^{5+} species (Table 6.1) in a ratio of 7:7:6:6:6 (TaF_5:$TaF_5.H_2O$: TaF_4OH:$TaF_4.HSO_4$:$TaF_3OH.HSO_4$) to give a total of 32 Ta^{5+} species, were investigated.

Table 6.2 – Composition and dimensions of the simulated systems

3D periodic system	Aqueous/Organic phase	Box size (Å^3)
1x1x1	**4 M** H_2SO_4: 1 Ta species, 21 HSO_4^-, 21 H_3O^+, 179 H_2O / 3 D2EHPA, 1-octanol, 48 cyclohexane	26.3x26.3x26.3
	10 M H_2SO_4: 1 Ta species, 54 HSO_4^-, 54 H_3O^+, 50 H_2O / 3 D2EHPA + 1-octanol + 48 cyclohexane	27.4x27.4x27.4
4x4x2	**4 M** H_2SO_4: 32 Ta species, 672 HSO_4^-, 672 H_3O^+, 5696 H_2O / 96 D2EHPA, 32 1-octanol, 1536 cyclohexane	105.0x105.0x52.5
	10 M H_2SO_4: 32 Ta species, 1728 HSO_4^-, 1728 H_3O^+, 1600 H_2O / 96 D2EHPA + 32 1-octanol + 1536 cyclohexane	109.7x109.7x54.8

6.2 Computational Methods

Materials Studio 2016 from Dassault Systèmes BIOVIA was used for the computational modelling [13]. The DFT calculations were performed with DMol^3, Amorphous Cell and Forcite modules and graphical displays generated with BIOVIA Materials Studio 2016. Firstly, a geometry optimisation [14, 15] was done within DMol^3 for all the different molecules. It was previously shown [12] that the Perdew-Burke-Ernzerhof (PBE) [16] correlation gave the best results for reactions pertaining to Ta. Accordingly, the generalised-gradient approximation (GGA) with the PBE [16] correlation,

with the DNP+ (double numerical plus polarisation with addition of diffuse functions) basis set, basis file 4.4 and Tkatchenko-Scheffler (TS) dispersion correction [17] were used. The core treatment parameter was set to 'All Electron', treating all electrons as if they were valence electrons. Furthermore, a smearing of 0.005 Hartree (Ha) was chosen for all the calculations [18] to facilitate self-consistent field (SCF) convergence. The solvation model COSMO (conductor-like screening model) [19, 20] was chosen to simulate a solute within a solvent. For the solvent (H_2O) of the aqueous phase containing TaF_5, H_2SO_4 and H_2O, a dielectric constant of 78.54 was used. For the organic phase, which consisted of cyclohexane, D2EHPA and 1-octanol, the solvent was cyclohexane with a dielectric constant of 2.02.

After the geometry optimisation, three-dimensional (3D) periodic systems were constructed using the Amorphous Cell module. The molecules that represent both the organic and aqueous phases were mixed in a predetermined number and ratio with a density of 1 $g.cm^{-3}$ at 298 K to represent laboratory conditions. After the periodic systems were obtained, the Forcite module was used to relax the system by geometry optimisation using the Universal force field (UFF) [21-24] with atom-based electrostatic and van der Waals equations [23]. This was followed by energy minimisations using molecular dynamics (MD) for 1000 steps with UFF, while the electrostatic and van der Waals interactions were calculated with the Ewald summation method [25, 26] starting from random velocities. The production stage (demixing simulations) again used MD runs for 2 ns (NVT ensemble) with 1 fs steps at 298 K and a pressure of 1 atm. To control the temperature, Nosé dynamics [27-29], again with the Ewald summation method [25, 26], were chosen for the electrostatic and van der Waals interactions.

Of each of the 3D systems, a concentration profile of all the particles/molecules was calculated in a given layer. The values are relative to a random distribution and range from 0 (no particles in the layer) to a maximum value corresponding to the total number of bins if all particles reside in the same layer. The sum over all layers is equal to the total number of bins. The bin size was 0.5 Å.

6.3 Results and Discussion

The following section is divided into two parts, first discussing the 1x1x1 system (Section 6.3.1), followed by a discussion of the 4x4x2 3D system (Section 6.3.2). Section 6.3.1 is divided into five sections discussing the five Ta^{5+} species listed in Table 6.1 in the two H_2SO_4 systems (4 M and 10 M). The different colours used throughout this paper indicate different atoms, with white being hydrogen (H), red oxygen (O), grey carbon (C), yellow sulphur (S), purple phosphorous (P), teal fluorine (F) and blue Ta.

6.3.1 1x1x1 3D systems

6.3.1.1 TaF_5 systems

The first species investigated was TaF_5 in 4 M H_2SO_4. As was stated in the Computational Methods, the 3D periodic systems were constructed using the Amorphous Cell module of Materials Studio. This 3D system (shown in the supplementary section Figure S1) represents perfect mixing of the biphasic solution at laboratory conditions (298 K, 1 atm). Figure 6.1 shows various snapshots of this system after 2 ns simulation time, including the total modelled system (Figure 6.1A), the concentration profiles of all the species present (Figure 6.1B), and then various species of the total modelled system, i.e. the aqueous phase (Figure 6.1C), the organic phase (Figure 6.1D) and the interface (Figure 6.1C).

In Figure 6.1A two main regions are visible: to the middle and top of the periodic cell a circular region containing H_2SO_4 and H_2O (i.e. the aqueous phase) and to the bottom and sides of the periodic cell cyclohexane, D2EHPA and 1-octanol (i.e. the organic phase). The occurrence of these distinctive regions is indicative of phase dissolution. The aqueous phase seems to have formed a water droplet within the organic phase, implying that extraction would occur from within a droplet of the aqueous phase to the surrounding organic phase. Furthermore, it can be seen that TaF_5 is situated within the organic phase, indicating that extraction occurred from the aqueous phase into the organic phase.

This is also visible from the concentration profile (Figure 6.1B), where when the aqueous phase concentration was at a maximum, the organic phase concentration was at a minimum and vice versa, confirming separation of the two phases. However, there are two regions (cell parameters 2 – 4 and 15 – 17 Å) were both phases are present, forming the interface. Figure 6.1D shows that the extractants lay on the interface with the O atoms of D2EHPA in the direction of the aqueous phase, creating strong hydrogen bonds, while the TaF_5 has moved to the organic phase. Of the 3 extractant molecules, none were found in the first interfacial region (2 – 4 Å, Figure 6.1B), two extractants were found within the second interfacial region (15 – 17 Å) and the third extractant was within the bulk of the organic phase (purple line - Figure 1B). This means that, before extraction, the extractants are surface active, but as soon as the D2EHPA-TaF_5-$5H_2O$ system is formed, this newly formed macro molecule moves into the organic phase, where TaF_5, surrounded by 5 H_2O molecules, is ‘released’ in the organic phase and D2EHPA can return to the surface. The TaF_5 (green line - Figure 6.1E) lay within the bulk of the organic phase, confirming extraction from the interface to the organic phase.

From Figure 1C and D it is also clear that, at the interfacial region, the H_2O and cyclohexane molecules were mixed (Figure 6.1C and D), which could lead to the formation of emulsions, which is why a modifier [30] (1-octanol in this case) was added to the SX system as is visible in the

bottom left of the periodic cell (Figure 6.1E). In a previous MD study [31], it was found that, when increasing the modifier, i.e. alcohol concentration, the aqueous phase changed from a linear slab to a drop with a diameter of 10 Å, which increased the interfacial area and hence the extraction rate. According to Figure 6.1E, the 1-octanol did not lie near the interface, indicating that it was not surface active and therefore did not aid in the extraction process.

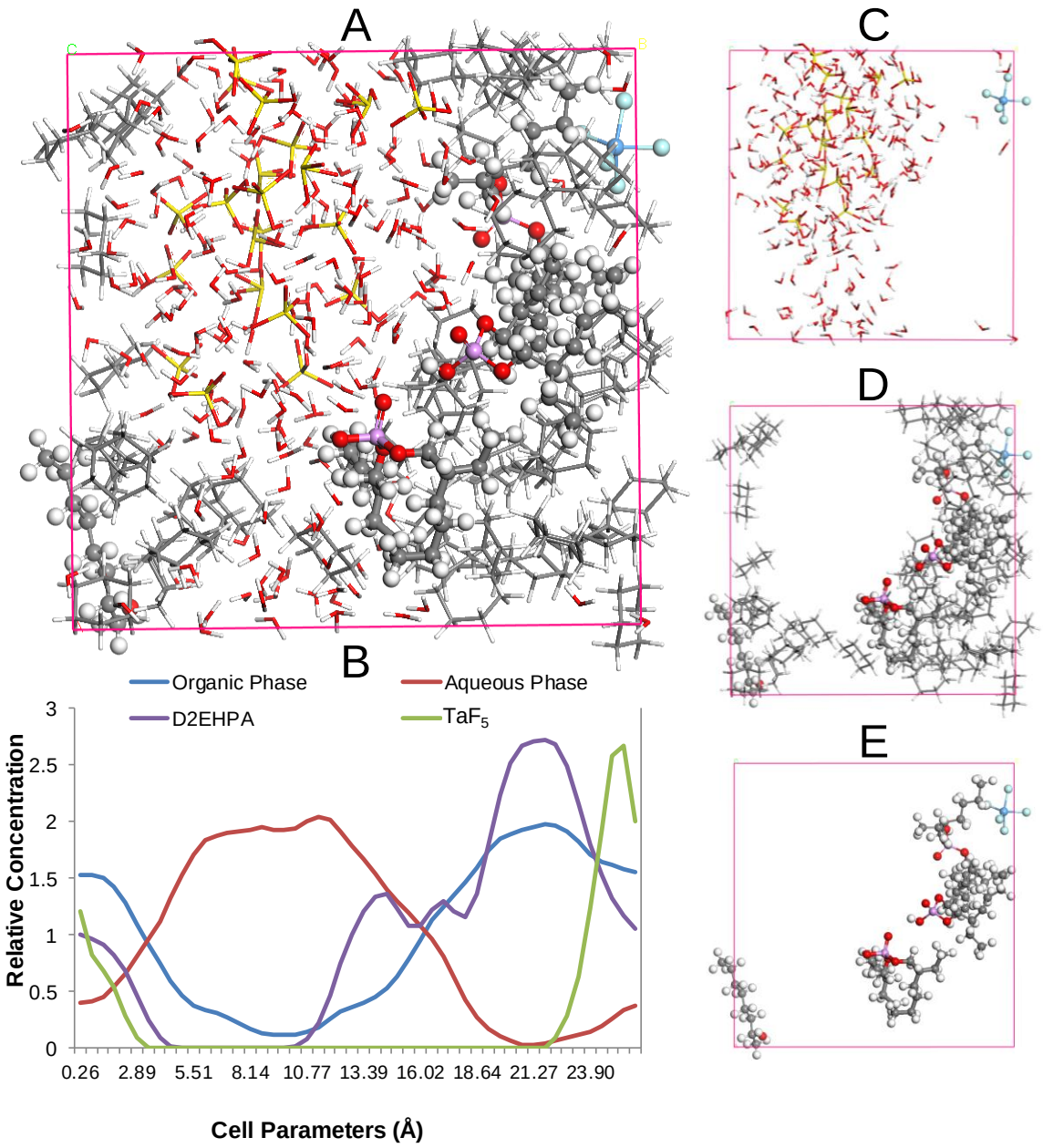

Figure 6.1 – Snapshot of system I at 2 ns (4 M H_2SO_4: TaF_5, 21 HSO_4^-, 21 H_3O^+, 179 H_2O; Org: 3 D2EHPA, 1-octanol, 48 cyclohexane) where (A) shows the total modelled system, (B) density profiles of all the species present, (C) the aqueous phase containing H_2SO_4, H_2O and TaF_5, (D) the organic phase containing cyclohexane, D2EHPA, 1-octanol and TaF_5, and (E) the surface-active species D2EHPA, 1-octanol and TaF_5.

In Figure 6.1C it can be seen that the TaF_5 molecule is surrounded by 4 to 6 H_2O molecules when it is extracted to the organic phase. This was confirmed in the previous chapter (Chapter 5) were it was shown that more than 5 H_2O molecules were needed to hydrate TaF_5. Similarly, Wilson et al. [32] showed that when metalate anion species extracted with phosphor-based extractants, the metal species were surrounded by H_3O^+ and H_2O to form a hydration sphere or a 'water pool' which was extracted into the organic phase. If it is assumed that the species present during SX is TaF_5, then it can be concluded that extraction will occur in 4 M H_2SO_4 from an aqueous droplet into an organic bulk solution.

From the experimental SX data it was seen that, when the H_2SO_4 concentration was increased to 10 M, the extraction percentage of Ta increased from 20% to 90% [10]. Figure 6.2 shows this simulated system of TaF_5 in 10 M H_2SO_4 after 2 ns of simulation time. In Figure 6.2A phase separation can again be seen, however this time with the aqueous phase in the top, bottom and right of the snapshot and the organic phase having formed a droplet in the middle of the periodic cell. This inverse is probably due to the decrease in the number of H_2O molecules (replaced by H_2SO_4 molecules), leading to fewer hydrogen bonds, which supports the formation of droplets. Similar to the 4 M system, TaF_5 is situated in the organic phase, again indicating that extraction occurred.

From the concentration profile (Figure 6.2B), it can again be seen that, when the organic phase concentration (blue line) was at its highest, the aqueous phase concentration (red line) was at its lowest, confirming phase separation. The extractant concentration peak (purple line) overlaps with the organic concentration peak, confirming that the extractants lay within the organic phase. The concentration profile shows that the TaF_5 (green line) was in the aqueous phase, however, from Figure 6.2A, C and D it can be seen that Ta was actually in the organic bulk. This discrepancy is due to the way the concentration profile was calculated and constructed. The concentration values are relative to the total distribution and range from 0 (no particles in the layer) to a maximum value corresponding to the total number of bins if all particles reside in the same layer. The sum over all layers is equal to the total number of bins. Therefore, in the space between 0 and 3 Å (Figure 6.2B) the most abundant molecules are the aqueous phase with the organic phase as a droplet in between when compared to Figure 6.2A and therefore TaF_5 is shown in the concentration profile to be located within the aqueous phase.

Figure 6.2C shows the aqueous phase situated to the top, right and bottom of the cell. Similar to the 4 M system, it can be seen that H_2O molecules had also been pulled into the organic phase, which in turn could lead to emulsion formation. Different from the 4 M system, the TaF_5 during extraction was surrounded by 2 to 3 H_2O molecules on average. This decrease in the number of H_2O molecules could be due to the increased H_2SO_4 concentration.

Figure 6.2D shows the organic phase in the form of a droplet, with the extractants and 1-octanol on the edge of the droplet, and the hydrogen atoms of 1-octanol in both cases oriented in the direction of the aqueous phase. Hence it seems that, with increasing H_2SO_4 concentration, the extraction preferentially occurred from the bulk aqueous phase to the organic droplet. Comparing Figure 6.2D and the snapshot of the interface (Figure 6.2E), it can be seen that the three D2EHPA molecules are surface active, while the 1-octanol molecule was surface inactive, lying in the middle of the cell within the bulk organic phase.

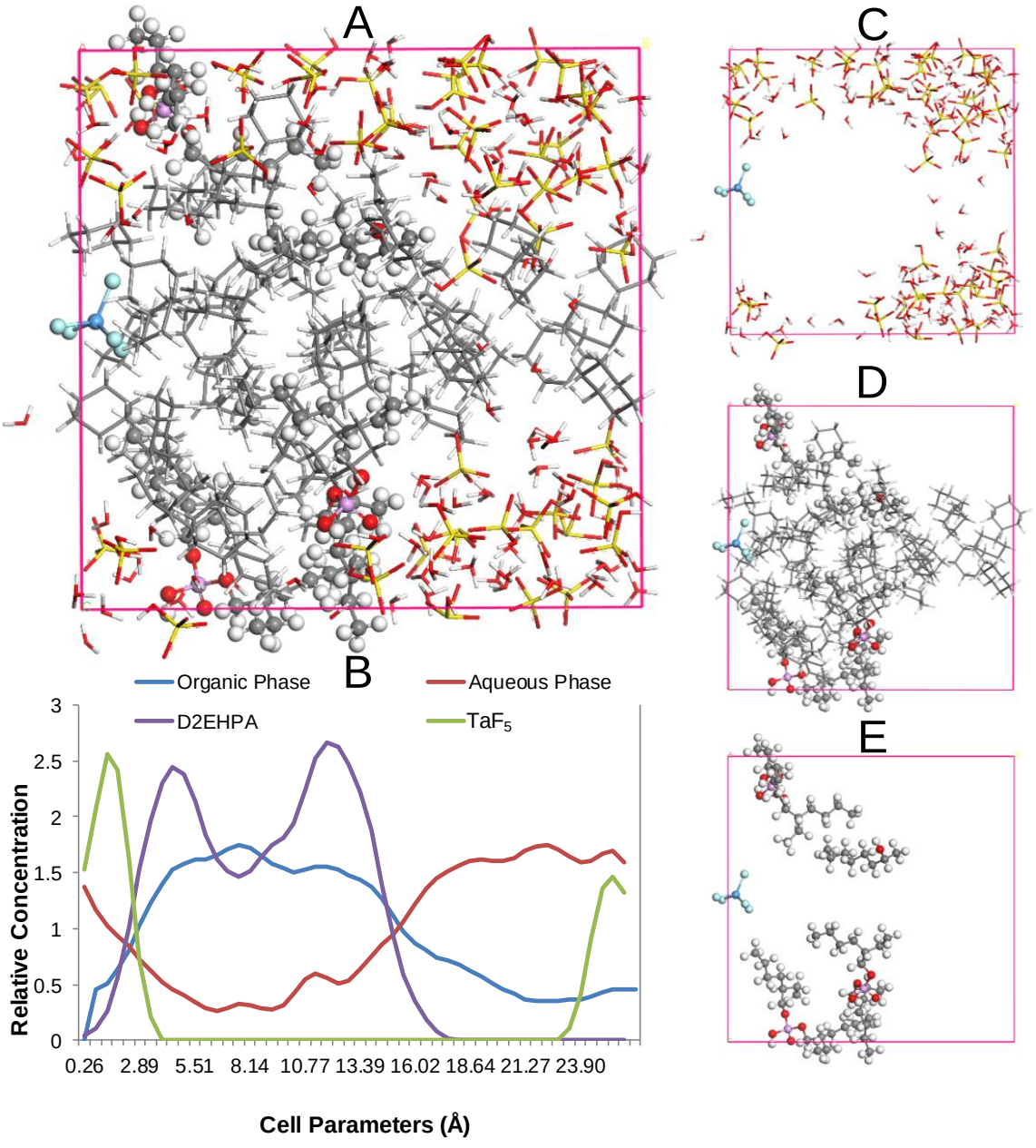

Figure 6.2 – Snapshot of system II at 2 ns (10 M H_2SO_4: TaF_5, 54 HSO_4^-, 54 H_3O^+, 50 H_2O; Org: 3 D2EHPA, 1-octanol, 48 cyclohexane), where (A) shows the total modelled system, (B) density profiles of all the species present, (C) the aqueous phase containing H_2SO_4, H_2O and TaF_5, (D) the organic phase containing cyclohexane, D2EHPA, 1-octanol and TaF_5, and (E) the surface-active species D2EHPA, 1-octanol and TaF_5.

To be sure that extraction occurred due to the presence of D2EHPA and not as an artifact of modelling, the same initial 3D systems of A and B (Figure S2), without any D2EHPA and 1-octanol present, were modelled maintaining the same concentration of the other species. Figure 6.3 shows the snapshots of TaF_5 in both a 4 and 10 M H_2SO_4 system without D2EHPA and 1-octanol after 2 ns simulation time.

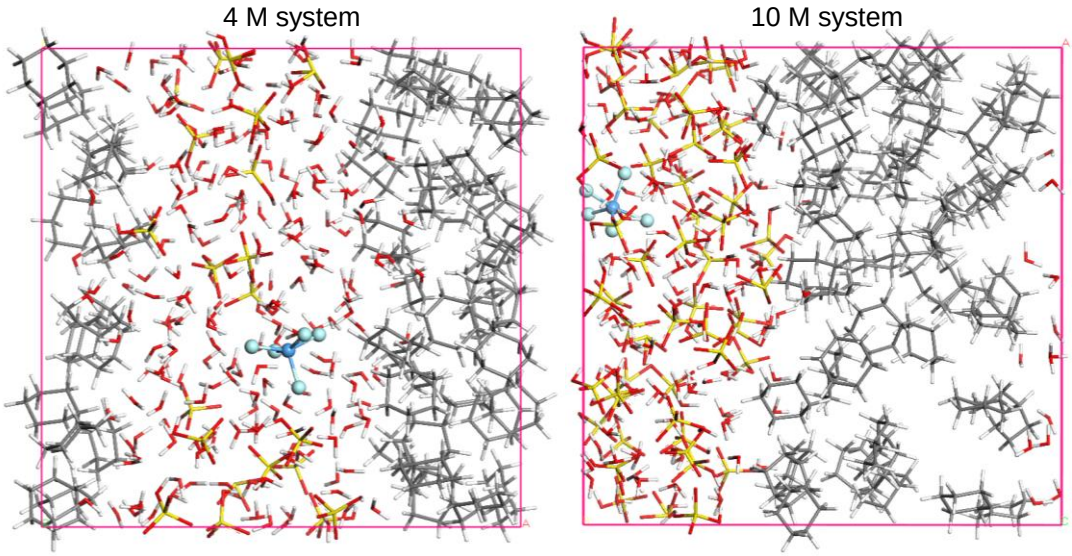

Figure 6.3 – Snapshot of TaF_5 in the 4 and 10 M H_2SO_4 systems without the extractant D2EHPA and 1-octanol. Composition for 4M was TaF_5, 21 HSO_4^-, 21 H_3O^+, 179 H_2O, 48 cyclohexane and for 10M was TaF_5, 54 HSO_4^-, 54 H_3O^+, 50 H_2O, 48 cyclohexane.

The relative positions of the linearly columned interface have changed. It is clear that in both systems the TaF_5 was surrounded by 4 to 6 H_2O molecules, but had not been extracted from the aqueous phase to the organic phase, clearly showing the effect when D2EHPA was omitted. Some H_2O molecules had migrated to the organic phase, which could result in experimental third phase formation (emulsion) confirming the need for 1-octanol.

6.3.1.2 $TaF_5.H_2O$ systems

In this section, the migration of the second species that could have formed, i.e. the hydrated $TaF_5.H_2O$, is discussed. In Figure 6.4, the possible distribution of $TaF_5.H_2O$ in a 4 M H_2SO_4 is presented after a 2 ns simulation time. Linearly separated phases were observed as had been the case when omitting D2EHPA and 1-octanol for TaF_5, with the aqueous phase to the left and right of the cell and the organic phase in the middle. From visual inspection, it seems that the $TaF_5.H_2O$ molecule lay on the interface, with the bonded H_2O directed towards the organic phase and the F-atoms toward the aqueous phase. From the concentration profile (Figure 6.4B) it can

again be seen that there are distinct organic and aqueous phases with two interfacial regions (cell parameters 8 – 9 Å and 22 – 23 Å). Whereas the extractants were within the organic phase region, the $TaF_5.H_2O$ was positioned between the bulk of the organic and the interface, indicating extraction. From a previous paper [12] it was shown that $TaF_5.H_2O$ is most likely to exist in a water system and if it is assumed to be the species present in low acidic (4 M H_2SO_4) conditions, extraction occurs at the bound H_2O site.

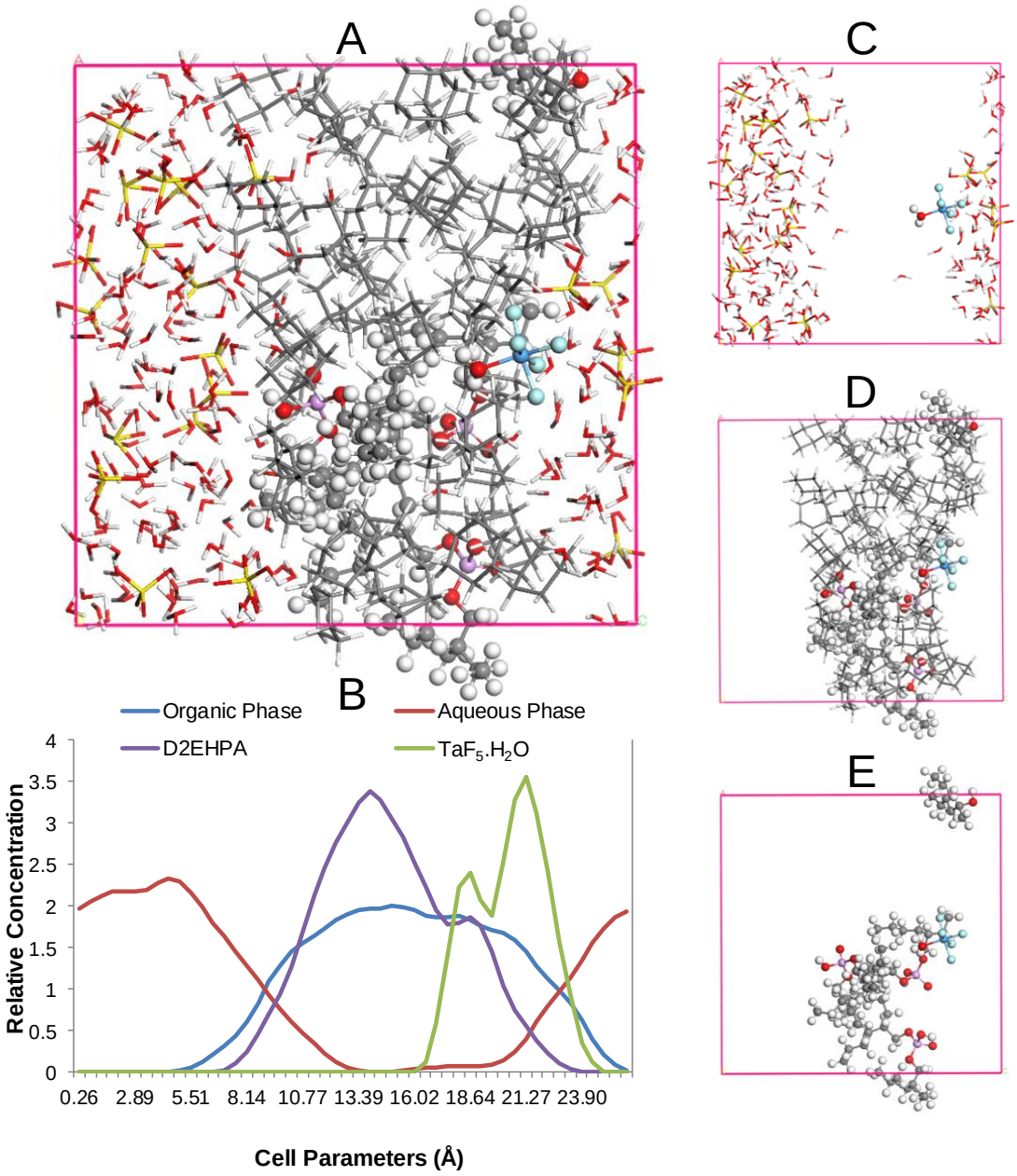

Figure 6.4 – Snapshot of system III at 2 ns (4 M H_2SO_4: $TaF_5.H_2O$, 21 HSO_4^-, 21 H_3O^+, 179 H_2O; Org: 3 D2EHPA, 1-octanol, 48 cyclohexane), where (A) shows the total modelled system, (B) density profiles of all the species present, (C) the aqueous phase containing H_2SO_4, H_2O and $TaF_5.H_2O$, (D) the organic phase containing cyclohexane, D2EHPA, 1-octanol and $TaF_5.H_2O$, and (E) the surface-active species D2EHPA, 1-octanol and $TaF_5.H_2O$.

According to Figure 6.4C, the $TaF_5.H_2O$ was situated on the edge of the aqueous phase with one of the bounded H_2O in the direction of the organic phase and the F-atoms (directed at the aqueous phase) surrounded by additional H_2O molecules. Similar to the TaF_5 system it can be seen that H_2O and H_3O^+ molecules are pulled into the organic phase, forming a mixed phase or possibly an emulsion (third phase). According to Figure 6.4D, the extractants and 1-octanol were again positioned on the edges of the organic phase. From the interface (Figure 6.4E) it seems that the H_2O group of $TaF_5.H_2O$ was coordinated with one extractant, indicating that extraction occurred due to the hydration sphere of TaF_5.

Subsequently, $TaF_5.H_2O$ was modelled in a 10 M H_2SO_4 system and the snapshots are shown in Figure 6.5. In Figure 6.5A it can be seen that phase dissolution occurred, again with the aqueous phase to the sides and the organic phase in the middle. Similar to the TaF_5-10 M H_2SO_4 system (Figure 6.2), the organic phase (Figure 6.5D) formed a droplet within the aqueous phase and the $TaF_5.H_2O$ formed an additional hydrogen bond with a nearby H_2O molecule, which was oriented towards the organic phase, while the bound H_2O was stabilised through hydrogen bonding by the aqueous phase. This confirms that extraction is likely.

From the concentration profile (Figure 6.5B) it is evident that clear aqueous (red line) and organic (blue line) regions formed with areas of mixing (cell parameters 8 – 9 Å and 23 – 24 Å) indicative of the interfacial region. Both the extractants (purple line) and the $TaF_5.H_2O$ (green line) were located within the organic phase.

Comparing snapshot C and D it can be seen that phase overlap occurred near the bottom of the snapshot, indicating possible formation of emulsions. From the interface snapshot (Figure 6.5E), it can be seen that $TaF_5.H_2O$ was in the vicinity of, but not bound or coordinated to the extractants, indicating that extraction had already occurred. Similar to the TaF_5-10 M H_2SO_4 system, extraction occurred from a bulk aqueous solution toward an organic droplet, possibly due to the change in the H_2O concentration.

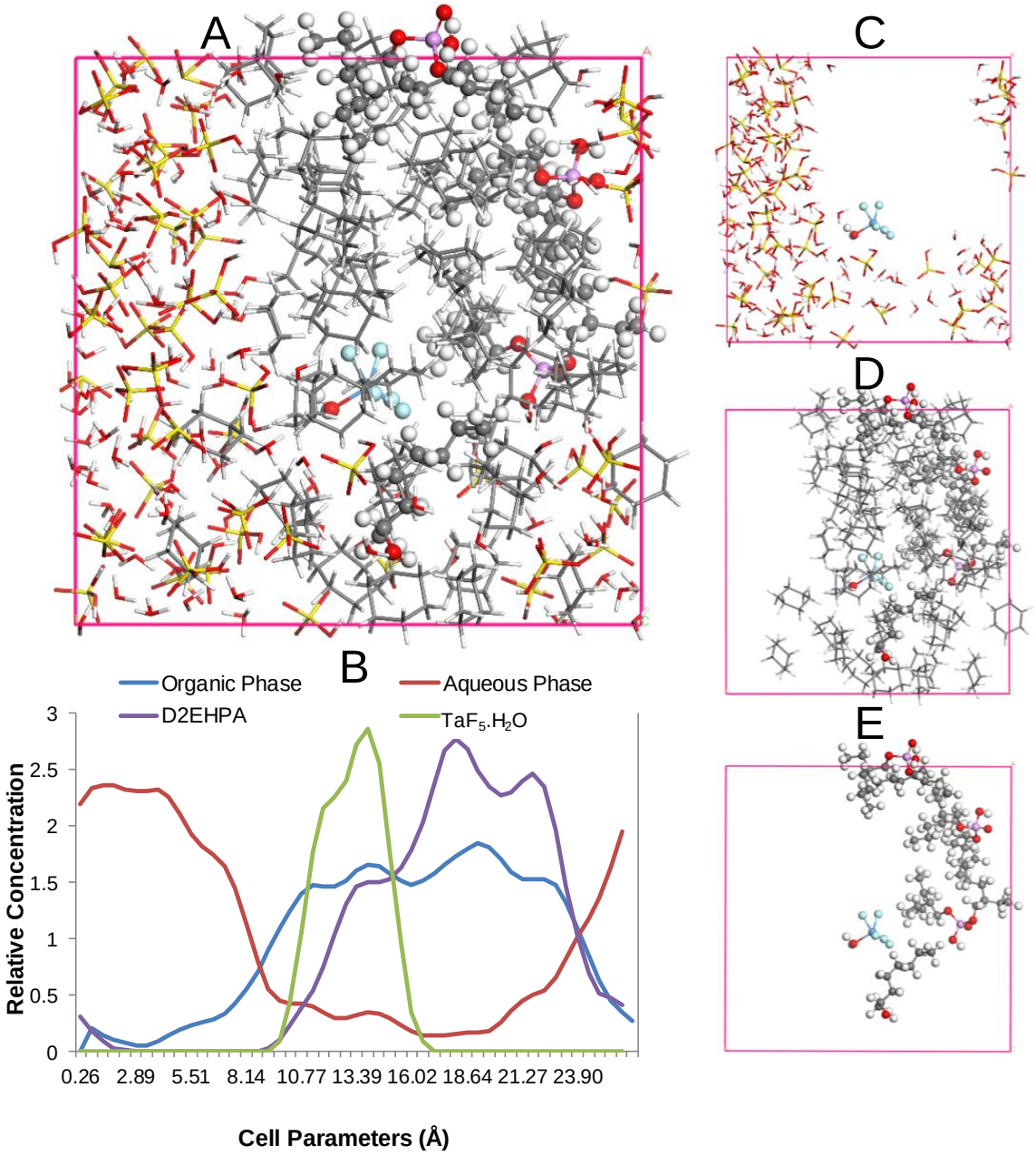

Figure 6.5 – Snapshot of system IV at 2 ns (10 M H_2SO_4: $TaF_5.H_2O$, 54 HSO_4^-, 54 H_3O^+, 50 H_2O; Org: 3 D2EHPA, 1-octanol, 48 cyclohexane), where (A) shows the total modelled system, (B) density profiles of all the species present, (C) the aqueous phase containing H_2SO_4, H_2O and $TaF_5.H_2O$, (D) the organic phase containing cyclohexane, D2EHPA, 1-octanol and $TaF_5.H_2O$, and (E) the surface-active species D2EHPA, 1-octanol and $TaF_5.H_2O$.

To again confirm whether extraction of $TaF_5.H_2O$ occurred due to the presence of D2EHPA, the initial systems of $TaF_5.H_2O$ in 4 and 10 M H_2SO_4 was modelled in the absence of D2EHPA and 1-octanol (Figure S3). Similar to the TaF_5 systems, the final simulation data showed that i) $TaF_5.H_2O$ was surrounded by an additional 4 H_2O molecules, ii) $TaF_5.H_2O$ did not extract from the aqueous phase and iii) some H_2O molecules had migrated towards the organic phase, suggesting possible third phase formation. In the 4 M system ($TaF_5.H_2O$-4 M-without D2EHPA), the two

phases separated to form linear columns similar to the TaF_5-4 M-without D2EHPA system (Figure 6.3), however, in the 10 M system ($TaF_5.H_2O$-4 M-without D2EHPA) the organic phase formed a droplet in an aqueous bulk solution similar to the $TaF_5.H_2O$-10 M-D2EHPA (Figure 6.5). This again confirms that 1-octanol increased phase dissolution and D2EHPA extracted $TaF_5.H_2O$ from both 4 and 10 M aqueous phases.

6.3.1.3 TaF_4OH systems

It was shown in a previous paper [12] that ~10 kcal/mol energy had to be added to the system to form the third molecule under discussion, TaF_4OH. This species therefore is only likely to form when aqueous solutions are aged or heated for example. Figure 6.6 shows the simulated SX data of TaF_4OH in 4 M H_2SO_4 after 2 ns. The bulk of the aqueous phase (Figure 6.6A and C) is to the left in the form of a droplet within the bulk organic phase (Figure 6.6D), with some break-away in the middle towards the right. TaF_4OH is situated toward the bottom of the bulk solution, again surrounded by five H_2O molecules. Again, the extractants were on the edge of the bulk organic phase with the O atoms directed towards the aqueous phase. However, when comparing snapshot C and D, it seems as though the organic phase had both properties of a bulk solution (right of the snapshot) and a droplet (having a less dense part in the middle where the aqueous phase showed break-away). The break-away section showed significant mixing of the two phases, suggesting third phase formation, which in turn could hinder extraction.

Extraction of TaF_4OH may not have occurred as i) the TaF_4OH was on the interface (Figure 6.6A and C) and ii) the extractants were not coordinated with the TaF_4OH (Figure 6.6E). Comparing Figure 6.6A and the concentration profile (Figure 6.6B) confirms that aqueous (blue line) and organic regions (red line) had formed an interfacial region between 11 and 13 Å. Both the extractants (purple line) and TaF_4OH (green line) seem to be situated in both phases, possibly indicating third phase formation. It is interesting to note that the extraction percentages during the actual SX experiments declined more than 50 % when aqueous solutions were aged for 3 days before use. It seems that the experimentally observed decline in extraction could be due to the formation of specific Ta species such as TaF_4OH.

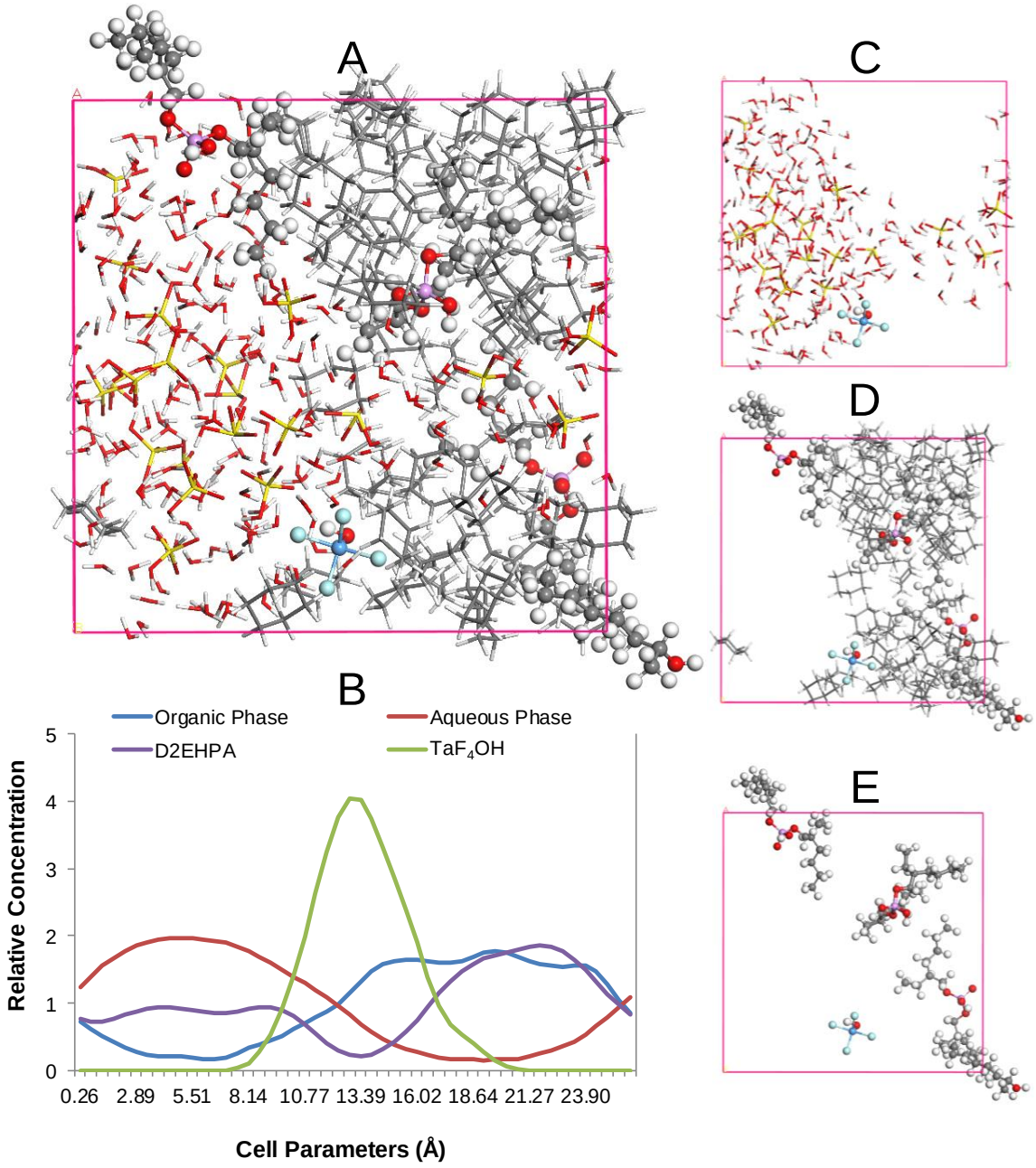

Figure 6.6 – Snapshot of system V at 2 ns (4 M H_2SO_4: TaF_4OH, 21 HSO_4^-, 21 H_3O^+, 179 H_2O; Org: 3 D2EHPA, 1-octanol, 48 cyclohexane), where (A) shows the total modelled system, (B) density profiles of all the species present, (C) the aqueous phase containing H_2SO_4, H_2O and TaF_4OH, (D) the organic phase containing cyclohexane, D2EHPA, 1-octanol and TaF_4OH, and (E) the surface-active species D2EHPA, 1-octanol and TaF_4OH.

To further support and validate this tendency, TaF_4OH was added to a 10 M H_2SO_4 solution and the simulated extraction results are shown in Figure 6.7. Similar to the 4 M system (Figure 6.6), the aqueous phase (Figure 6.7A) was situated to the left and far right of the snapshot, indicating phase dissolution, whereas the TaF_4OH was situated within the bulk of the aqueous phase close to the interface, showing possible non-extraction. Similar to the previous system, break-away in this case was observed in the organic phase, showing both properties of a bulk solution and a

droplet. The extractants were again on the edge of the bulk organic solution, with the O atoms oriented towards the aqueous phase, confirming their surface activity.

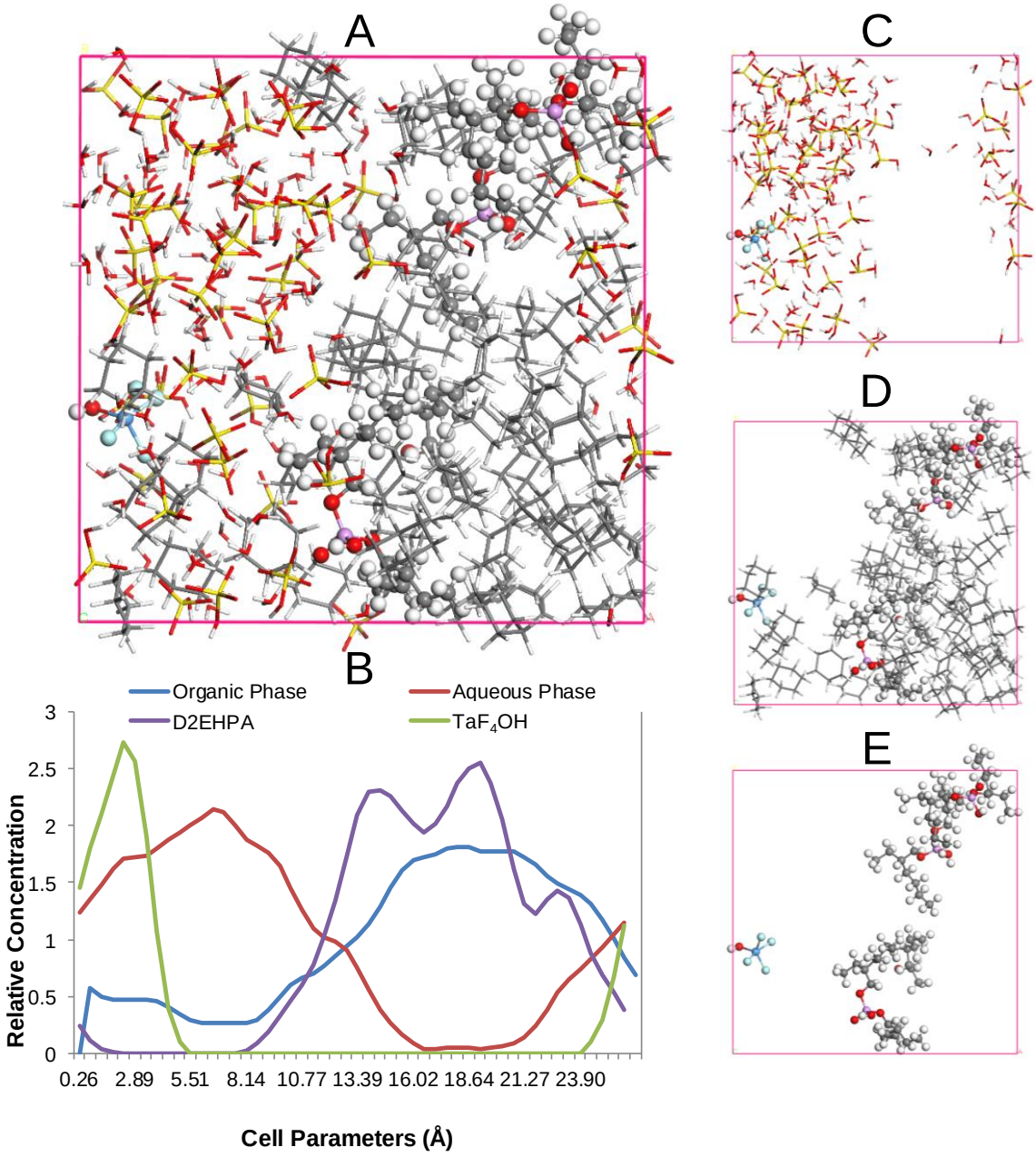

Figure 6.7 – Snapshot of system VI at 2 ns (10 M H_2SO_4: TaF_4OH, 54 HSO_4^-, 54 H_3O^+, 50 H_2O; Org: 3 D2EHPA + 1-octanol + 48 cyclohexane), where (A) shows the total modelled system, (B) density profiles of all the species present, (C) the aqueous phase containing H_2SO_4, H_2O and TaF_4OH, (D) the organic phase containing cyclohexane, D2EHPA, 1-octanol and TaF_4OH, and (E) the surface-active species D2EHPA, 1-octanol and TaF_4OH.

According to Figure 6.7A, aqueous molecules were present in the upper part of this region, while mixing occurred in the lower part, indicating possible third phase formation. Since the TaF_4OH was also found in this area, the third phase could have contributed to non-extraction. An interfacial

region was observed in the regions between 11 and 13 Å and between 23 and 25 Å, while the organic phase reached a maximum (and the aqueous phase a minimum) between 14 and 23 Å, confirming phase separation. According to the interface snapshot (Figure 6.7E), the TaF_4OH in 10 M was again not coordinated with the extractants, which is indicative of non-extraction. According to Figure 7B, the aqueous phase (red line) reached a maximum in the region of 1 to 10 Å.

When excluding D2EHPA and 1-octanol (Figure S4), the TaF_4OH did not extract and third phase formation occurred as had been observed previously. The 4 M system (TaF_4OH-4 M-without D2EHPA) again formed two linear phase columns while the organic phase formed a droplet within an aqueous bulk solution for 10 M system (TaF_4OH-10 M-without D2EHPA).

In conclusion, it was shown that when the aqueous phase was aged, TaF_4OH will probably be one of the species present. Irrespective of the acid concentration, the organic phases displayed simultaneous characteristics of a droplet and a bulk solution in the presence of TaF_4OH, while phase dissolution did not occur completely. This resulted in TaF_4OH being trapped in the formed third phase, leading to non-extraction.

6.3.1.4 $TaF_4.HSO_4$ system

The fourth species investigated was $TaF_4.HSO_4$. This species is likely to form when TaF_5 is added to an aqueous phase containing high concentrations of H_2SO_4. In the unlikely event that $TaF_4.HSO_4$ does form in low H_2SO_4 concentrations, the 4 M H_2SO_4 system was also investigated.

Figure 6.8 shows $TaF_4.HSO_4$ in the 4 M H_2SO_4 system, after 2 ns simulation time. From the aqueous phase snapshot (Figure 6.8A) it can be seen that a linear slab formed, with the organic phase at the sides and the aqueous phase situated in the middle of the snapshot, indicating dissolution of the biphasic solution. $TaF_4.HSO_4$ had hydrogen bonding with one H_2O molecule and was situated near the edge of the aqueous phase in the gap (organic phase) with the bound HSO_4 group in the direction of the organic phase, indicating possible extraction. Accordingly, similar to the $TaF_5.H_2O$-4 M system (Figure 6.4), the organic phase (Figure 6.8B) had two linear slabs to the left and right of the snapshot. The extractants lay on the edges of the organic phase with the oxygen atoms directed toward the aqueous phase. The concentration profile confirmed the two interfacial regions (3 – 4 Å and 16 – 17 Å) as well as the fact that the extractants (purple line) were mainly within the organic phase region (blue line) while the $TaF_4.HSO_4$ (green line) was in the organic bulk, indicating extraction.

In Figure 6.8E it can be seen that the HSO_4 group of $TaF_4.HSO_4$ was directly coordinated with one extractant, whereas in the $TaF_5.H_2O$-4 M system, extraction occurred due to the hydration sphere around TaF_5. Comparing snapshots D and E (Figure 6.8) with each other, it can be seen that the extractants due to hydrogen bonding pull H_2O and H_3O^+ molecules into the organic phase, albeit less than in the TaF_4OH systems (Figure 6.6 and Figure 6.7).

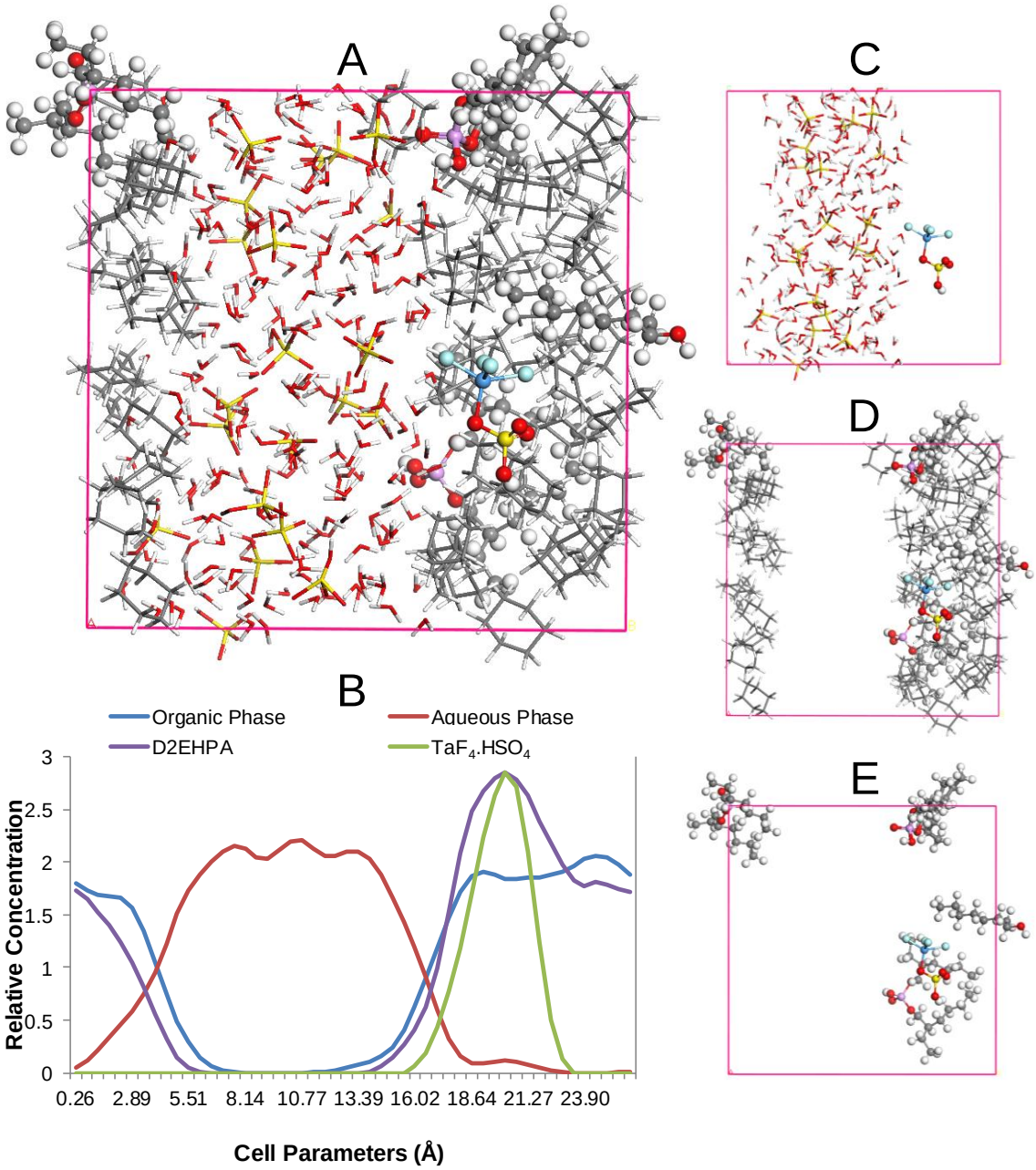

Figure 6.8 – Snapshot of system VII at 2 ns (4 M H_2SO_4: $TaF_4.HSO_4$, 21 HSO_4^-, 21 H_3O^+, 179 H_2O; Org: 3 D2EHPA, 1-octanol, 48 cyclohexane), where (A) shows the total modelled system, (B) density profiles of all the species present, (C) the aqueous phase containing H_2SO_4, H_2O and $TaF_4.HSO_4$, (D) the organic phase containing cyclohexane, D2EHPA, 1-octanol and $TaF_4.HSO_4$, and (E) the surface-active species D2EHPA, 1-octanol and $TaF_4.HSO_4$.

Figure 6.9 presents the snapshot results after 2 ns when $TaF_4.HSO_4$ was added to the 10 M H_2SO_4. From Figure 6.9A, phase separation can be clearly observed. The aqueous molecules were concentrated to the sides of the snapshot with two clear regions (organic phase) to the top and bottom of the snapshot, indicative of an organic droplet within an aqueous phase. $TaF_4.HSO_4$, with hydrogen bonds to two surrounding H_2O molecules, was situated to the bottom of the snapshot on the edge between the two phases, indicating possible extraction.

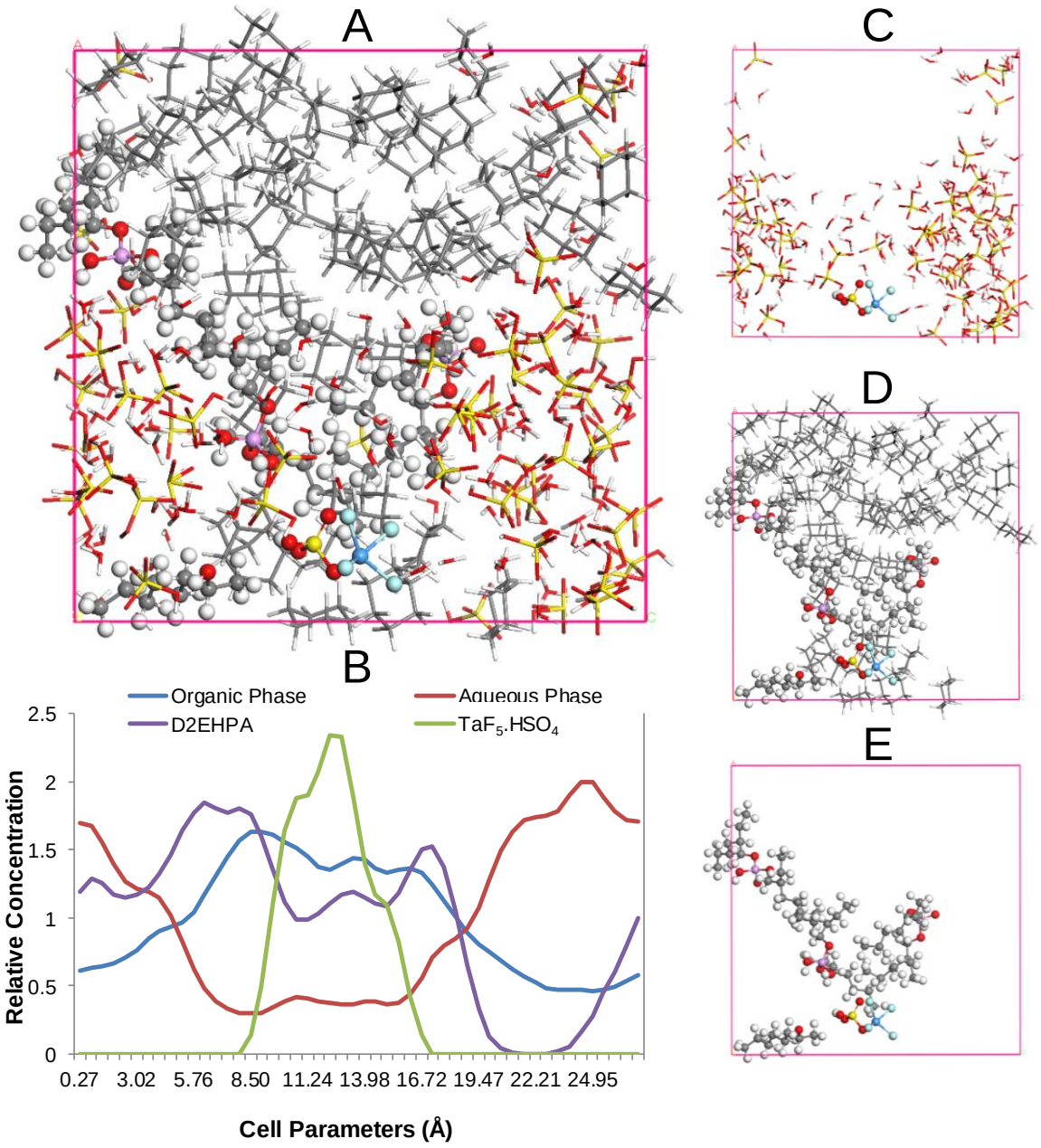

Figure 6.9 – Snapshot of system VIII at 2 ns (10 M H_2SO_4: $TaF_4.HSO_4$, 54 HSO_4^-, 54 H_3O^+, 50 H_2O; Org: 3 D2EHPA, 1-octanol, 48 cyclohexane), where (A) shows the total modelled system, (B) density profiles of all the species present, (C) the aqueous phase containing H_2SO_4, H_2O and $TaF_4.HSO_4$, (D) the organic phase containing cyclohexane, D2EHPA, 1-octanol and $TaF_4.HSO_4$, and (E) the surface-active species D2EHPA, 1-octanol and $TaF_4.HSO_4$.

The organic phase (Figure 6.9B) was situated to the top, through the middle and at the bottom of the snapshot, confirming phase separation. Therefore, as the H_2SO_4 concentration increased in this system, the concentration of H_2O molecules decreased resulting in the formation of aqueous droplets in the organic phase. Similar to the other systems, the extractants lay on the edges of the organic phase with the oxygen groups directed toward the aqueous phase. It can also be seen that $TaF_4.HSO_4$ was coordinated with one extractant at the interface (Figure 6.9E).

Comparing the total system (Figure 6.9A) with the concentration profile (Figure 6.9B), it can be seen that, while the organic phase (blue line) increased with decreasing aqueous phase (red line), there were always residuals of both phases present. This again indicates that both H_2O and H_3O^+ were pulled into the organic phase, leading to third phases. From the concentration profile, it can be seen that the extractants (purple line) lay from the interface to the bulk of the organic phase, whereas the $TaF_4.HSO_4$ species (green line) lay within the organic bulk region, confirming extraction.

To determine whether extraction of $TaF_4.HSO_4$ was due to the presence of D2EHPA, the 4 and 10 M systems were simulated without D2EHPA (Figure S5). The results were similar to the TaF_4OH without D2EHPA where $TaF_4.HSO_4$ did not extract and third phase formation occurred. Similar to TaF_4OH, the 4 M system ($TaF_4.HSO_4$-4 M-without D2EHPA) again showed phase dissolution into two linear columns, while the 10 M system ($TaF_4.HSO_4$-10 M-without D2EHPA) had an organic droplet within an aqueous bulk solution.

In conclusion, it seems that the $TaF_4.HSO_4$ that is assumed to form during SX with H_2SO_4 will extract in the presence of D2EHPA as extraction occurred from an aqueous droplet into an organic bulk solution in both the 4 and 10 M systems.

6.3.1.5 $TaF_3OH.HSO_4$ system

While we assumed that $TaF_4.HSO_4$ is formed in a TaF_5-H_2SO_4-environment, it is likely that $TaF_3OH.HSO_4$ could form during ageing of the solution as its formation was again slightly endothermic [Chapter 5]. Figure 6.10 shows $TaF_3OH.HSO_4$ in a 4 M system after 2 ns simulation time. According to Figure 6.10A, aqueous phase dissolution is evident as the molecules were situated in a droplet to the left, with some break-away at the top and bottom. The $TaF_3OH.HSO_4$ molecule is situated to the left in the bulk aqueous phase, indicating possible non-extraction. Comparing the total system (Figure 6.10A) with the concentration profile (Figure 6.10B), it seems that between 0 and 3 Å is a possible third phase interface containing $TaF_3OH.HSO_4$. Between 3 and 12.8 Å was mainly the aqueous phase, however again with some organic molecules and an extractant present, which could be indicative of third phase formation. From 12.8 to 16 Å was yet

another interfacial region, again with an extractant present, while the organic phase from 16 to 25 Å contained some aqueous molecules and an extractant, again indicative of third phase formation.

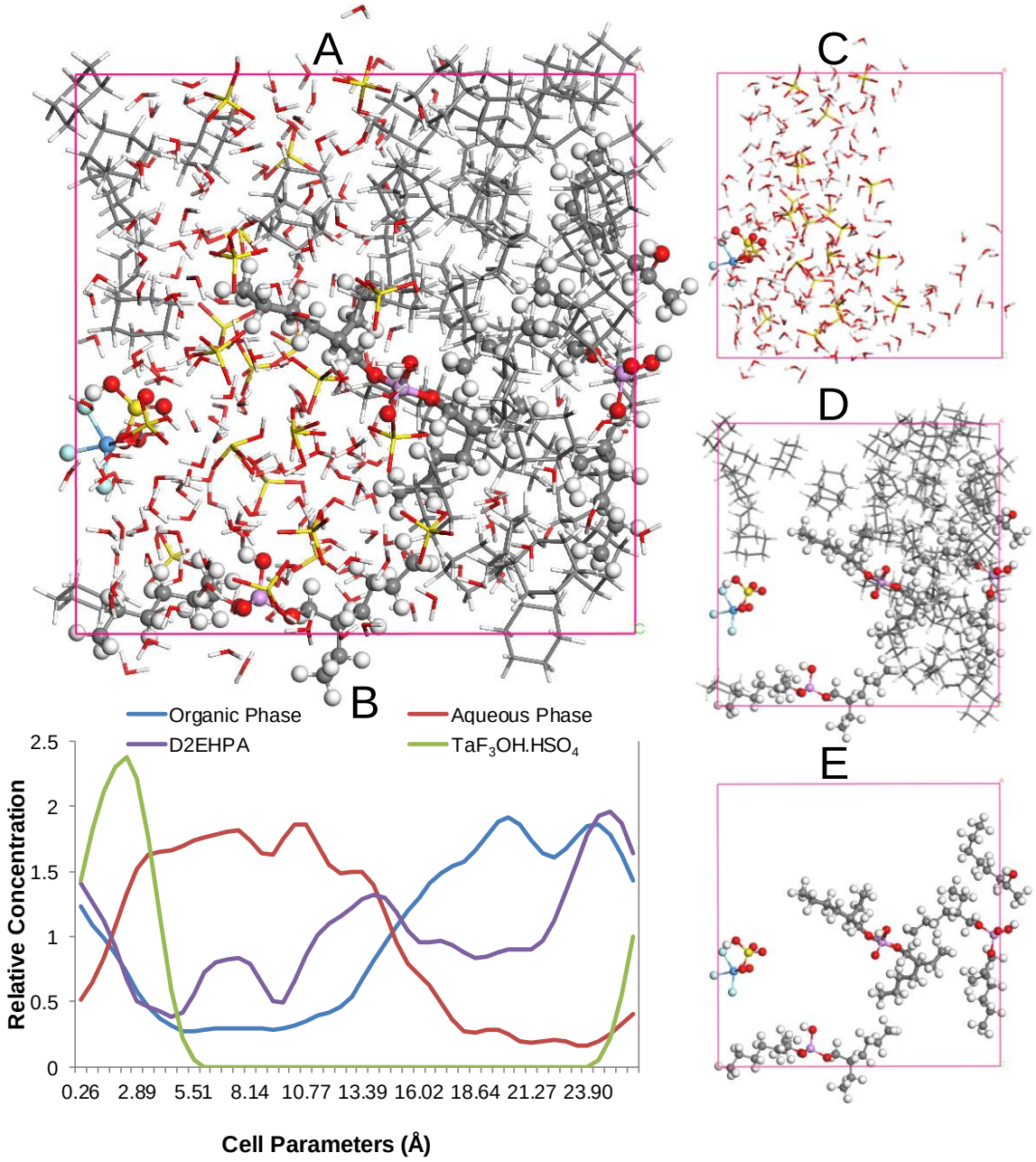

Figure 6.10 – Snapshot of system IX at 2 ns (4 M H_2SO_4: $TaF_3OH.HSO_4$, 21 HSO_4^-, 21 H_3O^+, 179 H_2O; Org: 3 D2EHPA, 1-octanol, 48 cyclohexane), where (A) shows the total modelled system, (B) density profiles of all the species present, (C) the aqueous phase containing H_2SO_4, H_2O and $TaF_3OH.HSO_4$, (D) the organic phase containing cyclohexane, D2EHPA, 1-octanol and $TaF_3OH.HSO_4$, and (E) the surface-active species D2EHPA, 1-octanol and $TaF_3OH.HSO_4$.

From the interface snapshot (Figure 6.10C) it is evident that $TaF_3OH.HSO_4$ is not coordinated with the extractants, again indicating non-extraction. The organic phase (Figure 6.10D) was

mostly situated in a column to the right of the snapshot, with break-away at the top and bottom. Similar to the previous system (Figure 6.8), the extractants lay on the organic edges. The significant phase overlap could lead to non-extraction as was the case for TaF_4OH (Figure 6.6).

Similar to the TaF_4OH system, it can be seen that by ageing the solution to form $TaF_3OH.HSO_4$, extraction becomes less likely. Literature [33] suggests that, by increasing the acid concentration, the ageing process might be reversed to lead to further extraction of metals.

The extraction of $TaF_3OH.HSO_4$ from a 10 M H_2SO_4 system (after a 2ns simulation time) is shown in Figure 6.11. The aquoeus phase (Figure 6.11A) was to the sides of the snapshot, with a circular clear part in the middle, indication phase dissolution with the organic phase forming a droplet (Figure 6.11B). $TaF_3OH.HSO_4$ was situated to the right on the edge between the phases, indicating possible non-extraction. The extractants were again on the edges, while $TaF_3OH.HSO_4$ was not coordinated with an extractant, indicating possible non-extraction (Figure 6.11E). Again, some H_2O molecules were present in the organic phase, indicating the formation of a third phase.

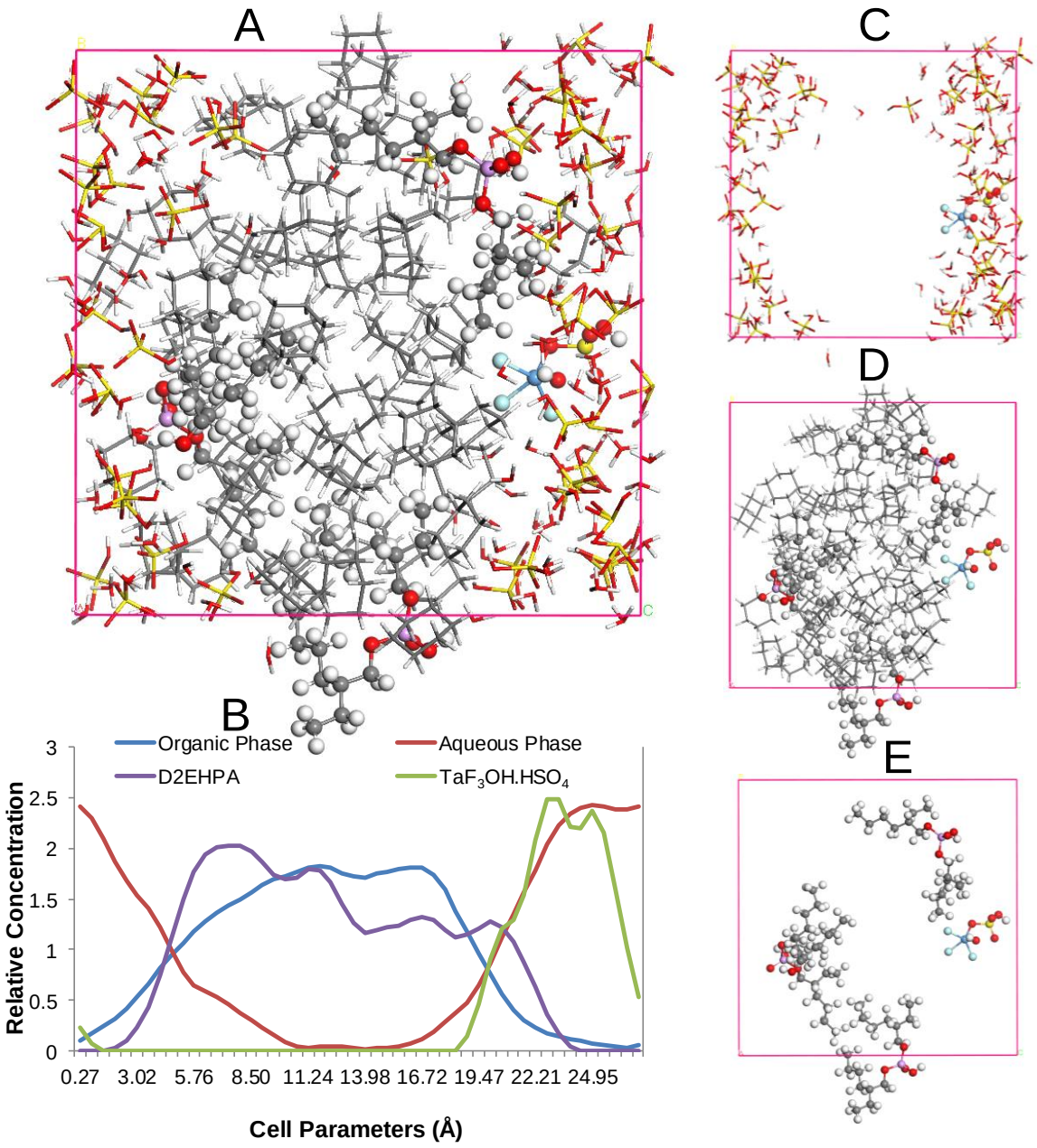

Figure 6.11 – System X (10 M H_2SO_4: $TaF_3OH.HSO_4$, 54 HSO_4^-, 54 H_3O^+, 50 H_2O; Org: 3 D2EHPA, 1-octanol, 48 cyclohexane), where (A) shows the total modelled system, (B) density profiles of all the species present, (C) the aqueous phase containing H_2SO_4, H_2O and $TaF_3OH.HSO_4$, (D) the organic phase containing cyclohexane, D2EHPA, 1-octanol and $TaF_3OH.HSO_4$, and (E) the surface-active species D2EHPA, 1-octanol and $TaF_3OH.HSO_4$.

In conclusion, when $TaF_3OH.HSO_4$ was present, possibly due to aqueous phase ageing, the organic phases displayed simultaneous characteristics of a droplet and third phase formation. Consequently, $TaF_3OH.HSO_4$ was trapped in the resulting third phase, leading to non-extraction.

6.3.2 4x4x2 3D systems

After investigating smaller systems (1x1x1) containing only one of each of the identified five molecules that could be present during SX, the next step was to increase the system size (4x4x2), combining all the Ta^{5+} species to obtain a more realistic system. Since these systems are 32 times larger than the 1x1x1 cells, they contained 7 TaF_5, 7 $TaF_5.H_2O$, 6 TaF_4OH, 6 $TaF_4.HSO_4$, and 6 $TaF_3OH.HSO_4$, apart from the acid, H_2O, extractant, modifier and organic solvent. The reason for this molar ratio was based on 1) adding the possible Ta^{5+} species identified in the previous chapters to determine their influence on each other, and 2) to have equal chances of extraction even though some of the species will only be present after ageing. At the beginning, it was ensured that the system was perfectly mixed (Figure S7). Again, both the 4 and the 10 M H_2SO_4 systems were investigated; however, a 2 ns simulation time was not sufficient for complete phase dissolution to occur. Therefore, the simulation time was increased to 10 ns, of which the obtained distribution is shown in Figure 6.12. Similar to the 4 M 1x1x1 systems, there were defined aqueous and organic phase regions (Figure 6.12A), where the aqueous phase formed droplets within an organic bulk.

The concentration profile (Figure 6.12B) shows that, when the aqueous phase (red line) reached a maximum concentration, the organic phase (blue line) reached a minimum and vice versa, indicating phase dissolution, similar to what had been observed for the 1x1x1 system. The concentration profile of D2EHPA (purple line) followed the same trend as the organic phase profile, which is indicative of surface activity. However, the Ta^{5+} concentration (green line), showed peaks at various locations over the whole cell, indicative of partial extraction as had been expected.

Figure 6.12C shows the aqueous phase with all the Ta^{5+} species. Similar to the results presented in Section 6.3.1, the TaF_5, $TaF_5.H_2O$ and $TaF_4.HSO_4$ extracted into the organic phase, while the TaF_4OH and $TaF_3OH.HSO_4$, the products of ageing, did not extract. In some cases, the H_2O molecules surrounding the Ta^{5+} were also co-extracted into the organic phase.

Figure 6.12D shows that the extractant lay on the interface (as was observed in Section 6.3.1), with the O atoms of D2EHPA in the direction of the aqueous phase, creating strong hydrogen bonds, while the Ta^{5+} had moved to the organic phase. Similar to the 1x1x1 system, it was found that the extractants are surface active, but as soon as the D2EHPA-TaF_5-$5H_2O$ system was formed, the chemical characteristics changed and the newly formed macro molecule moved into the organic phase where Ta^{5+}, surrounded by H_2O molecules, was ‘released’ into the organic phase and D2EHPA returned to the surface.

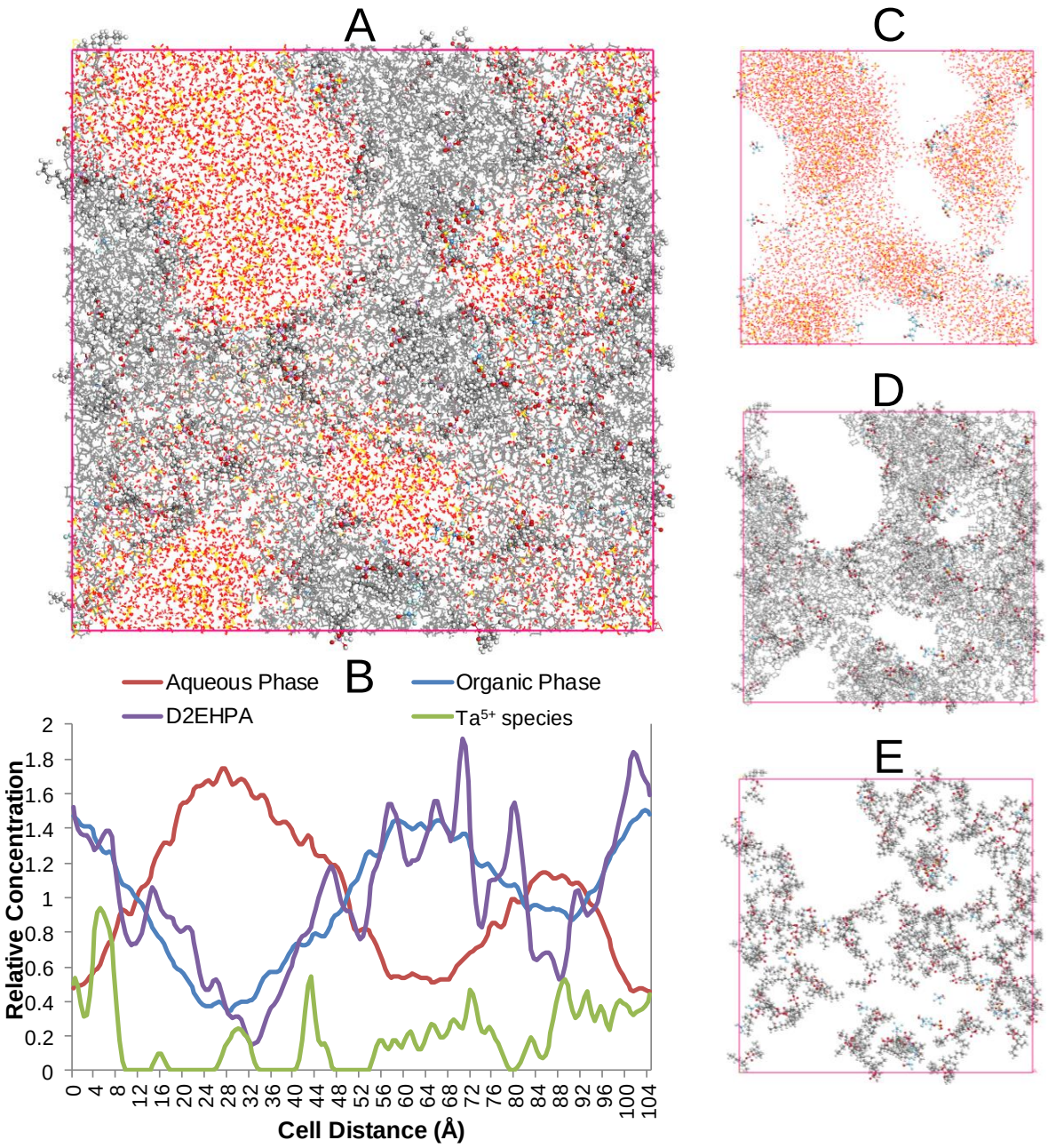

Figure 6.12 – 4x4x2 mixed system after 10 ns simulation time (4 M H_2SO_4: 7 TaF_5, 7 $TaF_5.H_2O$, 6 TaF_4OH, 6 $TaF_4.HSO_4$, 6 $TaF_3OH.HSO_4$, 672 HSO_4^-, 672 H_3O^+, 5696 H_2O; Org: 96 D2EHPA, 32 1-octanol, 1536 cyclohexane) where A shows the total modelled system, (B) density profiles of all the species present, (C) the aqueous phase containing H_2SO_4, H_2O and Ta^{5+}, (D) the organic phase containing cyclohexane, D2EHPA, 1-octanal and Ta^{5+}, and (E) the surface-active species D2EHPA, 1-octanol and Ta^{5+}.

Figure 6.13 shows the results for the simulation of a 4x4x2 system where the aqueous phase had a 10 M H_2SO_4 concentration. Similar to the 10 M 1x1x1 systems, the organic phase formed a bulk phase in the middle of the cell with droplets of the aqueous phase on all sides, indicating phase dissolution (Figure 6.13A). From the concentration profile (Figure 6.13B), phase dissolution is evident as the aqueous phase reached a maximum as the organic phase reached a minimum

and vice versa. From the results it is clear that the Ta^{5+} species were mainly located in two regions (21 – 55 Å and 75 – 109 Å), the first apparently at an interface and the second in a predominantly organic phase, again indicting partial separation. Comparing this apparent discrepant data with Figure 6.13C and D, it can be confirmed that, similar to the 1x1x1 systems, the TaF_5, $TaF_5.H_2O$ and $TaF_4.HSO_4$ molecules extracted, while TaF_4OH and $TaF_3OH.HSO_4$ were concentrated within the interfacial region.

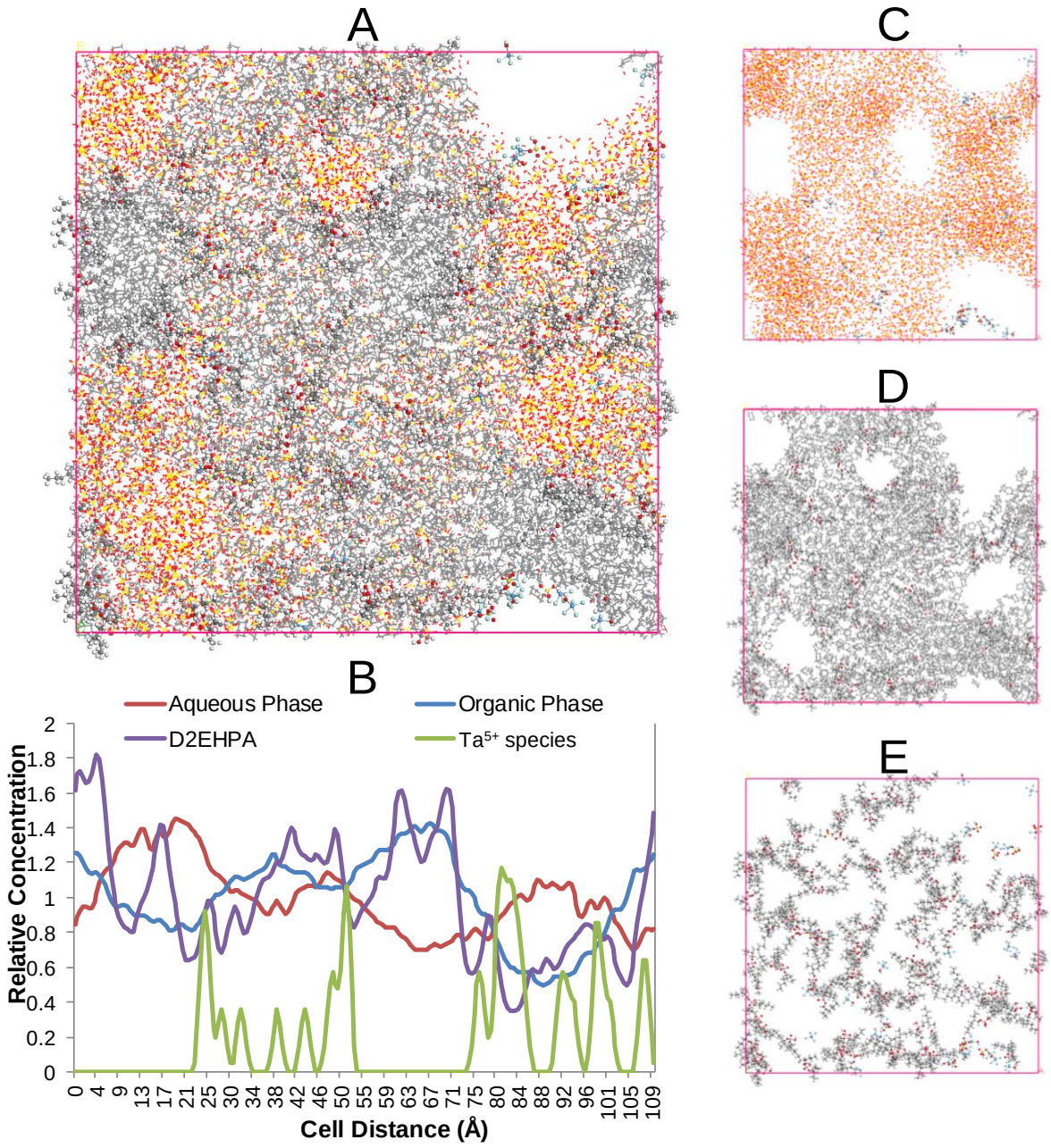

Figure 6.13 – 4x4x2 mixed system after 10 ns simulation time (10 M H_2SO_4: 7 TaF_5, 7 $TaF_5.H_2O$, 6 TaF_4OH, 6 $TaF_4.HSO_4$, 6 $TaF_3OH.HSO_4$, 1728 HSO_4^-, 1728 H_3O^+, 1600 H_2O; Org: 96 D2EHPA, 32 1-octanol, 1536 cyclohexane) where A shows the total modelled system, (B) density profiles of all the species present, (C) the aqueous phase containing H_2SO_4, H_2O and Ta^{5+}, (D) the organic phase containing cyclohexane, D2EHPA, 1-octanal and Ta^{5+}, and (E) the surface-active species D2EHPA, 1-octanol and Ta^{5+}.

When comparing the 4 M and 10 M results (Figure 6.12 and Figure 6.13), it can be concluded that in a low H_2SO_4 concentration environment, the $TaF_5.nH_2O$ where n = 4 – 6 was formed, before being extracted into the organic phase. If, however, ageing and therefore the formation of TaF_4OH occurs, extraction would not occur. In the 10 M it was seen that two Ta species formed in the aqueous phase, $TaF_5.nH_2O$ where n = 4 – 6 and $TaF_4.HSO_4.nH_2O$ where n = 2 – 3. However, both of these Ta^{5+} systems were extracted into the organic phase. Again, with the formation of $TaF_3OH.HSO_4$ as an ageing product, extraction would not occur.

6.4 Conclusion

Due to a lack in Ta speciation data, molecular modelling was used to determine the behaviour of Ta-containing salts in a H_2SO_4 medium during SX, focussing on TaF_5, $TaF_5.H_2O$, TaF_4OH, $TaF_4.HSO_4$ and $TaF_3OH.HSO_4$. Using a 1x1x1 system it was seen that, when the H_2SO_4 concentration was set to 4 M, the aqueous phase tended to form a droplet within an organic bulk solution, while more break-away between the phases occurred when the H_2SO_4 concentration was increased to 10 M.

From the different species it can be concluded that $TaF_5.H_2O$ is the most likely to be present in a low acidic medium (4 M H_2SO_4), which can be extracted with D2EHPA. If ageing of this solution would occur, TaF_4OH would from, which was not extracted either with or without D2EHPA, irrespective of the H_2SO_4 concentration. In high acidic media (10 M H_2SO_4) $TaF_4.HSO_4$ is the species most likely to be present for extraction. From the simulations, it was seen that this species can only be extracted if D2EHPA was present for both 4 and 10 M H_2SO_4 concentrations. If ageing of this solution would occur, $TaF_3OH.HSO_4$ would form, which showed no extraction with and without D2EHPA, irrespective of the H_2SO_4 concentration. These results were confirmed when using the 4x4x2 system.

6.5 References

[1] E. Bidari, M. Irannejad, M. Gharabaghi, Solvent extraction recovery and separation of cadmium and copper from sulphate solution, Journal of Environmental Chemical Engineering, 1 (2013) 1269 - 1274.

[2] M. Noori, F. Rashchi, A. Babakhani, E. Vahidi, Selective recovery and separation of nickel and vanadium in sulfate media using mixtures of D2EHPA and Cyanex 272, Separation and Purification Technology, 136 (2014) 265 - 273.

[3] X. Li, C. Wei, Z. Deng, M. Li, C. Li, G. Fan, Selective solvent extraction of vanadium over iron from a stone coal/black shale acid leach solution by D2EHPA/TBP, Hydrometallurgy, 105 (2011) 359 - 363.

[4] J.R. Kumar, H.I. Lee, J.Y. Lee, J.S. Kim, J.S. Sohn, Comparison of liquid-liquid extraction studies on platinum(IV) from acidic solutions using bis(2,4,4-trimethylpentyl) monothiophosphinic acid, Separation and Purification Technology, 63 (2008) 184 - 190.

[5] R.K. Biswas, M.A. Hayat, Solvent extraction of zirconium(IV) from chloride media by D2EHPA in kerosene, Hydrometallurgy, 63 (2002) 149 - 158.

[6] M.S. Lee, R. Banda, S.H. Min, Separation of Hf(IV)–Zr(IV) in H_2SO_4 solutions using solvent extraction with D2EHPA or Cyanex 272 at different reagent and metal ion concentrations, Hydrometallurgy, 152 (2015) 84 - 90.

[7] Z. Zhu, C.Y. Cheng, Solvent extraction technology for the separation and purification of niobium and tantalum: A review, Hydrometallurgy, 107 (2011) 1 - 12.

[8] G.J.-P. Deblonde, V. Wiegel, Q. Bellier, R. Houdard, F. Delvallée, S. Bélair, D. Beltrami, Selective recovery of niobium and tantalum from low-grade concentrates using a simple and fluoride-free process, Separation and Purification Technology, 162 (2016) 180 - 187.

[9] O.S. Ayanda, F.A. Adekola, A review of niobium-tantalum separation in hydrometallurgy, Journal of Minerals & Materials Characterization & Engineering, 10 (2011) 245 - 256.

[10] M.J. Ungerer, H.M. Krieg, G. Lachmann, D.J.v.d. Westhuizen, Comparison of extractants for the separation of TaF_5 and NbF_5 in different acidic media, Hydrometallurgy, 144-145 (2014) 195 - 206.

[11] D.S. Flett, Solvent extraction in hydrometallurgy: the role of organophosphorus extractants, Journal of Organometallic Chemistry, 690 (2005) 2426 - 2438.

[12] M.J. Ungerer, C.G.C.E. van Sittert, D.J. van der Westhuizen, H.M. Krieg, Molecular modelling of tantalum penta-halides during hydrolysis and oxidation reactions, Computational and Theoretical Chemistry, 1090 (2016) 112 - 119.

[13] Material Studio Modelling Environment, Accelrys Software Inc., San Diego, 2012.

[14] J.P. Perdew, Y. Wang, Accurate and simple analytic representation of the electron-gas correlation energy, Physical Review B, 45 (1992) 13244 - 13249.

[15] B. Delley, Ground-state enthalpies: evaluation of electronic structure approaches with emphasis on the density functional method, The Journal of Physical Chemistry A, 110 (2006) 13632 - 13639.

[16] J.P. Perdew, K. Burke, M. Ernzerhof, Generalized gradient approximation made simple, Physical Review Letters, 77 (1996) 3865 - 3868.

[17] A. Tkatchenko, M. Scheffler, Accurate Molecular Van Der Waals Interactions from Ground-State Electron Density and Free-Atom Reference Data, Physical Review Letters, 102 (2009) 073005.

[18] B. Delley, Modern Density Functional Theory: A tool for chemistry, in: J.M. Seminario, P. Politzer (Eds.) Theoretical and Computational Chemistry, 1995.

[19] A. Klamt, G. Schüürmann, COSMO: a new approach to dielectric screening in solvents with explicit expressions for the screening energy and its gradient, Journal of the Chemical Society, Perkin Transactions 2, (1993) 799 - 805.

[20] B. Delley, The conductor-like screening model for polymers and surfaces, Molecular Simulation, 32 (2006) 117 - 123.

[21] A.K. Rappé, K.S. Colwell, C.J. Casewit, Application of a universal force field to metal complexes, Inorganic Chemistry, 32 (1993) 3438 - 3450.

[22] C.J. Casewit, K.S. Colwell, A.K. Rappé, Application of a universal force field to main group compounds, Journal of American Chemical Society, 114 (1992) 10046 - 10053.

[23] A.K. Rappé, C.J. Casewit, K.S. colwell, W.A. Goddard III, W.M. Skiff, UFF, a full periodic table force field for molecular mechanics and molecular dynamics simulations, Journal of American Chemical Society, 114 (1992) 10024 - 10035.

[24] C.J. Casewit, K.S. Colwell, A.K. Rappé, Application of a universal force field to organic molecules, Journal of American Chemical Society, 114 (1992) 10035 - 10046.

[25] M.P. Tosi, Evaluation of electrostatic lattice potentials by the Ewald method, Academic Press, New York & London, 1964.

[26] P.P. Ewald, Die Berechnung optischer und elektrostatischer Gitterpotentiale, Annalen der Physik, 369 (1921) 253 - 287.

[27] S. Nosé, A molecular dynamics method for simulations in the canonical ensemble, Molecular Physics, 52 (1984) 255 - 268.

[28] S. Nosé, A unified formulation of the constant temperature molecular dynamics methods, The Journal of Chemical Physics, 81 (1984) 511 - 519.

[29] S. Nosé, Constant temperature molecular dynamics methods, Progress if Theoretical Physics Supplements, 103 (1991) 1 - 46.

[30] A.D. McNaught, A. Wilkinson, IUPAC. Compendium of chemical terminology, 2nd ed., Blackwell Scientific Publications, Oxford, 1997.

[31] N. Sieffert, G. Wipff, Alkali cation extraction by calix[4]crown-6 to room-temperature ionic liquids. The effect of solvent anion and humidity investigated by molecular dynamics simulations, The Journal of Physical Chemistry A, 110 (2006) 1106 - 1117.

[32] A.M. Wilson, P.J. Bailey, P.A. Tasker, J.R. Turkington, R.A. Grant, J.B. Love, Solvent extraction: The coordination chemistry behind extractive metallurgy, Chemical Society Reviews, 43 (2014) 123 - 134.

[33] L. De Beer, D.J. Van der Westhuizen, H.M. Krieg, Solvent extraction and separation of hafnium from zirconium using Ionquest 801, The Journal of The Southern African Institute of Mining and Metallurgy, 116 (2016) 93 - 99.

6.6 Supplementary Information

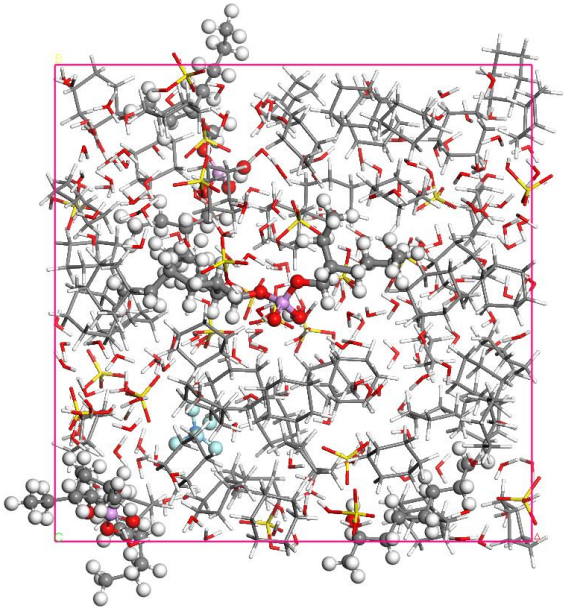

Figure S1 – System A (4 M H_2SO_4: TaF_5, 21 HSO_4^-, 21 H_3O^+, 179 H_2O, Org: 3 D2EHPA, 1-octanol, 48 cyclohexane). A snapshot of perfect mixing before the MD runs.

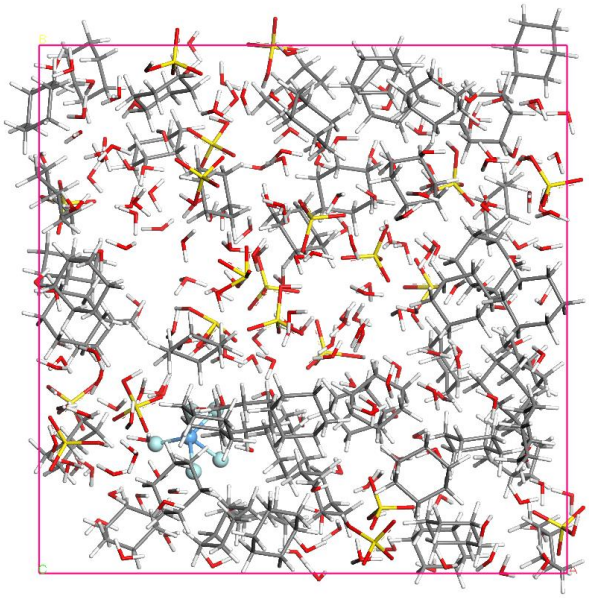

Figure S2 – 4 M acid system containing TaF_5 without extractants or modifier (21 HSO_4^-, 21 H_3O^+, 179 H_2O, Org: 48 cyclohexane). A snapshot of perfect mixing before the MD runs.

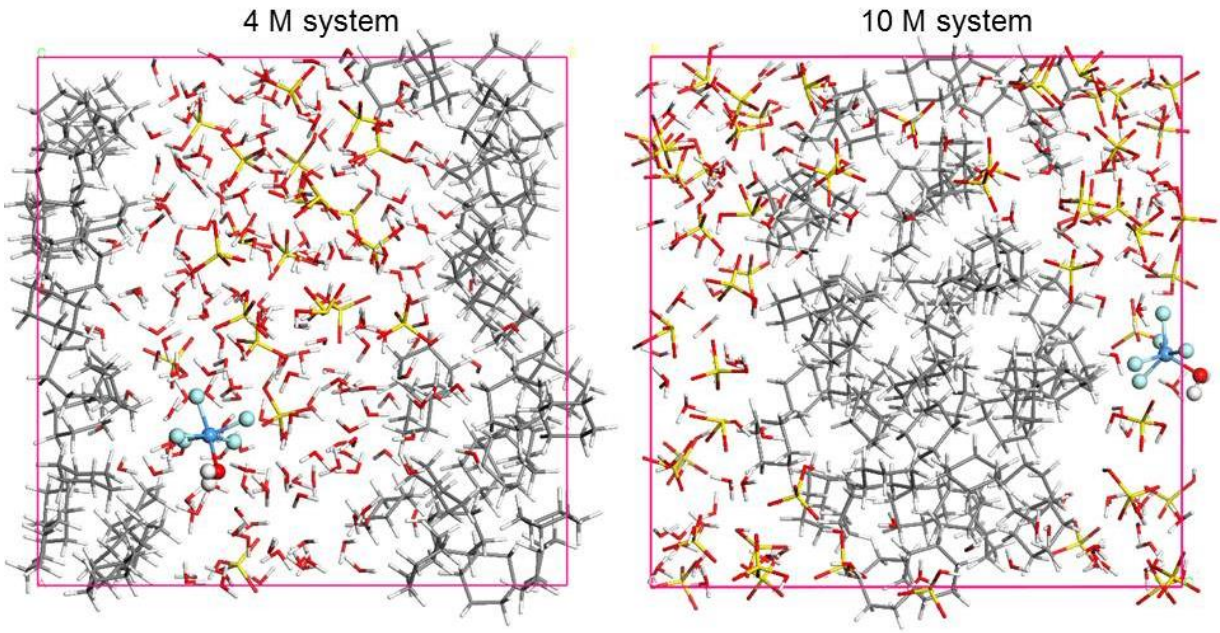

Figure S3 – $TaF_5.H_2O$ in the 4 and 10 M acid systems without the extractants D2EHPA and 1-octanol.

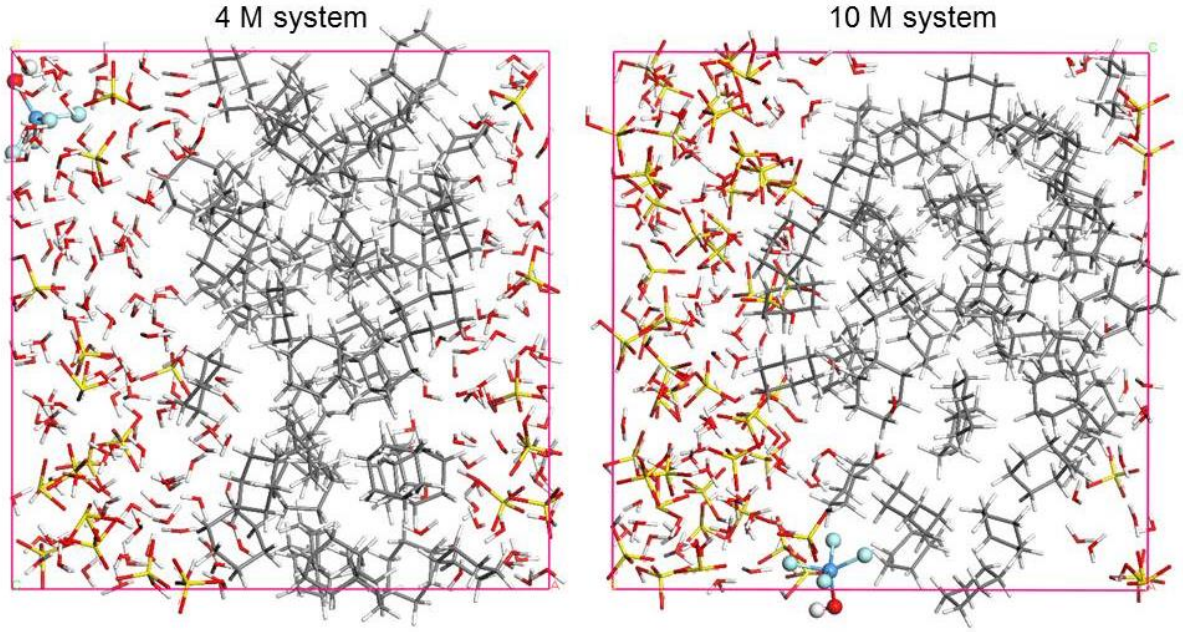

Figure S4 – TaF_4OH in the 4 and 10 M acid systems without the extractants D2EHPA and 1-octanol.

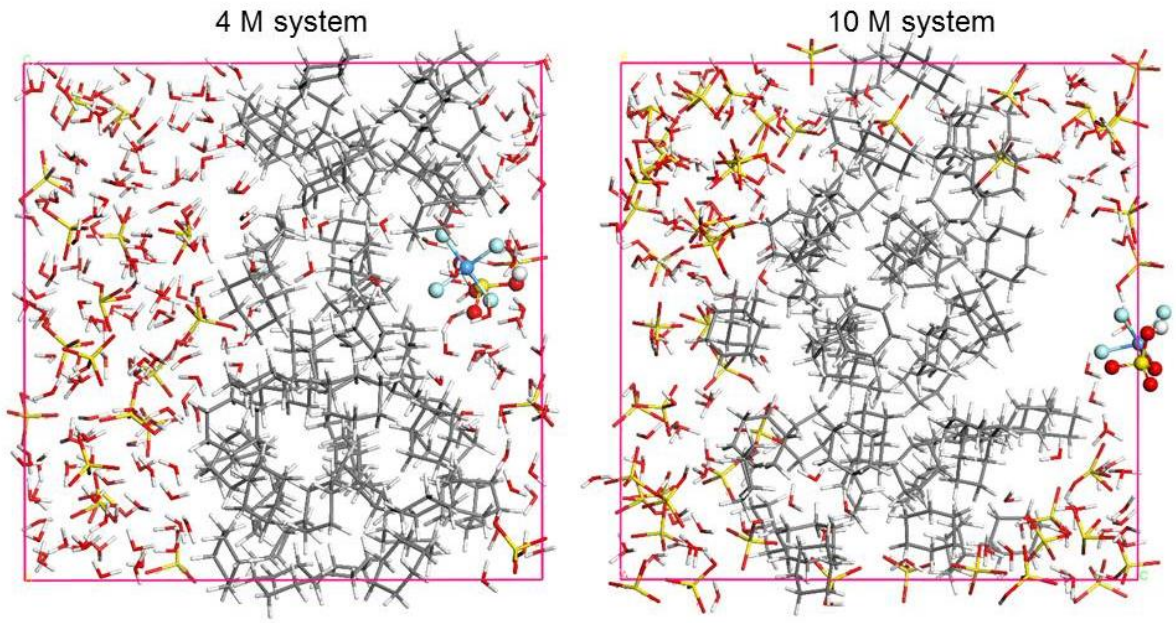

Figure S5 – $TaF_4.HSO_4$ in the 4 and 10 M acid systems without the extractants D2EHPA and 1-octanol.

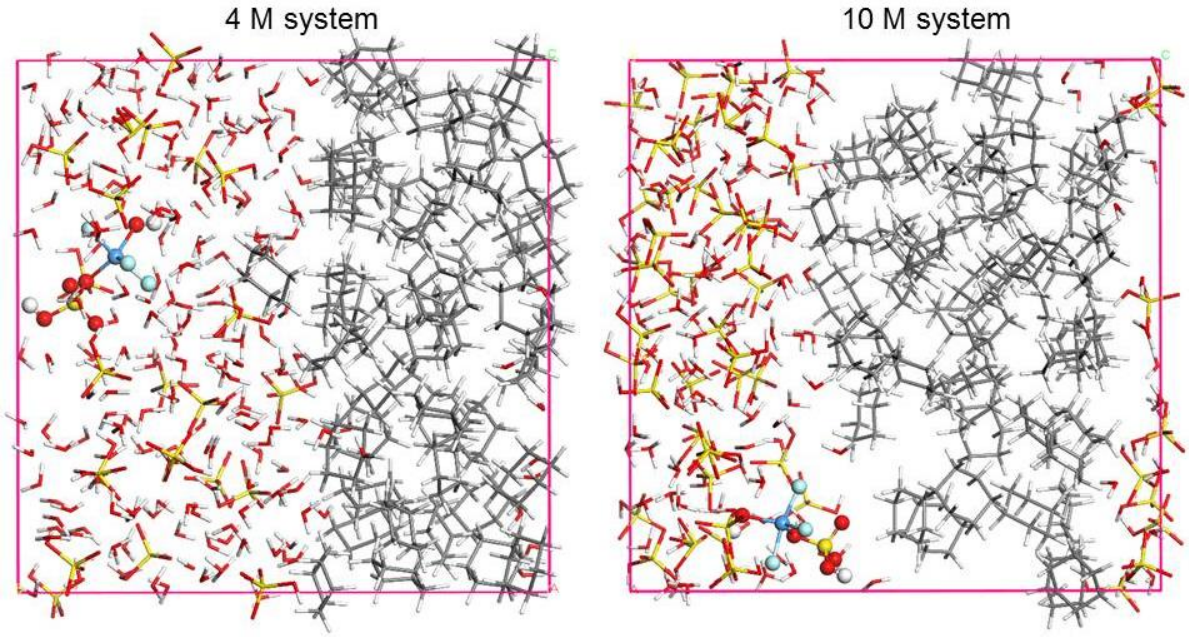

Figure S6 – $TaF_3OH.HSO_4$ in the 4 and 10 M acid systems without the extractants D2EHPA and 1-octanol.

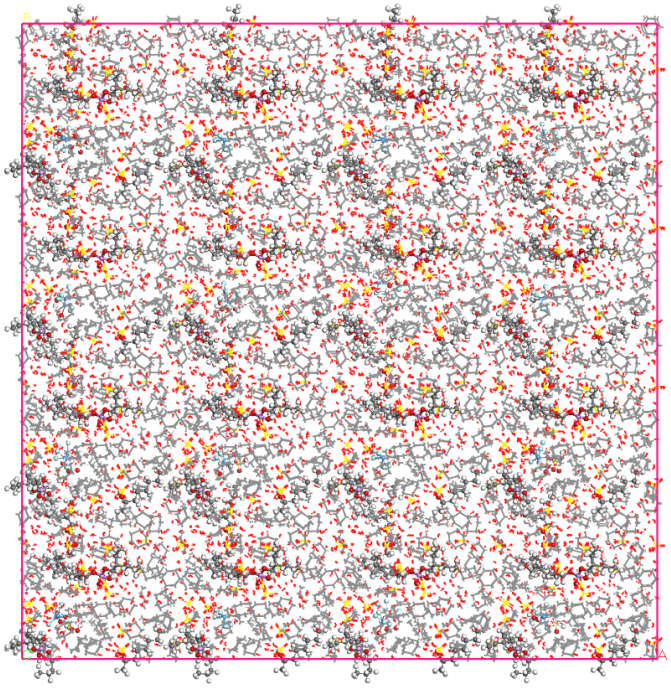

Figure S7 – Geometry optimised 4x4x2 mixed system (4 M H_2SO_4: 7 TaF_5, 7 $TaF_5.H_2O$, 6 TaF_4OH, 6 $TaF_4.HSO_4$, 6 $TaF_3OH.HSO_4$, 672 HSO_4^-, 672 H_3O^+, 5696 H_2O, Org: 96 D2EHPA, 32 1-octanol, 1536 cyclohexane).

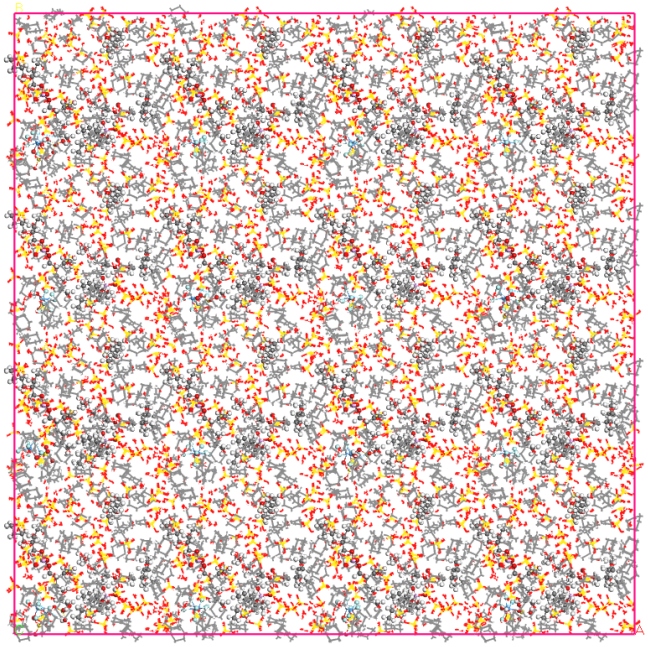

Figure S8 – Geometry optimised 4x4x2 mixed system (10 M H_2SO_4: 7 TaF_5, 7 $TaF_5.H_2O$, 6 TaF_4OH, 6 $TaF_4.HSO_4$, 6 $TaF_3OH.HSO_4$, 1728 HSO_4^-, 1728 H_3O^+, 1600 H_2O, Org: 96 D2EHPA, 32 1-octanol, 1536 cyclohexane).

EVALUATION AND RECOMMENDATIONS

7.1 Introduction

Although a conclusion was presented within each experimental chapter, it is the purpose of this chapter to summarize, interpret and evaluate the key findings obtained during the study and make recommendations for future work. The successes and shortcomings of this study will be discussed by evaluating the achievements attained compared to the objectives set in Chapter 1.

According to Chapter 1, the aim of this study was to use molecular modelling to investigate the solvent extraction (SX) of tantalum (Ta) on a molecular level, comparing the theoretical obtained data with experimental data. In other words, to investigate and understand, through the use of molecular modelling, the species and reactions that may form or occur during the SX process of specifically Ta. To achieve this aim, various objectives where identified (Chapter 1):

i. Geometry optimisation of all the components (metal species, ions, acids and extractants) involved in the SX process.
ii. Compiling energy profiles to investigate various reaction equations to determine the most probable reaction pathway and subsequent mechanisms of SX.
iii. Simulation of the organic and aqueous phases in periodic systems (creating unit cells).
iv. Combining the periodic organic and aqueous phases to simulate the SX process.
v. Compare experimental SX results with the modelled SX results.

The following sections will demonstrate that the above-mentioned objectives were successfully achieved (Section 7.2 – Evaluation) and possible areas of improvement (Section 7.3 – Recommendations) will be discussed.

7.2 Evaluation

An in-depth literature study of experimental data on SX of Ta and Nb, as well as modelled data of Ta species, revealed that the literature was limited. Therefore, method development was the first step in establishing the use of molecular modelling for this study. This was followed by investigating various species present during SX and reaction pathways for the formation of these species.

7.2.1 Method development

A case study was selected (Chapter 3) where various functional/basis set combinations were used to model $TaCl_5$ species and reactions, comparing the obtained modelled data to literature.

The methods were repeated using TaF_5 and again all the data was compared. When evaluating this data, it became clear that the PBE(DNP+) combination gave the best correlation with previous modelling and that this model was suitable for future work on TaF_5. Even though all the data compared well with literature, the drawback was that all these species and reactions were calculated with an implicit solvent model (COSMO), although all the species in the experimental SX setup would be in an aqueous phase where the H_2O molecules in the system have an effect on the whole SX system.

The next step for the model development (Chapter 4) was to investigate the effect of implicitly and explicitly adding H_2O molecules to the H_2SO_4 system, again using different functional/basis set combinations. It was seen that our modelled data correlated with other published work, even though COSMO was not used in previous studies. Since COSMO had effected not only the geometry optimisation, but also the vibrational frequencies of the molecules, it was recommended to use COSMO for simulations at infinite dilution.

The final step of this section was to expand the model to combine periodic systems to determine the behaviour of each of the Ta^{5+} species that may form during SX (from Chapter 5) in a complete SX system (Chapter 6).

According to some literature, it was recommended to construct the organic and aqueous phases separately. This was done where the phases were combined, after which simulations were carried out for mixing and de-mixing of the phases. However, using this approach, perfect mixing of the phases was not obtained. To overcome this the system was heated in cycles from 300K to 500K to obtain mixed phases which again resulted in incomplete mixed phases. Since the purpose of this simulation was to simulate laboratory conditions, the SX samples were modelled at room temperature. Subsequently, it was decided to combine all the relevant species in the predetermined quantities as a complete periodic system at laboratory conditions (298 K and 1 atm) to run the simulations.

It was decided to first construct small scale (1x1x1) periodic systems containing single metal species in two different acid media (4 and 10 M H_2SO_4). The second part was to combine all the Ta^{5+} species in a 4 and 10 M H_2SO_4 4x4x2 system. By combining all the species as stated in the method, perfect mixing was obtained.

However, the drawback of this method was the limited number of atoms and molecules that could be simulated in the periodic systems. To run these SX simulations at true concentrations of each specie present, more than 100 000 molecules would have to be added to the periodic system, which in turn would increase the computational resources needed to run this calculation beyond those available for this study. Even with these simplifications in this study, the observed tendencies agreed with the experimental SX tendencies observed. We were able to confirm with

the molecular dynamics (MD) study that the 2 ns and 10 ns simulation time was suggested from literature for the 1x1x1 and 4x4x2 periodic systems respectively, gave results that were in good agreement with literature.

7.2.2 Species

Due to the lack in experimental and modelling speciation data, various Ta species and geometries were investigated. As stated in the previous section, a case study was selected whereby different species resulting from both the $TaCl_5$ and TaF_5 reactions with H_2O were simulated (Chapter 3). Here it was shown, both from other modelled data and this study, that even though experimental literature suggested that various oxy-halide species ($TaOX_3$ and TaO_2X, with X = Cl or F) could form, these formations were unlikely. The most likely species to form however were $TaX_5.H_2O$ and TaX_4OH.

The next section entailed the investigation of H_2SO_4 species in different size H_2O environments (Chapter 4). Although PBE(DNP+) did not necessary gave the best results for the H_2SO_4/H_2O system when compared to literature, it was important to keep the method the same throughout this study for comparison reasons.

The main conclusions from Chapter 3 and 4 were that $TaF_5.H_2O$, TaF_4OH, HSO_4^- and H_3O^+ are the most likely species to be present during SX. These were investigated further in Chapter 5, where the behaviour of Ta in an aqueous sulphuric acid environment was investigated. To reduce the amount of calculations it was decided to use the PBE(DNP+) combination from the first step (method development) in combination with COSMO from the second step. When TaF_5 reacted with H_2SO_4 and H_2O, various reactions, species and geometries were proposed. It was seen that that initially $TaF_5.H_2O$ and after ageing of the solution TaF_4OH formed in a H_2O environment (or low acid concentration). In a H_2SO_4 medium $TaF_4.HSO_4$ was most likely to form while $TaF_3OH.HSO_4$ formed to a lesser degree after ageing. The formation of all other species, including $TaOF_3$ were endothermic. The main drawback in this chapter was the lack of speciation data in literature, and thus these species cannot be compared in terms of existence or stability.

After the construction of the 1x1x1 and 4x4x2 periodic systems, MD simulations were carried out to simulate the de-mixing of the phases and extraction of the Ta^{5+} species. According to Chapter 5, the most likely species that formed ($TaF_5.H_2O$, $TaF_4.HSO_4$) were also most likely the species that were extracted to the organic phase. Contrary, the species that most likely formed after ageing (TaF_4OH and $TaF_3OH.HSO_4$) did not extract to the organic phase, confirming the

effect of ageing on SX. These MD simulations are in good agreement with our previous experimental work.

7.2.3 Reaction pathways

In terms of reaction pathways and energies, it was seen from the first part (Chapter 3) that TaF_5 and $TaCl_5$ reacted in a similar way. When TaF_5 reacted with H_2O, results showed it was unlikely to form oxyfluoride species, including $TaOF_3$ and TaO_2F. However, the formation of $TaF_5.H_2O$ and TaF_4OH was exothermic, which was in good agreement with literature.

From the energy calculations of H_2SO_4 and H_2O (Chapter 4), it was determined that the formation of $H_2SO_4.H_2O$, $HSO_4^-.H_2O$ and $H_2SO_4.2H_2O$ was possible. However, it was shown that with the explicit addition of H_2O molecules, HSO_4^- and H_3O^+ are the most likely species to exist in a bulk solution. In addition, it was shown that the explicit addition of H_2O molecules resulted in the lowering of the overall reaction energies and thus in the stabilisation of the systems. This effect of the lowering energy with increasing water was also confirmed in literature.

From the various reactions investigated in a 1:1:10 metal:acid:water ratio (Chapter 5), multiple hydrogen bonds formed which stabilised the different acid species, again resulting in the lowering of the reaction energies. Although it was shown that different reactions were possible between TaF_5, H_2SO_4 and H_2O, according to their energies, only four species are most probably available during extraction, namely $TaF_5.H_2O$ and $TaF_4.HSO_4$, and if ageing occurred TaF_4OH and to a lesser degree $TaF_3OH.HSO_4$.

During the SX simulations (Chapter 6), it was seen that, similar to the experimental data, the extractant D2EHPA selectively extracted $TaF_5.H_2O$ and $TaF_4.HSO_4$. In addition, it was seen from the experimental data that if the solution was aged, which lead to the formation of TaF_4OH or $TaF_3OH.HSO_4$, extraction did not occur. As was mentioned earlier, speciation of Ta data is limited in literature. However, the data form Chapters 3 and 4 are in good agreement with the available literature data. Seeing how the data in Chapters 5 and 6 are based on the data from Chapters 3 and 4, it can be concluded that the data presented in Chapters 5 and 6 are acceptable.

To conclude, all five the objectives set out at the beginning of this study were met. With this study a new method was developed to model various Ta species in an aqueous phase containing both H_2O and H_2SO_4. Furthermore, this study can be seen as a benchmark for the simulation of Ta during SX. With that said, the following section includes recommendations to be considered for improving future work.

7.3 Recommendations

Although the aim and objectives of this study have been attained, various limitations and opportunities for further research on the molecular modelling of an SX system became apparent during this study.

Aqueous phase:

i. For a more detailed understanding of the Ta^{5+} species that may form, a species distribution curve against acid concentration could be constructed.
ii. As analytical techniques improve over time, samples of the different phases could be analysed for comparison with the theoretical data obtained.
iii. During the SX process, both Ta and Nb were present in the system. In this study the focus was on Ta. However, it is expected that Nb will react in a similar way. Therefore, the main results from this study could be repeated for Nb, considering however that Nb does not only have the 5+ but the 3+ oxidation state as well.
iv. In the beginning of the study an assumption was made that TaF_5 is a single metallic species, however, literature has suggested that Ta can also be found as tri- and tetra-metallic crystals. This leads to the question, whether these crystals stay tri- and tetra-metallic or are they broken up in an acid environment? Furthermore, how does the extractants interact with and extract these tri- and tetra metallic species?

Organic phase:

i. In the SX simulations it was assumed that D2EHPA did not react with H_2SO_4 from the aqueous phase when contacted. Some papers have however suggested that D2EHPA deprotonates and therefor another point of interest could be the effect of the H_2SO_4 concentration on the species of D2EHPA.
ii. Other extractants, including MIBK (methyl isobutyl ketone) and TBP (tributyl phosphate) have been used for the separation and extraction of Ta and Nb. It would be interesting to see what the effect of other extractants might be on this system.

Modelling:

i. Within the modelling, the size of the system is always proportional to the number of computational nodes available. As bigger computational systems and more CPUs become available, bigger reaction systems, for the simulation of more realistic liquid phases, will be feasible.

ii. The model developed in this study could also be applied for systems containing other metals like Zr and Hf, or metals with the same oxidation state as Ta and Nb or metals that extract with D2EHPA.

APPENDIX A
ARTICLE 1

Computational and Theoretical Chemistry 1090 (2016) 112–119

Contents lists available at ScienceDirect

Computational and Theoretical Chemistry

journal homepage: www.elsevier.com/locate/comptc

Molecular modelling of tantalum penta-halides during hydrolysis and oxidation reactions

M.J. Ungerer, C.G.C.E. van Sittert, D.J. van der Westhuizen, H.M. Krieg *

Focus Area: Chemical Resource Beneficiation, North-West University, Private Bag X6001, Potchefstroom 2531, South Africa

ARTICLE INFO

Article history:
Received 5 February 2016
Received in revised form 8 June 2016
Accepted 8 June 2016
Available online 9 June 2016

Keywords:
DFT
Modelling
Tantalum
Chloride
Fluoride
Speciation

ABSTRACT

The transition metals tantalum (Ta) and niobium (Nb), which are usually found together in nature, have similar chemical and physical properties, making their separation challenging. There are various methods available for the separation of these two metals, including reduction, fluorination, chlorination and solvent extraction (SX) (Ayanda and Adekola, 2011). In a recent study investigating the suitability of SX for the separation of Ta and Nb, it was shown that speciation data would be required to help explain the distribution data obtained. Since traditional speciation techniques cannot be readily applied for Ta and Nb, it was decided to determine the suitability of molecular modelling for this purpose. To investigate the suitability of modelling for this application a case study was selected where it was hypothesised that when TaF_5 is dissolved in water, it could react stepwise with water to finally form tantalum penta-hydroxide ($Ta(OH)_5$) and other oxyfluoride species including $TaOF_3$. Due to the fact that literature on TaF_5 reactions with water is limited, $TaCl_5$ and its reactions was used to develop the model (method). As part of the model development and verification, DFT was used to calculate the energy needed for these reactions, comparing different functionals and basis sets. The validated model was then applied to TaF_5 as a case study. From the results it was confirmed that the reaction of TaX_5 (X = Cl or F) with water to form $Ta(OH)_5$ and Ta_2O_5 is an endothermic reaction, while the formation of $Ta(H_2O)F_5$ and TaF_4OH was exothermic.

1. Introduction

While several techniques have been proposed for separation and purification of various metals [1], solvent extraction (SX) is widely used for amongst others copper (Cu), nickel (Ni), iron (Fe), platinum group metals (PGMs), zirconium (Zr), hafnium (Hf), tantalum (Ta) and niobium (Nb). Ta and Nb are valuable metals with various high-end uses, where Ta is used in the nuclear industry as cladding material, as capacitors, as high power resistors and to make high strength corrosion resistant alloys, while Nb is used in super alloys for jet engines and heat resistant equipment. Ta and Nb, which co-occur in mineral deposits, have near identical properties making their separation challenging.

In a recent study Ungerer et al. [2] studied the SX based separation of Ta and Nb, using alternative and safer chemicals while investigating the suitability of membrane-based solvent extraction (MBSX). While partial separation of Ta and Nb was achieved, it was not possible to predict extraction behaviour prior to experimental testing, due to the current absence of speciation data for Ta and Nb. Speciation data for Ta and Nb is not available, possibly due to their insolubility in most aqueous liquids [3,4] and because they are UV inactive making the detection and identification of the aqueous species difficult. An alternative method that could however be suitable for predicting the speciation and hence extraction of Ta and Nb is molecular modelling [5]. Applying molecular modelling to SX could for example entail a step-by-step analysis of the extraction process on a molecular level, thereby determining the molecular properties as well as the system reactions occurring during SX.

According to the previously published data [2], the SX process of Ta and Nb can be divided into three parts: (1) the aqueous phase containing water soluble tantalum (V) penta-fluoride (TaF_5), (2) the organic phase containing the extractant and diluent and (3) the interface where these two phases make contact. For the modelling of the first step (TaF_5 in an aqueous environment), the molecular structure of TaF_5 is required. Since single crystals of TaF_5 do not form readily, they exist as oligomeric penta-fluorides with three possible structure types [6], neither the experimentally determined molecular structure of TaF_5 is well known, nor have these properties been modelled. However, for $TaCl_5$ both the molecular structure [7] as well as its interaction in an aqueous environment have been modelled [8,9]. If it is assumed that TaF_5

* Corresponding author.
E-mail address: henning.krieg@nwu.ac.za (H.M. Krieg).

http://dx.doi.org/10.1016/j.comptc.2016.06.011
2210-271X/

has a similar symmetrical structure and behaviour in water than $TaCl_5$, (an assumption that will be evaluated in this paper), then $TaCl_5$ could be used to validate the novel modelling approach before applying the modelling to a compound of which the structure and behaviour is unknown.

According to Agulyansky [7] $TaCl_5$ has a trigonal bipyramidal structure, assuming above mentioned similarity, TaF_5 would have a similar trigonal bipyramidal structure. The differences between TaF_5 and $TaCl_5$ will be discussed further in Section 3.

Using the above information, it is the aim of this paper to develop a molecular modelling approach to validate the structure of TaF_5 while determining the possible hydrolysis and subsequent oxidation reactions thereof in an aqueous environment. However, as stated above limited experimental or modelling data is available for the reactions of TaF_5 to verify the suitability of the newly developed model. Hence, the paper was subdivided into two sections. Firstly, the model will be verified in terms of the structure of $TaCl_5$ as well as its possible hydrolysis and oxidation reactions. Once the correlation of the modelled and literature data has been demonstrated for $TaCl_5$, a case study is presented where the verified model will be used to confirm the structure of TaF_5 as well as to calculate its possible hydrolysis and oxidation reactions. In a final step a brief section is presented discussing the possible transition states found during the most likely hydrolysis reaction of TaF_5 to $TaF_4(OH)$.

2. Computational methods

2.1. Model verification ($TaCl_5$)

For the molecular modelling of $TaCl_5$ and its reactions with H_2O in an aqueous environment, the DMol^3 module of the Biovia Materials Studio 6.1 software from Dassault Systems (previously Accelrys) [10] was used in conjunction with the DFT semi-empirical dispersion interaction correction module (DFT-SEDC). For comparison five different combinations of functional and basis sets were used to determine the structure of the $TaCl_5$ molecule (geometry optimisation [11,12]), as well as its hydrolysis and oxidation reactions.

(1) Generalised-gradient approximation (GGA) with Perdew–Wang correlation functional (PW91) [11] and DND (double-numeric polarisation plus d-functions) basis set with basis file 4.4 and OBS dispersion correction. (DND is comparable with the Gaussian 6-31G* basis set.)
(2) GGA PW91 functional with basis set DNP (double-numeric polarisation functions), with basis file 4.4 and OBS dispersion correction. (DNP is comparable with the Gaussian 6-31G** basis set.)
(3) GGA PW91 functional with basis set DNP+ (double numerical plus polarisation, with addition of diffuse functions) with basis file 4.4 and OBS dispersion correction. (DNP+ is more accurate than a Gaussian basis set (Gaussian 6-31G**) of the same size.)
(4) GGA with Perdew–Burke–Ernzerhof (PBE) [13] correlation, with basis set DNP+ and basis file 4.4.
(5) Becke exchange plus Lee–Yang–Parr correlation (B3LYP) [14,15] hybrid exchange–correlations energy functional, with basis set DNP and basis file 4.4.

For the calculations done with PBE(DNP+) and B3LYP(DNP), no dispersion correction was added. Only Tkatchenko–Scheffler (TS) [16] and Grimme [17] dispersion corrections were available in these settings and in both TS and Grimme the element coverage for Ta was unavailable. Under the electronic properties, smearing of 0.005 Hartree (Ha) was chosen for all the calculations [18]. Furthermore, the conductor-like screening model (COSMO) [19] was used to simulate the molecules within a solvent. In this case the solvent was water, with a dielectric constant of 78.54.

After the geometry optimisation process, single point energy calculations were done to calculate various electronic properties with the same settings that were used for the geometry optimisations. The calculations were done at 0 K and an energy correction term was added to give Gibbs free energy values at 298.15 K. The zero-point vibrational energy (ZPVE) was included in all calculations. Frequency calculations were used to confirm optimised structures (minimum energy) and transition states (one imaginary frequency).

2.2. Case study (TaF_5)

For the molecular modelling of TaF_5 and its hydrolysis and oxidation reactions, the DMol^3 module of the Biovia Materials Studio 6.1 software from Dassault Systems (previously Accelrys) [10] was used with the GGA PBE functional [13]. The basis set used was DNP+ with basis file 4.4, which includes diffuse functions. Under the electronic properties, smearing of 0.005 Hartree (Ha) was chosen [18]. The single point energy calculations were done as described in Section 2.1. A potential energy surface (PES) scan was done by a stepwise shortening of the distance between the Ta atom of TaF_5 and the O atom of one of the surrounding H_2O to determine the energy and geometry change during the formation of $Ta(H_2O)F_5$.

3. Results and discussion

3.1. Model verification ($TaCl_5$)

3.1.1. Geometry optimisation of $TaCl_5$

The $TaCl_5$ molecule was geometrically optimised with the five functional and basis set settings (Section 2.1). The bond lengths and bond angles between the Ta and the five Cl atoms were measured and compared to experimental literature as shown in Table 1.

From Table 1 it can be seen that according to the modelled values the two Ax Cl atoms (Cl3 and Cl4) have longer bond lengths than the three Eq Cl atoms (Cl1, Cl5 and Cl6), which correlates with various literature sources [6,20,21]. This implies that the three

Table 1
Calculated and experimental literature values of bond lengths and bond angles of $TaCl_5$.

Bond/angle	Literature [6]	PW91 (DND)	PW91 (DNP)	PW91 (DNP+)	PBE (DNP+)	B3LYP (DNP)
Ta–Cl1 (Å)	2.284	2.327	2.327	2.327	2.321	2.331
Ta–Cl3 (Å)	2.426	2.381	2.381	2.379	2.379	2.385
Ta–Cl4 (Å)	2.426	2.381	2.381	2.379	2.380	2.385
Ta–Cl5 (Å)	2.284	2.317	2.317	2.317	2.321	2.314
Ta–Cl6 (Å)	2.284	2.317	2.317	2.317	2.322	2.321
Cl1–Ta–Cl6 (°)	120.00	120.61	120.61	120.80	119.96	122.40
Cl1–Ta–Cl5 (°)	120.00	120.61	120.61	120.80	120.13	121.16
Cl1–Ta–Cl3 (°)	90.00	89.28	89.28	89.54	89.99	88.94
Cl1–Ta–Cl4 (°)	90.00	89.28	89.28	89.54	90.00	89.94

Eq Cl atoms push the two Ax Cl atoms out of the plane, making the Ax bond lengths longer and hence the bond strength weaker. From the experimental literature values [6] the difference in bond lengths between the Ax and Eq Cl atoms is 0.142 Å, where with the modelling it was found to be 0.065 ± 0.006 Å. This difference is due to literature values are for crystals where the modelled values are simulated for a liquid. Previous theoretical values calculated with ab initio B3LYP method [8] showed Ax and Eq bond length to be 2.337 Å and 2.287 Å respectively. The modelled bond lengths are closer to the experimentally observed values [6] than the values presented by Siodmiak et al. [8]. In terms of the bond angle the values with PW91(DND), PW91(DNP) and PW91(DNP+) were similar with a 0.22 ± 0.04° deviation from each other and differed by 0.66 ± 0.006° from literature [6]. The bond angles calculated with PBE(DNP+) differed by 0.007 ± 0.006° from literature [6]. The modelled data from B3LYP(DNP) showed a 1.42 ± 1° average deviation from literature [6]. Calculations with PW91(DND), PW91(DNP), PW91(DNP+) and PBE(DNP+) yielded realistic values in a relatively short calculation time, whereas B3LYP(DNP) calculations were time consuming with a generally greater deviation in bond lengths and angles.

To further confirm the stability of the molecule structure, the model was used to determine the vibrational frequencies of the $TaCl_5$ which were compared to experimental literature values. Since $TaCl_5$ is a nonlinear molecule with $3N - 6$ degrees of freedom and $N = 6$ atoms, $TaCl_5$ has 12 degrees of freedom and therefore 12 types of molecular vibrations (stretching and bending modes). Of these 12 only 8 vibrations are experimentally observed because the symmetry class E is double degenerated, which means that both the degenerated modes are observed as a single infrared absorption band [8]. Table S1 shows the experimental literature and modelled vibrational frequencies for the 8 molecular vibrations of $TaCl_5$ calculated with the five functional and basis set settings stated in Section 2.1.

Comparing all five functional and basis sets with each other, the frequencies are within 6 cm^{-1} from each other. The frequencies obtained with PW91(DND), PW91(DNP) and PW91(DNP+) were similar with a deviation less than 4 cm^{-1} from each other. The modelled values are lower than the experimental literature values, because the experimental frequencies of $TaCl_5$ are in the gas phase and the modelling within an ideal system cannot simulate all the stretching and bending vibrations. Also the frequencies shown here are calculated harmonic vibrational frequencies (ω) without a scaling factor [22,23] to account for the error between harmonic vibrational frequency and fundamental vibrational frequency (ν). The modelled frequencies had a standard deviation of less than 10% with literature, except for ω_6 and ω_8. The e'' vibrational mode is formally symmetry forbidden, but coupling may let the ω_6 and ω_8 vibration mode mix with other vibrations, leading to this error in symmetry assignment [24]. The obtained results of vibrational frequencies are shifted higher because of electron correlation and anharmonicity effects in the theoretical treatment used within the modelling, which in turn could cause the bond length over estimation seen previously.

3.1.2. Hydrolysis and oxidation reactions of $TaCl_5$

In Fig. 1, the most important hydrolysis (shown as Reaction 1–5) and oxidation (Reaction 6–12) reactions that might occur are presented. While various other reactions and geometries may occur during this reaction, the probability of only those reactions shown in Fig. 1 was determined. For the purpose of this discussion, first the hydrolysis reactions (Reaction 1–5) and then the oxidation reactions (Reaction 6–12) will be discussed.

$TaCl_5$ has five Cl atoms that can be individually replaced by OH groups (Reaction 1–5), when reacting with five consecutive H_2O molecules, finally resulting in the formation of tantalum pentahydroxide ($Ta(OH)_5$). During these reactions with H_2O, the OH group can either substitute a Cl in the axial (Ax) or in the equatorial (Eq) positions. When considering these orientations of the substitution (Reaction 1–5 (Fig. 1)) a significant number of conformers can be produced as is shown in Fig. 2.

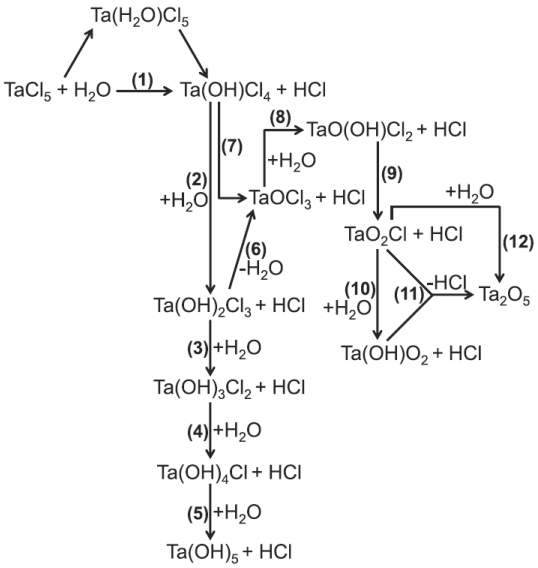

Fig. 1. Possible hydrolysis and oxidation reaction scheme of $TaCl_5$ with H_2O.

All 12 geometries presented in Fig. 2 were geometrically optimised and single point energy calculations were done. Again the five functionals and basis set settings were compared as had been done in Section 3.1.1 for the bond lengths, angles and vibrational frequencies. The relative energies of the conformers are presented (Table 2) relative to the conformer where a single OH group was Eq coordinated.

$TaCl_4OH$ has two conformers, one where the OH group is in the Eq position (OH-E) and one where it is in the Ax position (OH-A). The OH-E conformer has a lower energy than the OH-A conformer for all the functionals and basis sets and is therefore most likely to form. Siodmiak et al. [8,9] also found the OH-A conformer to have a higher energy than OH-E, by an average of 1.03 kcal/mol, which correlates best with the results obtained from the PW91(DNP) calculation. The lowest correlation was observed for PW91(DNP+). $TaCl_3(OH)_2$ has three conformers, (i) both OH groups are in the Eq position (EE), (ii) one OH group is Ax and the other Eq (AE) and (iii) both OH groups are Ax (AA). The EE conformer was lower in energy, followed by the AE conformer and then the AA conformer according to all the functionals and basis sets. This was confirmed by Siodmiak et al. [8,9] who found the AE conformer to have a higher energy than EE, by an average of 0.85 kcal/mol with the AA conformer having the highest energy with an average of 1 kcal/mol. While the tendency is the same the differences observed in this study were slightly higher, which could be attributed to the fact that different models being compared. The literature values stated here were done with Gaussian 98, Ta had a quasi-relativistic core potential and the oxygen and hydrogen atoms were calculated with a 6-31G** basis set.

$TaCl_2(OH)_3$ has three conformers, where the OH can be oriented either EEE, AEE or AAE. The EEE conformer had the lowest energy, followed by AEE and then AAE. Similar tendencies were again observed by Siodmiak et al. [8,9]. With $TaCl(OH)_4$ two conformers were investigated, i.e. AAEE and AEEE. According to Table 2, the

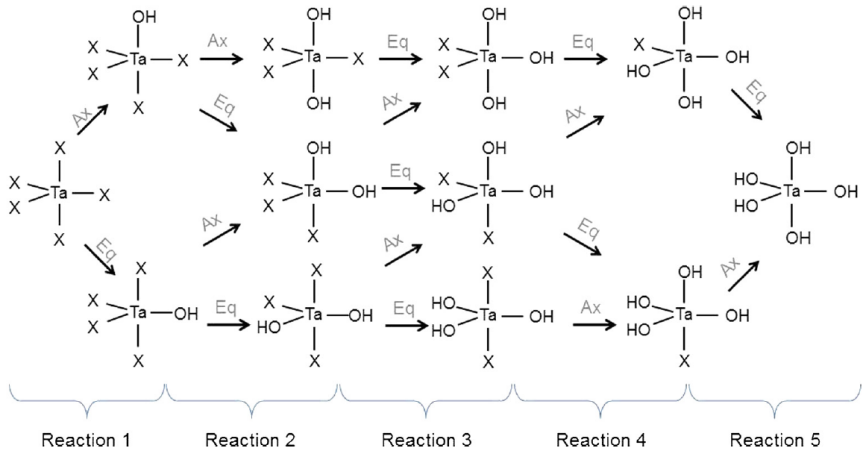

Fig. 2. Proposed TaX_5 (X = Cl or F) hydrolysis reaction scheme considering the orientation of substitution.

Table 2
Relative energies (kcal/mol) of tantalum hydroxyl chloride conformers.

Molecule[a]	PW91 (DND)	PW91 (DNP)	PW91 (DNP+)	PBE (DNP+)	B3LYP (DNP)
$TaCl_4OH$					
E	0.0	0.0	0.0	0.0	0.0
A	1.32	1.03	0.27	1.52	1.38
$TaCl_3(OH)_2$					
EE	0.0	0.0	0.0	0.0	0.0
AE	1.35	1.08	1.51	1.34	1.99
AA	2.92	3.00	3.95	2.44	2.91
$TaCl_2(OH)_3$					
EEE	0.0	0.0	0.0	0.0	0.0
AEE	1.70	2.00	2.24	1.43	0.56
AAE	0.41	0.48	−0.73	0.74	0.84
$TaCl(OH)_4$					
AAEE	0.0	0.0	0.0	0.0	0.0
AEEE	0.05	0.10	−0.84	0.16	0.51

[a] E and A refer to the equatorial or axial position of the OH group respectively.

AAEE conformer has a lower energy than the AEEE conformer. From these results it seems when an OH group bonds and evicts an HCl, both the first and the second OH will preferentially replace an Eq Cl. However, with the introduction of the third OH group, a rearrangement takes place to preferentially yield either AAE or AEE in almost equal form. In the fourth replacement again an Eq attachment was observed yielding AAEE preferentially before $Ta(OH)_5$ is formed in the final step.

When considering the subsequent oxidation reactions (Fig. 1, Reaction 6–12), various oxyfluoride species are formed. Due to their importance much of this discussion will however focus on $TaOCl_3$ and TaO_2Cl. $TaOCl_3$ and TaO_2Cl, the structure of which is shown in the supplementary section (Figs. S1 and S2 respectively), were also geometrically optimised with the five functional and basis set settings described in Section 2.1. The obtained bond lengths, angles and vibrational frequencies are given for $TaOCl_3$ and TaO_2Cl in Tables S2 and S3 respectively. Since there are no experimentally determined bond lengths and angles for the molecular structure of these two molecules, the modelled values were compared to modelled values obtained by Siodmiak et al. [8] who used an ab initio method with B3LYP at 0 K.

For $TaOCl_3$ the modelled values (Table S2) with regards to bond lengths differed 0.038 ± 0.007 Å from literature and less than 0.013 Å from each other. Comparing the bond angles the modelled data differed by less than 1° from literature and less than 0.4° from each other. $TaOCl_3$ is a nonlinear molecule with 9 degrees of freedom, where only 6 vibrations are experimentally observed. Table S2 shows the literature and modelled vibrational frequencies for the 6 molecular vibrations of $TaOCl_3$ (ω_1–ω_6), where ω_1 is assigned to the Ta–O bond stretch, ω_2 to the Ta–Cl symmetric bond stretch, ω_3 to the Cl–Ta–Cl symmetric bending, ω_4 to the Ta–Cl asymmetric bond stretch, ω_5 to the O–Ta–Cl bending and ω_6 to the Cl–Ta–Cl asymmetric bending. All the modelled values correlate with literature values (error = 10%), except for ω_6 (error = 15%) which probably mixes with other vibrations as was observed for $TaCl_5$ (see Table S1). The core treatment parameter with these calculations was 'All Electron' and this theoretical treatment of electron correlation and anharmonicity might account for the difference in frequency between the literature and modelled values.

While Ta in the +5 valence state is expected to have an sd^4 hybridisation structure, TaO_2Cl has most likely an sd^2 hybridisation structure because of the double bonds with oxygen. Accordingly one could expect that $TaOCl_2$ had a planar structure, however the modelling results revealed a nonplanar structure as shown in Fig. S2. In an ideal sd^2 structure, the ligand–metal–ligand angle would be 90°, but because of ligand–ligand repulsion and metal–ligand overlap these angles deviate from 90° [25], resulting in a

trigonal pyramidal structure which has been confirmed by Siodmiak et al. [9]. According to the results obtained (Table S3) the bond length error with all five functional and basis sets were 0.01 Å compared to each other and less than 0.03 Å compared to literature. With regards to the modelled bond angles, the O–Ta–O angle with PBE(DNP+) and PW91(DND, DNP, DNP+) was slightly smaller than the literature value, while being bigger when modelled with B3LYP(DNP). Comparing the values obtained from the modelling to the literature modelled results there were a less than 2% deviation in bond angle. When the planar structure was modelled, the bonds became longer (Ta–O = 1.768 Å, Ta–Cl = 2.404 Å) and the energy was higher, indicating a more unstable structure.

TaO_2Cl is a nonlinear molecule with 6 degrees of freedom, while only 4 vibrations are experimentally observed. Table S3 shows the literature and modelled vibrational frequencies for the 4 molecular vibrations of TaO_2Cl. The vibration of ω_1 is assigned to the Ta–O bond symmetric stretch, ω_2 to the Ta–Cl bond stretch, ω_3 to the Cl–Ta–O_2 symmetric bending and ω_4 to the Ta–O bond asymmetric stretch. Again the literature values were obtained from the modelled values of Siodmiak et al. [8]. The modelled frequencies differed by 6% from literature values, except for ω_3 that had an error of 17%, which mixes with other vibrations of O–Ta–O bending.

While previously the energies of individual reagents and products were presented, Table 3 shows the modelled energies of formation ($\Delta H_f^{298.15K}$/kcal/mol) for Reaction 1–12 with all five functional and basis set settings to determine a possible reaction mechanism will emerge for the formation of oxyhalide species. Accordingly Reaction 1 and 2 were moderately endothermic with the PW91 functional and three basis sets, while being exothermic with PBE(DNP+) and B3LYP(DNP). Theoretical literature [8,9] also showed Reaction 1 and 2 to be exothermic. Reactions 3–12 were moderately endothermic (except for Reaction 9 which was strongly endothermic) irrespective of the functional used, which is possibly why the experimental observation of the oxychloride has been particularly difficult [26].

With regards to Reaction 1 and 2, the modelling results with PW91(DND), PW91(DNP), PW91(DNP+) showed the reactions to be endothermic and had an average of 2 kcal/mol deviation from each other and differed by 9.6 ± 1.2 kcal/mol from theoretical literature. B3LYP(DNP) and PBE(DNP) correlated to literature and also showed Reaction 1 and 2 to be exothermic, with an average deviation of 5.5 ± 1.2 kcal/mol, but B3LYP(DNP) was computationally the most expensive to use and had the highest bond angle deviation of 1.42 ± 1°. Theoretical literature [8] did not show the formation of $TaO(OH)Cl_2$ in Reaction 8, but showed Reaction 8 and 9 together where $TaOCl_3$ reacted with water to form TaO_2Cl directly with the reaction energy at 78.7 kcal/mol, This high energy value could indicate a multistep reaction taking place and by indicating a two-step reaction (as shown by Reaction 8 and 9) the energy values decreased. The lowest energy values for both Reaction 8 and 9 were achieved with B3LYP(DNP) (1.54 and 46.61 kcal/mol respectively) followed by PBE(DNP+) (3.77 and 52.41 kcal/mol respectively), which implies that the two-step reaction proposed in this study is more likely.

Based on all these results it was decided that calculations on TaF_5 and its related species will be done with PBE(DNP+) combination which gave the best computational time to accuracy compromise.

3.2. Case study (TaF_5)

The case study follows the same outline as was used in the model verification presented in Section 3.1 where first the geometry variables (bond lengths, bond angles and vibrational frequencies) were modelled and compared to literature values, before calculating the hydrolysis and oxidation reactions of TaF_5 and comparing these to the results presented on the reactions discussed for $TaCl_5$. Finally a more detailed reaction mechanism is presented for the most likely hydration mechanism of TaF_5 forming $Ta(H_2O)F_5$.

3.2.1. Geometry optimisation of TaF_5

The TaF_5 molecule was geometrically optimised (as in Section 2.2) and the bond lengths and bond angles between the Ta and the five F atoms were determined (Table 4) and compared to experimental literature values.

From Table 4 it can be seen that the two Ax F atoms (F3 and F4) have longer bond lengths than the three Eq F atoms (F1, F5 and F6), which has been confirmed in experimental literature [20,21], as was observed with $TaCl_5$. The bond angle between the Ax F atom and Eq F atom of TaF_5 (Table 4) was 90° ± 0.01, while the bond angle between the Eq F atoms was 120° ± 0.1, as was expected and seen in the modelling of $TaCl_5$. Modelled and experimental literature values differ because the modelled values in this study were obtained from a single TaF_5 molecule where the experimental literature values were derived from four metal atoms as a unit cell (Ta_4F_{20}) [27] and a trimeric unit cell (Ta_3F_{15}) [6]. Because of the rigidity of the crystal structure, distortion of bonds and angles can occur [28], which explains the deviation from unity (90° and 120°) observed when working with tetra- and trimeric unit cells. When comparing the results of TaF_5 with $TaCl_5$, the bond length of Ta–F was shorter than the bond length of Ta–Cl, as the atom radius of F is smaller than that of Cl. Similar to $TaCl_5$, TaF_5 is a nonlinear molecule with 12 vibrational modes of which 8 were observed as shown in Table 5.

Because the availability of vibrational data for TaF_5 is limited, 0.1 g TaF_5 salt (Sigma-Aldrich product, 99.5% purity) was used to determine the infrared (IR) spectrum on a Bruker bench top diamond tip infrared spectrometer, where two main peaks were observed at 634 and 682 cm^{-1}. The IR spectrum of TaF_5 was also obtained from vibrational calculations and again two main peaks were observed at ~631 and 667 cm^{-1}, which correlates with the

Table 3
Energy of formation ($\Delta H_f^{298.15K}$/kcal/mol) of tantalum chloride and oxychloride reactions with water.

	Literature [8,9]	PW91 (DND)	PW91 (DNP)	PW91 (DNP+)	PBE (DNP+)	B3LYP (DNP)
(1) $TaCl_5 + H_2O \rightarrow TaCl_4OH + HCl$	−8.6	2.13	1.82	2.25	−0.94	−2.67
(2) $TaCl_4OH + H_2O \rightarrow TaCl_3(OH)_2 + HCl$	−7.4	1.06	1.11	2.41	−0.13	−3.89
(3) $TaCl_3(OH)_2 + H_2O \rightarrow TaCl_2(OH)_3 + HCl$		4.15	4.06	4.67	3.53	0.80
(4) $TaCl_2(OH)_3 + H_2O \rightarrow TaCl(OH)_4 + HCl$		6.50	6.18	7.13	5.18	2.29
(5) $TaCl(OH)_4 + H_2O \rightarrow Ta(OH)_5 + HCl$		11.01	10.92	10.43	10.61	9.39
(6) $TaCl_3(OH)_2 \rightarrow TaOCl_3 + H_2O$	16.6	5.61	6.13	8.51	8.18	1.14
(7) $TaCl_4(OH) \rightarrow TaOCl_3 + HCl$	9.2	6.68	7.24	10.92	8.05	−2.76
(8) $TaOCl_3 + H_2O \rightarrow TaO(OH)Cl_2 + HCl$	78.7	4.99	4.83	5.12	3.77	1.54
(9) $TaO(OH)Cl_2 \rightarrow TaO_2Cl + HCl$		52.54	52.67	53.62	52.41	46.61
(10) $TaO_2Cl + H_2O \rightarrow Ta(OH)O_2 + HCl$		10.46	10.31	10.36	8.52	6.93
(11) $TaO_2Cl + Ta(OH)O_2 \rightarrow Ta_2O_5 + HCl$		6.01	6.13	6.62	7.22	3.55
(12) $2\ TaO_2Cl + H_2O \rightarrow Ta_2O_5 + 2\ HCl$		16.47	16.44	16.98	15.74	10.49

Table 4
Modelled and experimental literature values of bond lengths and angles of TaF_5.

Bond/angle	Experimental literature		PBE(DNP+)
	Edwards [27]	Ischenko [6]	
Ta–F1 (Å)	1.75 ± 0.02	1.846 ± 0.005	1.89 ± 0.02
Ta–F3 (Å)	2.06 ± 0.02	2.062 ± 0.002	1.93 ± 0.02
Ta–F4 (Å)	2.07 ± 0.02	2.062 ± 0.002	1.93 ± 0.02
Ta–F5 (Å)	1.78 ± 0.05	1.846 ± 0.005	1.89 ± 0.02
Ta–F6 (Å)	1.78 ± 0.05	1.846 ± 0.005	1.89 ± 0.02
F1–Ta–F6 (°)	103.6 ± 2	96.4 ± 1.5	120 ± 0.5
F1–Ta–F5 (°)	123.6 ± 2	173.1 ± 2.1	120 ± 0.5
F1–Ta–F3 (°)	94.8 ± 2	96.4 ± 1.5	90 ± 0.5
F1–Ta–F4 (°)	95.8 ± 2	83.5 ± 0.6	90 ± 0.5

Table 5
Modelled vibrational frequencies[a] (cm^{-1}) with PBE(DNP+) for TaF_5.

Frequency	Wavenumber (cm^{-1})
$\omega_1(a'_1)$	674
$\omega_2(a'_1)$	640
$\omega_3(a_2'')$	642
$\omega_4(a_2'')$	239
$\omega_5(e')$	642
$\omega_6(e')$	191
$\omega_7(e')$	89
$\omega_8(e'')$	240

[a] Modelled vibrational frequencies indicate the harmonic vibrational frequency without a scaling factor.

experimental values (modelling data error = 5%). A shift in the modelled data was observed which could be due to the correction term used in COSMO which was added to account for H_2O molecules surrounding TaF_5.

3.2.2. Hydrolysis and oxidation reactions of TaF_5

Both the energies of formation of the hydrolysis and oxidation reactions are presented in Table 6, including the orientation of the hydrolysis substitutes, as has been done for $TaCl_5$ (Section 3.1.2) using the same reactions and conformers shown in Figs. 1 and 2 respectively.

When considering the hydrolysis reaction (Reaction 1–5 in Table 6), the energy of TaF_4OH with the OH group in the Ax and Eq position was −2.35 and −4.80 kcal/mol respectively for Reaction 1, implying that although the reaction was instigated from an Eq position, the molecules shifted to form a lower energy product where the OH group is in the Ax position. These values and transitions are similar to those observed for the $TaCl_5$ reactions. From the differences observed between the Ax and Eq position of the H_2O molecule, the energy of the TaF_4OH molecule was calculated where the OH group was situated in the Ax and Eq positions (Supplementary Data – Fig. S4).

Table 6
Energy of formation of TaF_5 reactions with water (PBE(DNP+)).

		$\Delta H_f^{298.13K}$/(kcal/mol)
(1) $TaF_5 + H_2O \rightarrow TaF_4OH + HF$	E	−2.35
	A	−4.80
(2) $TaF_4OH + H_2O \rightarrow TaF_3(OH)_2 + HF$	EE	5.87
	AA	5.32
	AE	5.20
(3) $TaF_3(OH)_2 + H_2O \rightarrow TaF_2(OH)_3 + HF$	EEE	6.29
	AEE	7.67
	AAE	6.20
(4) $TaF_2(OH)_3 + H_2O \rightarrow TaF(OH)_4 + HF$	AAEE	10.93
	AEEE	10.32
(5) $TaF(OH)_4 + H_2O \rightarrow Ta(OH)_5 + HF$		10.90
(6) $Ta(OH)_2F_3 \rightarrow TaOF_3 + H_2O$		12.35
(7) $TaF_4(OH) \rightarrow TaOF_3 + HF$		15.78
(8) $TaOF_3 + H_2O \rightarrow TaO(OH)F_2 + HF$		5.93
(9) $TaO(OH)F_2 \rightarrow TaO_2F + HF$		54.92
(10) $TaO_2F + H_2O \rightarrow Ta(OH)O_2 + HF$		7.66
(11) $TaO_2F + Ta(OH)O_2 \rightarrow Ta_2O_5 + HF$		6.35
(12) $2\ TaO_2F + H_2O \rightarrow Ta_2O_5 + 2\ HF$		14.01

For Reaction 2, the energy of $TaF_3(OH)_2$ was higher at 5.20 and 5.32 kcal/mol with the OH groups in the axial–equatorial (AE) and axial–axial (AA) positions respectively, followed by the equatorial–equatorial positions (EE) at 5.87 kcal/mol. Since the Eq OH groups are 120° from each other in the EE position, the two Ax F groups have longer bond lengths, because they are pushed out of the plane which therefore could result in these bonds more readily participating in the substitution reaction.

In Reaction 3, three OH groups were substituted onto the Ta atom for which three different molecules for $TaF_2(OH)_3$ were identified, i.e. AAE, with the relative energy 6.20 kcal/mol, AEE, which yielded a relative energy of 7.67 kcal/mol and EEE with a relative energy of 6.29 kcal/mol. From these results it can be seen that the energy between the AAE and EEE conformer are similar with the AEE conformer at a higher energy. These results are similar to the conformers formed during the hydrolysis of $TaCl_5$, where EEE was at the lowest energy followed by AAE and then AEE.

For Reaction 4, two geometries were identified for $TaF(OH)_4$, i.e. AAEE (OH group added Eq to AAE), with a relative energy of 10.93 kcal/mol, while a similar relative energy (10.32 kcal/mol) was attained for AEEE (OH group added Eq to AEE). In the last reaction (Reaction 5), all five F atoms are replaced by five OH groups to form $Ta(OH)_5$ which has a relative energy of 10.90 kcal/mol. It is clear from Table 6 that the energy increased with increasing OH groups. From these results it is clear that although the OH group approached from an Eq position the molecule rearranges to form the OH-A conformer, where a second OH group approaches again form the Eq position to form the AE conformer. Rearrangement takes place again to form AA conformer and when the third substitution takes place, the AAE conformer is formed, followed by AAEE.

As shown for $TaCl_5$ (Table 3), it is again apparent that the oxidation of TaF_5 (Reaction 6–12 in Table 6) is unlikely to occur spontaneously. Unlike for $TaCl_5$ where the first two hydrolysis reactions were likely (exothermic), only the first hydrolysis reaction (Reaction 1) was exothermic when using TaF_5 (Table 6) with a significant difference between the E and A conformers.

In an attempt to explain this difference in energies between the two conformers, the transition energies for the first hydrolysis reaction were determined and are presented in Fig. 3. It is clear from this analysis that between the reagent (TaF_5 – Point A) and the product (TaF_4OH – Point E), three transition states (Points B, C and D) are possible. Point A in Fig. 3 shows the reagents TaF_5 and H_2O of which the energies were set to 0 kcal/mol. All subsequent energies were calculated relative to these two molecules. After optimisation of the structure, the H_2O molecule was modelled from both an Ax and Eq position respectively. However at the lowest energy for the first transition (Point B), the H_2O was in the Eq position in both cases, with energies of approximately −20 kcal/mol, indicating an exothermic reaction with no distinct orientation preference.

In the next step it seems that the H_2O bonded to the TaF_5 (Point C). For this state the only observable difference was that when the H_2O molecule approached from the Ax position (Fig. 3 point C), the H atoms of the H_2O molecule turned towards the Eq position while when the H_2O molecule approached from the Eq position, the H atoms had turned towards the Ax position. The reaction energy at this point was only slightly higher than Point B at −18 kcal/mol,

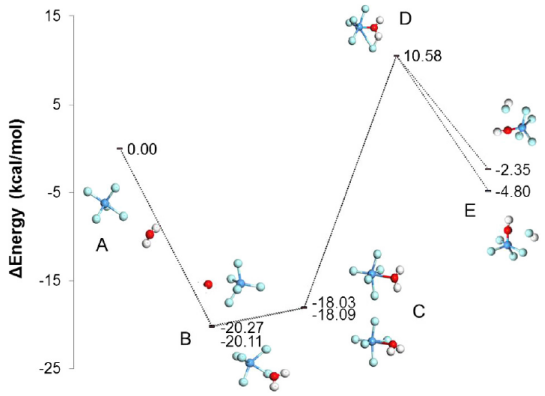

Fig. 3. Hydrolysis reaction of TaF_5 with regards to transition state energies.

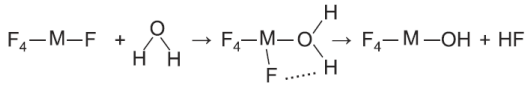

Fig. 4. Proposed mechanism for the reaction of TaX_5 (X = Cl or F) with one H_2O molecule (reproduced from Siodmiak et al. [9]).

confirming that the formation of $Ta(H_2O)F_5$ was also exothermic. It is interesting to note that the two Ax F atoms in Point C were distorted from a 90° angle to accommodate the H_2O molecule and possibly due to the formation of hydrogen bonds. To determine the degree of distortion, the bond lengths and bond angles were calculated and shown in Supplementary Data (Fig. S3).

In the third step, Point D in Fig. 3, a four membered cyclic ring was formed between the TaF_5 and bonded H_2O, by the association of an F atom and an adjacent H atom, which ultimately results in the release of HF and the formation of TaF_4OH, with the remaining OH group either in the Ax or Eq position. At this point the geometry changed from trigonal bi-pyramidal to square pyramidal. As the HF molecule moved further away from TaF_4OH, the geometry changed back to trigonal bi-pyramidal. It is interesting to note that Point D correlates perfectly with the mechanism proposed by Siodmiak et al. [9] for $TaCl_5$, when calculating the hydrolysis of $TaCl_5$ in water showing that the water molecule first bonded to the metal atom before evicting HCl. It can thus be concluded that when TaF_5 is dissolved in water, the water molecule firstly bonds to the Ta to form $Ta(H_2O)F_5$, followed by the formation of a cyclic transition state where one H atom of the water molecule bonds with one F atom, before evicting the HF group from TaF_4OH. This can also be expressed as shown in Fig. 4.

According to Fig. 3 10.58 kcal/mol was needed for the formation of the four membered cyclic ring, while the energy of the final TaF_4OH was −4.80 and −2.35 kcal/mol in the Ax and Eq position respectively, indicating that the Ax position yielded a lower energy state and therefore was more favourable to form. This correlates with the calculation made in Table 4, where the length of the Ax F atom was shown to be longer, therefore more unstable and thus favouring a reaction in this position.

4. Conclusion

Due to a lack of speciation data, molecular modelling was used to confirm the molecular structure of both $TaCl_5$ and TaF_5 while calculating the energies of the hydrolysis and oxidation reactions. To confirm the suitability of the model, the model was developed and then verified for $TaCl_5$ for which data is available before applying the verified model to TaF_5.

For the calculated bond lengths and bond angles of $TaCl_5$ PW91 (DND), PW91(DNP), PW91(DNP+) and PBE(DNP+) gave values that were closest to theoretical literature with an average deviation of 0.065 ± 0.006 Å for PW91 and 0.66 ± 0.006° for PBE(DNP+). While PBE(DNP+) had the smallest bond angle deviation of 0.007 ± 0.006, B3LYP(DNP) had the highest bond angle deviation of 1.42 ± 1° as well as a high computational cost. With regards to the frequency calculations the overall deviation between the functional and basis sets was 6 cm^{-1} and less than 10% with literature. When using this approach on a range of molecules it was shown that the larger basis set combination PBE(DNP+) was the most suitable.

When comparing the results from $TaCl_5$ (method verification) and TaF_5 (case study), similar data and trends were observed, verifying the suitability of the model for studying TaF_5 reactions with H_2O. For the hydrolysis reactions only TaX_4OH or $TaCl_3(OH)_2$ will form with lower energies when substitutes were in the Eq position. From the proposed oxidation reactions, it is evident that the oxyfluoride species $TaOX_3$ and TaO_2X will not form via these reactions as all oxidation reactions were endothermic both for $TaCl_5$ and TaF_5. According to the transition state energy calculations of TaF_5 with H_2O one H_2O molecule bonded to TaF_5 to form a stable $Ta(H_2O)F_5$ before the eviction of HF forming TaF_4OH, with a transition state energy of 10.58 kcal/mol.

Future work will entail the investigation of molecular modelling to determine the influence of acid on the metal–H_2O interaction thereby identifying the possible speciation in an aqueous phase as found during SX.

Acknowledgements

The authors would like to offer a special thanks to (i) The South African Nuclear Energy Corporation Limited (Necsa) and the New Metals Development Network (NMDN) of the Advanced Metals Initiative (AMI) and the Department of Science and Technology (DST) – South Africa for their financial support, (ii) The National Research Foundation of South Africa (NRF – Grant Number 89390) for their financial support, and (iii) The Center for High Performance Computing (CHPC) in Cape Town and the North-West University High Performance Computing (NWU-HPC) center for their support and resources.

Appendix A. Supplementary material

Supplementary data associated with this article can be found, in the online version, at http://dx.doi.org/10.1016/j.comptc.2016.06.011.

References

[1] O.S. Ayanda, F.A. Adekola, A review of niobium-tantalum separation in hydrometallurgy, J. Miner. Mater. Charact. Eng. 10 (2011) 245–256.
[2] M.J. Ungerer, H.M. Krieg, G. Lachmann, D.J.V.d. Westhuizen, Comparison of extractants for the separation of TaF_5 and NbF_5 in different acidic media, Hydrometallurgy (2014) 195–206.
[3] A. Timofeev, A.A. Migdisov, A.E. Williams-Jones, An experimental study of the solubility and speciation of niobium in fluoride-bearing aqueous solutions at elevated temperature, Geochim. Cosmochim. Acta 158 (2015) 103–111.
[4] R.L. Linnen, I.M. Samson, A.E. Williams-Jones, A.R. Chakhmouradian, 13.21 Geochemistry of the rare-earth element, Nb, Ta, Hf and Zr deposits, Reference Module in Earth Systems and Environmental Sciences – Treatise on Geochemistry, Geochemistry of Mineral Deposits, second ed., vol. 13, 2014, pp. 543–568.
[5] J. Narbutt, M. Czerwinski, Chapter 16: computational chemistry in modelling solvent extraction of metal ions, in: J. Rydberg, C. Musikas, G.R. Choppin (Eds.), Solvent Extraction Principles and Practice, 1992.

[6] A.A. Ischenko, V.P. Spiridonov, T.G. Strand, Joint Norwegian – Soviet electron diffraction studies of molecular structures in the gas phase. II. Inorganic compounds, Acta Chem. Scand. A 42 (1964) 651–673.
[7] A. Agulyansky, The Chemistry of Tantalum and Niobium Fluoride Compounds, Elsevier, Amsterdam, 2004.
[8] M. Siodmiak, G. Frenking, A. Korkin, Initial reactions in chemical vapor deposition of Ta_2O_5 from $TaCl_5$ and H_2O. An ab initio study, J. Chem. Phys. A 104 (2000) 1186–1195.
[9] M. Siodmiak, G. Frenking, A. Korbin, On the mechanism of chemical vapor deposition of Ta_2O_5 from $TaCl_5$ and H_2O. An ab initio study of gas phase reactions, Mater. Sci. Semicond. Process. 3 (2000) 65–71.
[10] Material Studio Modelling Environment, Accelrys Software Inc., San Diego, 2012.
[11] J.P. Perdew, Y. Wang, Accurate and simple analytic representation of the electron-gas correlation energy, Phys. Rev. B 45 (1992) 13244–13249.
[12] B. Delley, Ground-state enthalpies: evaluation of electronic structure approaches with emphasis on the density functional method, J. Phys. Chem. A 110 (2006) 13632–13639.
[13] J.P. Perdew, K. Burke, M. Ernzerhof, Generalized gradient approximation made simple, Phys. Rev. Lett. 77 (1996) 3865–3868.
[14] A.D. Becke, Experimental investigation of highly exergonic outer sphere electron transfer reactions, J. Phys. Chem. 88 (1984) 2547–2551.
[15] C. Lee, W. Yang, R.G. Parr, Development of the Colle-Salvetti correlation-energy formula into a functional of the electron density, Phys. Rev. B 37 (1988) 785–789.
[16] A. Tkatchenko, M. Scheffler, Accurate molecular van der Waals interactions from ground-state electron density and free-atom reference data, Phys. Rev. Lett. 102 (2009) 073005.
[17] S. Grimme, Semiempirical GGA-type density functional constructed with a long-range dispersion correction, J. Comput. Chem. 27 (2006) 1787–1799.
[18] B. Delley, Modern density functional theory: a tool for chemistry, in: J.M. Seminario, P. Politzer (Eds.), Theoretical and Computational Chemistry, 1995.
[19] B. Delley, The conductor-like screening model for polymers and surfaces, Mol. Simul. 32 (2006) 117–123.
[20] F. Marchetti, G. Pampaloni, S. Zacchini, ^{19}F NMR spectroscopy as useful tool for determining the structure of coordination compounds of MF_5 (M = Nb, Ta), J. Fluorine Chem. 131 (2010) 21–28.
[21] M. Hargittai, Molecular structure of metal halides, Chem. Rev. 100 (2000) 2233–2301.
[22] A.P. Scott, L. Radom, Harmonic vibrational frequencies: an evaluation of Hartree–Fock, Møller–Plesset, quadratic configuration, density functional theory and semiemperical scale factors, J. Phys. Chem. 100 (1996) 16502–16513.
[23] J.P. Merrick, D. Moran, L. Radom, An evaluation of vibrational frequency scale factors, J. Phys. Chem. A 111 (2007) 11683–11700.
[24] S.K. Kang, H. Tang, T.A. Albright, Structures for d^0 ML_6 and ML_5 complexes, J. Am. Chem. Soc. 115 (1993) 1971–1981.
[25] C.R. Landis, T. Cleveland, T.K. Firman, Making sense of the shapes of simple metal hydrides, J. Am. Chem. Soc. 117 (1995) 1859–1860.
[26] J. Aarik, K. Kukli, A. Aidla, L. Pung, Mechanisms of suboxide growth and etching in atomic layer deposition of tantalum oxide from $TaCl_5$ and H_2O, Appl. Surf. Sci. 103 (1996) 331–341.
[27] A.J. Edwards, The structures of niobium and tantalum pentafluorides, J. Chem. Soc. (1964) 3714–3718.
[28] D.G. Gorenstein, D. Kar, Effect of bond angle distortion on torsional potentials. Ab Initio and CNDO/2 calculations on dimethoxymethane and dimethyl phosphate, J. Am. Chem. Soc. 99 (1977) 672–677.